The Origin of Basaltic Lava Flow Textures

Thesis

The Origin of Basaltic Lava Flow Textures

A thesis presented for the degree of Doctor of Philosophy

By

Marie-Noëlle Guilbaud

M.Sci.
Université Blaise Pascal, Clermont-Ferrand
France

Department of Earth Sciences
The Open University

March 2006

Abstract

This study addresses the links between the surface morphologies, internal structure, and microtexture of basaltic lava flows. The AD 1783-84 Laki eruption in south Iceland produced a 600 km^2 basaltic lava flow-field dominated by rubbly pāhoehoe surface morphology. Field observations and aerial photograph interpretation show that the lava surface gradually changed from spiny to slabby and then to rubbly along single flows through repetitive crust disruption at the active front. The rubble was compressed into ridges when lava advance was obstructed and during large lava surges that coincided with the opening of new eruptive fissures. Fluid lava was transported in an extensive network of tubes that formed within the flows.

Petrological study of Laki near-vent tephra and lava surface samples shows that, during the eruption, the magma lost ~ 1 wt.% of water during ascent, which induced melt undercooling and triggered groundmass crystallization. This caused an ~ 10% anorthite gap across plagioclase phenocrysts and drove considerable microlite formation (up to 30 vol.%) in the early stages of flow. It is estimated that fluid lava was transported from the vent to the most distal active front, 60 km from the vent, with cooling rates of < 0.5°C/km.

Young lava flow-fields in the Reykjanes Peninsula (Iceland), and some flows from the flood basalts of the Columbia River Province (USA), have surface and internal structures intermediate between rubbly pāhoehoe and 'a'ā. The increasing size and decreasing number density of plagioclase microlites with increasing depth in these flows, as in the Laki lavas, indicate that solidification rates decreased sharply inwards. Differences between sections are attributed to variations in lava bulk composition and the transport mode, duration of emplacement, and interaction with surface water of the fluid lava. Pāhoehoe and 'a'ā have low and high plagioclase number densities respectively, with an inverse correlation with the average size and aspect ratio of plagioclases. Rubbly pāhoehoe lavas have intermediate characteristics. This correlation between lava surface morphologies and plagioclase textural characteristics provides a tool that may be useful for inferring eruption and emplacement processes from textural measurements of flow interiors in ancient basaltic lava flow-fields.

Remerciements

À ma mère et mon père qui m'ont encouragée tout au long de ce travail.

À ma sœur pour nos éclats de rire (te souviens-tu de mon volcan de sable?).

À Antoine pour nos balades en France et en Angleterre.

À tous mes fantastiques amis français (et belges) pour leur soutien outre-manche (Anne & Nico, Laetitia, Nicolas P., Marie, Vinciane, Séverine, Nicolas L., Laure-Sophie, etc).

Acknowledgements

To Steve Self, Steve Blake and Thorvaldur Thordarson for fantastic assistance in the field, great cooking and lively discussions about lavas and everything else. Special thanks to Steve for teaching me how to write proper English. I learnt so much: thank you Steve! Thank you Thor!

To Harry Pinkerton and Mike Widdownson for making the Viva a good and enjoyable experience.

To Steve Blake for his large input to my plots and his unconditional support and assistance at any time throughout these 3 ½ years. Great!

To Lazlo Keszthelyi who, with Steve S and Thor, pointed out the significance of rubbly pāhoehoe lavas and whose work and ideas contributed to this thesis.

To Steve Self and Mike Widdowson who took me to the amazing place that is the Columbia River Plateau and up to Mont St Helens. To Steve S for a wonderful trip to Socompa, too!!

To Herve Diot, Christian Moreau, Olivier Femenias and others from the University of La Rochelle who passed their passion for field-geology onto me, and encouraged me to follow my ambitions.

To Ken Hon who took me to watch gentle pāhoehoe flows during my unforgettable semester at the University of Hawaii at Hilo in Aug-Dec 2000. Thanks for all my friends there at that time (Laure-So, Laelani, Oscar etc).

To my office mates and great friends (Kirti, Ralf, Christian, John, Anne, Jose, Caco, Eliza, Elska, Charlotte, Wesley, Matt). I'll miss our lunch and tea breaks (and flour-free cakes—special thanks to Anne).

To my lovely housemates (Russell, Ziggy, Olwyn, Aaron, Caitlin, Mary, Jen, Bob, Liz) who have made my stay in England a truly fun experience and shared my good and bad days, enduring my countless complaints about British food and weather (sorry).

To my music companions and fantastic friends (Julia, Anne, Roshan, John, Mikele, Diego, Antonio). Vive Marmite! Longue vie à Marmite!

To my running companions (Julia, Benedicte, Fatima) who helped me stay in good shape and keep my breath to finish this work.

To Laurence for his contribution to celebrate the Viva!

To the magic of Iceland and its welcoming people; special thanks to the family running the Hunkubakkar guest house: thanks to Nico for renting me his bedroom, running across Icelandic grasslands, and giving bread to the horses; thanks to his parents for cooking me wonderful soups and Icelandic lamb.

To Safak Altunkaynak for being the first Turkish person (and maybe the last!) to have flown to Iceland with Iceland Express to meet me there; for surviving the bad temper of the Icelandic weather; for crossing rubbly lava flow-fields, and sharing Icelandic lamb with Norwegians.

To John Murray for introducing me to active flows on Etna; having me drive a Land Rover with the windscreen coated with flies through south England, France and Italy with an itchy swollen arm and >40° in-car temperature (one week later: "I think there is air conditioning in the car but I did not bother turning it on!" ☺).

To Benjamin van Wyk de Vries for his support and an unforgettable walk on the roof of the Vicarage one night.

And last, but not least:

To all the staff (a special thanks to Ashea who took great care of me), technicians (especially: Andrew Tindle for EMP; Michelle Higgins and Kay Green for thin-section preparation and polishing; John Taylor and Andy Loyd for posters; John Watson for XRF; John Holbrook and Liz Lomas for finances; Janet Dryden; Louise Thomas and others for VMSG) and the academics of The Open University. If there is English hospitality: then this must be it!

Thanks again to Steve Self, Steve Blake and Thor:
A great team!!!

Table of Contents

List of Figures

List of Tables

Chapter I

Introduction

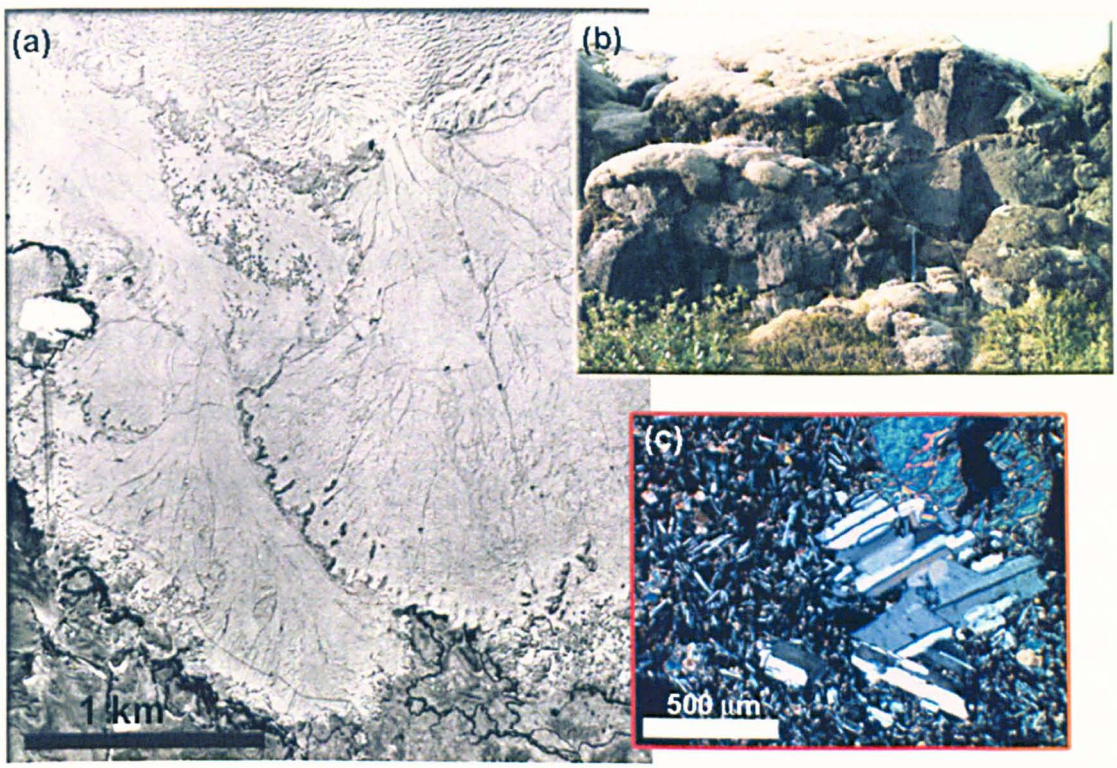

Figure 1.1: Pictures of Laki lava: (a) Extract of aerial photo of distal margin of flow-field (Eldhraun); (b) picture of river cut through marginal lobes (Eldhraun, location E3); (c) photomicrograph of lava core texture (lava core sample L7-5).

This study addresses the links between the surface morphologies (Fig. 1.1a), internal structure (Fig. 1.1b), and microtexture (Fig. 1.1c) of basaltic lava flows.

1.1 GENERAL INTRODUCTION

Basaltic lavas are the most common volcanic product on Earth and their eruption represents a frequent volcanic hazard that has important social and economical impacts, sometimes causing significant property and infrastructure damage. There is still a considerable challenge in accurately predicting lava flow trajectories during their eruption and emplacement.

Lava flows are, indeed, extremely complex phenomena. Molten lava is a mixture of silicate melt, crystals, and bubbles, and its properties vary in space and time due to the formation of viscosity gradients caused by cooling at the margins of the flow. A myriad of interconnected processes such as cooling, degassing, and crystallization controls the dynamics of lava flows, interacts with their surface morphology, and links strongly to eruptive conditions and the local topography (e.g., Peterson & Tilling, 1980; Crisp et al., 1994; Soule et al., 2004). Thus, the emplacement of lavas during an eruption can have extremely variable dynamics, showing fluctuations in the rates of advance of the flows and changes in their direction of propagation, resulting in the formation of complex lava flow-fields (Lipman & Banks, 1987; Mattox et al., 1993).

There are many ways to study lava flow processes, which include rheological and thermal measurements on the field or in the laboratory (e.g., Pinkerton & Norton, 1995; Hon et al., 1994; Bailey et al., 2005; Gottsmann et al., 2004), analogue and theoretical modelling (see reviews by Griffiths (2000) and Costa & Macedonio (2005); also Harris et al., 2004, 2005), and observations of active flows (e.g., Peterson & Tilling, 1980; Kauahikaua et al., 2003). This study proposes to link the surface morphologies and internal structure of solidified lava flows to investigate flow emplacement processes, and to investigate the way the flows are influenced by eruption parameters. This is achieved by combining field and aerial photo observations to petrological and textural studies.

The surface morphology of basaltic sub-aerial lavas (hereafter simply called lava) is generally classified into pāhoehoe (helluhraun in Icelandic) and 'a'ā (apalhraun in Icelandic). These terms were taken from the language of the Hawaiian and the Icelandic people who referred to the contrast between the smooth and easy-to-walk-on surface of pāhoehoe lavas and the dark, irregular, and jumbled surface of 'a'ā lavas that makes them difficult to cross (Fig. 1.2, see also Fig. 1.3). This study has developed from the work of T. Thordarson, S. Self, and L. Keszthelyi in Iceland on lavas from the 1783-84 Laki eruption, and from historic fissure eruptions on Reykjanes Peninsula (T. Thordarson, pers. comm. 2002), and also on lavas from the Columbia River Basalts in the USA. At all these places, they observed that a large fraction of the lava was covered by a surface layer of fragmented pāhoehoe slabs, which they called "rubbly pāhoehoe lava" (Keszthelyi & Thordarson, 2000, Keszthelyi et al., 2000, 2001).

Figure 1.2: Photograph of thin active pāhoehoe sheet flow (left) going over older 'a'ā flow (right). Photograph on bottom left shows inflating small (20 to 30 cm-thick) pāhoehoe lobe breaking out from margin of active flow. Note small-scale shattering of surface crust of the lobe caused by cooling-induced contraction of elastic skin. Pictures taken by author in September 2000 on Kilauea coastal plain.

This doctoral study is aimed at understanding the origin of basaltic lava flow textures, with a special emphasis on rubbly pāhoehoe lavas. The three places where rubbly pāhoehoe lavas have been observed have distinct characteristics in terms of the age and

duration of the eruptions, the size of the lava flow-fields, and their conditions of exposure (Table 1.1). It is noteworthy that this variety represents a major component in my attempt to address the origin of basaltic lava flow textures.

The main part of this work (Chapters 2 and 3) was conducted on lava flows from the Laki eruption because their surface is exposed almost in its entirety, and of the independent information that is available on the eruption chronology and timing of lava flow emplacement from previous work on historical accounts (Thordarson & Self, 1993; Thordarson et al., 2003). Also, the excellent state of preservation of lava selvages allowed detailed analysis of variations in the crystallinity of the flows during transport. The internal structure of the flows is only exposed along the flow margins that are covered by a thin layer of rubble. In contrast, the much larger-volume lava flows of the 15 to 16-Ma-old Columbia River basalts can only be studied in vertical section. These lavas, dominated by pāhoehoe sheet lobes, represent longer emplacement times, and so are of added interest to decipher the plausible link between crystal textures and emplacement processes. Finally, the significance of Reykjanes Peninsula lava flow-fields relies on their smaller extent, and thus easier investigation, the wide range of surface morphologies displayed, and the presence of some good sections through the flows. In Chapter 4, the field characteristics of flows from Reykjanes Peninsula and the Columbia River Basalts will be introduced and compared to those of Laki in a detailed study of sections through each set of flows studied. Finally, some conclusions on which factors and processes control the formation of rubbly pāhoehoe textures will be presented.

Table 1.1: Comparison of characteristics of lava flow-fields investigated

Location	Size of individual lava flow-fields	Maximum thickness of single flows	Surface exposure	Internal exposure	Age; duration of individual eruptions
Laki, south Iceland (1)	~15 km^3, 600 km^2	40 m	Very good	Poor	1783-84; 8 months
Reykjanes Peninsula, south-west Iceland (2)	0.07–0.26 km^3, 3–7 km^2	10 m	Very good	Poor to good	11-13th century; months/years?
Columbia River basalts Washington state, USA (3)	2,000–3,000 km^3, 10^4–10^5 km^2 (estimate)	100 m–1 km	Absent	Very good	15-16 Ma, decades?

Sources: (1) Thordarson & Self (1993), (2) Jónsson (1978), (3) Tolan et al. (1989) and Self et al. (1997).

1.2 LAVA FLOW SURFACE MORPHOLOGIES

Figure 1.3 presents some of the features that are commonly observed at the surface of well-defined pāhoehoe and a'ā flows, and will be referred to in the text. One of the main tasks of this study was to infer the mode of emplacement of lavas that present surface morphologies and internal structures intermediate between pāhoehoe and 'a'ā flows, and are called rubbly pāhoehoe lavas. The main distinctive features of these are the predominance of angular vesicular clasts (pāhoehoe crust fragments) in the top rubble and the common absence of rubble at the base of the flows (in contrast to a'ā).

The first part of this study, presented in Chapter 2, is dedicated to the study of the Laki lava surface morphologies and aims to propose a physical model for the formation of rubbly pāhoehoe along the flows. For that purpose, a total of 2 months of fieldwork was completed and combined with the study of aerial photographs to understand the organization of the lava flow-field at different scales. The samples collected during fieldwork were then studied petrologically, the results of which are presented in Chapter 3. In Chapter 4, the results of a similar investigation of the surface morphologies of lava flows observed on Reykjanes Peninsula in South Iceland (2 weeks of fieldwork) are given, along with the study of sections across ~ 50-m-thick lavas from the Columbia River Basalt Group (part of a 2-week expedition to the Columbia River Plateau). The author also spent a few days on Kilauea volcano (Hawaii, USA) before her PhD and also on Etna (Italy) and La Réunion (France) during the course of her PhD (see field pictures shown in Fig. 1.2 and 1.3).

This study is largely based on the recognition of specific features across the lava flow-fields and in the interior of the flows. It thus firmly builds on the extensive work that has been conducted over the past 50 years on the mode of emplacement of active lavas. This latter has been principally based on the observation of the persistently active Hawaiian volcanoes and on Mt Etna. The work that has shaped the current understanding of the

emplacement of lava flows is summarized below, keeping to the chronological order of the studies and focusing on lava surface morphologies and controlling factors. The early work by Einarsson (1949) on Hekla 1947–48 lavas should also be acknowledged.

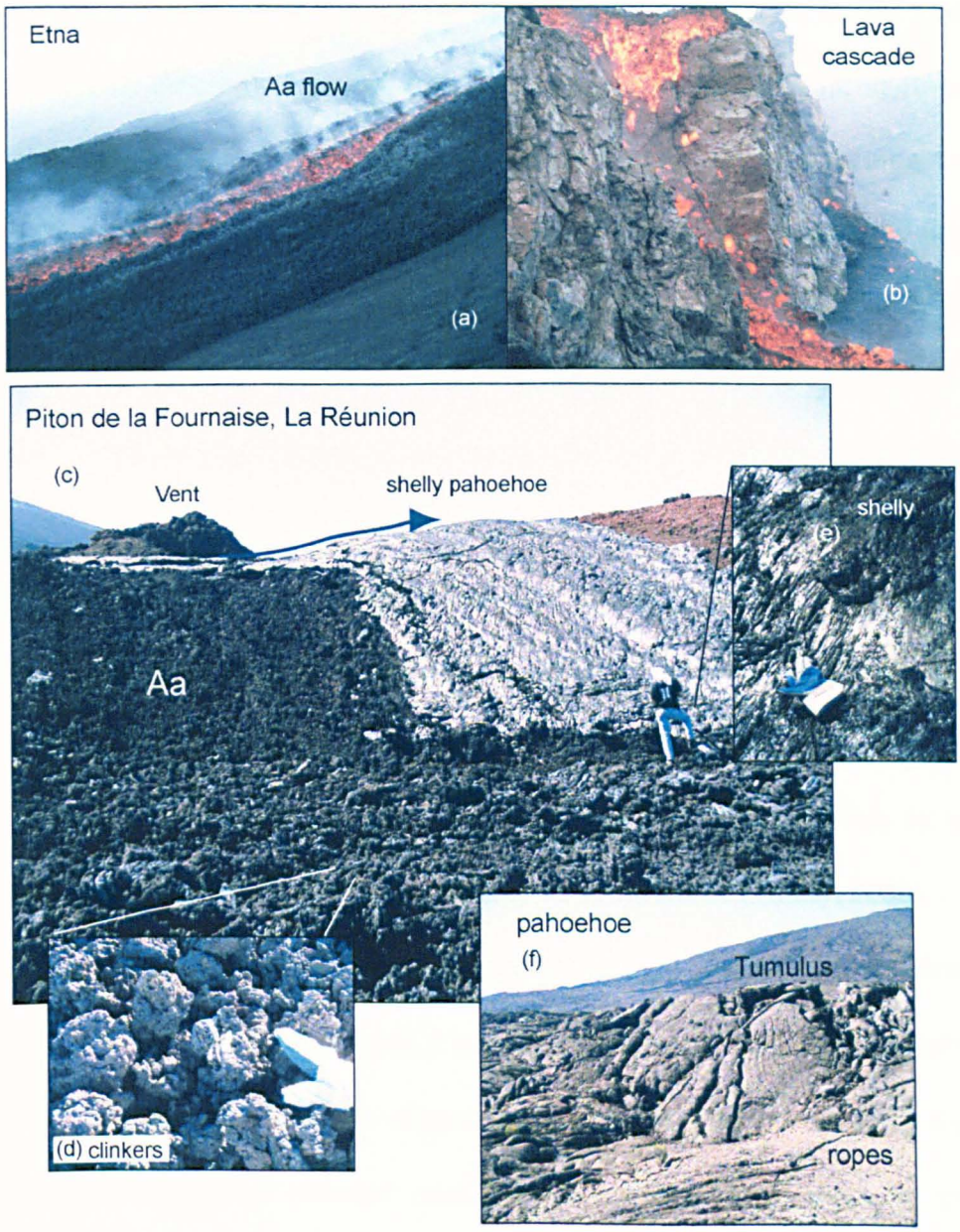

Figure 1.3: Surface features of typical pāhoehoe and 'a'ā flows produced during eruption of Mt Etna (Sicily) in Sep 2004 (a, b), and observed on Piton de la Fournaise (PF) volcano (Indian Ocean; c to f). (a) 2-days-old 'a'ā lava flow ~ 100 m from source, note channelized flow centre and stagnant margins covered by clinkers. Visible degassing of lava exposed to air. (b) Down-slope part of the same flow which cascades down old dikes. Note detachment of lava in blocks that coalesce back into a lava flow at bottom. (c) Few-days-old solidified 'a'ā flow from the May 2004 PF eruption which developed inside flows initially emplaced as shiny shelly pāhoehoe. (d) Closer view of clinkery surface of 'a'ā flow. Blocks show viscous deformation and include pieces with shelly pāhoehoe surface. (e) Smooth and glassy surface of shelly pāhoehoe. Note formation of thin threads of glass on lava surface; cut in half, these show long internal tubes. (f) Surface of extensive sheet pāhoehoe flow-field that formed during period of sustained activity in the 18th century (Lénat et al., 2001). Similar features occur on Kilauea coastal plain. Pictures by author.

Fundamental observations on Hawaiian pāhoehoe and 'a'ā were made by Wentworth & MacDonald (1953) who accurately described the morphologies and mode of advance of each lava type, underlining the more viscous character of 'a'ā flows and their low vesicularity when compared to pāhoehoe. Studying the field characteristics of active pāhoehoe flows at different distances from the vent, Swanson (1973) and Swanson & Fabbi (1973) highlighted the influence of gas loss during fire fountaining and tube transport on the rheology and thus surface morphologies of the lavas. Later, building on the rheological measurements by Shaw et al. (1969), Hulme (1974) modelled the flow of lava as a Bingham fluid and proposed that yield strength, ground slope, and lava flux are the main factors controlling the pāhoehoe-'a'ā transitions. The well-known impact of volatile degassing on raising magma liquidus temperatures and forcing crystallization was used by Sparks & Pinkerton (1978) to explain the eruption of crystal-rich viscous 'a'ā lavas from volcanoes such as Mount Etna that have high initial volatile content and thus are submitted to large undercooling upon eruption, as compared with the volatile-poor tholeitic magmas typically erupted at Hawaiian volcanoes. The impact of this phenomenon has increasingly been recognized from a large variety of settings (e.g., Cashman & Blundy, 2000).

Observing transitions from pāhoehoe to 'a'ā along single Hawaiian flows, Peterson & Tilling (1980) defined shear strain and viscosity as the main causes of morphological changes, thus accounting for the often-observed formation of 'a'ā flows on steep slopes and during periods of high lava effusion rates. In his comprehensive work on pāhoehoe morphologies, Walker defined and explained the formation of tumuli, lava pits, and many other vesicular features in the lavas, stressing the interconnected roles of lava internal pressure, underlying topography, and local supply rates (e.g., Rowland & Walker, 1987; Walker, 1989; Walter, 1991; Wilmoth & Walker, 1993). Many of the terms used in this study derive from his work (see Chapter 2).

The latest eruption of Mauna Loa in 1984 was intensely studied, and produced a wealth of information on the growth of an 'a'ā-dominated lava flow-field (e.g., Lipman & Banks, 1987). In particular, the process of degassing-induced crystallization of the erupted lava, initially proposed by Sparks & Pinkerton (1978), was recognized from the textural and petrological study of near-vent quenched lava samples and its role on the increase in the bulk lava viscosity quantified (Lipman & Banks, 1987; Crisp et al., 1994).

During the last two decades, the Pu'u' Ō'ō eruption of Kilauea has provided a natural laboratory for the study of the growth of a large pāhoehoe-dominated flow-field; the range of lava features formed was recently reviewed by Kauahikaua et al. (2003). The seminal work by Hon et al. (1994) on the growth of active sheet flows emplaced on sub-horizontal slopes led to the recognition of inflation (endogenous growth) as the main process governing the emplacement of pāhoehoe lavas and formation of an extensive network of tubes in sheet flows. They empirically defined a simple relation that links the thickness of the crust formed over the lava to the root of its duration of uplift by inflation, which is consistent with uniform conductive cooling of the lava in the crust. Features typical of inflation were subsequently identified from exposures through the very large (> 50 m thick) lava flows of the Columbia River Basalts (Self et al., 1996, 1997; Thordarson & Self, 1998) and the application of the empirical relationship between time and crustal thickening defined by Hon et al. (1994) allowed the former to demonstrate the long duration of emplacement of the flows, which favours long-lasting and steady eruptive episodes. Inflation was thus defined as a general mechanism by which lava can be emplaced and transported for long distances under near-isothermal conditions (Thordarson, 1995; Self et al., 1996, 1997, 1998; Keszthelyi & Self, 1998). Self et al. (1997) and Thordarson & Self (1998) defined general terms for describing the organization of lava flow-fields, which will be used here.

Studying variations in lava groundmass crystallinity along active channelized flows, Cashman et al. (1999) revised the relation established by Peterson & Tilling (1980) by stressing the role of groundmass crystallinity on morphological changes through its impact on yield strength. This link was subsequently strengthened by textural data collected along a set of Hawaiian flows (Polacci et al., 1999; Soule et al., 2003), and modelling of the impact of crystals on flow rheology (Saar et al., 2001; Soule & Cashman, 2005). The recognition of the formation of different surface crusts from similar batches of magma led Hon et al. (2005) to recommend that the use of the words of pāhoehoe and 'a'ā should be restricted to flows which have a solidified crust. Scaling the Peterson & Tilling (1980) relation to actual data, he also shows that the range of morphologies lava that can develop under different shear rates depends on its composition, crystal content, and temperature. Hawaiian lavas seem to show the "perfect combination" to develop a wide range of morphologies under slightly different shear rates. It should be noted that the data they show is solely from Hawaiian lavas. Finally, the most recent progress is towards the development of a new range of thermal imagery techniques to accurately measure temperature changes along lava flows and model them (e.g., Pinkerton et al., 2002; Harris et al., 2004, 2005), which will hopefully help to improve poorly-constrained models of lava flow emplacement, and may allow us to review ideas on lava cooling.

1.3 LAVA TEXTURES AND PROCESSES OF COOLING, DEGASSING, AND CRYSTALLIZATION

A fundamental control upon the way lava flows are emplaced is the cooling of the lava during transport (e.g., Crisp & Baloga, 1990; Griffiths, 2000). This influences the rheology of the lava by acting on lava viscosity, and reflects the thermal efficiency of the lava transport system, relating to crust formation, shear rates, and surface morphologies. The effect of degassing dominates over cooling when the magma ascends to the surface, erupts at the vent, and when the lava is transported over the first hundred of meters from the vent

(e.g., Sparks & Pinkerton, 1978; Lipman et al., 1985). Crystallization is the product of cooling and degassing; in turn, it acts upon lava rheology, by creating crystal networks in the melt that further increases viscosity and impedes flowage. Crystal textures record these processes, which are used in this thesis to understand rubbly lava emplacement. Figure 1.3 summarizes the main factors that cause lava to cool, lose gas, and thus crystallize, and locates them on the path of the magma and lava during an eruption. Four main stages can be defined: 1) magma maturation at depth; 2) magma ascent to the surface; 3) lava transport at the surface, that can be separated into a near-vent region and medial and distal zones; and 4) the solidification of lava within the flows during and after emplacement (i.e., after flowage).

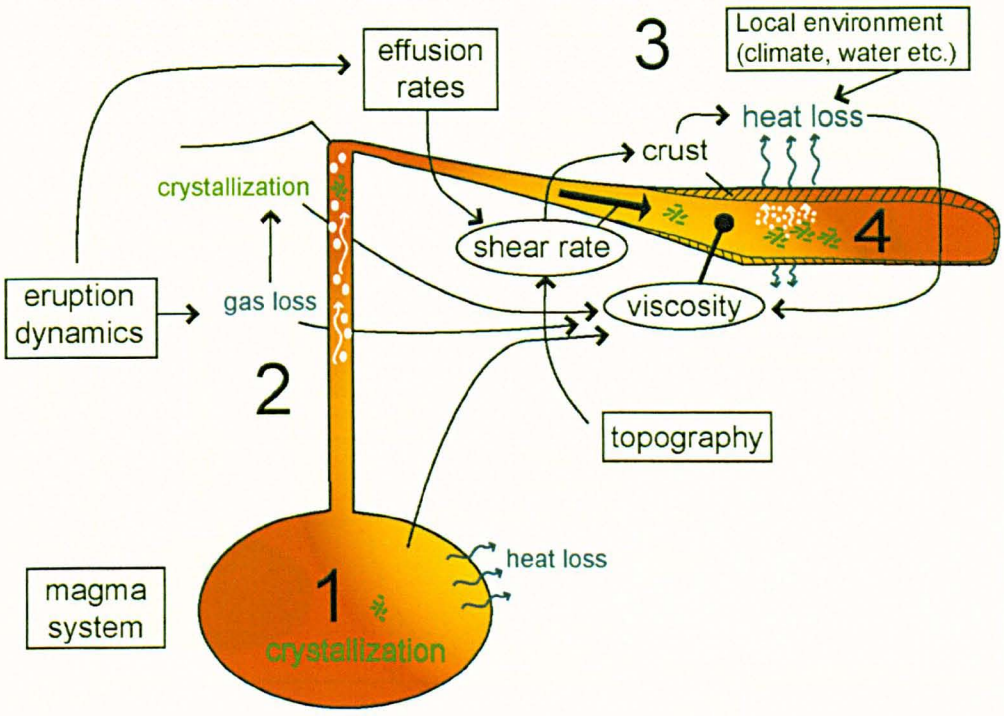

Figure 1.4: Sketch of the processes that affect magma and lava during transport. Arrows show the major links. Numbers are mentioned in the text.

The way the above stages influence the shear rate impacted on the lava, and its viscosity is reported in Fig. 1.5 (redrawn from Peterson & Tilling, 1980, and Hon et al., 2003). Pāhoehoe and 'a'ā fields, in such diagrams, define the type of crust that will form on the lava when it is quenched on contact with the air. Hence a single batch of lava, when transported (i.e., in fluid state), can go from one side of the diagram to the other (i.e., from

left to right), which realistically accounts for the formation of different surface morphologies depending on the imposed shear rate (see Hon et al., 2003 for more explanations). Changes in the crystal content of the lava and its induced effect on the lava viscosity would obviously not be reversible. It is worth noting that the viscosity can however decrease due to the release of latent heat following crystallization, thus counterbalancing the impact of crystal content on lava fluidity. Another counteracting factor is the evolution of the liquid in response to crystallization, which acts to enhance the viscosity of the residual liquid. One aim of this study is to specify the location of so-called rubbly pāhoehoe morphologies in such representations of the rheological path of lava.

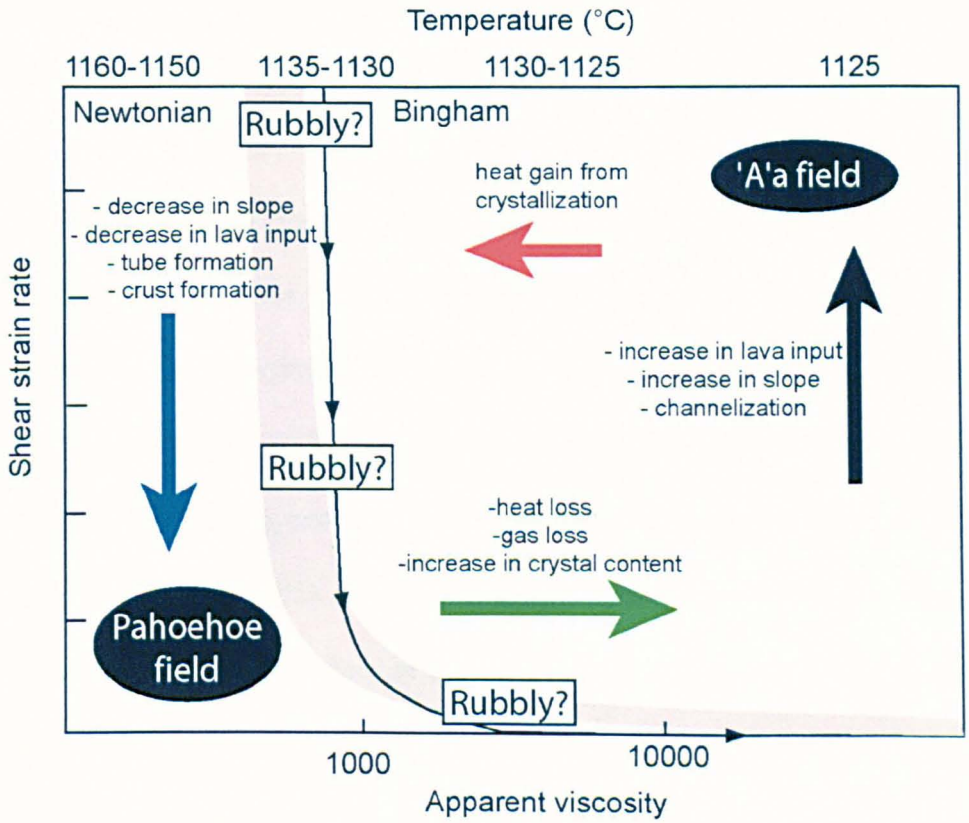

Figure 1.5: Diagram of shear-strain-rate versus apparent Newtonian viscosity redrawn from Hon et al. (2003) showing relation of pāhoehoe and 'a'ā lavas with respect to the position of an element of liquid lava in this representation (see also Peterson & Tilling, 1980). Note that this representation is based on a model of rheology of Bingham type. Grey domain defines Transition Threshold Zone which is broad limit between pāhoehoe and 'a'ā fields (Peterson & Tilling (1980)). It does not necessarily represent rubbly pāhoehoe field. Thin black line represents particular position of liquid lava with given yield strength and Bingham viscosity with arrows showing possible rheological evolution of an element of fluid lava during transport due to changing shear rates (see Hon et al., 2003). The major factors that cause changes in the position of an element of liquid lava in this diagram are shown. Note that the range of x-y values were defined by Hon et al. (2003) using data on Hawaiian lavas. Hypothetical position of rubbly pāhoehoe field by author.

How this thesis will approach the different processes represented on Figure 1.3 is now defined. The first part (Chapter 2) will focus on stage 3 of the emplacement of Laki lavas from the point of view of the mode of transport developed by the flows and the physical processes that affect surface morphologies, such as effusion rates, shear strain, and topography. The second part (Chapters 3 and 4) will address the coupled role of cooling, degassing and crystallization on the lava during all stages defined above. Chapter 3 will concentrate on their role during the eruption and emplacement of the Laki lava during the stages 1, 2, and 3. In Chapter 4, the internal cooling and solidification processes (stage 4) are tackled, grouping field, petrological, and textural work on flows from Laki, Reykjanes Peninsula, and the Columbia River Basalts. This part will expand on other studies done on Hawaiian lavas, and thus address the differences between pāhoehoe and 'a'ā crystal textures.

In order to unravel the role of cooling and degassing processes on lava rheology, crystal and glass compositions were analysed and crystal textures were quantified. Crystal compositions can be interpreted in terms of the chemistry of the magma during crystallization, and coupled with glass (liquid) compositions, they can provide information about the conditions of temperature, pressure, and water content prevailing during their formation (e.g., Putirka, 2005). Chapter 3 shows how this method was employed to reconstruct the crystallization history of the Laki magma during eruption. The size, shape, zoning pattern of the crystals and their distribution in the products were further used to infer the rates of crystallization. In Chapter 4 these observations are coupled with the analysis of the textures using the CSD method, Crystal Size Distribution.

The interpretation of crystal textures is based on the concept of magma undercooling and its link with crystallization kinetics. The following sections review the processes involved and their signature in the texture of magmatic products. Nucleation and growth are competing mechanisms, whose rates are controlled by the thermal regime of the

system. The driving force is the bulk chemical free energy between crystal and melt, which is proportional to the difference between the liquidus temperature (T_{liq}) and the magma temperature (T_m) (i.e., degree of undercooling, ΔT) (e.g., Dowty, 1980b). Theory and experiments consistently show that nucleation and growth rate functions define a bell-shape relationship with ΔT, with the nucleation rates defining a higher peak than growth rates (see Fig. 1.6) (e.g., Brandeis et al., 1984; Kirkpatrick, 1981; Couch et al., 2003).

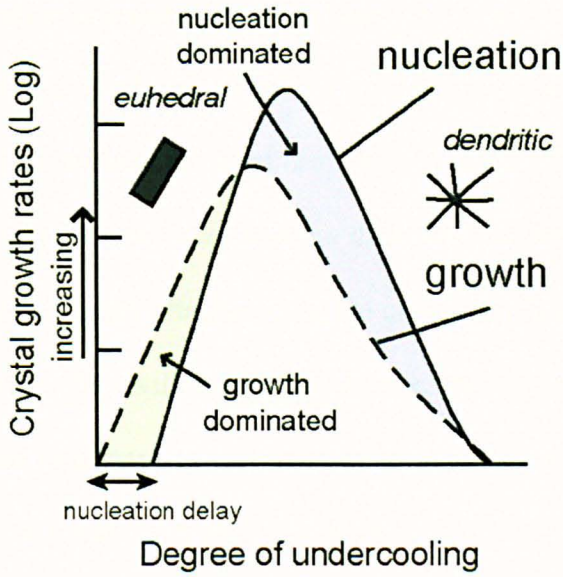

Figure 1.6: Variation of nucleation and growth rates with degree of undercooling. Note dominance of growth over nucleation rates at low degrees of undercooling (green domain), and dominance of nucleation rates at higher degrees of undercooling (blue domain). Vertical scale is logarithmic. Shape of curves was taken from model presented by Brandeis & Jaupart (1987a). Typical crystal shapes at low and high undercooling conditions (euhedral and dendritic respectively) are shown schematically.

Crystal nucleation is thought to largely control the final texture of an igneous rock, in that it determines the initial distribution of crystals in the melt, which then controls the maximum size each crystal can reach (e.g., Marsh, 1988; Cashman, 1990). As shown in Figure 1.5, nucleation is very sensitive to undercooling; nucleation rates thus show large variations in magmatic products (Cashman, 1990). Experiments show that a finite amount of energy (or undercooling, as shown above) is required for nucleation to proceed. Commonly called nucleation delay, this barrier represents the energy required for nuclei to reach a critical size at which they are stable and thus grow. This holding effect is partly

reduced in natural melts by the presence of heterogeneities that provide sites for nuclei and substrates for crystal growth such as bubbles or pre-existing crystals (i.e., heterogeneous nucleation, Lofgren, 1983). The abundance of these nuclei and the nature of the substrates available can then control the pattern of crystallization. Varying these parameters in experiments, Lofgren (1983) showed that the entire range of basaltic textures could be reproduced.

Even though nucleation is critical for crystallization, the ensuing growth of the crystals is fundamental in that it controls the chemical evolution of the residual melt, and also governs the amount of latent heat released. For growth to be effective, elements have to diffuse from the liquid to the interface (volume diffusion), across the interface (interface diffusion) and atoms to be finally attached onto the crystal surface (surface diffusion). The limiting factor in these transfers will thus define the mechanism and rates of growth.

These processes are important in that they determine the response of the magma to processes that destabilize the system, and thus drive re-equilibration (i.e., reduction of free energy). In the case studied, these are mainly rapid degassing events during magma ascent and the cooling of the lava during transport (i.e., Fig. 1.4). Brandeis et al. (1984) note that the latent heat released by crystallization can buffer the cooling rates and result in the attainment of an equilibrium state at which crystal growth rates are low. Consistent with this observation, Keszthelyi (1995) measured a sharp temporary decrease in lava cooling rates through the first few centimetres of active pāhoehoe lobes, which he attributes to the initiation of crystallization.

The impact of cooling rates on the mode of crystallization of basaltic melts, and more particularly on plagioclase formation that is the dominant phase in crystallising basalt melts, has been well studied experimentally, especially by Kirkpatrick, Lofgren, and co-workers (e.g., Kirkpatrick, 1981; Lofgren, 1983). They showed that the shape of plagioclases, in particular, varies widely with the degree of undercooling (or cooling rates)

because of changes in the growth mechanisms of the crystals in diffusion-limited conditions (see above and Fig. 1.7). Thus, the skeletal shape of crystals is a definite indication of high cooling rates. Also, the formation of zoning across the crystals may reflect disequilibrium growth (high growth rates), which may *not* involve chemical disequilibrium. Inclusion of matrix glass and microlites in the crystal rim may occur due to the breakdown of planar surfaces along the crystal borders with formation of embayment later closed by crystal overgrowth (e.g., Kohut & Nielsen, 2004). By contrast, the formation of planar, crystallographic faces commonly called "euhedral shape" is indicative of interface-controlled growth and suggests low temperature gradients and equilibrium conditions (slow growth rates). Other aspects of plagioclase crystallization and the use of crystal size distributions are presented in Chapter 4 and reviewed by Cashman (1990, 1993).

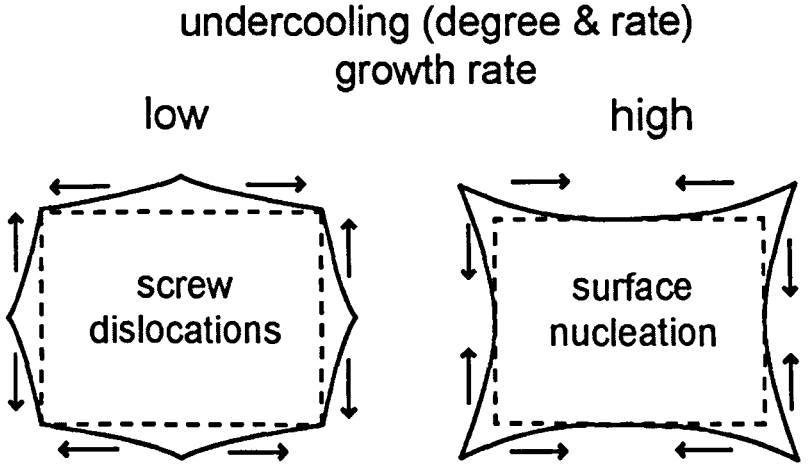

Figure 1.7: Schematic representation of combined effect of crystal growth rates and degree and rate of undercooling on dominant growth mechanism of crystals (redrawn from Kirkpatrick, 1981). Arrows indicate direction of crystallization steps (or growth increments). Low to medium degree of undercooling (interface-controlled growth): *Screw dislocation mechanism* whereby the crystal layer grows from the centre of the faces outwards, and achieves planar surfaces (low surface energy). High degree of undercooling (diffusion-controlled growth): *Surface nucleation mechanism* that favours crystallization from crystal corners (better diffusion at corners due to larger contact with fluid) and migration of crystallization steps towards the centre of the faces.

Crystallization kinetics can also impact on the phase equilibria of magmas because of their high dependence on the structure of the minerals. They can change the sequence of phases crystallizing out of a melt because of the differential nucleation and growth rates of

separate minerals. In other words, different mineral phases may react in a different way to a single undercooling imposed to the system (e.g., Cashman, 1993). Olivine, clinopyroxene, and feldspar were experimentally shown to have increasing reluctance to nucleate and grow in that order (Gibb, 1974; Walker et al., 1976, 1978; Grove & Bence, 1977; Lesher et al., 1999; Donaldson, 1979), which is thought to relate to the increasing degree of complexity of their structures (Dowty, 1980a) and hence higher surface energies (Gibb, 1974). For plagioclase, the necessity of large structural re-arrangement for changes in the chemical range An_{30}-An_{90} may explain the crystallization delays and the tendency of the crystals to be irregularly zoned (Allègre et al., 1981, referring to Samoylovitch, 1979). Olivines show predictable nucleation delays of $\Delta T < 13°C$ from basaltic melt (Donaldson, 1979), although plagioclase nucleation is highly variable (Gibb, 1974).

The effect of processes of cooling and degassing on crystallization kinetics, that this study most specifically tackles, will now be addressed. The role of the former on increasing the undercooling of the melt seems obvious. Perhaps less evident, however, is the fact that exsolution of water from the melt, that almost invariably occurs when magma decompresses when rising to the surface, is a major factor for causing large degrees of ΔT. It produces a large increase in magma liquidus temperatures that is unlikely to be compensated by some crystallization or cooling before the magma reaches the upper parts of the conduit, or even the surface, just because of the restricted amount of time available. An additional effect of water degassing and cooling is that they increase the viscosity of the residual liquid, which will slow the diffusion rates of elements through the liquid, in turn favouring disequilibrium crystallization and large crystallization rates.

As well as water content, crystallization kinetics will also be affected by magma chemistry and specific conditions of pressure and temperature. Grove et al. (1992) and Gaetani et al. (1992) clearly showed the large impact of water content on the stability of mineral phases. Hammer & Rutherford (2002) and Couch et al. (2003) have focused on

using dynamical petrological experiments to quantify pressure effects on crystallization kinetics that are applicable to the eruption of Pinatubo dacite and Montserrat andesite. The starting material in both experiments had ~71 wt.% SiO_2 and a calculated viscosity of ~10^4 Pa/s at liquidus temperature (PELE model; Boudreau, 1999). It is to be noted that the evolved composition of the material used by Couch et al. (2003) compared to a typical andesite comes from that they used a material representative of the groundmass composition of Montserrat andesite. These two sets of experiments consistently_show a correlation between decompression rates and thus timing of degassing with the composition, morphology, size, and number density of forming crystals. Nucleation and growth rates peak at ΔT ~150°C for the groundmass composition of Montserrat andesite in Couch et al. (2003) experiments, while the maximum nucleation rate is at ΔT ~210°C for Pinatubo dacite as shown by the experiments of Hammer & Rutherford (2002). The crossover of each curve delimitates a region of dominant growth rate at low ΔT, and large nucleation rates at higher ΔT (ΔT 34-93°C and ΔT >139°C, respectively, see Hammer & Rutherford, 2002). Larsen (2005) obtained the same trends from similar experiments on Aniakchak rhyodacite, but for lower ΔT (maximal nucleation rates for ΔT = 95°C). For basaltic melts, the peaks of nucleation and growth rates are expected to occur at lower undercooling due of the higher diffusivity of elements in those compared to andesitic and dacitic melts (Lowry et al., 1982).

The specific subjects approached in each Chapter will now be re-stated, showing how they link together to unravel the questions raised.

1.4 SUMMARY

- This study attempts to characterize the mode of emplacement of rubbly pāhoehoe lavas. Those have surface characteristics different from the typical pāhoehoe and 'a'ā lava types, and their study therefore may provide fundamental information about the factors controlling lava rheology and surface morphologies.

- This work was separated into three main parts that represent the chapters forming the main body of the thesis:
  - Chapter 2: The Laki lava flow surface morphologies are examined through a combination of field study, aerial photograph mapping, and examination of historical accounts. This investigation aims to develop a physical model for the formation of rubbly pāhoehoe morphologies for the Laki lavas.
  - Chapter 3: The petrology and petrography of glassy samples of tephra and lava that represent different stages in the evolution of the Laki magma and lava during eruption is studied in order to understand the role of degassing and cooling processes on the morphological features described in Chapter 2.
  - Chapter 4. The surface characteristics of rubbly lavas observed along some flows on Reykjanes Peninsula and in sections through the Columbia River basalts is described, using a similar approach to that used in Chapter 2. This part focuses on the description of sections through the flows, including some from the Laki lavas and others from Hawaiian lavas, and uses petrographical observations assisted with CSD analysis to characterise the cooling and solidification processes that take place inside flows with distinct surface morphologies. The link between lava textures, eruption parameters and emplacement processes is finally addressed.

Chapter II

Morphology, surface structures, and emplacement of lavas produced by Laki, A.D. 1783–1784

This chapter is published as:

Guilbaud, M.-N., Self, S., Thordarson, T., and Blake, S., 2005, Morphology, surface structures, and emplacement of lavas produced by Laki, A.D. 1783–1784, *in* Manga, M., and Ventura, G., eds., Kinematics and dynamics of lava flows: Geological Society of America Special Paper 396, p. 81–102.

Some of the information included was used in the following co-authored paper:

Keszthelyi, L., Thordarson, T., McEwen, A., Haack, H., Guilbaud, M., Self, S., Rossi, M., 2004, Icelandic analogs to Martian flood lavas: Geochemistry, Geophysics, Geosystems, v. 5, no. 11.

2.1 ABSTRACT

The A.D. 1783–1784 Laki eruption in Iceland was one of the largest basaltic eruptions in historical times. In only 8 months, >14 km^3 of lava was erupted, creating a ~600 km^2 lava flow field. The flow field presents a wide range of surface morphologies that can be subdivided into shelly, spiny, slabby, and rubbly pāhoehoe types. This report constitutes the first comprehensive description of the Laki lava flow field, and links the overall flow field organization seen on aerial photographs with key textural features observed in the field. By examining the transitions between the different surface morphologies, a conceptual model for the formation of a rubbly pāhoehoe surface during the emplacement of a lava flow could be presented. Patterns in the distribution of surface morphologies in the Laki flow field are combined with information from historic accounts to determine the impact of pre-existing topography and changes in lava supply rate on flow morphology. The majority of Laki flows were initially emplaced as inflating pāhoehoe sheets with hummocky margins. These gradually developed rubbly pāhoehoe surfaces through progressive disruption of crust immediately behind the hummocky margin or at the active flow front. This sequence was repeated when fluid lava stored within the interior of the inflating sheet lobes broke through at the flow front to advance the flow. The quasi-absence of 'a'ā-type clinkery crusts shows that the lava never reached the point of continuous surface deformation by tearing of core lava at the leading edge of the flow. The Laki lavas have surface characteristics different from pāhoehoe and 'a'ā, and the term rubbly pāhoehoe is appropriate for the dominant surface texture on the Laki flow field.

2.2 INTRODUCTION

During the AD 1783-84 Laki eruption, 14.7 km^3 of lava was erupted in only 8 months, which is considerably larger than the volume of lava produced in common historic basaltic eruptions. By comparison, the Pu'u 'Ō'ō eruption has only produced ~2.2 km^3 of lava in 20 years of near-continuous activity (Heliker & Mattox, 2003). Thus, lava eruption and effusion rates at Laki were exceptionally high, and the largest values estimated have been compared with those involved during flood basalt eruptions (Thordarson & Self, 1993; Self et al., 1997).

The surface morphology of the Laki lava field shows a number of characteristics that depart significantly from classic pāhoehoe and 'a'ā, which were themselves initially defined from Hawaiian lava flow-fields (Wentworth & Macdonald, 1953). Its characteristic feature is an extensive cover of fragmented, but typical, pāhoehoe crust, hence the designation of this crust type as "rubbly pāhoehoe" (Keszthelyi & Thordarson, 2000; Keszthelyi et al., 2001). Moreover, this surface morphology has been identified in many other Icelandic lava flow fields (Keszthelyi et al., 2004). Interestingly, it also characterizes some lava flows in the Columbia River flood basalts (Self et al., 1997), and lavas in drill cores through the Kerguelen plateau (Keszthelyi, 2000, 2002), whereas it does not appear to any large extent in Hawaiian lava flow-fields. The large-scale surface features on Laki lavas have similarities to those seen on images of some lavas flows on the surface of Mars (Keszthelyi et al., 2000, 2004).

The Laki eruption sequence is well constrained (Thordarson & Self, 1993 and references therein), and because the surface of the lava is accessible almost in its entirety, the Laki lava flow-field represents an ideal site to study rubbly lava textures in relation to emplacement dynamics. Understanding these textures will increase our knowledge of the products of large-volume basaltic eruptions and lava transport processes.

This account constitutes the first comprehensive description and map of the Laki lava flow-field. It concentrates on linking the global flow-field organization observed from aerial photographs with key textural features observed in the field. Combining these observations with eye-witnesses accounts (Steingrímsson, 1788), a conceptual model of rubbly pāhoehoe formation can be presented. The distribution of surface morphologies is explored to determine the impact of topography and variations in lava supply rate on the morphological features.

The general setting of the eruption, the characteristics of the magma involved, the eruption chronology, and terminology used is first introduced. Next, the basic surface and internal characteristics of shelly, spiny, slabby and rubbly pāhoehoe lava types on the Laki flow-field are defined. The distribution of lava types in separate sectors of the flow-field is then presented, the morphological transitions are examined, and, in some places, the evidence is interpreted and the processes that formed them are discussed. This section contains detailed field descriptions that some readers may wish to pass over, going straight to the general interpretations given in the section entitled "Model of emplacement of the Laki lavas". Finally, a brief set of conclusions is presented. A detailed description of the petrology and petrography of the Laki lava, and an analysis of the role of degassing and cooling in the origin of specific textures, will be presented in Chapter 3.

2.3 BACKGROUND

The Laki eruption is thought to be part of a 2-year-long volcano-tectonic episode on the Grímsvötn volcanic system, in the East Volcanic Zone of south Iceland (Thordarson & Self, 1993 and references therein, Fig. 2.1). The eruption took place along a volcanic fissure-swarm linked to Grímsvötn central volcano, and created a NE-trending 27 km-long fissure, along which more than 140 vents were opened (see Thordarson & Self, 1993; Thordarson et al., 1996, 2003). The cause of the eruption is thought to be related to the

building of compressive stresses and subsequent failure of the crust above the feeding magma reservoir (Gudmundsson, 1987), while the fissure follows the principal direction of shear stress generated by plate-pull in Iceland (Gudmundsson, 2000). The cause for the migration of the eruptive activity along the fissure from SW to NE, thus towards the central volcano, is not known.

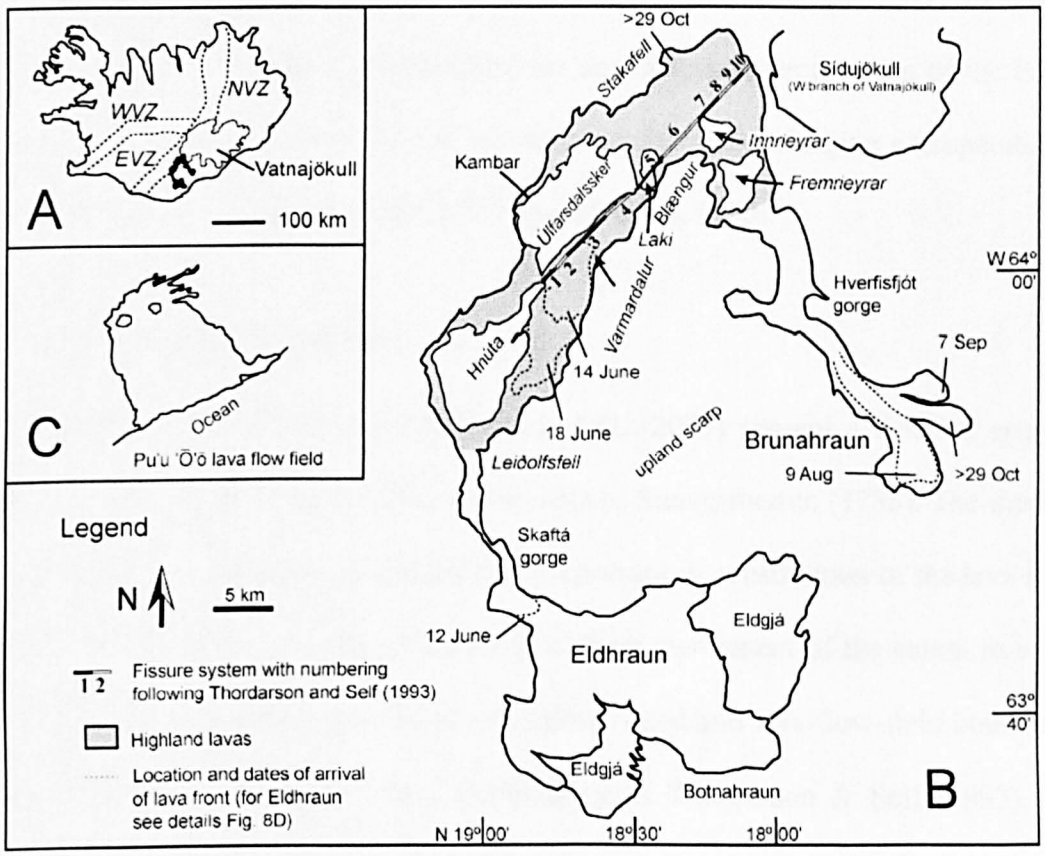

Figure 2.1: Location and general map of the Laki lava flow-field. A) Location map of Laki fissure and lava flow-field (filled in black) in Iceland; EVZ, NVZ WVZ refer to approximate extent of East, North and West Volcanic Zones, respectively. B) Map of the Laki lava flow-field with location of places cited in the text; extent of highland lavas in grey; Sídujökull is part of the Vatnajökull ice-cap. C) Outline of extent of Pu'u 'O'o lava flow-field in 2004 at the same scale as Fig. 1B.

2.3.1 Petrology of the lava

Products of the eruption are quartz-tholeïte basalt of uniform composition, implying efficient magma homogenisation in a large reservoir prior to eruption (e.g. Sigmarsson et al., 1991; Thordarson et al., 1996). Mineral phases are plagioclase (An_{95-40}), clinopyroxene (Wo_{24-42} En_{31-51} Fs_{14-35}), olivine (Fo_{75-40}) and Fe-Ti oxides (mainly titanomagnetite) (e.g.,

Grönvold, 1984). Total lava crystallinity varies between 20 and 35 vol.% in glassy selvages, and rises to 90 vol.% in samples from the core of the lava. Phenocrysts (> 100 μm) comprise <3 vol.% of the rock and between 5 and 30 vol.% of the groundmass matrix is occupied by microphenocrysts (20–100 μm) and microlites (<20 μm). Tephra clasts are poorly crystalline (0 to 10 vol.% total crystallinity, Thordarson et al., 1996) and do not contain microlites, which suggests that these formed during flowage. Fe-Ti oxides are absent in lava glassy selvages indicating that the emplacement temperature of the lava is above their temperature of appearance in the melt. Geothermometres give a temperature of emplacement between 1110 and 1130°C (Thordarson et al., 1996).

2.3.2 Chronology of the eruption

Thordarson & Self (1993) and Thordarson et al. (2003) present a detailed eruption chronology, on the basis of the eyewitness accounts of Steingrímsson (1788). The mode of magma discharge from the fissure and the major episodes in construction of the lava flow-field are more specifically reported here, along with an assessment of the extent to which the lava interacted with water, snow or ice. Localities cited and lava flow-field boundaries are given on Fig. 2.1, using the same terminology as Thordarson & Self (1993). The *Eldhraun branch* refers to the part of the lava that reached the coastal plain by flowing down the Skaftá gorge. It does not include lava that now fills the gorge. The term *Brunahraun branch* designates, in the same way, the lava emerging out of the Hverfisfljót gorge, and spreading onto the flat coastal plain.

The fissure can be divided into 10 partially overlapping segments that opened successively from southwest to northeast during the eruption. The fissure system cuts across the older hyaloclastite hill of Laki. This hill has been taken as a reference point to differentiate between the SW cone row and the NE cone row of the fissure (Thordarson & Self, 1993). Fissure segments 1 to 5 are part of the SW row; 6 to 10 are part of the NE row.

Each fissure segment corresponded to a separate eruptive episode, and each eruptive episode began with sub-plinian activity followed by vigorous Hawaiian-type lava fountaining associated with a high gas- and ash-loaded eruption column. Magma discharge rate increased rapidly from the fissure, at eruption rates from 1 to 5 × 10^3 m^3 s^{-1}, and lavas quickly spread onto the highlands at effusion rates from 2 to 8 × 10^3 m^3 s^{-1}. Relatively late during each episode, the fissure vent segments evolved into a row of single vents in the form of tephra-spatter cones (there are also two tuff cones along segments 4 and 6). Lavas were then produced at much lower rates at each fissure, probably mainly from breaches through the cones, while the main activity shifted north-eastwards. Thordarson and Self (1983) discuss the sub-surface mechanisms for the eruption.

The eruption started on the 8th of June 1783. During episodes 1 and 2 (8 to 14 June) lavas invaded the Skaftá river bed on the north of the Hnúta ridge and filled partially its gorge to emerge on the coastal plain as a lava surge on 12 June, forming the beginning of the Eldhraun branch. Magma discharge peaked during the opening of fissure 3, when segments 1 and 2 were still active (Thordarson & Self, 1993). The lava partly covered the Varmárdalur valley, reached the Skaftá gorge and emerged onto the coastal plain a few days later, enlarging the Eldhraun coastal branch (for more details see Thordarson et al., 2003). Episodes 4 and 5 (23 June–20 July) delivered surges of lava to the coastal plain, further expanding the lava flow-field. During episodes 6 to 10, lava covered the Skaftá flood plain at the south of Stakafell and then headed southwards towards the Hverfisfljót river gorge. Lava emerged from the gorge on 7 August. The coastal lava branch of Brunahraun was formed in five main surges lasting until the end of October. The fissure emitted lava until 7 February 1784.

In summary, accounts show that advance of the flows was intermittent and strongly related to fluctuations in magma discharge. Throughout the eruption, lava was delivered to the coastal plain in major surges. In the periods between each surge, the lava supply was

lower and steadier. The lavas produced during the early fountaining episodes are those that reached the coastal plain, whereas the flows formed later in each episode produced short flows now covering the highlands.

Historical accounts and field evidence testify of the interaction of lava flows with water at many stages of their emplacement. The first lavas emplaced over an area interacted explosively with the water-loaded substratum, producing extensive groups of rootless cones (see Thordarson & Self, 1993, and references within, and Thordarson et al., 1998). These are now partially covered by later-emplaced lava flows. The water outflow from the Skaftá and Hverfisfljót river gorges onto the coastal plain was reported to dwindle and then to stop completely just before the arrival of the first lava surge out of each gorge, which occurred the 10 June for Skaftá river gorge and the 3 August for Hverfisfljót river gorge (see Thordarson & Self, 1993; Thordarson et al., 2003). According to accounts, the river outflow from the Skaftá river gorge resumed just before the emergence of lava from the Hverfisfljót river gorge (14–29 September), and then stopped again. Lava flows were reported invading river streams during their emplacement on the coastal plain, which must have caused major disruption of the course of the rivers. As for the potential contact of the lava with snow, accounts do not mention any snow fall during the course of the eruption. They do not report, either, of lava flowing over snow or ice, hence, the area is presumed to have been devoid of snow cover when the eruption started. Further pertinent details will be given when describing separate zones of the flow-field.

2.4 METHODS AND TERMINOLOGY

2.4.1 Terminology for flow-field organization and lava emplacement

The structure of the Laki lava flow-field is complex and its largest-scale elements are best observed in aerial photographs. A few terms have been selected to describe the organization of the flow-field. They are *lava flow-field, lava flows* and *lava lobes*. These

were adopted from others by Self et al. (1997) and are adapted here for the Laki case. In the text below, morphological keys that allowed us to distinguish the limits of each different flow element are described. The term *branch* is used here as a non-specific geographical term referring to distinctive parts of the flow-field. It can describe individual lobes, flows or simply separate parts of the flow-field, and does not have a genetic implication.

The term *lava flow-field* designates the entire lava product of the eruptive event. The extent of the Laki lava flow-field is easily traced since it is the most recent volcanic product in the area (apart from ash deposits), and because its relatively young surface has suffered limited post-emplacement erosion and coverage by sediments.

A *lava flow* is a lava body formed by the solidification of an individual outpouring of lava from the vent. It would then correspond, ideally, to a single episode of magma effusion during the eruptive event. Morphologically, a lava flow has steep monoclinal margins and a continuous top. It rarely forms a single stretch of lava but consists of a succession of lobate segments that represent the sequential emplacement of the lava flow ("lobe by lobe emplacement" described in Hawaii, see Hon et al., 1994). These lava flow segments are what the term *lava lobes* refers to here. An *outbreak lobe* is a lava lobe that originated from local breakage of the front of a source lobe by release of the lava contained in its core. Finally, it should be noted that lava lobes occur on several scales. For instance, a metre- or kilometre-scale lava lobe defined on aerial photographs can be found to be composed of cm- to m-scale lava lobes in the field. *Toes* are small, centimetre- to decimetre-sized, budding lava lobes.

When lobes are produced by outbreaks from along the margin of a single large source (generally a larger lobe), they may merge laterally by coalescence of their individual surfaces into a continuous crust and then expand the surface of the source lobe. Continual inflation of the homogenized lobe typically produces a broad lava body with a very flat

upper surface and steep monoclinal uplift margins (Hon et al., 1994). This type of lobe is called here a *sheet lobe*, referring to its morphology. The term *hummocky* describes the highly irregular upper surface of a lava flow composed of numerous lava lobes which failed to coalesce completely and underwent differential inflation, creating features called *tumuli* (dome-shaped features, singular, *tumulus*) and *lava-rise pits* (circular depressions) (Walker, 1991). Lava rise pits are common in sheet lobes and form when the lava initially flowed as a thin layer around an obstacle, and then inflated around it. The initial obstacle appears then as a depression bounded by very steep up-lifted margins, which is often covered by breakouts that emerged from underneath the surrounding inflated crust (Walker, 1991). The fractures and open gashes created by inflation processes and propagating through the interior of the lava crust will be called *inflation clefts*, following Walker (1991). The term *crack* will be reserved to describe long fractures of km scale that are not specifically related to inflation processes. When the cracks are associated with an extensional component, therefore exposing the lava underneath, they will be called *extensional cracks*. Also common in many flow-fields, *surface breakouts* emerge from the interior of flows, breaking through the upper crust and spreading over the surface.

2.4.2 Thickness of upper lava crust as a chronometre

As illustrated in the next sections, the interior structure of the flow is dominated by the division into an upper lava crust and a lava core (as defined in Self et al., 1997). Several studies of many other basaltic lavas have shown that the upper crust is formed during active inflation and on-going degassing of the flow (Hon et al., 1994) and that this structure is indicative, alone, of an inflation-dominated emplacement (Cashman & Kauahikaua, 1997). Hon et al. (1994) found that the thickness of the crust in active Hawaiian sheet flows is proportional to the square root of the time during which fluid lava

is continuously supplied in the interior of the flow. To calculate the time during which the flow inflated, it is only needed to invert their equation, giving:

$$t = 164.8\ C^2,$$

where t is the time (hr) and C the upper crust thickness (m).

This has important implications for our work and useful applications. It allows us to estimate the amount of time needed to form a given crust fragment in the flow-field, and therefore it tells us the amount of time elapsed before the disruption of the surface took place. The only assumption that is made in applying this "chronometre" is that the thermal properties and heat transfer processes of Laki lava flows were sufficiently close to Hawaiian lavas such that they show a similar cooling rate. This condition has been examined by Keszthelyi et al. (2004), using the model presented by Keszthelyi & Denlinger (1996). They found that any realistic differences in thermal properties should not result in more than a 25% uncertainty. Accordingly, forming a 1-cm-thick crust requires ~1 min, although it takes about 1.5 hour (± 20 min) to build a crust of 10 cm in thickness and about 7 days (± 1.4 days) to form a 1-m-thick crust. A 5-m-thick crust would need ~5 ± 1 months of inflation.

2.5 DESCRIPTION OF LAKI LAVA TYPES

Lavas of the Laki lava flow-field can be classified according to their surface morphology on the basis of the characteristics of the outer surface of the lava and on the type of fragments covering that surface. Spiny, slabby, and rubbly pāhoehoe types are distinguished (Table 2.1). The text refers briefly to a shelly pāhoehoe type, which possesses a very vesicular outer surface and is typical of near-fissure Hawaiian flows (described by Wentworth & Macdonald, 1953; Swanson, 1973). The general characteristics of these lava types are described below but it is worth noting that, at Laki, there is often complete transition between these types. The characteristics of each of these

types also vary within the flow-field. A practical issue in studying the lava in the field is the presence of a green moss (*Racomitrium*) which covers almost the entire lava surface, commonly forming a 5–10-cm-thick carpet. When accustomed to it, it appears that this moss highlights the morphological differences between the surface types rather that hiding them: it can also be lifted up to uncover the surface of the lava, when necessary. The surface textures of the Laki lava is first presented, followed by details of the internal structure. The features described will then be interpreted towards the end of the paper.

Table 2.1: Summary of lava types and process of formation

Lava type	Formation process	Figure number
Shelly pāhoehoe	Flow of gas-rich lava along fissure	2.2A
Spiny pāhoehoe	Small-volume breakouts of lava through active flow front	2.2B, 2.2C, 2.4, 2.5A, 2.5C, 2.5D, 2.9, 2.10A, 2.10B, 2.11D
Slabby pāhoehoe	Extensive surface deformation of large inflated flow by fragmentation of thin outer crust	2.2E, 2.3A, 2.7B, 2.8C, 2.9, 2.10A, 2.10B, 2.11C
Rubbly pāhoehoe	Repeated cycles of inflation and surface crust brecciation of slabby pāhoehoe lobes; compression of fragments at surface creates ridges of rubble	2.2H, 2.2F, 2.2G, 2.3B, 2.3C, 2.5B, 2.8C, 2.9

2.5.1 Surface morphologies

Shelly pāhoehoe texture occurs on small lobes or large flat-topped sheet lobes with a smooth vesicular surface (Fig. 2.2A) which are restricted to the proximal sector around the fissures. These surfaces quickly evolve to spiny pāhoehoe away from source.

Spiny pāhoehoe lavas typically consist of multiple lobes 5–20-m-long, to larger-scale sheet lobes with a coherent crust, smooth at metre scale and rarely fragmented (Figs. 2.2B, 2.2C, 2.2D). Sheet lobes bordered by hummocky marginal lobes compose the larger-scale morphology of a flow branch dominated by spiny pāhoehoe surfaces. The surface of sheet lobes is typically buckled, with evenly distributed polygonal inflation clefts. Lava rise pits are common within the sheet lobes and along their margins (Fig. 2.2D). Marginal inflated lobes form tumuli with deep axial and lateral inflation clefts. Centimetre- to decimetre-scale coarse ropes are common and, on a centimetre scale, the surface of the lava is slightly irregular, covered by numerous millimetre- to centimetre-long spines.

Slabby surfaced lava is characterized by a jumble of large tabular to curved pieces of spiny pāhoehoe crust, dislocated and tilted-up on the flow surface (Fig. 2.2E). Lava rise pits and inflation clefts are also common on these flows. The thickness of individual crustal slabs ranges from a few centimetres to several decimetres but is most commonly 20–50 cm and sometimes the slabs are imbricated. Smaller-sized rubble is often mixed in between the slabs as a minor component (see next section for description of this rubble). The external surfaces of the slabs may be coherent and slightly spiny or convoluted with ropy features and stretched toes attached to the slab interior. Some slabs have undersides covered by numerous glassy protrusions typical of gas blister walls. In other cases scrape marks are present (Fig. 2.3A) and many slabs have a reddish contorted base.

Rubbly pāhoehoe lavas differ from slabby-surfaced lavas by being largely dominated by loose blocks of pāhoehoe lava crust generally <10 cm in size (Figs. 2.2G, 2.3B, 2.3C, see also Keszthelyi et al., 2004). These are often piled in metre-sized mounds forming elongated and sinuous ridges (ridged rubbly type, see Fig. 2.2G) along margins of individual lobes or in front of obstacles. A large variety of types of rubble has been observed, changing around the Laki flow-field and also within the same pile. Usually present at the top of the pile, the largest blocks are commonly 20–50 cm thick and 1–2 m across, similar to these described above. Coherent slabs >1 m thick are uncommon and often form collections of slabs with almost identical thickness and basal-scrape marks. Filling the gaps are smaller fragments of slabs with similar characteristics. Fragments of pāhoehoe toes can be also found. Denser blocks are also observed, typically 10–20 cm in thickness. They have angular edges and resemble slow-cooled lava from the inner part of the flow, and their outer faces may correspond to cooling joints. A minor component of centimetre-size rubble (usually the smallest fragments found at a given place) shows evidence of deformation by plastic tearing. Their shape is irregular and they are intensely fragmented.

The larger scale features described below are common to slabby and rubbly pāhoehoe surfaces. The term *plate* refers here to a specific feature, a rounded to polygonal-shaped flat area of intact surface of lava crust, from 10 m to 1 km across, and surrounded by a ring of disrupted slabs (slabby pāhoehoe surface type) or mounds of rubble (rubbly pāhoehoe type, see Fig. 2.2F). *Grooves* form linear depressions (Fig. 2.2H) with an upstream tip characterized by curved ridges, and they have also been described as wakes (Keszthelyi et al., 2000). *Cracks* form sigmoid-tipped lineaments on the lava surface, easily seen on aerial photographs, and 1–5-m-wide, linear depressions on the ground. They are often characterized by squeeze-ups of crystalline and degassed lava along their axis.

2.5.2 Internal structure

The internal structure of shelly, spiny, and rubbly pāhoehoe types is now described. Internal subdivisions are based mainly upon the vesicularity of the lava. A thick vesicular upper lava crust (with or without rubble), a dense lava core and a thin vesicular lower lava crust (with or without rubble) are distinguished. Complete cross-sections through the flows were found only at 10 locations along river cuts at the margin of the flow-field on the coastal plain, where the flow is dominated by 1–4-m-thick pāhoehoe lobes with 20–50-cm-thick vesicular surface rubble (Fig. 2.4).

Shelly pāhoehoe-surfaced lavas are thin-crusted flows (<30 cm thick) with a very vesicular upper crust (>70 vol.%) underlain by a gas blister, a large cavity occupying the lobe interior and starting about 10 cm below the upper surface. Because of this feature, Swanson (1973) referred to this lava type as cavernous flows.

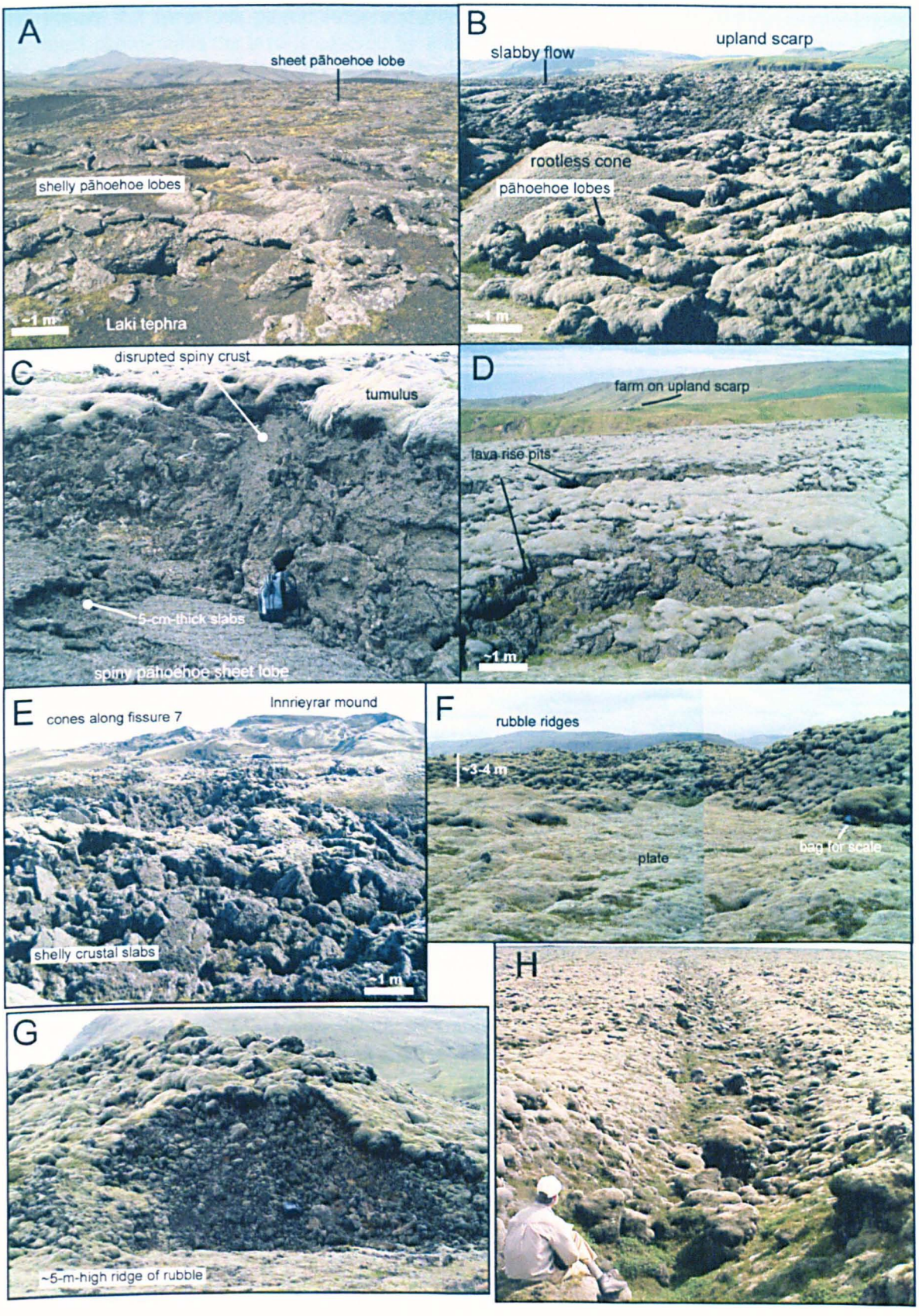
A
sheet pāhoehoe lobe
shelly pāhoehoe lobes
~1 m
Laki tephra
B
slabby flow
upland scarp
rootless cone
pāhoehoe lobes
~1 m
C
disrupted spiny crust
tumulus
~5-cm-thick slabs
spiny pāhoehoe sheet lobe
D
farm on upland scarp
lava rise pits
~1 m
E
cones along fissure 7
Innrieyrar mound
shelly crustal slabs
~1 m
F
rubble ridges
~3-4 m
plate
bag for scale
G
~5-m-high ridge of rubble
H

Figure 2.2 (previous page): Representative photographs of different surface morphologies (on most photographs the lava is covered by moss). A) Shelly pāhoehoe lavas near fissure 4, looking north; note cavities in lava. B) Small pāhoehoe lobes invading rootless cone field on foreground, slabby-surfaced flow in background, and upland scarp (in distance), along margin of the Eldhraun branch. C) Spiny-surfaced pāhoehoe sheet lobe overridden by flow with tumulus; note localized disruption of sheet lobe surface into thin slabs and disruption of sides of tumulus, margin of the Eldhraun flow-field locally uncovered with moss. Day-pack for scale. D) Overview of large pāhoehoe sheet lobe with ~20-m-wide and ~2-m-deep lava rise pits; Eldhraun northeast margins looking north towards upland scarp. E) Slabby flow with ~30-cm-thick shelly pāhoehoe slabs, near cones from fissure 7. F) Plate forming flat depression in between ridges of rubble; Eldhraun central area. G) Road cut through 5-m-high ridge of rubble, Eldhraun central area. H) Groove feature forming km-scale linear depression in rubbly surface, Eldhraun central area (photograph courtesy of L. Keszthelyi).

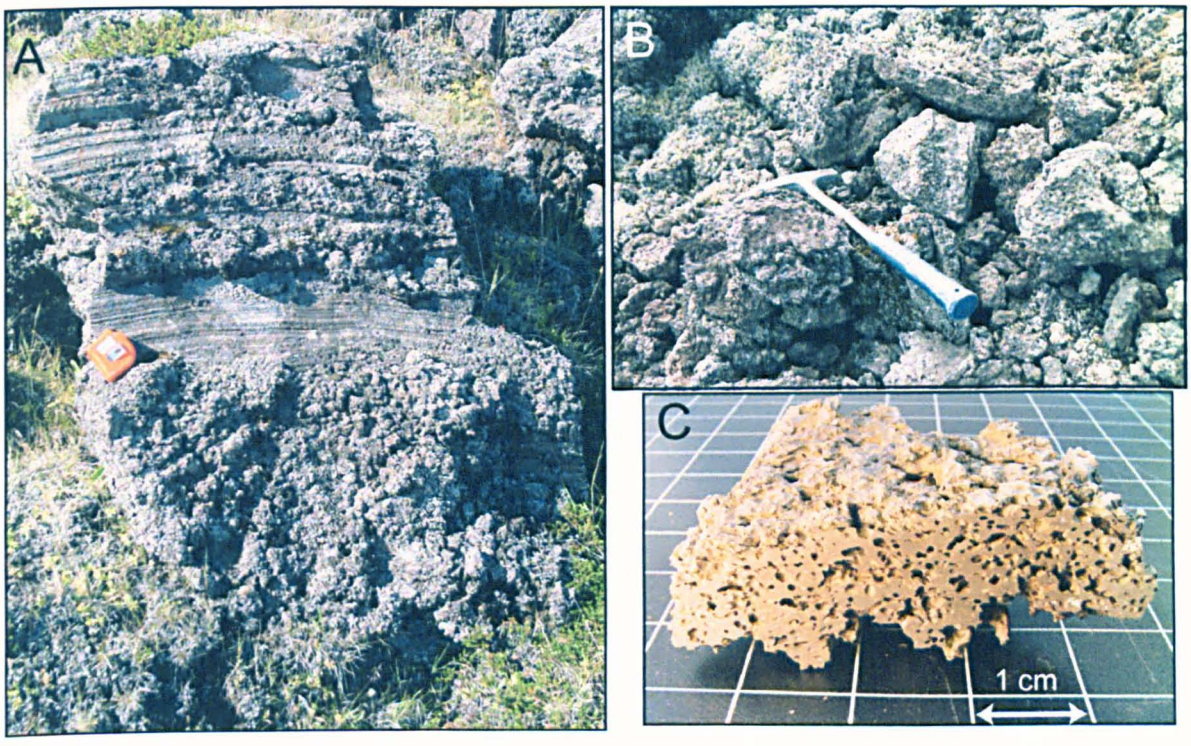

Figure 2.3: Photographs of surface fragments. A) Scrape marks at base of pāhoehoe slab overturned at front of flow; note lateral continuity of marks (> 70 cm long). B) Close-up of ~5-cm-size rubble composing the ridge in Figure 2.2F; note vesicularity of clasts. C) Section through slightly contorted rubble; note vesicularity of interior and stretching of vesicles parallel to the surface.

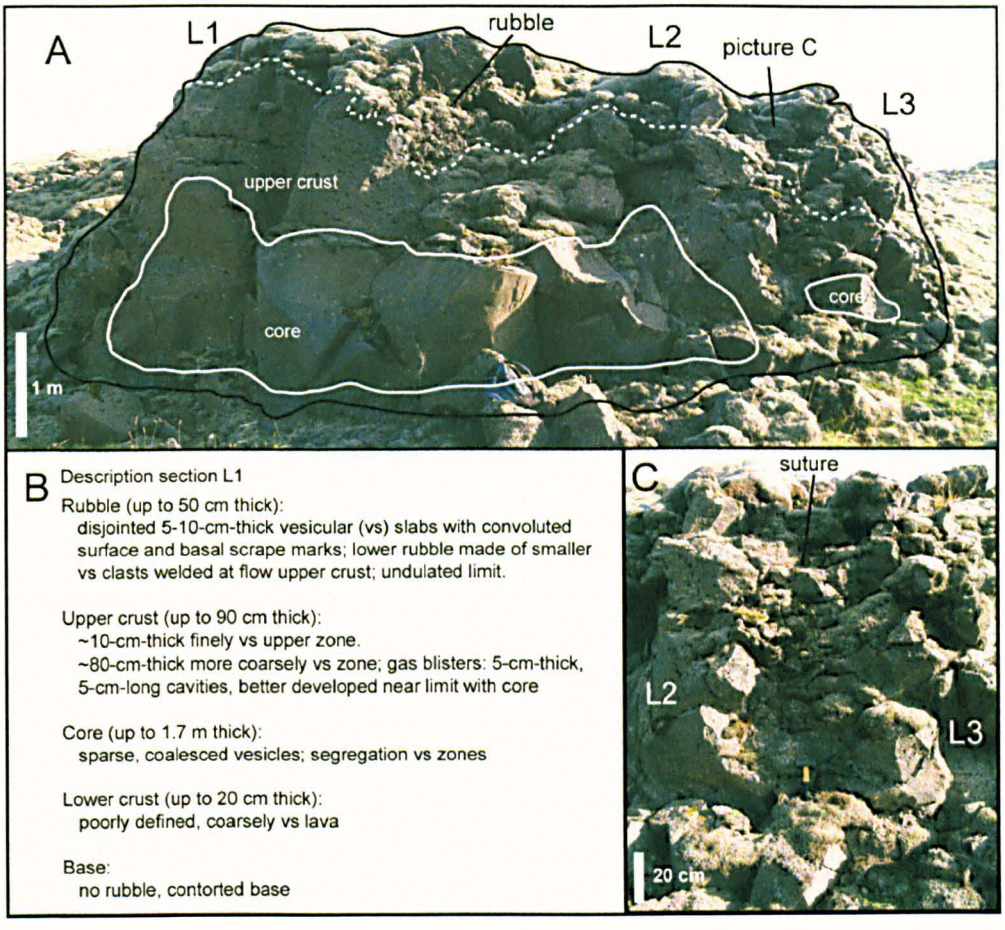

Figure 2.4: Photographs and sketch of exposure through 7-m-long and 6-m-wide lobe, Eldhraun margin. This lobe is composed of 3 individual lobes (labelled L1, L2, L3) partially merged together, which, in section, have distinctive upper crusts (the dashed line indicates the limit between upper crust and rubble—see in A). The cores of L1 and L2 merge into a single body. L3 forms an independent lava body but its upper crust is linked to the lateral margins of L2 by interleaved sheets of lava (a feature called lava suture—see text for description and close-up photograph 4C). Characteristics of L1, in section, are described in the lower left corner of the Figure (B).

For lobes with spiny pāhoehoe surface, the upper crust is less vesicular (20–30 vol.%) and forms 30–50% of the total unit thickness. Gas blisters often separate thin slabs of upper crust from the underlying lava. Vesicles are small, closely spaced, almost spherical, and often coalesced. The average size of vesicle increases inwards and the upper crust can be divided into an upper finely vesicular zone and a lower more coarsely vesicular zone, the proportion of each varying. The limit of the upper crust with the core is often marked by the presence of megavesicles which form in horizontal layers. The core of the flow is formed by dense, poorly vesiculated to non-vesicular lava. In lobes <1 m thick, the inner

part of the lava is coarsely vesicular. Segregation features are common characteristics of the cores of thicker lobes, but can be observed in smaller lobes. The lower crust of the flow units appears to be invariably ~30 cm thick. The base of the sections is generally spiny and coherent or composed of small toes.

At the junction between two adjacent spiny pāhoehoe lobes, or lobes with thin rubble, vertical stacks of interleaved lava plates connected to the lateral margins of each lobe were found (Fig. 2.4C). Underneath this suture, the crust and core of the two lobes in contact is connected (Fig. 2.4A). Sheet-like protrusions of lava were seen in several parts of the flow-field, either emerging from the core of the flow and dipping outwards in lava rise pits, or vertical and inside the axial cleft of a tumulus structure (Fig. 2.5). These protrusions commonly have a lamellar structure with imbrications of thin layers of lava and, often, vertical lineations on their surfaces (Fig. 2.5D).

Lobes that show some rubble at the top have the same internal structure as described for spiny pāhoehoe lobes. Some rubble is present at the base of lobes with thick top rubble. To my knowledge, complete sections through Laki flows with thick (>2 m) rubble (i.e., from the middle part of the flow-field) do not exist. It is, however, possible to observe the upper part of the flows (rubble and upper crust) in features such as lava rise pits or inflation clefts. The features described here were found at the western margins of the Eldhraun flow-field but are very likely to be found in other parts of the flow-field. In one typical section exposed in a 20-m-wide lava rise pit, the base is formed by a 2.3-m-thick vesicular upper crust which is characterized, in its lowest part, by sheet-like protrusions of lava attached to the outer surface and plunging inwards (towards the core of the flow). A 1.5-m-thick rubble layer lies on top of the crust. The lowest rubble clasts (5–10 cm in size) are strongly welded and connected down to the crust, with fingers of largely degassed lava crust rising into the rubble. When small (a few cm wide), these intrusions are finely crystallized and vesicle-poor. Larger intrusions sometimes show a chilled margin (a few

cm thick) that is virtually vesicle free (Fig. 2.5). By contrast, the interior of the intrusion is vesicular (~10–20 vol.% vesicles). The transition between the upper crust and thick rubble is often undulating and, lying over the rubble, there are 30–50-cm-thick pāhoehoe-like crustal slabs, tilted-up on the surface. At another location exposed along an inflation cleft at the front margin of the same flow, surface breakouts were seen, intruding the upper rubble (Fig. 2.5A).

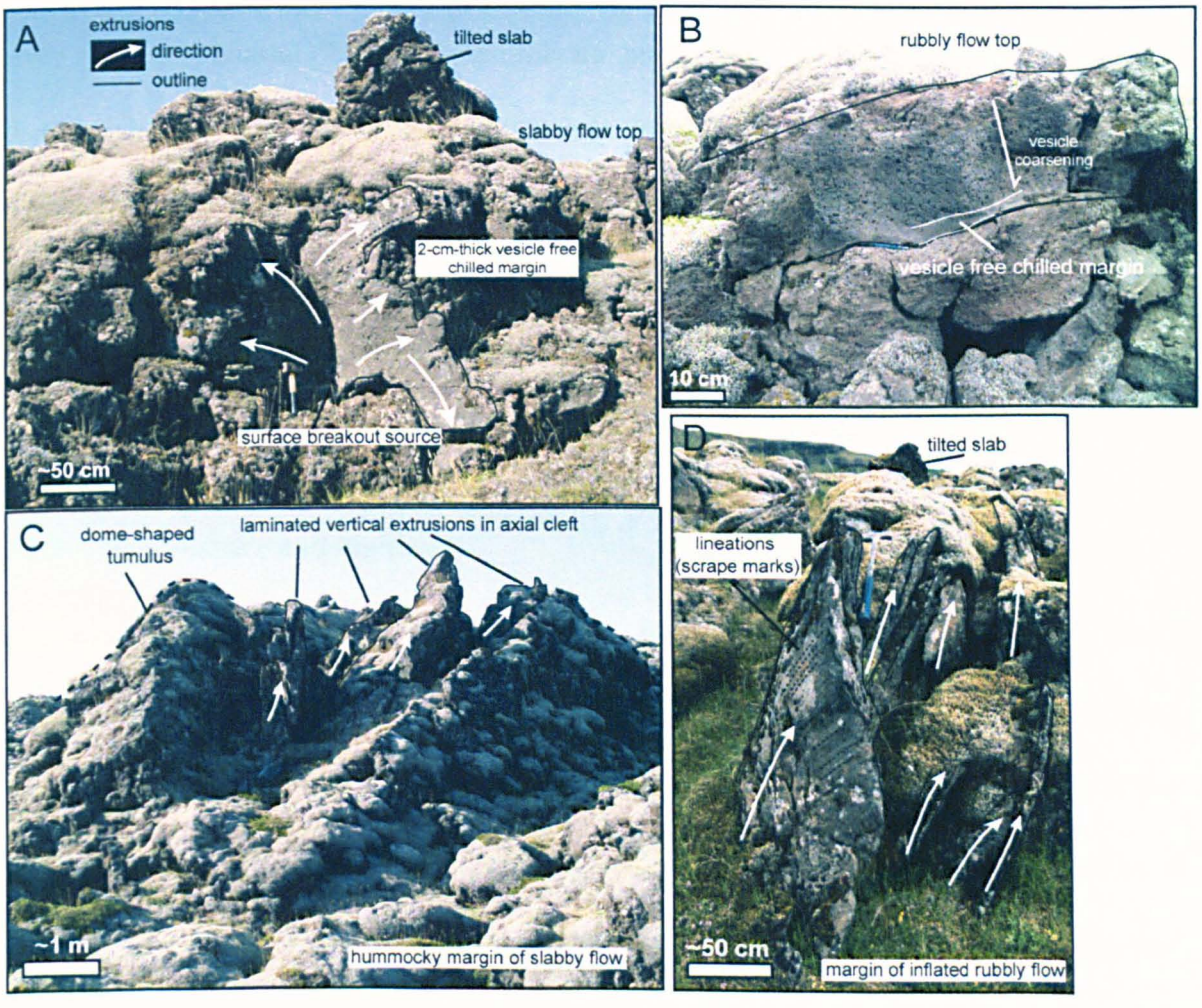

Figure 2.5: Photographs of different types of intrusions of lava into flow-top rubble. A) Surface breakout. B) Close-up of 30-cm-thick intrusion in thick rubbly part of the Eldhraun branch. C) Vertical extrusions exposed inside axial inflation cleft of a tumulus. D) Imbricated vertical extrusions; note lineations on surface of lava and sheet morphology of extrusions (arrows indicate direction of extrusions).

2.6 DISTRIBUTION OF LAVA SURFACE MORPHOLOGIES IN THE FLOW-FIELD

Different surface types on the Laki flow are easily recognized on aerial photographs due to the lower degree of light reflectance of irregular surfaces compared to smooth ones; rubbly surfaces appear darker on the photographs than pāhoehoe surfaces. By a combination of field and aerial photograph interpretation, the description of surface types is separated into three main geographic zones (Fig. 2.1): 1) near-fissure and highlands, 2) river gorges, 3) coastal plain, i.e., the Eldhraun and Brunahraun branches. These areas are distinguished by their distance from the vent and the pre-eruption topography. On the highlands and near the fissure the terrain was variable, from flat and open to channelled and steep. The pre-existing gorges were narrow and probably had a relatively regular slope. The areas on the coastal plains were nearly flat and open, although covered by historic and pre-historic flows pre-dating the Laki eruption.

2.6.1 Near-fissure and highlands

Early-formed flows. Lavas exposed near the fissure were mainly produced by small effusion-rate flows during the late stages of eruptive episodes. However, early-formed flows are exposed in a narrow zone located on the north side of the southwest part of the cone row, along the south flank of the Úlfarsdalssker mountain, and are identified by a cover of Laki tephra (Fig. 2.2A). They emerge in broad sheets from fissure segments, and later-formed cones, bombs, and spatter rest on their proximal part. These flows form fan-shaped sheet lobes with patches of slabby surface. Disruption of the surface crust is observed at localities where the flow edges encountered barriers (previously-formed cones or hyaloclastite mounds). The lavas are often shelly near source but change down-flow to spiny in a few ten metres. These lavas are the most pāhoehoe-like on the Laki flow-field.

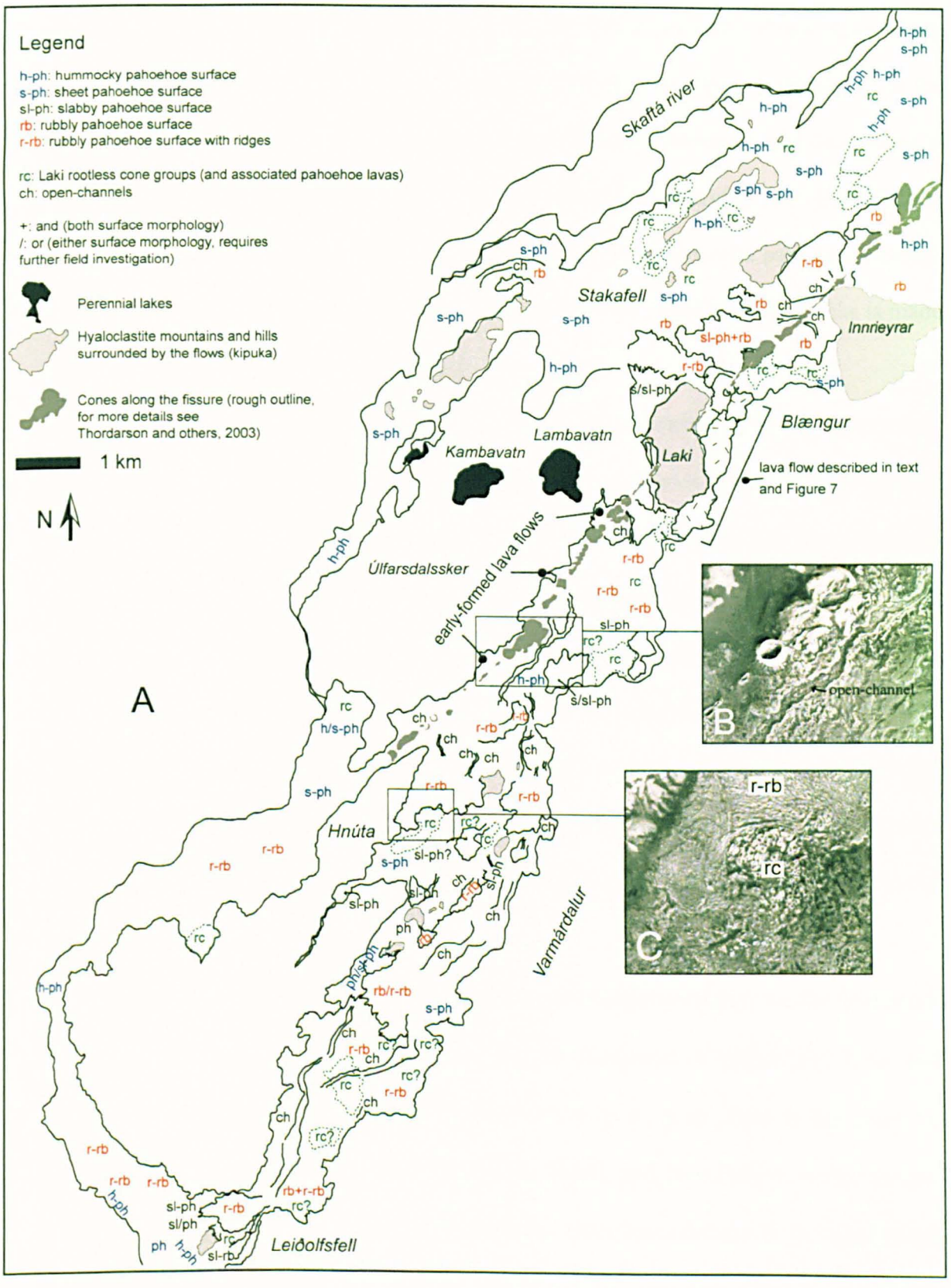

Figure 2.6: Distribution of lava surface types near fissure and on surrounding highlands. A) Structure map of lava flows. B) Aerial photographs of an open-channel linked to cones of fissure 3. C) A ridged rubbly flow surface developed behind a rootless cone field; areas described in text are indicated.

Later-formed flows. The source of the later-formed flows generally shows <1-km-long open channels emerging from breaches through the cones. The channels developed in the centre of pre-established shelly to spiny pāhoehoe flows and commonly lead down-flow to rubbly-surfaced lobes. The surface of a fan-shaped lava flow emerging from the NE cone row on the north side of Innrieyrar hill (Fig. 2.6) shows, in its proximal part, rafted blocks a few tens of m across made of spatter piles. The lava surface around these blocks is made of stacked shelly pāhoehoe crustal fragments (Fig. 2.2E).

Lavas produced by the SE and NW cone rows are distinctly different in terms of dominant surface type. In the Varmárdalur valley and downstream towards the entrance of the Skaftá gorge, surfaces of lavas from the SE cone row are largely slabby to rubbly even though there can be large changes in surface type along single flows. The front of thick rubbly-surfaced flows often buts against rootless cones or hyaloclastite hills, with presence of higher ridges at the contact. Important breaks in slope in that area follow a SW-NE direction and are associated with hyaloclastite hills and mounds. Along these steep slopes the lava flows often have open channels with formation of short, fan-shaped, rubbly-surfaced flows at the base of scarps. Sheet- and hummocky-surfaced flows are mostly located in marginal areas of the valley.

By contrast, lavas produced from the NE row, and which flowed into the flat area south of the Stakafell hyaloclastite mountain, are mainly composed of hummocky lavas and sheet lobes with some minor patches of lava with slabby surfaces. Prior to the eruption, this area was a floodplain connecting the rivers Skaftá and Hverfisfljót to the glacier, which is consistent with the abundance of rootless cones formed there in the Laki lavas. Lava that flowed south from the western end of the NE row first filled a long valley located west of Blængur and west of Innrieyrar and Fremrieryrar. They form a kilometre-scale lobe there with surface characteristics grading from slabby to rubbly down-flow. Flows that were produced from the east-end of the fissure row and flowed towards the

Hverfisfljót river gorge are mainly of hummocky and sheet pāhoehoe type, although some lobes show slabby to rubbly surfaces in areas where the flow was laterally confined.

To improve the understanding of transitions in surface morphologies, a 5-km-long flow derived from fissure segment 6, east of the Laki hill (Fig. 2.7) was investigated. First, the surface characteristics are described, and then interpreted in terms of emplacement of the whole flow. The most proximal part (1 on map in Fig. 2.7) has a surface composed of thick rubble and is linked to the breached vent cone by a ~50-m-wide channel. Surface rubble of the flow issuing from the channel is accumulated into ridges perpendicular to the flow direction and which increase sharply in height from the source to the flow front. Rubble ranges from 5-cm-long fragmented blocks to 50-cm-thick slabs of pāhoehoe crust. In the central part of the flow, the rubble ridges pile up behind a kipuka of low bumpy ground composed of tephra layers from eruptions predating the Laki eruption, which had been surrounded by early-formed hummocky pāhoehoe lobes. Downstream of the rubble ridges (2 on Fig. 2.7), the lava surface is composed of a wide sheet of pāhoehoe-surfaced lava with marginal, smaller lobes. The transition between the two different surfaces is marked by disruption of the sheet-like pāhoehoe surface. Upstream from the transition, along the southern edge (3 on Fig. 2.7), the margin of the flow is composed of tumuli of various sizes with thick slabs of disrupted surface crust showing basal scrape marks (Fig. 2.7A). The thickness of the slabs varies from a few centimetres to 1 m and spatial relationships between slabs indicate that the crust was compressed perpendicular to the flow (Fig. 2.7B). A few hundred metres downstream from the transition, the surface of the centre of the flow becomes markedly more disrupted, changing from areas with tilted slabs and large plates, to rubbly-dominated areas (4 on Fig. 2.7). There, the lateral margin of the flow is composed of sheet lobes and successions of pāhoehoe lobes, separated from the main body by long cracks. The flow gets narrower in that part of the flow-field, laterally constrained by the adjacent hyaloclastite mounds. In the very narrow and steep area, a small channel

developed in the centre of the flow and rubble was piled into ridges. At the bottom of the steep slope, the lava flow becomes wider and has a slabby to rubbly-dominated surface (5 on Fig. 2.7). The flow terminates behind a field of rootless cones.

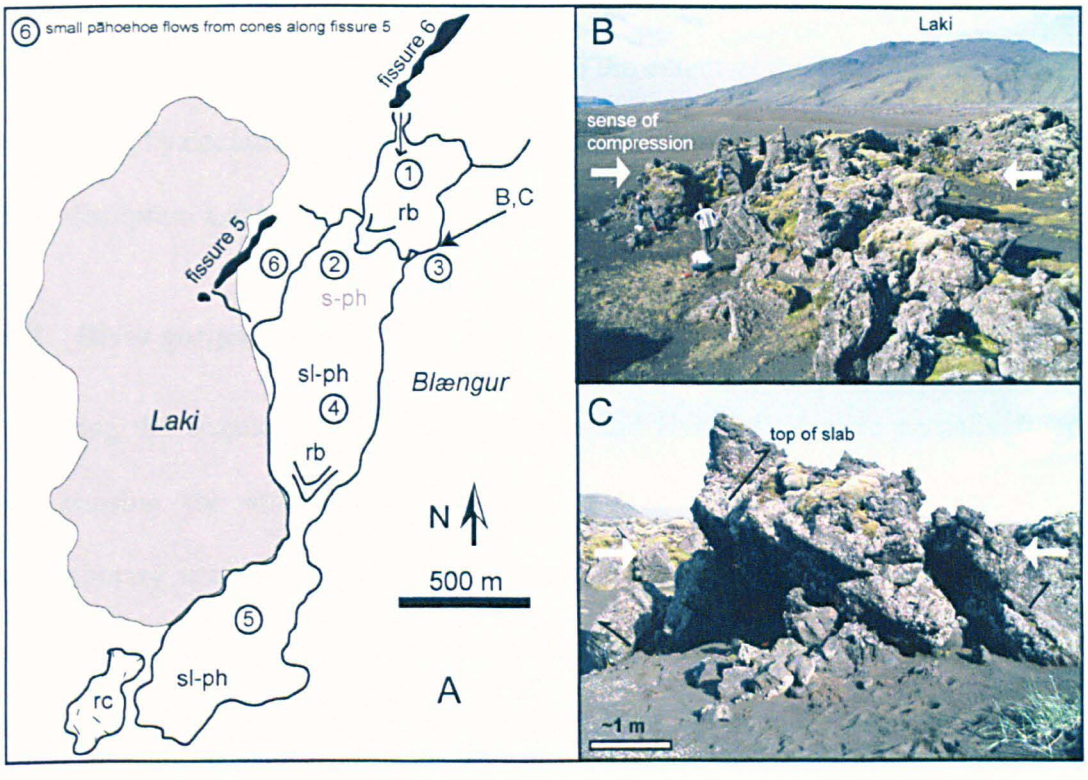

Figure 2.7: Map (A) and photographs (B, C) of disrupted margin of flow described in text. On map, circled numbers are locations described in the text; on photographs, filled arrows indicate direction of compression as inferred from field features. B) Large-scale view of margin; people for scale. C) Close-up view of slabs; thin arrows point towards the top of each slab as inferred from downward vesicle coarsening; slabs are ~60 cm thick.

The emplacement of this lava flow is envisioned as follows. First, as the proximal rubble is made of disrupted pāhoehoe crust; pāhoehoe lavas had to form initially. Lava fountaining along the fissure may have produced rapidly spreading, broad thin flows of fluid lava forming sheet pāhoehoe lobes with frontal breakout lobes. At the active front, flow growth by inflation proceeded as lava kept being supplied. The presence of thick pāhoehoe slabs on the lava surface and along the margins suggests emplacement durations of several days. The sudden confinement of the flow as it progressed downstream may account for the surface disruption of the central part of the flow due to the effect of

increased internal pressure (4 on Fig. 2.7). At a late stage, the proximal surface of the flow (1 on Fig. 2.7) was highly fragmented and the fragments compressed. It is speculated that the brecciation may have coincided with the breaching of the feeding cone, giving rise to the formation of an open channel in the centre of the flow and therefore increasing the internal flux of lava. Along the margins, where the extent of the flow was restricted by the surrounding hyaloclastite mountains, sudden augmentation of the internal lava flux caused brittle disruption and lateral compression of the disrupted fragments.

2.6.2 River gorges

During the eruption, the gorges of Skaftá and Hverfisfljót were partially filled with lava, causing the stream flow from the gorges onto the coastal plain to cease. Contemporary accounts do not give clear descriptions of the flow of lava in the river gorges (e.g., if it was covered by a crust, or forming a channelled flow) because these areas were difficult to access during the eruption. Most descriptions refer to the flow as it emerged from the gorge onto the flat coastal areas. Soon after the eruption stopped, the flow of water in the gorges resumed, eroding most of the surface. The river edges are now extremely hazardous to investigate.

Aerial photographs show that, in the gorges, surface-exposed lava exhibits mainly hummocky and sheet pāhoehoe morphologies, with small lobes with rubbly surfaces. In the upper part of the Hverfisfljót gorge, an extensive system of tubes and various inflation structures have been explored by Wood & Watts (2002). They also reported "fan-shaped surface breakouts" with "a corrugated surface of transverse ridges", features that clearly refer to rubbly pāhoehoe surface breakouts. These flows are likely to be a late product of the eruption.

2.6.3 Coastal plain

Lavas exposed on the coastal plain constitute the main part of the total eruption output. The Eldhraun branch, alone, contains ~5 km^3 of lava (Thordarson & Self, 1993), one third of the total volume erupted, and was produced when the effusion rate was the highest.

Eldhraun branch. Spatial relationships between the diverse lobes demonstrate that the Eldhraun branch (Fig. 2.8) is formed of a single large lava flow composed of connected breakout lobes, here called sub-branches. The main part of the flow was emplaced in ~1 month, from 12 June to 20 July 1783 (Fig. 2.8D). Successively fed by fissures 1 to 5, this flow covered ~20 km from the fissure to the Skaftá gorge, was confined for ~20 km in the gorge, and travelled ~25 km from the gorge exit to the distal front, across the nearly flat coastal plain, partially covering the older lava flow-fields of Eldgjá and Botnahraun and invading coastal distributaries of the Skaftá River (Fig. 2.8D). The large-scale morphology of the flow is that of a single lobe (here called the central lobe) developed at the exit of the gorge that splits into three sub-branches (Fig. 2.8A). The eruption chronology suggests that this central lobe was mainly constructed by lava produced during episodes 1 and 2 (from 8 to 14 June, see Fig. 2.8D). During episode 3, a main surge coming from the gorge was followed by the formation of the SE sub-branch, which flooded a river plain and was emplaced in 4 days (from 20 to 24 June). During episodes 4 and 5, the SW and NE sub-branches were established.

Historical accounts describe the flow advance across the coastal plain. Arrivals of lava surges out of the gorge were accompanied by large-scale surface disruptions; e.g., June 12: "*a lava surge emerged out of the Skaftá River gorge with enormous effluence, cracking, din, and rumble*" (from Steingrímsson's account, after Thordarson et al., 2003). It is likely that the disrupted lava mentioned was made of the crust of flows previously emplaced on the plain. The lava is also described as invading cavities in older lava flows. Descriptions also report that during the formation of the flow-field, periods of piling-up of

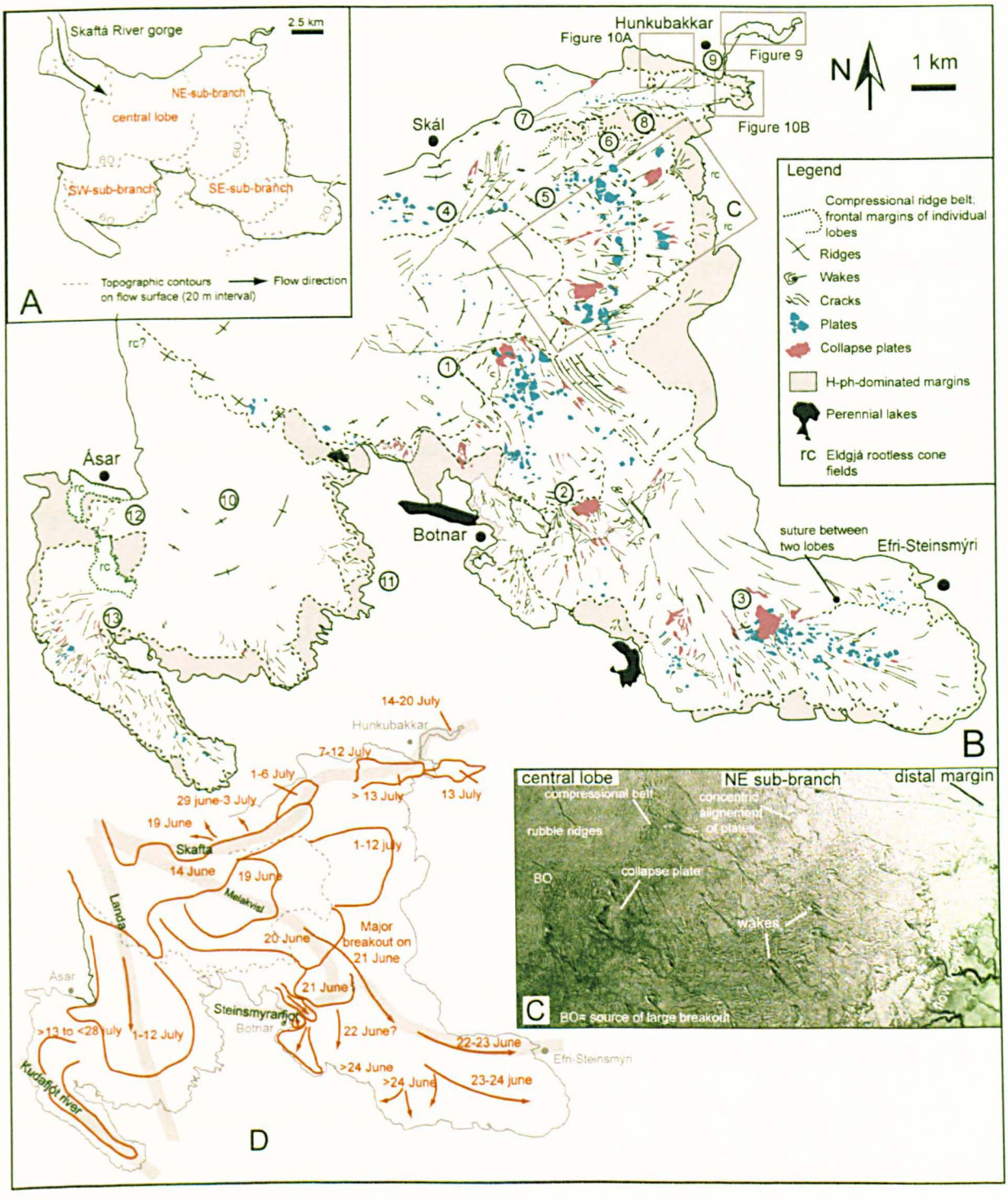

Figure 2.8: Surface features on Eldhraun branch. A) Outline map of Eldhraun branch with names of different sub-branches as used in text. B) Structural map of lava flow surface of Eldhraun branch showing major surface features and arrangement of main lobes; boxes give location of other Figures as indicated; circled numbers are locations referred to in text. In key, h-ph—hummocky pāhoehoe. C) Aerial photograph of area shown on B illustrating surface characteristics of the three components described in the text and their transition; BO indicates source of large breakout through the frontal compressional belt of central lobe. D) Outline of Eldhraun branch showing pre-existing river courses (grey bands) and dates of formation of main lava lobes (modified from Thordarson et al., 2003).

lava lobes alternated with periods of almost complete disruption of the surface accompanied by rapid advance of the lava flow.

Surfaces from the up-flow end (gorge exit) to the terminus are rubbly to spiny pāhoehoe-dominated, respectively. The morphology of the central lobe, the sub-branches, and then the distal margin will be described, and the formation of surface features at specific areas will be interpreted. Figure 2.8C shows an aerial photograph that illustrates the transitions across these three components.

Central lobe. The central lobe forms a fan-shaped structure about 5 km long and wide. A belt of compressional ridges defines the front of the lobe (Fig. 2.8C). Kilometre-long segmented cracks initiate from the centre of the lobe and extend towards the distal edges. The predominant surface feature of the lobe is concentric ridges of rubble (Fig. 2.8C); the surface is solely composed of rubble and sparse plates. Ridge height increases from 1 to 5 m, on average, from the up-flow end to the terminus of the lobe, and ridges are 30–40 m wide. Within a single ridge, the rubble varies from small, broken, 10-cm-sized toes to 20–50-cm-thick slabs often with contorted surfaces and smooth edges. Some blocks are made of imbricated slabs, and others of whole lobes with medial gas blisters (probably derived from surface breakouts). A drop in level of the lava surface and a change in surface morphology mark the limit of the central lobe, where sub-branches head off to the southwest and south-east. The transition between the central lobe and the sub-branch to the northeast is different and will be detailed below.

Down-flow sub-branches. The common morphological feature of these sub-branches is a progressive increase in surface brecciation along single flow units, with formation of plates, ridges, and cracks.

The SE sub-branch, which was formed in 4 days, can be divided into three distinct large lobes (sources: 1, 2 and 3 on Fig. 2.8). The limit between each large lobe is marked by a compressional ridge belt that is partially breached, probably due to frontal breakouts,

and generally followed by a drop in topography. The ridge belt separating the most proximal large lobe from the following one down-flow is located directly east of Botnar farm (2 on Fig. 2.8). It is characterized in the field by a 10-m-high rubbly front carrying slabs up to 1 m thick. Just down-flow from the belt, smaller breakout lobes ~10–30 m long emerge from both the rubbly front and from the large lobe downstream, and spread over lava rises belonging to an older lava field partially covered by the flow. As seen on aerial photographs, the central parts of the large lobes generally show numerous grooves and cracks. Along the length of each large lobe, the surface changes from flat to slabby and then to rubbly-dominated. The point of emergence of each large lobe (1, 2 and 3 on Fig. 2.8) is characterized by a large angular depression marked by transverse cracks (similar to the distinctive dark grey patch on aerial photograph, Fig. 2.8C). This feature is composed of a gently up-warped flat area covered by thin slabs, followed down-flow by disconnected plates (see Keszthelyi et al., 2004, for field observations and photographs).

The NE sub-branch was built in a period of at least 6 days. The surface of the lobe near its source has numerous plates, ridges, cracks and grooves. Ridges formed after the plates, deforming their edges; cracks were the latest structures to form. The transition of the central lobe with the sub-branch (4 on Fig. 2.8) is marked by the presence of ~6-m-high ridges carrying up to 60-cm-thick crustal slabs. Along the north limit of the branch, just south of Skál farm, the ridges are orientated parallel to the upland scarp with large plates between them. From the central lobe towards the east (5 on Fig. 2.8), the NE sub-branch shows an alternation of 2–3-m-high ridges with ~20-cm-thick slabs and higher ridges (5–6 m high) with 50–60-cm-thick slabs. Large plates 10–50 m across form a concentric alignment (Fig. 2.8C). The eastern front of the branch, where it comes in contact with the margin of the lateral breakout lobe described below (6 on Fig. 2.8), is a 15-m-high flow front covered by rubble. From that front to ~50 m up-flow, the rubble includes clusters of 1.5-m-thick slabs formed by brecciation of highly inflated frontal breakouts.

Three kilometres east of Skál farm, a large lobe breaks out from the northeast lateral margin of the branch (7 on Fig. 2.8). It stretches eastwards for ~5 km and was formed in 6 days, filling a small river valley. The lobe is composed of a central part disrupted by plates aligned along the flow centre and a hummocky dominated margin. The lobe's central part is characterized by ~ 2 m-high ridges of rubble with large 25–40 cm-thick crustal slabs. Near the flow centre, a 5-m-wide lava rise pit, linked to a crack, exposes ~1.5 m of upper crust overlain by 2-m-thick rubble. Closer to the hummocky lateral margins, cracks form segmented longitudinal depressions, 1–4 m wide and 1–2 m in depth. In these structures the rubble is 2–3 m thick and is very often intruded by auto-intrusive dikes up to 2 m high. Lava rise pits of 3–4 m in depth with 1–2 m of rubble were observed along the margin of the main lobe. The southern marginal hummocky lobes interfinger with similar lobes emerging from the main part of the NE branch (8 on Fig. 2.8), indicating that these two large parts of the flow-field were emplaced at the same time.

South of Hunkubakkar farm, a 2-km-long lobe branches from near the eastern end of the long lateral lobe and fills a narrow gorge located between the upland scarp and an extensive Eldgjá rootless cone field (9 on Fig. 2.8). This gorge was occupied by a river before the eruption, and is now filled by an overflow from the Skaftá River. The lobe shows a remarkable range in surface morphologies (Fig. 2.9). First, starting from the small road leading to Hunkubakkar and progressing eastwards, and ignoring the first slabby-surfaced lobe (probably a late breakout), the lobe has a central part with a flat upper-surface disrupted into 10-m-scale plates (the latter have tilted, 1-m-wide and 15–20-cm-thick slabs at their margins). The surface transforms towards the margin into rubble with ridges parallel to the margin, and is separated from a hummocky outer margin by long cracks, parallel to the front. Along the margin, inflated pāhoehoe lobes from 30 cm to 3 m high surround Eldgjá rootless cones. The surface of the central part also changes down-flow to rubbly. Where the gorge widens, the rubbly-surfaced lobe stops and thick, elongate

pāhoehoe sheet lobes emerge from underneath the rubble (Fig. 2.9B). Further down-flow, the separate sheet lobes merge into a single lobe with a central part disrupted into large plates (Fig. 2.9C). Even further along, the surface changes to rubbly and the last flow component is a 200-m-long lobe composed of a package of small sheet pāhoehoe lobes that are seen in section along the river (Fig. 2.9D). The building of this last lobe coincides with a narrowing of the gorge. The internal structure of the front of the thick rubbly lobe is also exposed along the river; it forms a single thick inflated flow with a thick homogeneous core. Also, the cores of the numerous lobes that are exposed along the flow margins show hackly cooling joints, indicating lava interaction with water.

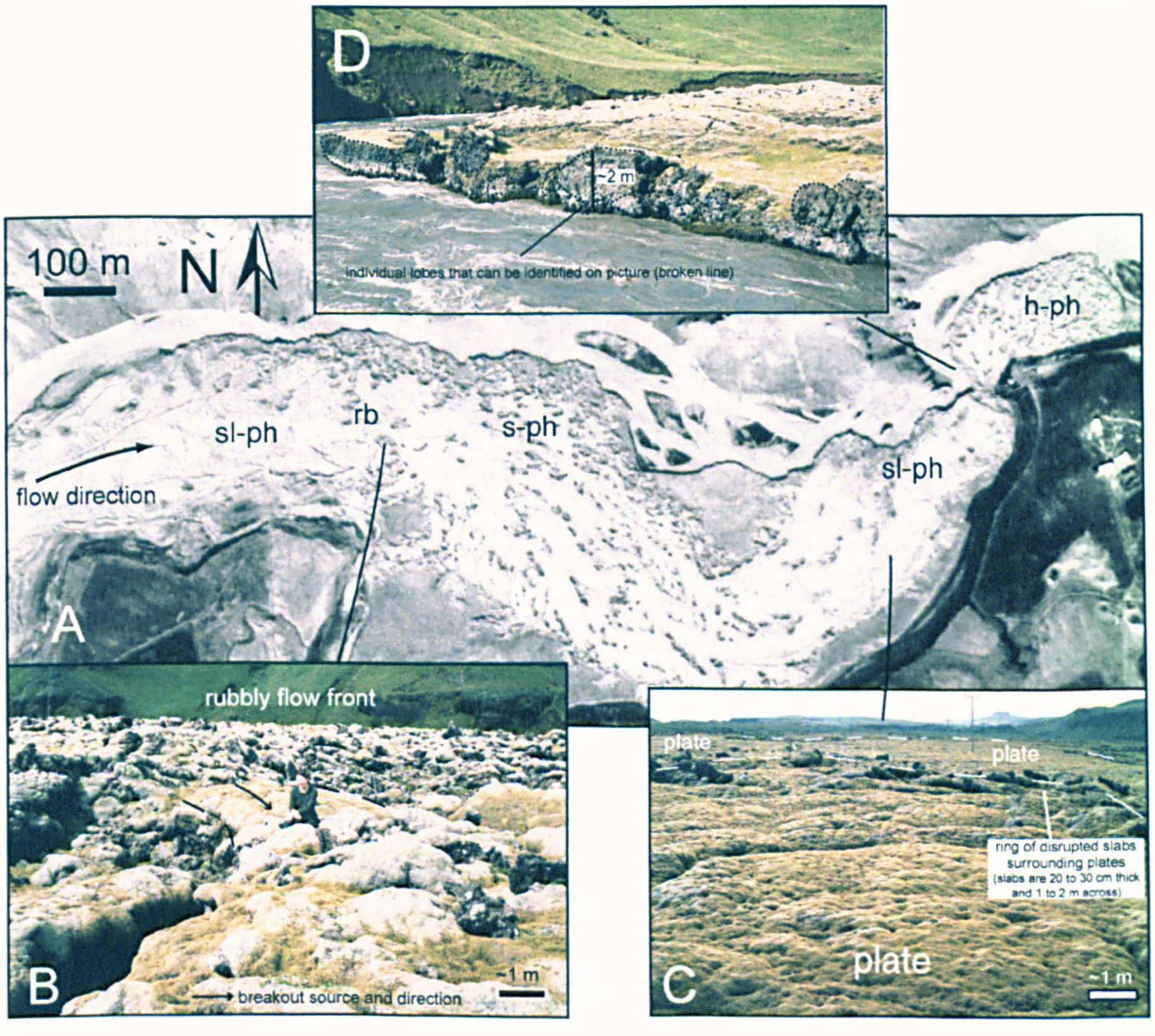

Figure 2.9: Surface features on ~2-km-long lobe discussed in text. A) Aerial photograph. Surface type: s-ph—sheet pāhoehoe lobe, sl-ph—slabby pāhoehoe lobe, h-ph—hummocky pāhoehoe lobes. Photographs of specific surface morphologies: B) large breakout of sheet pāhoehoe lobe through front of rubbly lobe; C) plates disrupting centre of lobe; D) river cut through margin of most distal lobe, note superposition of small lobes.

The succession of surface morphology along single lobes illustrates that separate stages lead to the formation of a rubbly-surfaced lobe from smaller pāhoehoe lobes partially coalesced into sheet pāhoehoe lobes. The sequence of brecciation appears to have been repeated if fluid lava stored within the interior broke through at the flow front, generating a succession of connected lobes with an increasing degree of surface brecciation along their lengths. The ubiquity of lava rise pits and inflation clefts along the flow, and with every type of surface morphology, shows that inflation was an important flow-growth mechanism throughout emplacement. The successive large outbreaks through the flow front correspond to locations where the river gorge filled by the lava becomes narrower. The advance of the flow front may have been slowed when it approached this constriction, leading to an increase in internal lava pressure, inflation, followed by deformation of the flow surface, and finally lava outbreak from the flow interior when the internal pressure overcame the resistance of the crust. Variations of crustal slab thickness across the lobe, in the proximal part, were noticed by Keszthelyi et al. (2004) and attributed to two stages of crustal disruption. The first stage of disruption affected the margins, producing 5-cm-thick slabs (~ 40 min of inflation). In the second stage, the surface crust of the central part of the lobe was broken-up into 20–30-cm-thick slabs (after ~ 4 hr of inflation). This two-stage disruption may simply reflect the processes described above, i.e., increase in lava internal pressure caused by topographic constraints upon the flow of lava, pressure being released by brittle fracture of the outer solidified lava crust, and outbreak of the liquid lava interior at the flow front.

The SW branch consists primarily of a fan-shaped lobe that flowed from the front of the central lobe southwards, spreading over Eldgjá lavas (10 on Fig. 2.8). These are exposed beyond its southern flow front (Fig. 2.1). The central part of the lobe is rubbly-dominated and its south margin is bounded by a sequence of small lobes with slabby to rubbly surfaces (11 on Fig. 2.8). Along its southwest margin, south of Ásar farm, th

rubbly front of the central part of the lobe piled up behind rootless cones (12 on Fig. 2.8). West of the cones, the area is covered by sheet pāhoehoe and hummocky pāhoehoe lobes that emerged from the margins of the flow across the rootless cones, before the disruption of the upstream part of the flow into ridges of rubble. South of that location, an elongate lobe 1 km wide and 4.5 km long breaks out from the west margin of the main lobe, and stretches to the south, following a valley previously filled by the Kudafjót river (13 on Fig. 2.8). The surface of this lobe is slabby-dominated, with cracks and plates in the centre, and hummocky lobes along the margin.

The distal margin. The distal margin of the Eldhraun lava flow is bordered by numerous hummocky pāhoehoe lobes (Fig. 2.8). Transitions from the central parts of the main branches to the margin are diverse and investigation of these at several places provides insights into processes involved in flow advance.

The front and lateral margins of the 5-km-long NE lobe (7 on Fig. 2.8) have been examined in detail (Fig. 2.10). Along these margins, lava flowed around and over an extensive Eldgjá rootless cone field. The surface of the inner part of the flow is slab-dominated. Long cracks extend from the inner part of this lobe towards the margin and they connect downstream with the down-flow limit of the slabby part of the flow. The terminus of the flow is formed of sheet lobes and complex sequences of smaller lobes (described below). The nature of the transition between the slabby part of the flow and the leading hummocky-dominated part varies. At the lobe front (Fig. 2.10B), it is marked by a segmented 2–4-m-deep inflation cleft around which surface breakouts intrude the 1–3-m-thick top rubble (Fig. 2.5A). Large outbreak lobes branch directly from this margin and overlap previously emplaced lobes. At a few locations, sheet lobes are directly connected to the slabby part and the transition in surface type is more gradational.

The succession of surface morphologies is more variable and complex along the lateral margin of the lobe (Fig. 2.10A). On the aerial photograph, at the very left and very right,

there is no clear distinction between the different types of surface morphologies, and transitions cannot be pinpointed in the field: going towards the flow front, the ridged slabby part of the flow grades into a flatter surface, with abundant lava rise pits and some intact upper crust, from which emerge sequences of smaller lobes. Branches directly connected to the slabby part of the flow have a highly disrupted surface. Looking at the centre of the aerial photograph, the limits are somewhat sharper than at the very right and very left of the photograph as just described. The upstream front of the slabby part butts against Eldgjá rootless cones, with formation of ridges of rubble on the upstream side of the cones. On the opposite side of the cones, the lava forms large sheet-lobes bordered by inflation clefts in direct contact with the cones. Away from the cones, the limit between the two types of surface morphologies is characterized by lava rise pits and similarly formed segmented inflation clefts.

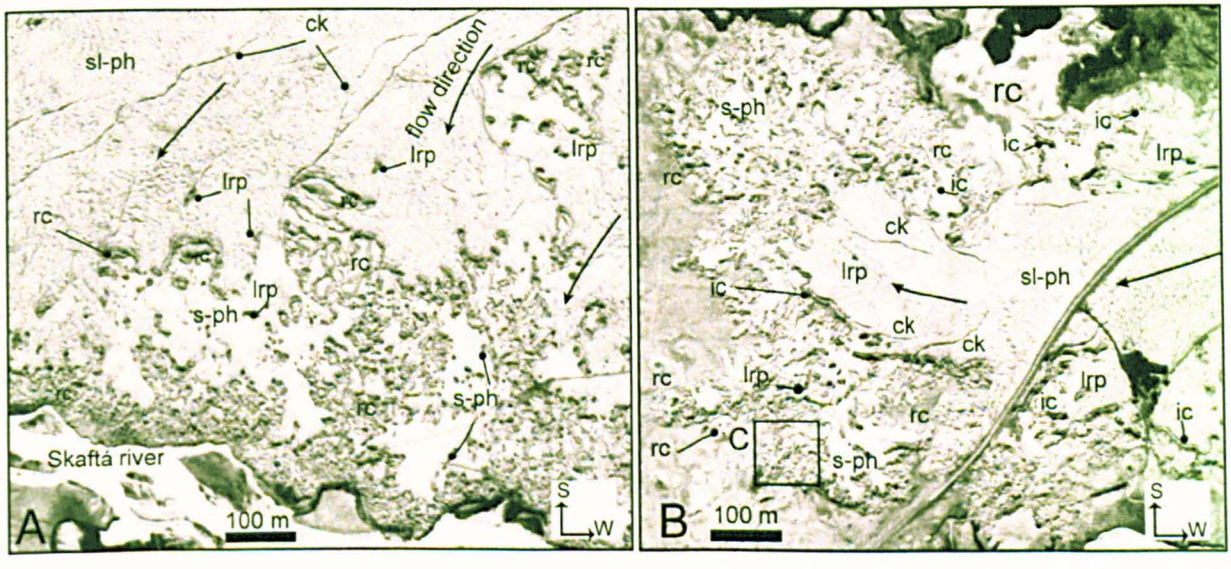

Figure 2.10: Aerial photographs of northern margin (A) and frontal termination (B) of 5-km-long lateral lobe, NE sub-branch of the Eldhraun branch (also indicated on Fig. 2.8); surface features discussed in text: s-ph—sheet pāhoehoe lobe, sl-ph—slabby pāhoehoe lobe, rc—Eldgjá rootless cones, lrp—lava rise pit, ck—crack, ic—inflation cleft; box C on B indicates location of complex sequences of distal lobes described in text.

The following scenario is proposed to form these features. First, it is clear that the advance of the flow front and formation of new crust (and "new" rubble) was achieved by formation and thickening of pāhoehoe lobes at the leading edge of the flow. While that was occurring, the slabby inner part of the flow was still actively inflating (as proved by the

presence of inflation clefts and lava rise pits). The formation of ridges on its surface was probably achieved by compression of the surface rubble by building of pressure in the fluid part of the flow, and was helped by the presence of obstacles such as the rootless cones. Cracks were formed at a late stage, as lava was still fed from the inner part of the lobe, flowing in pathways established underneath the slabby surface.

The following section will describe the complex organization of pāhoehoe lobes defining the terminus of the flow (for instance, box C on Fig. 2.10B). A typical sequence is composed of whaleback-shaped lava lobes, connected along their central axis to form a main lava body that is often bounded by laterally spreading lobes. Individual lobes range from 1–20 m long and 0.5–3 m thick, and the main lava body is usually thicker and longer than the lateral lobes. Axial and lateral inflation clefts develop along the thickest lobes, separating the steep flanks from the flat-topped central lobe axis. At the transition from one lobe to another, the surface of the distal front of the source lobe is often twisted and disrupted. The breakout lobe emerges from underneath the crust, causing a drop in topography. The surface of the lobes is also partially disrupted along the flanks with formation of some rubble along inflation clefts. This rubble is made of detached blocks from the uplifted upper crust.

Examination of the organization of these frontal lobes provides evidence that in any one area they formed almost simultaneously, and so contributed to the advance of the lava flow front. For instance, lava rise pits formed between adjacent inflating lobes that originated from the same main lava body but from different breakout sources. Also, some of the lobes overlap or are in direct contact, while other lobes unambiguously diverted the advance of others, and kept inflating. Sections through the front of individual lobes show that they are often composed of partially or completely coalesced smaller lobes that were emplaced side by side (illustrated in Fig. 2.4), or which piled up at the same location. These smaller lobes are generally produced by outbreak of lava from a single inflating

lobe. If these outbreaks of lava are separated in time, they can form a pile of lobes each with cooled outer crust. Finally, spreading in a radiating system from the main body, groups of such lobes manage to entirely cover the ground surface. During this process, the lava flux in the internal pathway within the main lava body is progressively delivered further down-flow, advancing the active front.

Brunahraun branch. This branch is composed of three separate lava flows which were emplaced sequentially, fed from lava surges out of the Hverfisfljót gorge: the NE, SW and SE flows (Fig. 2.11). The margins of these are hummocky. At the exit of the gorge, sheet pāhoehoe and hummocky pāhoehoe lobes cover the surface. These are likely to have come from late effusion of lava at low rates.

The SW flow was the first emplaced. Its surface morphology is, in its central part, slabby (Fig. 2.11C) and formed by a heterogeneous pile of angular blocks varying from small vesicular toes to 10–15-m-thick vesicular slabs overlain with ropy lava, and with denser finely vesicular clasts. Sparse in the flow-field, tumuli form rises where large parts of the crust are up-lifted and overlain by rubble (Fig. 2.11C).

The NE flow was the second large lava body to form. Most of the surface of this flow is covered by black aeolian sand, making the whole structure difficult to see. On aerial photographs, the centre of the flow appears slabby to rubbly with ridges and cracks.

Formed by flow of a final surge of lava in between the two existing branches, the central part of the SE flow consists mainly of thick pāhoehoe sheet lobes with numerous lava rise pits (Fig. 2.11D). The upper surface is mainly coherent, but is disrupted into thin slabs in some patches. In the centre of the flow, lava rise pits are 5–10 m deep. Seen in section in the lava rise pits, the upper crust of the flow is undulating. It preserved the shape of the smaller lobes that were initially emplaced, before the inflation of the whole lava surface.

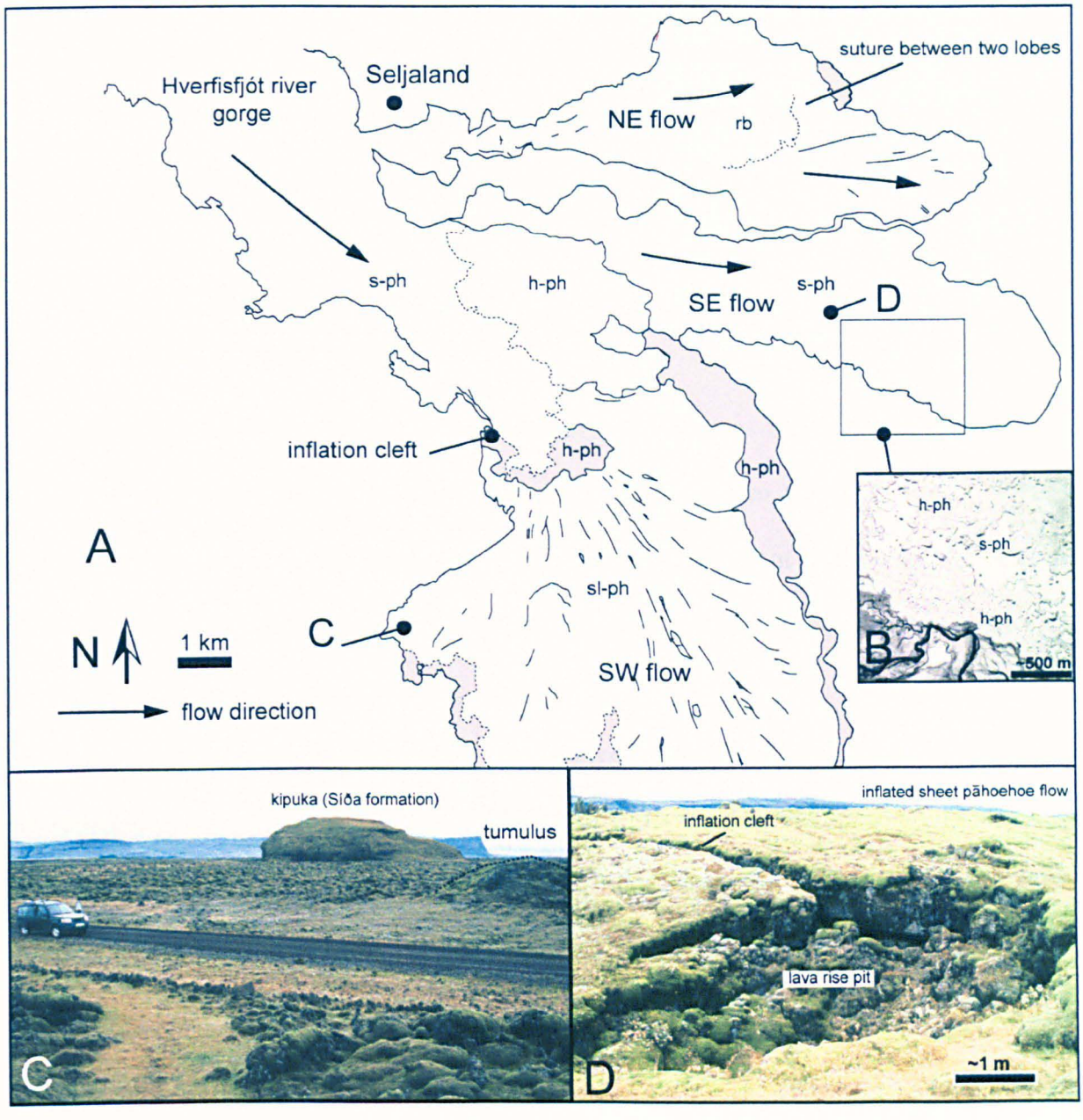

Figure 2.11: Organization and surface characteristics of Brunahraun branch. A) Structural map. Surface type: s-ph—sheet pāhoehoe surface, sb-ph—slabby pāhoehoe, h-ph—hummocky pāhoehoe, rb—rubbly pāhoehoe. B) Aerial photograph of sheet pāhoehoe characteristics described in text. C) Photograph of SW flow surface, looking east, with at right a tumulus. D) Photograph of 10-m-deep lava rise pit, characteristic feature of SE flow.

2.7 MODE OF EMPLACEMENT OF LAKI LAVAS

The analysis of diverse zones in the flow-field has revealed patterns in the structure of the flows expressed in the succession of surface morphologies. Below is described how, from these observations, the emplacement mode of lavas during the Laki eruption can be conceptualised (see Figs. 2.12, 2.13, 2.14).

2.7.1 Sequence of emplacement

There is no doubt that the flows were initially emplaced as thin lobes of pāhoehoe (Figs. 2.12A, 2.13A). During a period that varies from days to weeks, the thin lobes gradually coalesced into larger sheet lobes due to continued supply of lava from an up-flow source (Figs. 2.12B, 2.13B), as detailed above. At some time after that period, the surface was subjected to intense brecciation (Fig. 2.12C).

Along single kilometre-scale lobes, the degree of surface brecciation varies (as described, for instance, along the SE sub-branch of Eldhraun). At the up-flow end of the lobe, from the point of breakout and downstream, plates are produced by detachment of large intact pieces of previously formed crust, rafted along with the flow (Fig. 2.13C). Displacement of these rafts of crust exposes fluid lava underneath, forming collapse plates (as described along the Eldhraun SE sub-branch). Extensional cracks form along the margin, accompanying the extension and lateral spreading of the central part of the flow. Towards the flow front, deformation generally disrupts the flow surface into tilted slabs and mixed small rubble, and causes compression of rubble into ridges at the front. Then, after the major episode of disruption and when lava is still being supplied, the whole surface of the now rubbly-surfaced lobe starts inflating again, creating inflation clefts along the front and lava rise pits inside the flow (Fig. 2.12D). Repetition of the whole sequence leads to an increase in the thickness and diversity of the top rubble (Fig. 2.12E).

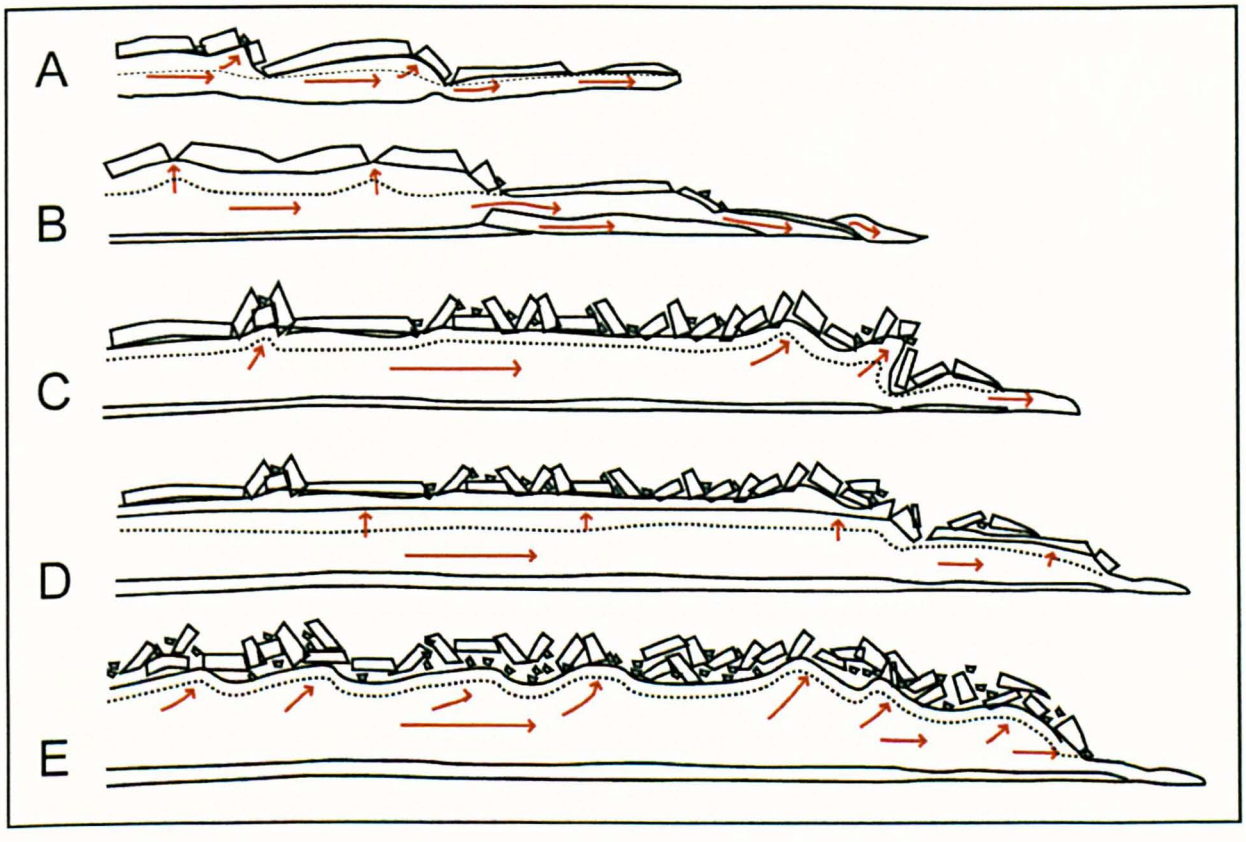

Figure 2.12: Representation of rubbly pāhoehoe flow emplacement scheme in section: A) emplacement of thin pāhoehoe lobes in sequence. B) Thickening of the flow by coalescence of small lobes into broad sheet lobes while smaller lobes begin to form at the active front. C) Disruption of the flow with rafting of large plates at the back and compression of the brittle outer surface at the front; some injections of lava from the core may form surface breakouts and protrusions. D) Renewed inflation of the whole surface due to continuing lava supply. E) Repeated brecciation of the surface producing thicker rubble at the top and progression of the "front of disruption".

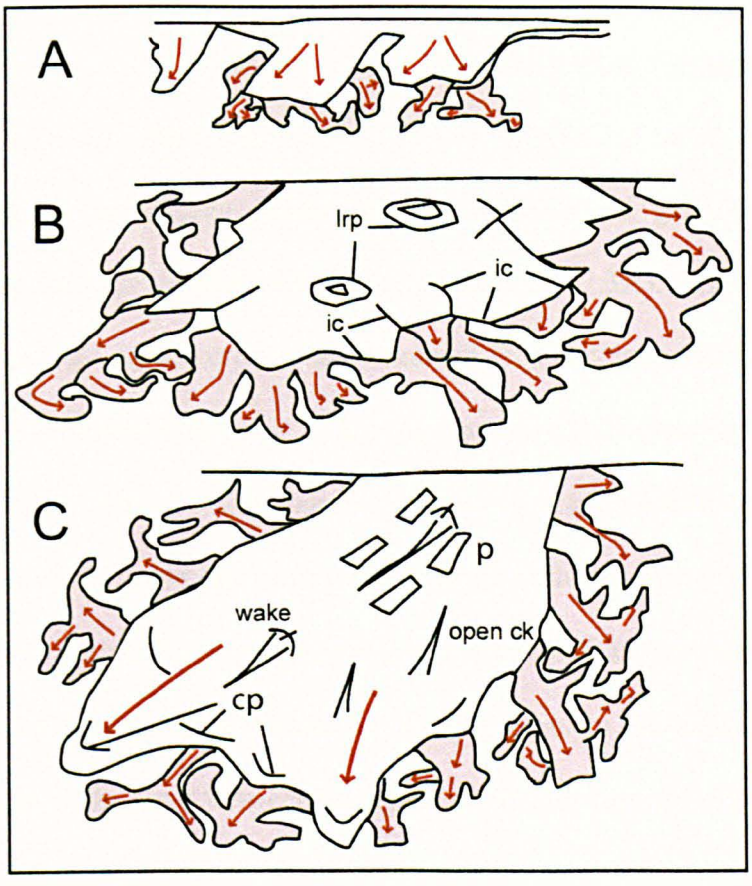

Figure 2.13: Representation of rubbly pāhoehoe flow emplacement scheme in plan view. Surface features: lrp—lava rise pit, ck—crack, ic—inflation cleft. A) Emplacement of thin pāhoehoe lobes (shaded area) along the active flow front. B) Coalescence of thin lobes into thick and broad sheet lobes (inflation surface in white on figure) with formation of lava rise pits in the centre of the flow, around rootless cones, and inflation clefts along the front. C) Large-scale disruption of surface causing detachment of plates (p) at back and compression (cp) at front; disrupted lobes partially override frontal lobes.

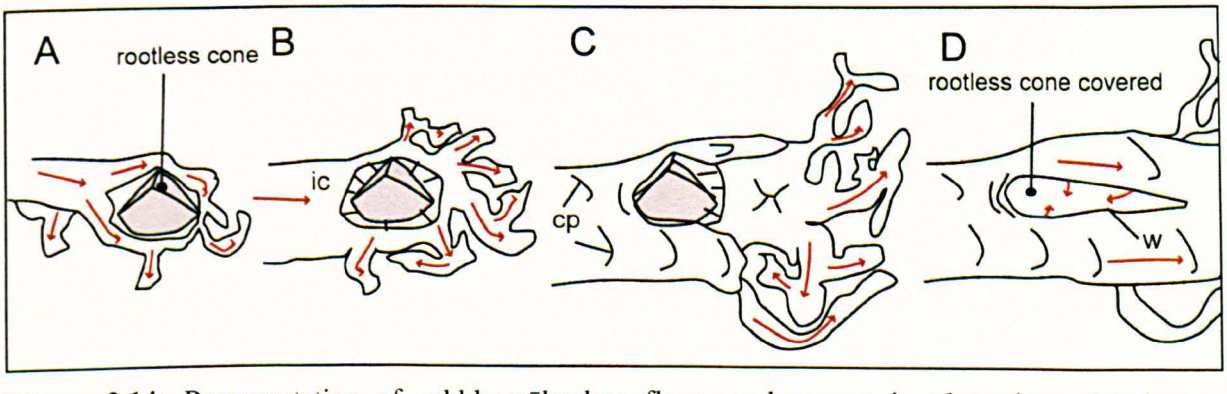

Figure 2.14: Representation of rubbly pāhoehoe flow emplacement in plan view, showing emplacement and brecciation of a lava flow coming in contact with an obstacle (here a rootless cone): A) thin lobes flow around the rootless cone. B) Thickening of flow by inflation and formation of inflation clefts (ic) around the rootless cones. C) Brecciation of lava flow surface upstream of rootless cone, and along its side. D) Creation of wake (w) at surface of flow and filling of depression by lava.

More detailed information on the processes involved in the surface brecciation comes from the diverse characteristics of the surface slabs and rubble. Undersides of slabs have characteristics indicating that they were disrupted by passive uplift of the upper crust followed by gentle brecciation (undersides characteristic of gas-blister roofs), or by dragging of hot, fluid lava underneath (scrape marks, Fig. 2.3A). Also, partial welding of plastic lava under the upper crust often occurred (reddish irregular base of slabs). To satisfy all these characteristics, the following sequence of events is proposed. During inflation, the brittle upper crust of individual lobes is already fractured by various clefts that expand through the solid crust and connect down to the viscous part (Hon et al., 1994, and also observed on Laki lava margins, see above). Gas pockets may accumulate underneath the crust, separating it from the moving core. In the absence of gas pockets, frictional stresses at the limit between the upper crust and core (producing scrape marks) lead to brittle failure of the crust. When lava breakout from the interior occurs, releasing the internal pressure, the crustal fragments are transported on top of the flow. Such crustal failure might be caused by a dramatic increase in lava input, or simply by continuous building of lava pressure that finally overcomes the tensile strength of the crust.

The low abundance of viscously torn fragments produced by auto-brecciation of lava before formation of a continuous crust indicates that, soon after disruption of the crust, a new crust begins to form, underneath the rubble. The undulating transition between the rubble and the upper crust suggests that the lower rubble partially sank into the flexible lava underneath, before or while the new crust formed. Sections through the upper crust of lobes with thick rubble demonstrates that their internal structure is very similar to pāhoehoe flows, and other features such as lava rise pits and lava sutures (Walker, 1991) suggest that they grew by inflation. During the process of inflation, sheet-like bodies of lava emerged from the interior of the flows and protruded the top rubble, probably taking advantage of existing openings in the upper crust. Formation of a chilled margin seems to

depend on the thickness of the intrusion and may be present when the lava came into contact with (possibly wet) rubble. This feature, very common in viscous flows, was referred to as a spine by Wentworth and Macdonald (1953).

The thickness of the slabs is indicative of the period of time during which the flow was steadily growing by the slow addition of lava to its interior, before disruption. In the descriptions given above, 5-cm-thick slabs are often referred to: these require 20 min of steady inflation before disruption. Forming thicker slabs requires an amount of time that increases with the square of the crust thickness. The thickest slabs observed reach 1.5 m, which is consistent with a two-week-long inflation period. The variety of rubble type and size commonly found at a single location then implies that the emplacement of the lava flows involved repetitively cycles of inflation and disruption of the surface of the lobes, as sketched in Figure 2.12. It should be noted that the time of formation of the flow upper crust when it is overlain by thick rubble may not follow the simple equation after Hon et al. (1994), presented above. The thick rubble may indeed act as an insulator against conductive heat loss through the flow surface and may then itself facilitate inflation (Keszthelyi et al., 2004). Also, the infiltration of substantial amounts of water through the fractured rubble and upper crust in the event of, for example, heavy rainfall or river runoff, could have enhanced the rates of downwards solidification of the lava; this would promote the formation of thicker upper crusts in limited amounts of time (see Chapter 4).

2.7.2 Influences on flow surface morphology

The effects of external parameters on the structure and disruption of the lava that were introduced in different parts of the above description are now revisited here in an effort to explain the large-scale distribution of surface morphologies.

Surges in lava supply rate. Variations in the rate of lava supply, together with the general topography of the area prior to eruption, have undeniably influenced both the shape and

volume of the flows and the location and intensity of the surface brecciation. Eruption dynamics modulated the volume and rate of lava emission, and the amount of degassing, along the fissure. Shelly pāhoehoe lavas were probably produced early during the opening of each fissure, at conditions of low effusion rates and relatively low fountaining (cf. the formation of shelly pāhoehoe on Hawaii; see Swanson, 1973). As magma discharge increased from the fissure, lava fountains increased in height and produced largely degassed lava that formed spiny pāhoehoe lobes which in places evolved into rubbly pāhoehoe lobes.

The link between the opening of new fissures and surges in lava from the gorge, on the coastal plain, is categorically established from historical accounts (Thordarson and Self, 1993). During high production rates, lava was able to rapidly reach the river gorges that channelled the lava towards the coastal areas. After each new fissure opening, large influxes of lava from the gorge to the coast mainly re-occupied the internal pathways established in the coastal lava flows, dramatically increasing the lava internal pressure. This forced the disruption of the flow surface by increasing friction stresses along the base of the upper crust, dragging large pieces of crust at the top of the flow, and producing compression of fragments at the front. If the lava supply was large enough, large frontal breakouts were generated by localized failure of the flow front, forming new lava flows, which probably covered smaller-volume frontal lobes. This mechanism must have prevailed throughout the formation of the Eldhraun branch: in the central part, multiple influxes of large volumes of lava caused repetitive large-scale disruption of the surface, producing the morphological characteristics of the central lobe. Vertical sections through the lava in the central zone of the Eldhraun branch, near the exit of the gorge, would probably reveal a stack of flows formed progressively with time, as each lava surge (three in total) emerged from the river gorge. Intermediate periods of low production rate were dominated by construction of the flow-field by inflation and lava surface disruption

progressed by increasing lava pressure in the large sheet lobes, near the flow front. The complex characteristics of plates and ridges in the central part of the NE sub-branch (described above, 5 on Fig. 2.8) may indicate several successive stages of brecciation of sheet pāhoehoe lobes formed along the active flow front. The morphology of the SE sub-branch records the progressive emplacement of large-scale lobes by merging of smaller lobes, followed by late and large increases in internal lava flux inside each lobe causing surface brecciation. For the Brunahraun branch, the arrival of each surge on the coast was separated enough in time to cause formation of distinctive lava flows, piled on top of each other at the exit of the gorge. In this case, an internal lava transport system was developed into the newly-formed flows, without replenishment of pre-existing pathways. Formation of the SW flow as the eruption waned can explain the absence of large-scale surface brecciation and domination of sheet pāhoehoe morphology, because of decreasing stress rates. Formation of these sheet lobes indeed requires a few months of sustained lava supply, probably lasting from the end of October 1783 until the end of lava production at the beginning of the following February.

Barriers to flow advance. In the highlands, mountain ridges and early-formed groups of rootless cones served as barriers to the advance of the flows produced in lower volumes during the waning stage of each eruptive episode. They forced the front of the short flows to come to a halt, inflate behind the barrier and then deform by compression of the viscous lava inside the flow, and cause piling-up of surface fragments at the front. In some cases, continued influx of lava from upslope formed new pāhoehoe lobes by breaking through the rubbly front and spreading around the obstacles. On the coastal plain, the initially emplaced pāhoehoe lobes flowed around Eldgjá rootless cones (Fig. 2.14A). When the lava surface gradually inflated, the rootless cones formed lava rise pits (Fig. 2.14B). Further supply of lava from behind produced disruption of the flow surface behind the cone (Fig. 2.14C) and when the flow was thick enough to move as a coherent body over them, the

surface was disrupted at the contact of the cone, creating a linear fracture (groove or wake) at the surface of the flow (Fig. 2.14D). A map drawn in 1771 by Holm (see Thordarson et al. 2003) suggests that, at the location of the front of the central lobe, there were some topographic rises, which could be the border of the large Eldgjá rootless cone field exposed along the edge of the Laki flow-field to the east (Fig. 2.1). This might then explain the formation of a large compressional belt and the temporary halt of the flows at that location. The upland scarp constituted an obstacle to the advance of the Eldhraun NE sub-branch, forming rubble ridges at the surface of the flow (4 on Fig. 2.8). The advance of the proximal, fan-shaped lobe of the SW sub-branch (10 on Fig. 2.8) was limited by the presence of Eldgjá lavas in the south (11 on Fig. 2.8) and rootless cones in the west (13 on Fig. 2.8), causing the surface of the upstream part of the flow to be compressed into ridges and lava to break out at the southwest edge (13 on Fig. 2.8).

Ground slope. It is clear that the mode of emplacement and deformation of the flows was influenced by the ground slope on which the flows are emplaced. The nearly flat slopes of the coastal plain may have greatly favoured the lateral spreading of the lava and the coalescence of the flows into single fan-shaped lobes while rapid and continuous growth of the flow-field was permitted by efficient lava supply from the gorge. On the highlands, the flowage of lava down the rough and confined terrains of the Varmárdalur valley favoured formation of elongate and rubbly-dominated flows whereas the lava flows emplaced on the flat and open terrains along the NE cone row mainly developed hummocky and sheet-pāhoehoe surfaces. This contrast in lava morphology could also be caused by the overall decline in magma discharge rate as the activity migrated towards the northeast.

River gorges. During most of the Laki eruption, fluid lava was transported from the highlands to the coastal plains through the river gorges which were completely filled by the lava up to the point of overflow (see Thordarson & Self, 1993, and references within). The lava in the gorges is now covered by late surface breakouts, which does not allow direct

investigation of the lava surface and mode of transport. Some inferences can although be made. The lateral restriction of the flows in the gorges (originally 150–160 m deep and 400–500 m wide, see Thordarson & Self, 1993, and references within) must have led to increased central flow rates and enhanced cooling at the margins. Consequently, a major channel may have formed in the central part of the flows, at least in an early stage. It is although likely that an efficient network of internal pathways rapidly developed. This was probably influenced by the continuous supply of large volumes of lava in the gorges which would have sustained low cooling rates, and also, mostly, to the down-flow spreading of the flows on the coastal plain, which probably lowered upstream flow rates, favouring formation of a coherent surface crust over the lava. Moreover, by focusing the flow, the river gorges may have allowed the lava to be emitted in large surges on the coastal plain, leading to periodic large-scale surface disruption of the sheet lobes already emplaced. The long distances reached by the lava and the pāhoehoe morphologies of the coastal flows argue against an increase in cooling rates during lava transport through the gorges.

Interaction of lava with water. The interaction of lava with water, as it invaded river streams, or flowed onto wet sediments, may have increased locally the lava internal solidification rates (see Chapter 4). It also led to lava fragmentation, and construction of fields of rootless cones which formed barriers to the flow advance (see above). It had however probably little direct impact on the efficiency of lava transport, the main lava transport system been established inside large sheet lobes, well upstream from the active flow front.

2.8 CONCLUSIONS

During the Laki eruption, large volumes of lava were delivered from lava fountaining along the fissure. Most of the lavas have surface morphologies significantly different from typical pāhoehoe and 'a'ā, and are defined as rubbly pāhoehoe. Detailed examination of the

surface morphology of the lava across the flow-field gives important insights into the mode of emplacement of the flows. Rubbly pāhoehoe lavas were initially emplaced as small pāhoehoe lobes but quickly developed a thick top layer made from brecciation and compression of the early-formed pāhoehoe crust behind (or at) the active front, principally by shearing at the base of the upper crust. This thick layer acted as an insulator for the liquid lava which was still being fed to the active front, therefore the advance of the flows was highly thermally efficient, and the final reach of the flows was mostly controlled by the duration of supply. Fed by a considerable volume of magma expelled almost continually along the fissure, the flows eventually formed one of the largest and most morphologically diverse basaltic lava flow-fields generated in historical time.

Chapter III

Role of syn-eruptive cooling and degassing on textures of lavas from AD 1783-84 Laki eruption, south Iceland

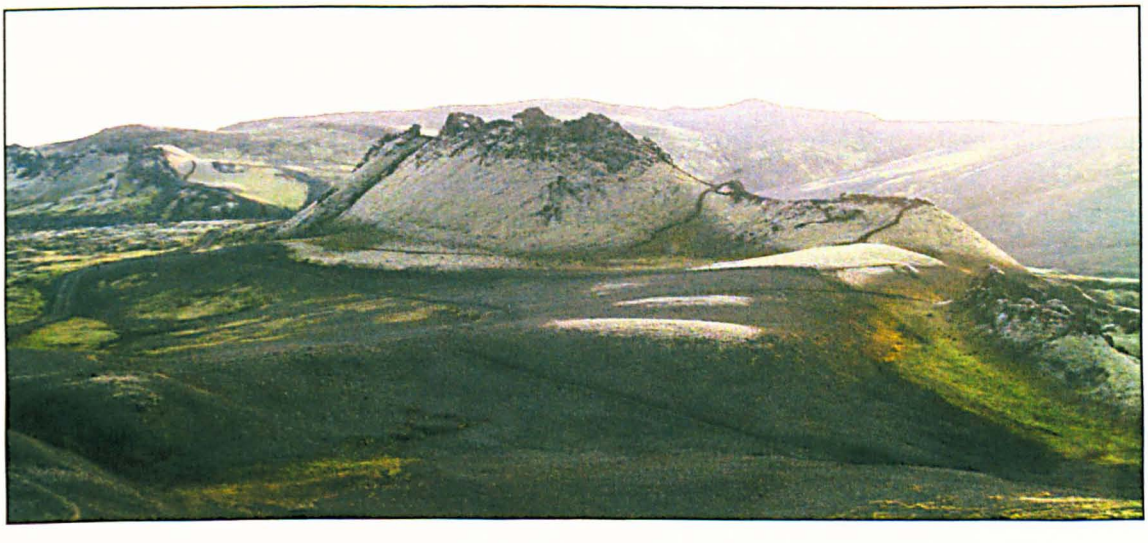

Cones along Laki fissure (near Laki mount)

3.1 ABSTRACT

Degassing-induced undercooling caused by decompression during magma ascent can produce key changes in the crystallization kinetics of basaltic magmas, controlling the phase proportions, style and amount of microlite crystallization, and thus the rheology, surface morphology, and final extent of the erupted lava. The AD 1783-84 Laki eruption in South Iceland is one of the largest and most explosive basaltic fissure eruptions of historical times. About 15 km^3 of homogeneous quartz-tholeiite magma was produced during 8 months of sustained Strombolian to Hawaiian activity. The flows gradually developed rubbly pāhoehoe surface morphologies through repetitive crust disruption at the active front. To study the role of syn-eruptive degassing and surface cooling on lava crystallinity and flow emplacement mechanism, the petrology and texture of glassy samples of tephra and lava were studied. Tephra and lava selvages consist of < 5 vol.% of phenocrysts and 7–30 vol.% of groundmass crystals made of plagioclase, olivine and clinopyroxene. Crystal and groundmass glass compositions were used to constrain crystallization conditions. The inferred evolution of the magma and lava during the eruption is as follows. Phenocryst cores formed when the magma was stored at the base of the Icelandic crust (at a depth of ~10 km), at near-liquidus temperature (~1150°C) and water-under-saturated conditions. As the eruption started, the magma rapidly ascended and degassed at shallow levels, losing ~1 wt.% of water. This caused the melt liquidus temperature to increase, triggering near-surface crystallization of microphenocrysts and forming a 10 mol.% anorthite gap at the margin of plagioclase phenocrysts. A considerable amount of microlites (up to 30 vol.%) formed in the flows, near the vent, as a result of a delay in the re-equilibration of the melt to the undercooling. This increased lava yield strength, causing the lava crust to fracture at a degree controlled by the amount of stress applied and the crust thickness. It is estimated that fluid lava was transported from the vent

to the most distal active front, 60 km from the vent, at cooling rates <0.2°C/km, similar in thermal efficiency to tube-fed lavas on Hawaii.

3.2 INTRODUCTION

The AD 1783-84 Laki eruption along the Grímsvötn volcanic system in South Iceland is one of the largest and most explosive basaltic eruptions historically recorded. The eruptive activity lasted for 8 months and produced ~15 km^3 of homogeneous quartz-tholeiite magma from a 27-km-long fissure opened along the East Volcanic Zone of Iceland (Grönvold, 1984; Sigmarsson et al., 1991; Thordarson & Self, 1993; Thordarson et al., 1996). The lavas produced by the eruption differ from the classical Hawaiian pāhoehoe and 'a'ā lava flow types as defined by Wentworth & Macdonald (1953) in that they are covered with a thick layer of fragmented vesicular crust (rubble) developed by repetitive surface disruption during flow emplacement (Keszthelyi et al., 2004; Chapter 2). One of the goals of this study was to determine the origin of the formation of rubbly pāhoehoe surface morphologies on the Laki lavas.

Lava viscosity and imposed shear are major controls on lava surface morphologies (Peterson & Tilling, 1980). The abundance of groundmass crystals in the lava has a determinant impact on the former since it causes the development of yield strength at crystal concentrations above 20–30 vol.%, which influences the mode of flow of the lava, its surface morphology, and thus its cooling regime (e.g., Cashman et al., 1999; Philpotts & Carroll, 1996; Hoover et al., 2001; Saar et al., 2001). It is well known that degassing of magma in the upper levels of a conduit can result in significant groundmass crystallization because water exsolution from the melt raises liquidus temperatures and increases crystallization rates (Sparks & Pinkerton, 1978). This effect can be important even for the small amounts of water generally dissolved in basaltic magmas (< 1 wt.%). For example, Lipman et al. (1985) showed that during the Mauna Loa 1984 eruption degassing-induced undercooling (~20–30°C) of the magma caused a 0.5–30 vol.% increase in the groundmass

crystallinity of the erupted lava. This resulted in a five orders of magnitude increase in the apparent viscosity of the flows as the eruption progressed (Crisp et al., 1994).

During the Laki eruption, large amounts of volatiles were released at the vent (Thordarson et al., 1996). This study aimed to determine the role played by degassing and cooling of the magma during the Laki eruption on the extent of crystallization of the lava and thus on its emplacement mechanisms. For that purpose, a set of glassy tephra and lava samples was collected to track the evolution of the magma from where it was quenched at the vent, and along the lava flow as magma was transported at various distances down-flow. To track compositional and textural variations, the major and trace element composition of groundmass glasses and their water concentration were analysed, as well as the composition of all crystal phases. Crystal shapes, numbers, and sizes were characterized.

This chapter describes successively: first, the texture of tephra and lava samples, the shape, size and composition of crystals present in the samples, and second, the composition of the tephra and lava groundmass glasses. Using calibrations of mineral-melt equilibria, the conditions of growth of the crystals are quantified in terms of temperature, pressure and water content. Textural information is interpreted in terms of crystallization kinetics. A model for the evolution of the magma during the first 5 episodes of the Laki eruption is then proposed. Finally, the implications of this work in terms of lava flow emplacement mechanisms and surface morphologies are discussed.

3.3 THE LAKI ERUPTION: BACKGROUND

The Laki eruption is thought to have been part of a 2-year-long volcano-tectonic event on the Grímsvötn volcanic system, in the East Volcanic Zone of south Iceland (Fig. 3.1a, Thordarson & Self, 1993 and references therein). The eruption involved the successive opening of 10 fissure segments along which > 140 spatter and tephra cones formed. The eruption intensity decreased during each eruptive episode and over the course of the

eruption. The lava flows produced developed different surface morphologies that are separated here into shelly, spiny, slabby and rubbly pāhoehoe types. Their main features and emplacement conditions are summarized in Table 3.1 (for more details see Chapter 2).

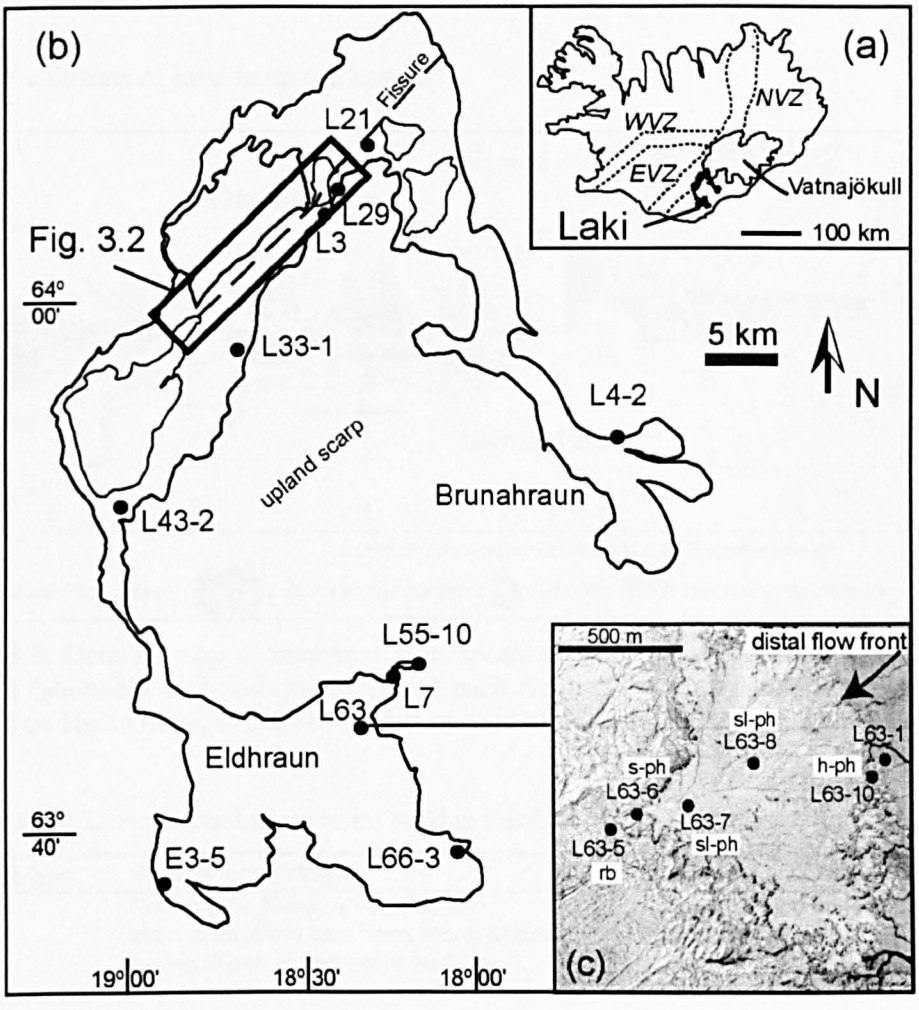

Figure 3.1: Laki lava flow-field. (a) Location of Laki fissure and flow-field in Iceland. (b) Map of Laki lava flow-field, location of samples analysed for glass and/or crystal compositions. (c) Aerial photograph of single lava lobe at distal margin of flow-field that was analysed for down-flow compositional and textural variations, and location of samples collected (L63).

Lava production rates were highest during the first 3 episodes, forming high lava fountains and reaching peak production rates of 2000–4000 m^3/s. At the very start of these episodes, the lava formed < 1-km-long flows with proximal shelly pāhoehoe surfaces that are exposed at the north of fissure segments 3 and 4 (Near-Vent Early Formed flows–NVEF). As production rates peaked, the flows formed large lava branches that were emplaced on the coastal plain, developing spiny to rubbly pāhoehoe surfaces (Fig. 3.1b). With progressive decline in magma production rates, fissures evolved into single vents, and lava

was produced at lower rates and in smaller volumes, forming shorter flows with spiny to rubbly pāhoehoe surfaces piling up on the highlands near the source fissures. Lavas defined here as Near-Vent Late-Formed flows (NVLF) are < 1-km-long flows with spiny pāhoehoe surfaces (similar in surface morphologies to NVEF) produced from late outflow of small volumes of lava from the cones.

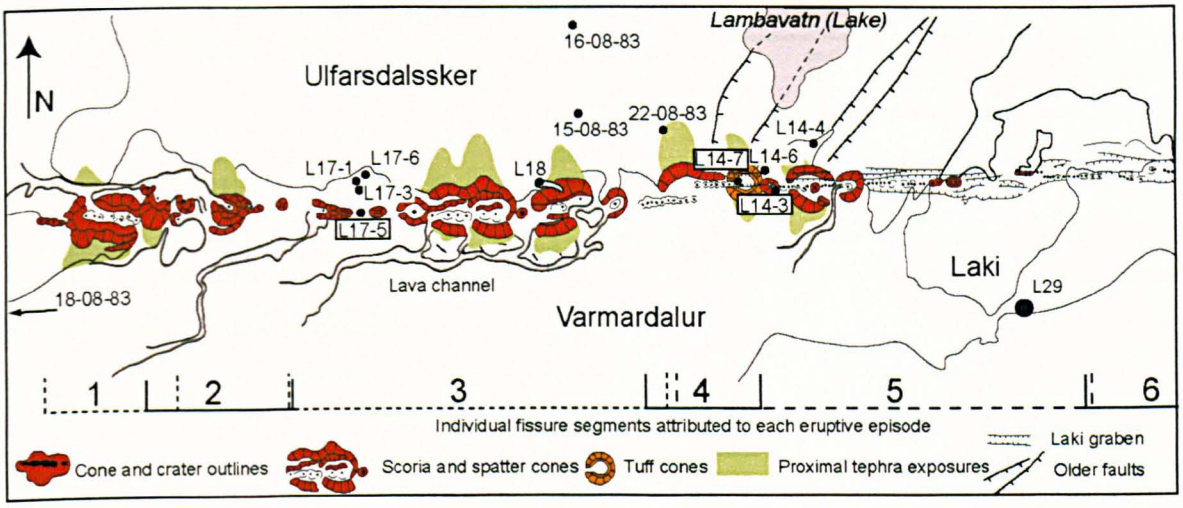

Figure 3.2: Detailed map of near-vent area, location of tephra and near-vent lava samples. The segments labelled 1 to 6 indicate extent of each fissure segment. Tephra sample 18-08-83 was collected on Hnúta ridge, slightly to the left of limit of map drawn (see arrow on figure).

Table 3.1: Surface morphological terms used in this Chapter (see Chapter 2 for details)

Pāhoehoe type	Surface morphology	Process of formation
Shelly	Gas-rich (> 30 vol.% vesicles and internal cavities) lava flows along fissure, proximal part of early-formed flows	Lava flows formed early in the eruptive episodes by low or absent fountaining along fissure
Spiny	Upper surface of the lava covered by mm-size protrusions	
Hummocky spiny	Interconnected 5 to 30-m-long lobes with largely coherent surface, forming lava field with complex multi-branching spiny pāhoehoe lobes	Breakout of lava through active flow front, forming successions of interconnected spiny pāhoehoe lobes
Sheet spiny	Lobe > 10 m in size, with flat and mainly coherent upper surface; often bordered with monoclinal inflation clefts	Coalescence of inflated individual breakout lobes into broader sheets
Slabby	Lobe which surface is formed by 20 to 50-cm-thick spiny pāhoehoe slabs	Extensive surface deformation of large inflated flow (sheet lobe) by fragmentation of surface lava crust
Rubbly	Lobe which surface consist of > 1-m-thick rubble made of slabs and cm-size spiny pāhoehoe clasts often piled up in ridges	Repeated cycles of inflation, surface crust brecciation and compression of slabby pāhoehoe lobes

3.4 METHODS

3.4.1 Sampling

The location of all the samples analysed is shown on Fig. 3.1 and 3.2. Table 3.2 is organised to show samples with, roughly, increasing distance from the vent source.

Table 3.2: Sample list with number of compositional analyses of each type

Sample no. Method (see text)	Sample location	D (km)	Sample type	Surface type	w-r XRF	H_20 FTIR	Plag EMP	Oliv EMP	Cpx EMP	Glass EMP
L13-4A	Coastal plain (Eldhraun)		lava core		1					
L3-1-4	Coastal plain (Eldhraun)		lava crust		1					
L4-4	Coastal plain (Brunahraun)		lava crust		1					
L7-6	Coastal plain (Eldhraun)		lava core		1					
15-08-83	Unit S2, section 98, Eystrisker	0	tephra							11
16-08-83	Unit S3, section 114, Vikradalur	0	tephra			1				5
18-08-83	Unit S1, section 144, Hnuta	0	tephra			4	65	8	61	10
22-08-83	Unit S2, section 94, Eystrisker	0	tephra				89	6	22	10
L14-3	Near-vent early-formed	0.05	lava selvage	shelly						6
L14-6	-	0.2	lava selvage	spiny sheet		3	103	80	34	5
L14-7	-	0.05	lava selvage	shelly						4
L17-1	-	0.25	lava selvage	spiny sheet			195	22	50	7
L17-3	-	0.1	lava selvage	spiny hcky		3				6
L17-5	-	0.01	lava selvage	shelly						7
L17-6	-	0.3	lava selvage	spiny sheet						5
L18-1	Near-vent late-formed	0.08	lava selvage	spiny hcky		7	80	86		8
L3-01	Highlands	3	lava selvage	spiny hcky			55	10	11	
L21-1	-	0.5	tephra (rc)				129	34	17	7
L29-10	-	2	lava selvage	spiny hcky			1	8	15	
L29-13	-	2	lava selvage	spiny hcky						6
L29-15	-	2	lava selvage	spiny hcky						9
L29-18	-	2	lava selvage	spiny hcky						7
L33-1	-	6	lava selvage	spiny sheet						5
L43-2	-	20	lava selvage	slabby		1				7
L4-2	Coastal plain (Brunahraun)	30	lava selvage	spiny hcky			187	67	46	10
E3-5	Coastal plain (Eldhraun)	45	lava selvage	spiny hcky			50	24	24	5
L7-1	-	50	lava selvage	spiny hcky			175	223	159	
L7-11	-	50	lava selvage	spiny hcky			24	11	12	
L55-10	-	54	lava selvage	spiny hcky						9
L63-10	-	49	lava selvage	spiny hcky						9
L63-1	-	49	lava selvage	spiny hcky						6
L63-5	-	48	lava selvage	rubbly						5
L63-6	-	48	lava selvage	spiny sheet						4
L63-7	-	48	lava selvage	slabby			34	39	14	5
L63-8	-	48	lava selvage	slabby						8
L63-9	-	48	lava selvage	rubbly			15	14		14
L66-3	-	55	lava selvage	spiny hcky			29	17		7
TOTAL					4	19	1248	656	453	207

D—distance from the vent. Location of tephra samples refers to Thordarson & Self (1993). Surface type: hcky—hummocky. Compositional data: w-r—whole-rock, H_2O—dissolved total water in groundmass glasses, Plag—plagioclases, Ol—olivines, Cpx—clinopyroxenes, Glass—groundmass glasses.

Samples of strombolian tephra corresponding to units S1, S2 and S3 produced by fissures 1 to 5 were collected and analysed to infer textural and compositional variations in the magma quenched at the vent during the first five episodes, the most productive period of the eruption (Thordarson & Self, 1993). They will be taken as representing the state of

the magma before surface transport. The tephra consists of glassy lapilli made of brown pumice, black scoria, and achneliths (Thordarson et al., 1996). Small glassy pumice clasts were selected for glass analysis, as they are likely to have been least affected by cooling during flight; they thus preserve the state of the magma when emitted at the vent. For simplification, the term of tephra will refer to these types of clasts in the following text.

Glassy lava selvages preserve the composition and crystal content of the lava when quenched at the surface at any location, which was thus used to track the evolution of the fluid lava during transport. Three types of sampling were conducted. 1) NVEF flows observed at two locations from along the fissure (labelled L17 and L14) were sampled along their length to track down-flow variations in the lava properties at close distances to the vent (Fig. 3.2). These represent the lava produced shortly after the opening of fissure 3 and 4 respectively. Sample L18 was collected from a lava flow covering the flank of a cone built along fissure 3; it was thus produced at the end of episode 3 (NVLF, see Fig. 3.2) and its characteristics will be compared to lava produced early in the episode (i.e., L17 samples). 2) Lava glassy selvages were sampled from marginal hummocky lobes emplaced at different parts of the flow-field to track variations in the lava crystal content with distance travelled from the vent and thus infer the thermal efficiency of the Laki lava transport system. 3) A ~1-km-long lava lobe emplaced on the coastal plain was selected for extensive down-flow sampling to infer syn-emplacement cooling processes correlated with surface deformation (sample numbers starting with L63-, see Fig. 3.1c). The surface of this lava lobe changes from smooth and coherent, to slabby, and then to rubbly along its length; hummocky lobes branch from the most distal front. Different types of surfaces and rubble were sampled to study a plausible link between the lava crystal content and the lava surface morphology at centimetre and metre scale, and infer the evolution of the lava as it flowed under a thickening layer of rubble. Viscously torn fragments could not be analysed, however, because they did not preserve any quenched glass.

3.4.2 Whole rock, glass and crystal compositions

Whole rock major and trace elements were analysed for a selection of lava core samples from different locations in the flow-field, using ARL Fisons wavelength-dispersive X-ray fluorescence spectrometry (XRF). Analyses were carried out using fused glass discs and pressed pellets, following a standard procedure used routinely at the Open University, and described in detail in Ramsey et al. (1995). Crystal and groundmass glass compositions (hereafter simply called *glass*) were analysed using a Cameca SX100 electron microprobe (EMP), with a 20 kV accelerating voltage, 20 nA beam current, and a beam of 20 μm and 5 μm for glass and crystal analysis respectively. A summary of the analyses is shown in Table 3.2. For glass analysis, chips of USGS glass standard BHVO-2 were analysed at the beginning and the end of each run to assess the accuracy and repeatability of the measurements. Each run was composed of a maximum of 10 consecutive analyses of natural glass (probe points). Na was analysed first using a short counting time to minimize loss by volatilisation. Crystal-glass profiles were measured by programming a traverse through the crystal-glass boundary, using 10-μm beam diameter. The reproducibility of crystal microprobe analyses was of the order of ± 2 mol.% An, Fo and Wo for plagioclase, olivine, and clinopyroxene.

3.4.3 Water content of glasses

The H_2O content of the glass of selected tephra and glassy lava selvages was measured from doubly polished wafers using a Thermo Nicolet Nexus Fourier-transform infrared (FTIR) spectrometer coupled with a Continuum IR microscope. Standard EverGlo mid-infra-red source optics, a Ge-on-KBr beamsplitter, and a MCT-A detector (11,700–750 cm^{-1}) were used. The aperture was positioned so as to analyse patches of clear brown glass avoiding (as best as possible) crystals, microcrystalline areas that reflect post-emplacement cooling, vesicles, and areas previously analysed by EMP. Several points were analysed on each wafer, to assess the special homogeneity of the glasses and detect anomalous analyses

of crystalline material. The Beer Lambert law was applied to derive the total water content ($H_2O + OH^-$) following the method explained in Stolper (1982). The law is expressed as: $C = aw/(\epsilon\rho d)$, with C the total water content, a the intensity of the broad asymmetric peak measured graphically at ~3530–3550 cm^{-1} (OH stretching vibration, Scholze, 1959), w the molecular mass of H_2O (18·02 $g.mol^{-1}$), ϵ the molar absorption coefficient (61 $L.mol^{-1}.cm^{-1}$, after Dixon *et al.*, 1988), and ρ the glass density (2·75 ± 0·1 $g.cm^{-3}$, taken from Metrich *et al.*, 1991). The thickness d of the sample was measured with a Mitutoyo Digimatic Indicator micrometer with ± 3 μm uncertainty. Uncertainties due to inaccuracies in the determination of molar coefficients and to limitation of the background method are typically ~10 % (Dixon *et al.*, 1988). The characteristic peak of molecular water at ~1630 cm^{-1} was absent on the resulting spectra, which is a common feature of basaltic glasses with low water contents (Dixon *et al.*, 1988; Dixon *et al.*, 1995).

3.4.4 Textural analysis

The methods used are described in detail in Appendix A and briefly summarized here. Point-counting techniques and automatic analysis of backscatter (BSE) images were used to estimate crystal type and mineral phase proportions, respectively, from thin-sections of selected samples. Crystal numbers and sizes were manually quantified from BSE images using the hand tool of Scion Image (the procedure consisted in drawing lines across the crystals using the appropriate tool of the software, the software reporting the accurate length of the line drawn, which was taken as a precise measure of the crystal dimension). Crystal size distributions (CSD) were derived from manual crystal size measurement of plagioclase crystals (over 300 crystals per BSE image) which were corrected for stereological effects using the program ©CSDCorrections 1.36 by Higgins (2000) and an estimated crystal aspect ratio of 1:3:10 (calculated using Morgan & Jerram, 2006).

3.5 RESULTS

3.5.1 Lava and tephra textures

Figures 3.3 and 3.4 illustrate the texture of the glassy samples of tephra and lava analysed in this study. Results from point counting, plagioclase size distribution and BSE image analysis, and quantification of plagioclase shapes in selected tephra and lava samples are shown in Figs. 3.5 to 3.8 and Tables 3.3 to 3.6. Raw data on CSD is shown in Appendix B.

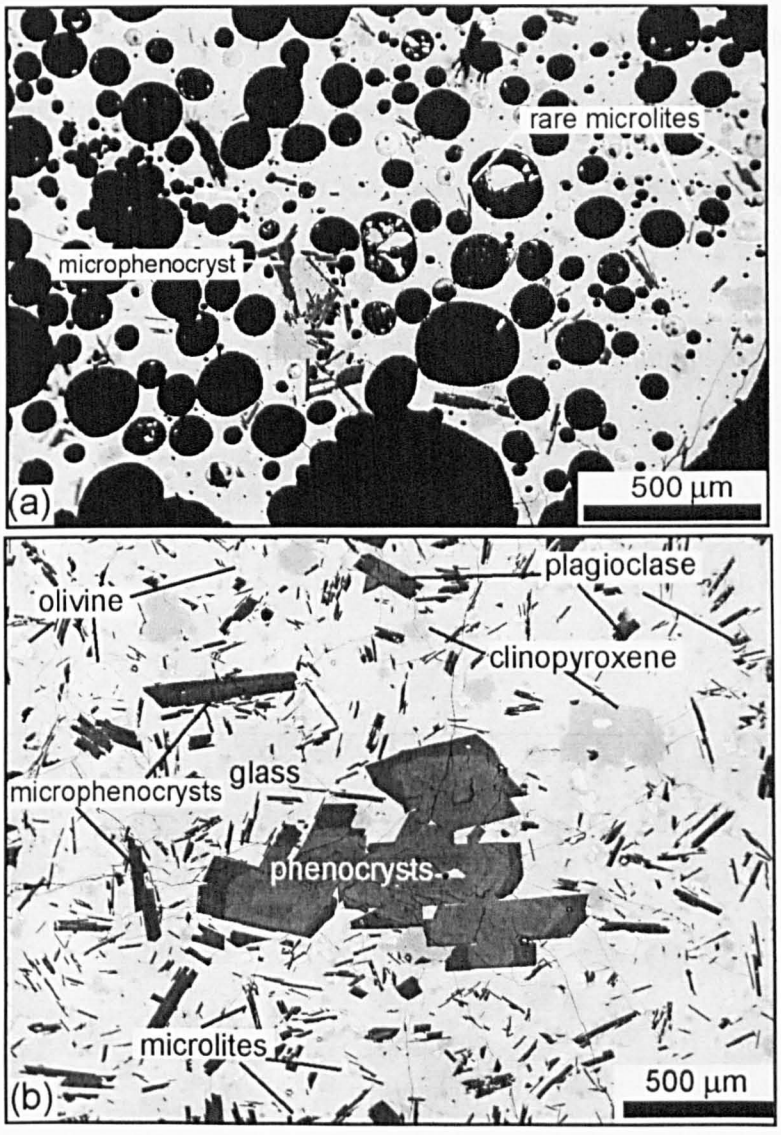

Figure 3.3: Electron microprobe backscatter images of glassy tephra (a) and lava (b) samples (18-08-83 and L17-1-1 respectively). Note different abundances of microphenocrysts and microlites between two samples. The tephra sample shown here is more crystalline and less vesicular than average.

Vesicularity. Tephra contains 50 to 80 vol.% of numerous round vesicles (Thordarson et al., 1996). Lava vesicularity ranges from 15 to 40 vol.% (Table 3.3; Fig. 3.5) and vesicles increase in size, abundance and degree of coalescence away from the outer glassy margin (Fig. 3.4). Three textural zones can be distinguished across the few outer centimetres of the lava surface (Fig. 3.4), corresponding to sharp gradients in the cooling rates of the lava surface (e.g., Oze & Winter, 2005). The outermost part (<5 mm) (zone 1) corresponds to a glassy selvage where crystals are set in a groundmass made of optically clear brown glass. In that zone, the solidification rate of the liquid lava exceeded the rates of crystallization. In zone 2 (transitional zone), dendrites cover the outer faces of the crystals (more particularly plagioclases, see Fig. 3.4); these were formed at high cooling rates. In the lava interior (zone 3), the groundmass is opaque, entirely cryptocrystalline due to intense crystallization during solidification.

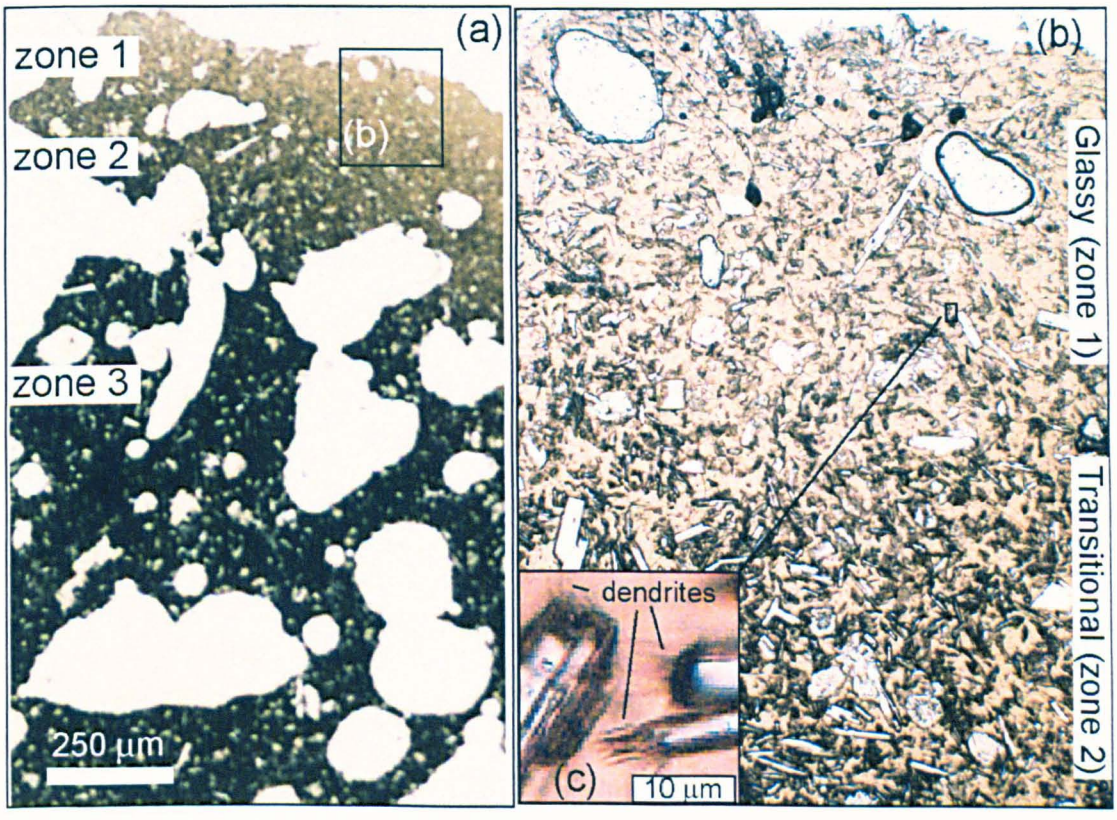

Figure 3.4: Textural zones in the outer margin of lava surface samples. (a) Photograph of 1 × 1.5 cm thin-section through outer margin of glassy sample L17-3; identification of textural zones discussed in text. (b) Photomicrograph (detail of figure a) of outer transitional and glassy zones (2.8 × 2.1 mm). (c) Photomicrograph of dendrites developing from tips of plagioclase microlites in transitional zone.

Crystallinity. Three crystal types composed of plagioclase, clinopyroxene, and olivine were identified in the eruptive products, primarily on the basis of their size. Phenocrysts are typically 100–500 μm in size, microphenocrysts 20 to 50 μm across and microlites <20 μm (Fig. 3.3). The limit between microphenocrysts and microlites is somewhat arbitrary and those are henceforth referred to as *groundmass crystals*. Phenocrysts compose 0 to 7 vol.% of the lava whereas microphenocrysts vary from ~10 to ~30 vol.% and microlites from ~15 to ~45 vol.% (Fig. 3.13, Table 3.3). Further along it will be shown that microlites spread a larger compositional range than microphenocrysts, which can be used to identify the two crystal types on backscatter images or using compositional analysis. Microscopic observations indicate that the lava contains more microphenocrysts than the tephra and that these are more abundant in samples collected from late-formed flows that cover the highlands (e.g., L29 samples). Plagioclase crystal size distributions (CSD) were measured for selected tephra and lava glassy samples to infer the relative rates of formation of each crystal type (e.g., Cashman & Marsh, 1988; Crisp et al., 1994). The size range defined by each crystal type is reflected by changes of slopes in the CSD plots (Fig 3.6); phenocrysts, microphenocrysts and microlites form straight lines in the CSD plots that decrease in slope and intercept in that order.

The total groundmass crystal content estimated by BSE image analysis is 5–8 vol.% in the tephra, and 20–40 vol.% in the lava (Fig. 3.7, Table 3.4). Plagioclase is the dominant mineral phase, varying from ~15 to ~25 vol.% in the lava, while clinopyroxene ranges from ~5 to ~15 vol.%, and olivine from ~2 to ~5 vol.%. It is noted that the higher estimation of groundmass crystals by the point counting technique is due to a post-emplacement crystallization during solidification in the opaque lava zone, i.e., zone 3 in Fig. 3.4; on the other hand, it is possible that microphenocryst abundance may be underestimated by BSE imaging (see Appendix A).

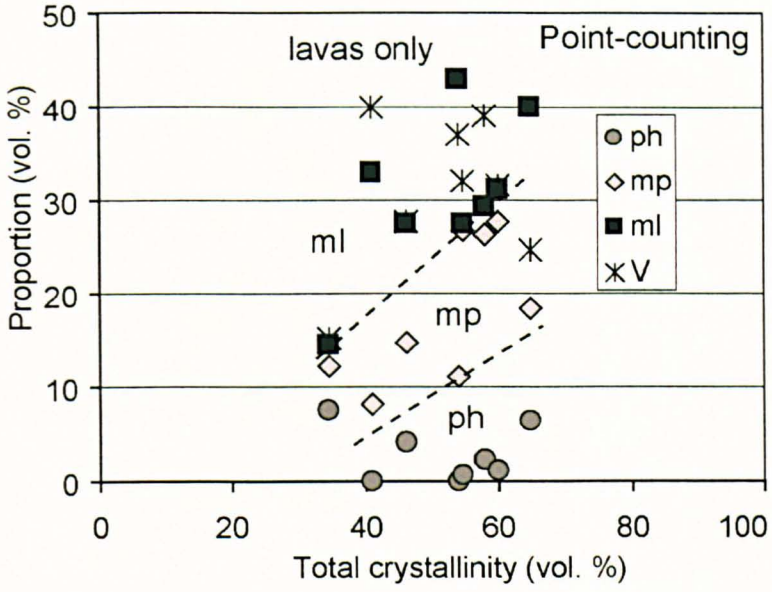

Figure 3.5: Plot of vesicularity (V) and crystal proportions (vol.%) against total crystallinity (results from point-counting technique). Crystal proportions normalised to 100% on vesicle-free basis. Microphenocrysts and microlites were differentiated mainly according to their size. Ph—phenocrysts, mp—microphenocrysts, ml—microlites.

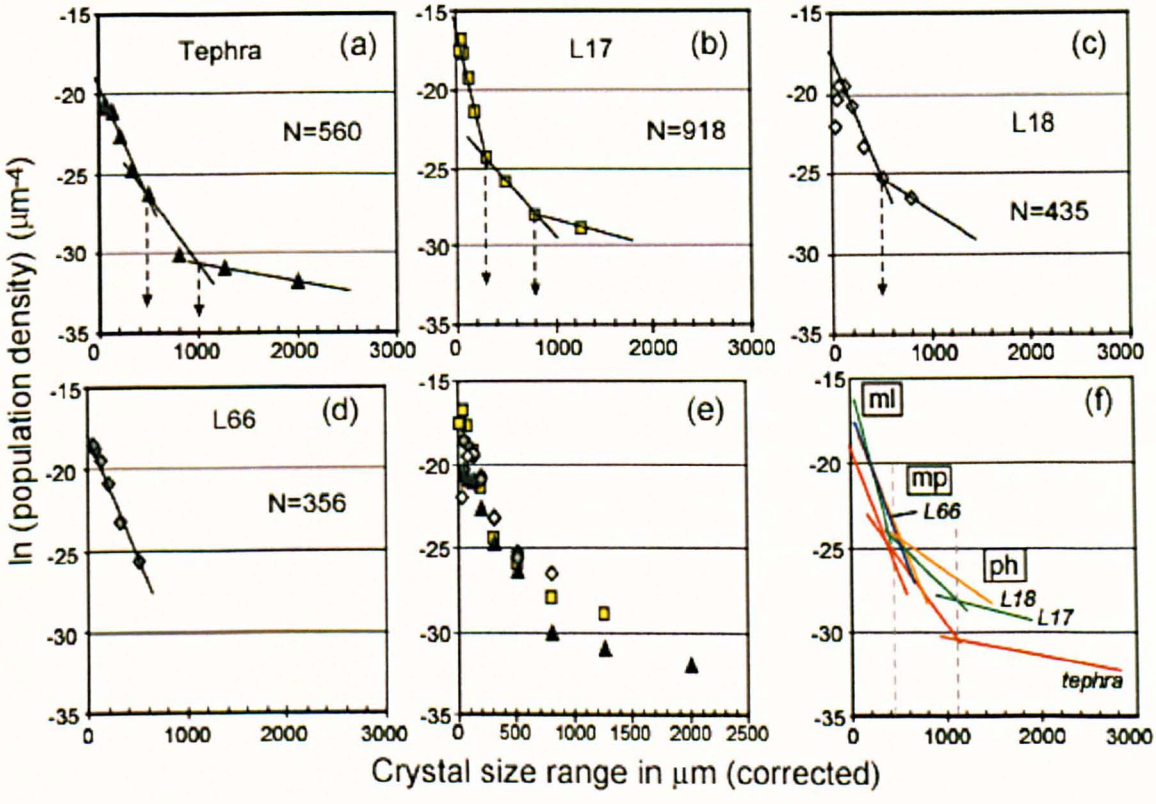

Figure 3.6: CSD plots of plagioclase population in selected samples. All data is plotted in (e). Plot of all fitted lines in (f). ml—microlites, mp—microphenocrysts and ph—phenocrysts. Crystal size represents long dimension of crystals calculated by program of Higgins (2000). Crystal content increases from tephra (a), to L17-1 (b), L66-3 (d), and to L18-1 (c) lava samples, coinciding with increase in CSD slope at small crystal sizes. N—total number of crystals counted in area studied.

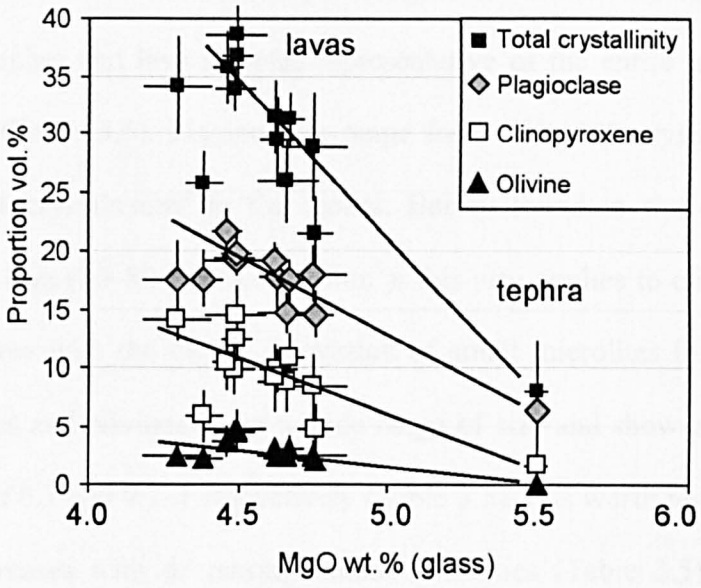

Figure 3.7: Plot of groundmass crystal phase proportions against glass MgO wt.% analysed by electron microprobe. Results from BSE image analysis (see Table 3.9).

Table 3.3: Proportions of vesicles and crystal types in selected lava samples.

Sample no.	Vesicularity	Microlites	Microphenocrysts	Phenocrysts	Total crystallinity
L7-1	40.0	32.8	8.2	0.0	41.0
L7-1	37.0	42.9	11.1	0.0	54.0
L7-1	39.0	29.3	26.3	2.3	57.9
L7-1	31.4	31.0	27.6	1.3	59.9
L7-1	32.0	27.5	26.6	0.7	54.9
L4-1	24.7	39.9	18.5	6.3	64.7
L4-2	15.4	14.7	12.3	7.6	34.5
L13-1	27.6	27.3	14.9	4.1	46.4

Results from point counts (vol.%). Crystal proportions normalized to 100% on vesicle-free basis.

Table 3.4: Modal proportions of selected samples determined using BSE image analysis

Sample no.	N	Area (mm^2)	Plagioclase	Clinopyroxene	Olivine	Total crystallinity
22-08-83	4	16.7	6.3 (3.7)	1.6 (2.1)	<0.1	7.9 (4.3)
L17-1	9	17.1	14.5 (1.9)	4.8 (1.9)	2.1 (0.8)	21.4 (3.2)
L18-1	10	16.2	17.6 (2.3)	5.8 (2.1)	2.3 (0.6)	25.8 (2.6)
L21-1	4	9.8	19.4 (0.8)	9.8 (2.0)	4.6 (0.7)	33.8 (1.7)
L43-2	5	9.5	18.0 (2.3)	8.3 (2.8)	2.5 (1.1)	28.9 (4.5)
E3-5	2	4.2	17.5 (3.3)	14.1 (1.6)	2.5 (0.9)	34.1 (4.2)
L55-10	10	12.4	17.7 (2.5)	9.7 (1.8)	2.4 (0.4)	29.3 (3.7)
L63-5	9	17.5	14.7 (1.6)	8.8 (2.6)	2.4 (0.7)	25.9 (3.5)
L63-6	7	15.6	19.2 (1.3)	14.5 (2.4)	4.7 (1.6)	38.5 (2.9)
L63-7	12	24.3	17.5 (1.8)	10.7 (2.1)	3.0 (1.1)	31.2 (2.2)
L63-8	10	21.7	19.2 (1.4)	9.2 (2.8)	3.0 (0.5)	31.4 (3.0)
L63-10	8	17.7	21.6 (2.0)	10.4 (2.2)	3.7 (1.2)	35.7 (3.0)
L63-1	10	16.3	19.9 (1.9)	12.4 (3.0)	4.6 (1.1)	36.8 (2.2)

All proportions normalized to 100% on vesicle-free basis. N—number of BSE images analysed. Area—total area analysed. Average of multiple analyses for each sample reported with standard deviation in brackets.

Crystal number densities and shapes. Plagioclase and olivine number densities were quantified for tephra and lava samples representative of the entire range in groundmass crystal content (Table 3.5). Plagioclases range from 160—450 crystals/mm^2 in the lava compared to 34 crystals/mm^2 in the tephra. Barely found in the tephra, olivines are abundant in the lava (20–80 crystals per mm^2); this also applies to clinopyroxenes. These observations agree with the higher proportion of small microlites in the lavas (i.e., Fig. 3.3). Plagioclases and olivines cover a wide range of size and show average aspect ratios (width/length) of 0.3 and 0.7–1 respectively (Table 3.5). It is worth noting that the average crystal size increases with decreasing number densities (Table 3.5), which is a direct consequence of mass balance constraints in the crystallization process (e.g., Marsh, 1988). More than 70% of plagioclase crystals, in both lava and tephra, display some form of clustering, branching, and/or intergrowth with other phases (Fig. 3.8, Table 3.6).

Table 3.5: Results of manual measurements of crystal sizes and numbers from BSE images

Sample no.	Area (mm^2)	N	Number density (mm^{-2})	Crystal sizes (μm) W	L	W/L
Plagioclase						
tephra	16.43	560	34	14.3 (12.2)	58.2 (41.3)	0.3 (0.2)
L17-1	2.04	918	450	8.1 (6.5)	32.8 (25.1)	0.3 (0.2)
L18-1	2.75	435	158	15.4 (10.9)	50.8 (39.3)	0.4 (0.2)
L66-3	1.84	356	194	12.5 (7.3)	54.1 (36.3)	0.3 (0.2)
Olivine						
tephra	16.43	0	0			
L17-1	4.93	289	59	14.5 (6.9)	21.8 (10.2)	0.7 (0.2)
L18-1	2.75	54	20	21.6 (9.4)	32.4 (18.1)	0.7 (0.2)
L66-3	1.84	61	33	19.6 (16.4)	30.0 (29.6)	0.7 (0.2)

Measurements from tephra done from BSE images of samples 16-08-83, 18-08-83 (all results were added). Lava samples chosen are representative of entire compositional range. Area—total area measured, N—number of crystals counted. Average of crystal width (W) and length (L) are reported with 1 standard deviation in brackets. Raw data was used to derive CSD plots.

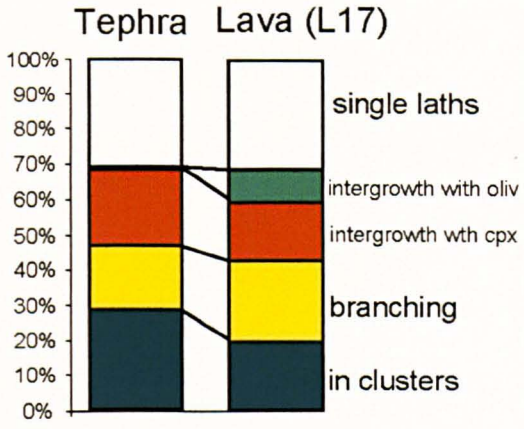

Figure 3.8: Proportion of plagioclase crystals with specific intergrowth pattern in tephra and lava samples. Oliv—olivine, cpx—clinopyroxene (data in Table 3.6).

Table 3.6: Manual quantification of plagioclase shapes and intergrowth pattern

Sample	Crystals in clusters	Crystals branching	Crystals in intergrowth with cpx	Crystals in intergrowth with olivine	Microphenocrysts	Phenocrysts
Tephra	158	104	121	4	15	7
Lava (L17)	177	215	152	86	21	1

Number of crystals of each type. cpx—clinopyroxene.

3.5.2 Crystal morphologies and compositions

Phenocrysts, microphenocrysts and microlites are different in terms of shape, compositional range and zoning pattern, and crystals in the lava are typically more evolved than in the tephra. Figure 3.9 summarizes these differences, Table 3.7 reports the representative composition of each crystal type (all data in Appendix C), and Figure 3.10 shows histograms of compositional ranges in terms of the cation ratios: An*= An/(An+Ab)= Ca/(Ca+Na); Fo= Mg/(Mg+Fe); Wo= Ca/(Ca+Mg+Fe); En= Mg/(Ca+Mg+Fe); Fs= Fe/(Ca+Mg+Fe); and En*= En/(En+Fs) see Table 3.7). Representative microprobe profiles across individual crystals are shown in Fig. 3.11. Plagioclases characteristically show small internal fluctuations in composition that are described as oscillatory zoning, and observed in phenocrysts, microphenocrysts and microlites. In the following, the characteristics of each crystal type are successively presented, but providing most details about plagioclases since these are the most abundant.

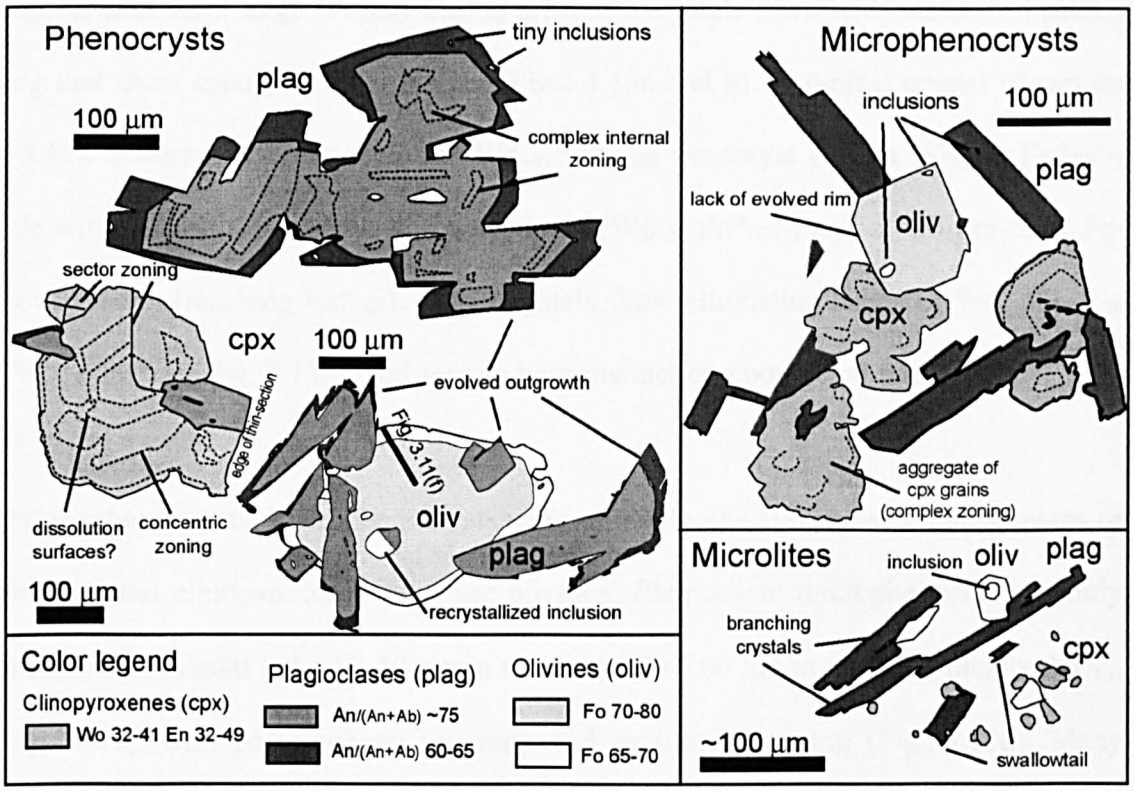

Figure 3.9: General characteristics of each crystal type. Compositional contours and crystal shapes were drawn from backscatter images. Location of profile across olivine phenocryst reported in Fig. 3.11f.

Table 3.7: Representative compositions of crystals

	Plagioclases				Clinopyroxenes					Olivines			
Crystal type	ph	ph	ph	xeno	ml	mp	ph	ph	xeno	mp	mp	ph	xeno
Location of analysis	rim	mantle	core	core	rim	core	core	rim	core	rim	core	core	core
SiO_2	54.16	52.09	50.14	46.52	50.15	50.42	51.43	51.55	52.63	37.51	37.79	38.05	39.04
TiO_2					1.65	1.22	0.96	1.23	0.77	0.08	0.05	0.00	0.00
Al_2O_3	28.78	29.74	31.55	33.78	3.17	3.49	2.94	2.15	2.10	0.03	0.05	0.00	0.03
Cr_2O_3					0.03	0.23	0.28	0.01	0.19	0.03	0.00	0.02	0.04
MgO	0.17	0.19	0.16	0.09	14.69	15.66	16.15	13.92	16.50	33.53	35.37	37.59	40.32
CaO	12.02	13.44	14.96	17.43	16.78	19.39	20.02	17.05	19.84	0.38	0.33	0.28	0.30
MnO					0.32	0.23	0.20	0.32	0.20	0.38	0.38	0.33	0.30
FeO	0.78	0.77	0.74	0.62	12.65	9.08	8.12	13.54	7.88	28.88	26.94	23.33	19.47
NiO					0.01	0.01	0.02	0.01	0.02	0.06	0.08	0.11	0.14
Na_2O	4.41	3.66	2.84	1.44	0.31	0.31	0.30	0.29	0.24	0.02	0.01	0.00	0.00
K_2O	0.13	0.07	0.05	0.03	0.00	0.01	0.00	0.01	0.00	0.00	0.00	0.00	0.00
Total	100.45	99.95	100.44	99.91	99.76	100.04	100.40	100.09	100.36	100.90	100.99	99.71	99.64
Formula													
Si	2.443	2.372	2.283	2.145	1.887	1.875	1.898	1.937	1.935	0.999	0.996	0.999	1.006
Ti					0.047	0.035	0.027	0.035	0.021	0.002	0.001	0.000	0.000
Al	1.530	1.596	1.693	1.835	0.141	0.153	0.128	0.095	0.092	0.001	0.002	0.000	0.001
Cr					0.002	0.006	0.008	0.000	0.006	0.001	0.000	0.000	0.001
Mg	0.012	0.013	0.011	0.006	0.824	0.869	0.888	0.780	0.905	1.332	1.390	1.471	1.549
Ca	0.581	0.656	0.730	0.861	0.677	0.773	0.792	0.687	0.782	0.011	0.009	0.008	0.008
Mn					0.011	0.008	0.006	0.011	0.006	0.009	0.008	0.007	0.007
Fe	0.029	0.029	0.028	0.024	0.398	0.282	0.251	0.426	0.242	0.643	0.594	0.512	0.419
Ni					0.000	0.000	0.000	0.000	0.000	0.001	0.002	0.002	0.003
Na	0.386	0.323	0.250	0.129	0.023	0.023	0.021	0.021	0.017	0.001	0.001	0.000	0.000
K	0.008	0.004	0.003	0.002	0.000	0.000	0.000	0.000	0.000	0.000	0.000	0.000	0.000
Total	4.989	4.993	4.998	5.002	4.007	4.023	4.019	3.992	4.004	2.999	3.002	3.001	2.993
Fo										67.4	70.1	74.2	78.7
Wo					35.7	40.2	41.0	36.3	40.5				
En					43.4	45.2	46.0	41.2	46.9				
An	59.6	66.7	74.3	86.8									
Or	0.82	0.41	0.31	0.20									

Major elements in wt.%. xeno—xenocryst, ph—phenocryst, mp—microphenocryst, ml—microlite. Formula based on 8 oxygens for plagioclases, 6 oxygens for clinopyroxenes, 4 oxygens for olivines.

Clinopyroxenes form large Wo_{36-42} En_{41-49} prismatic crystals often with sector and patchy zoning that show clearly in BSE images (Figs. 3.13a and b). A typical crystal shown on Fig. 3.13b features a distinct irregular $Wo_{\sim41}En^*_{78-80}$ xenocryst core, a Wo_{36-41} En^*_{76-78} mantle with straight outer faces, an evolved rim ($Wo_{\sim36}$ $En^*_{\sim71}$), and a ~20-μm-thick Fe-rich overgrowth (reaching $En^*_{\sim65}$). Other crystals show alternating bands of $Wo_{\sim39}$ $En^*_{\sim70}$ and $Wo_{\sim38}$ $En^*_{\sim75}$ (Fig. 3.13a), and sectors with distinct compositional pattern (Figs. 3.11l and 3.13a).

Microphenocrysts. Microphenocrysts consist mainly of ~100-μm-size intergrowths of plagioclase and clinopyroxene, with rare olivines. *Plagioclase* microphenocrysts mainly form branching tabular laths 20–50 μm in width and 50–100 μm in length, typically An^*_{61-64} (Fig. 3.10), with polysynthetic twinning and oscillatory zoning (Fig. 3.11d). Many crystals have skeletal overgrowths mostly developed at the corners, forming fine swallowtails or complex, blocky extensions (see Fig. 3.14b). Some have vesicles attached to or enclosed in the outer face. Round to irregular glass inclusions are common and may be abundant in some crystals, often occurring near the crystal centre and both aligned and elongated parallel to the outer faces. *Olivine* microphenocrysts are 60–100-μm, diamond to round in shape, and typically Fo_{69-72} (see Fig. 3.10), with normal zoned rims reaching Fo_{65} at the margin (Fig. 3.11g). Numerous crystals have skeletal to hopper morphologies at their corners, and rims enclose glass pockets (Figs. 3.15a–c). *Clinopyroxene* microphenocrysts typically form clusters of 20–50 μm granular crystals with radiating plagioclase laths. They are Wo_{36-41} En_{40-51} in the tephra, and slightly more evolved in the lava (Wo_{34-42} En_{40-51}). Some crystals show alternating bands of $Wo_{\sim39}$ $En^*_{\sim70}$ and $Wo_{\sim38}$ $En^*_{\sim75}$. Sector zoning is commonly seen (Figs. 3.13d and e), and the zoning is often patchy and highly irregular (i.e., Fig. 3.13c). Rims are evolved, forming a thin <10 μm light-grey band in BSE (Fig. 3.13c). In the lava, they often show re-entrants and anhedral, dendritic outgrowths, with some rounded to elongated ~10-μm-wide glass inclusions (Fig. 3.13f).

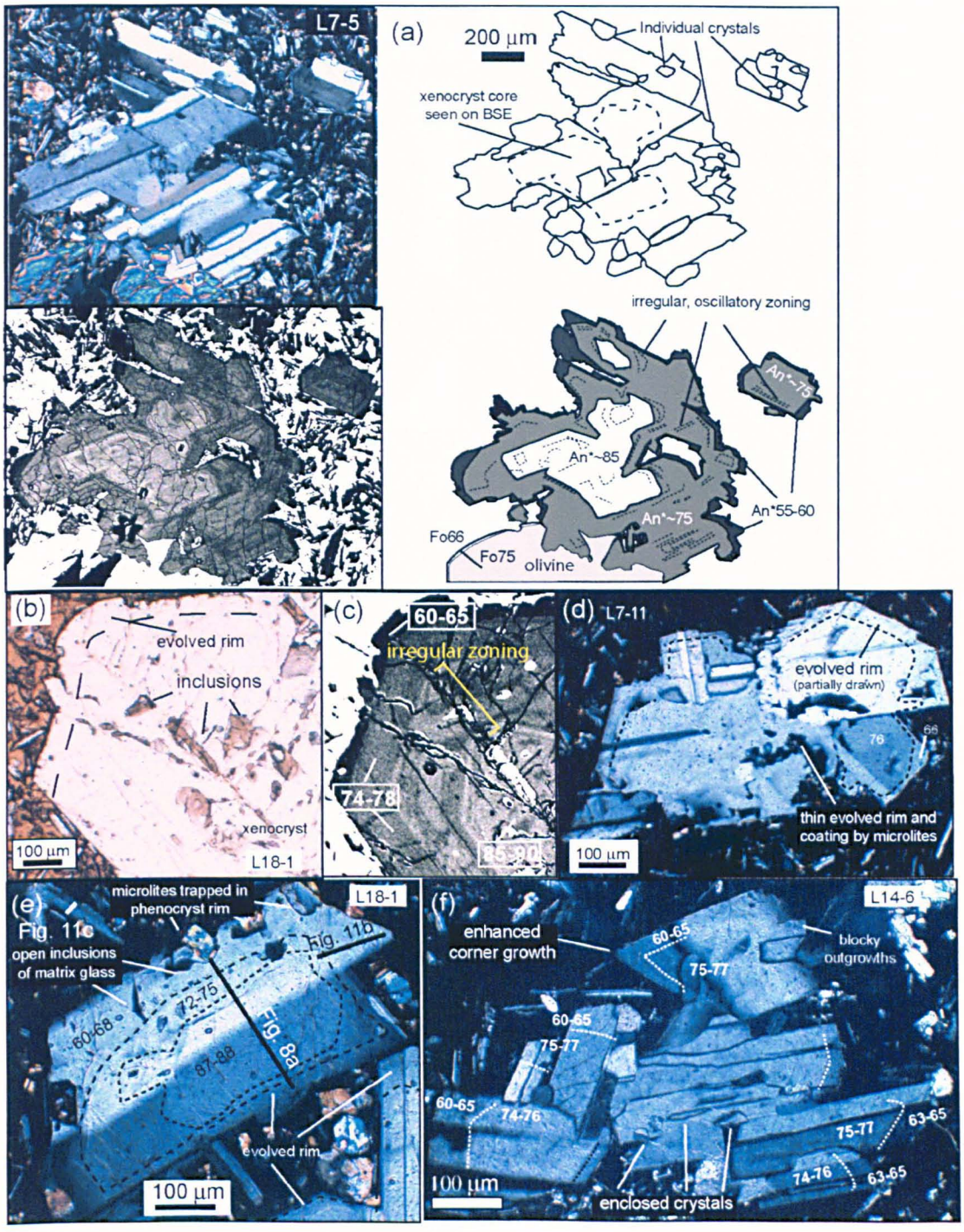

Figure 3.12: Characteristics of plagioclase phenocrysts. Numbers refer to composition of plagioclases in An*. Sample numbers are indicated on figures. (a) Plagioclase and olivine phenocryst cluster. Photomicrograph in polarized light and BSE image of cluster on top and bottom left, respectively. Note rounded individual crystals included in larger tabular crystals in cluster; xenocryst forms central part of cluster (see text). Photomicrograph in non-polarized light (b) and corresponding BSE image (c) of numerous inclusions present in xenocryst core of plagioclase phenocryst (white on BSE). (d) Plane-polarized light photomicrograph of phenocryst with corroded core and thin evolved overgrowth rim. Note nucleation of microlites on corroded surfaces. (e) Plane-polarized photomicrograph of angular phenocryst with primitive core and wide overgrowth rim including microlites and pockets of groundmass glass. Compositional profiles shown in Figs. 3.11a, b, and c are located on photograph. (f) Plane-polarized photomicrograph of cluster shown in Fig. 3.3b and sketched in Fig. 3.9. Note anhedral blocky morphology of overgrowths along phenocryst face on top right corner of photograph.

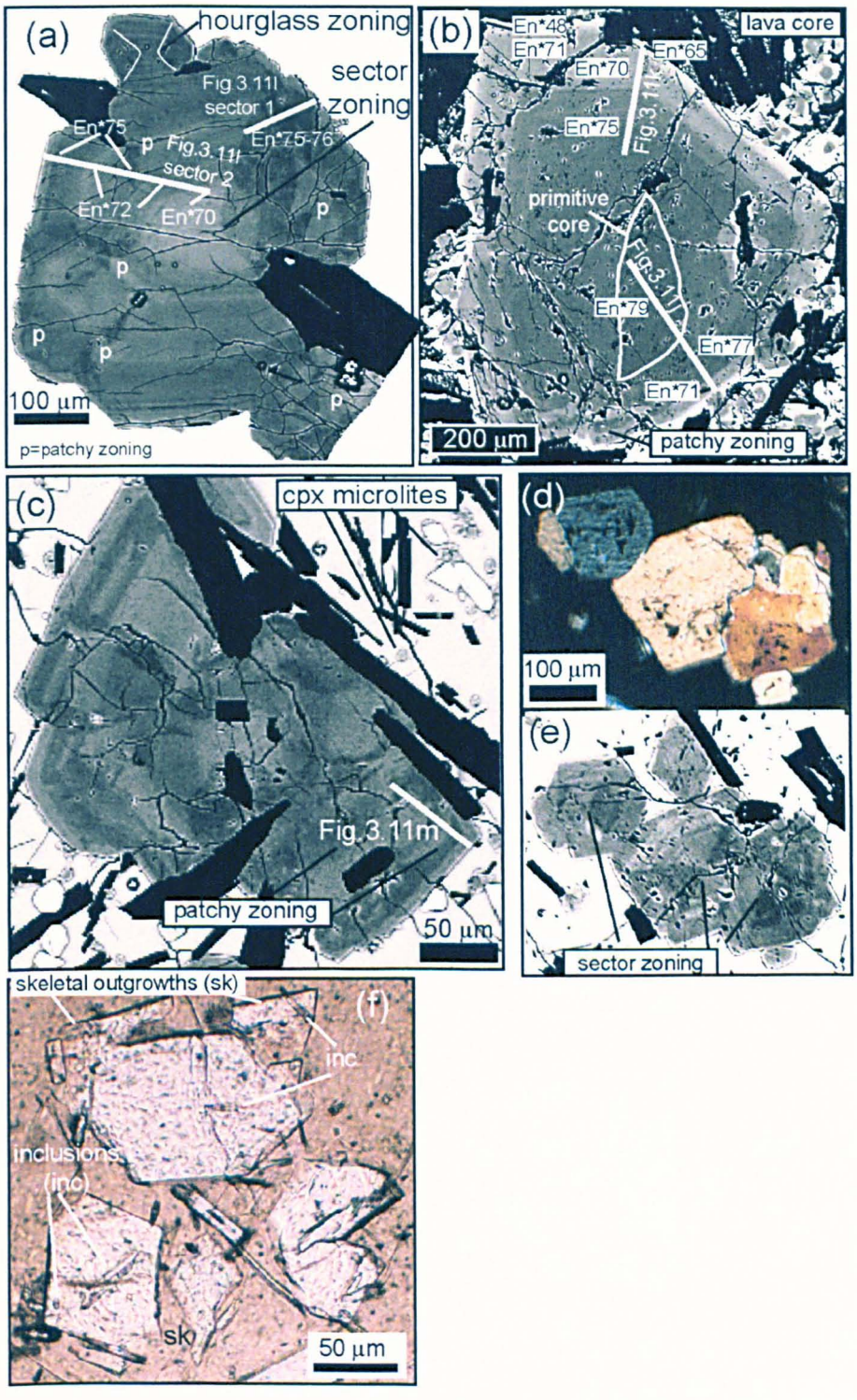

Figure 3.13: Characteristics of clinopyroxene phenocrysts and microphenocryst. Numbers indicate crystal compositions in En*. cpx—clinopyroxene. (a) BSE of phenocrysts, note sector zoning of larger crystal, and of smaller crystal attached on the edges (sample L17-1). Mg-rich areas form darker patches. Plagioclase phenocrysts in intergrowth show elongated inclusions. (b) BSE of phenocryst with xenocryst core described in text (sample L7-5). (c) BSE of irregularly zoned microphenocryst cluster (sample L17-1). Note lighter colour (more Fe-rich) and smaller size of surrounding microlites. Plane-polarized photomicrograph (d) and corresponding BSE (e) of microphenocryst cluster with distinct hourglass sector zoning (sample L14-6). (f) Photomicrograph of microphenocrysts with incomplete and angular outgrowths and irregular glass inclusions (sample L14-6).

Microlites. Microlites are subhedral to anhedral crystals that are dispersed in the groundmass or attached to microphenocryst and phenocryst rims. Similar in composition to microphenocrysts in the tephra (An^*_{61-64}, Fo_{72-75}, Wo_{32-41} En_{32-49}), they are more evolved in the lava (An^*_{53-64}, Fo_{63-69}, Wo_{32-41} En_{32-49}) (Fig. 3.10), where they commonly have high concentrations of minor elements (see Fig. 3.16 and caption). *Plagioclases* mainly form parallel branching laths, with swallowtail ends (irregular, V-shape extremities), and small glass inclusions parallel to the outer faces (Fig. 3.14a). Some form very thin tablets with irregular inclusions of glass and microlites that are defined as hopper shapes; others are high aspect ratio laths (Fig. 3.14a). *Olivines* are 5–40 μm, commonly polyhedral, with round to oval central glass inclusions (Figs. 3.15e–h). Some have skeletal outgrowths and irregular outer faces (Figs. 3.15e–h); others have incomplete outer faces with irregular glass inclusions, angular re-entrants and/or round embayments (Figs. 3.15d). *Clinopyroxenes* are <10-μm granular crystals that form clusters of light-grey grains on BSE images (Fig. 3.13c).

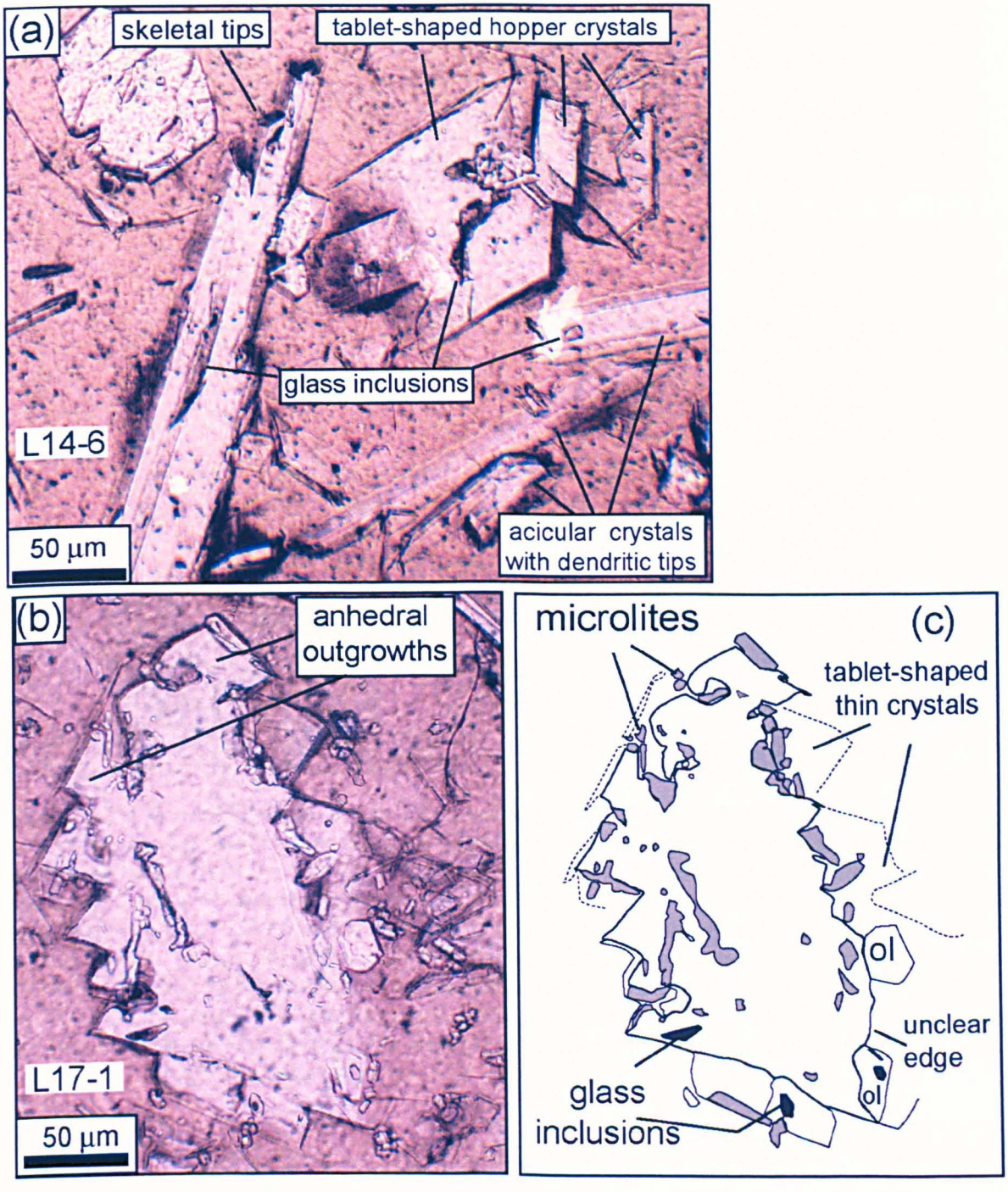

Figure 3.14: Skeletal habits of plagioclase microphenocryst rims and microlites. (a) Photomicrograph of skeletal to blocky hopper habits shown by microlites, note irregular inclusions of groundmass glass and microlites in the crystals, and acicular habits of some laths. (b) Plagioclase microphenocryst with thin, irregular-shaped outgrowths. Note that microlites and groundmass glass are incorporated in the outer rim of the crystals from which the outgrowths branch (see sketch on c).

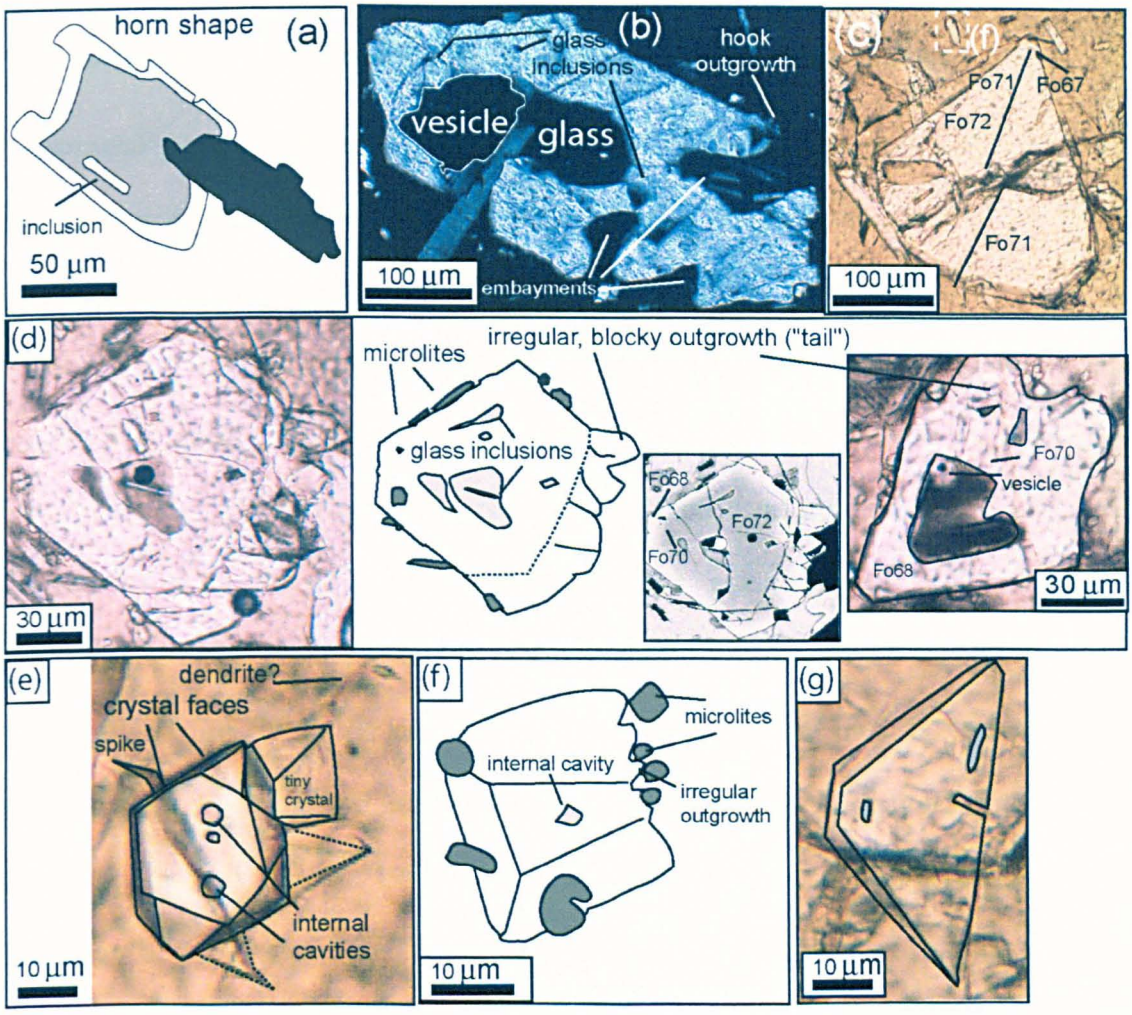

Figure 3.15: Skeletal habits of olivine microphenocryst rims and microlites. (a) Evolved outgrowth at microphenocryst corners (sketch from BSE image). (b) Crystal enclosing oval cavity partly filled with large vesicle and patch of clear glass with microlites; external face is incomplete, with C-shape and smooth re-entrants along lateral faces and hook-shaped outgrowth on corners (polarized light, sample L17-1). (c) Microphenocryst with pointy irregular outgrowth enclosing round-shape crystal (sample L14-6). (d) Crystals with V-shaped end hosting inclusions of similar shape, and showing a tail with blocky extensions and abundant microlites attached on surface (sample L17-3). (e) Touching microlites with round inclusions and pointy outgrowths (sample L14-6). Crystal faces are seen by transparency. (f) Microlite with irregular tail growing around tiny granular microlites (sample L17-1). (g) Triangular-shape microlite with inclusions of groundmass glass (L14-6).

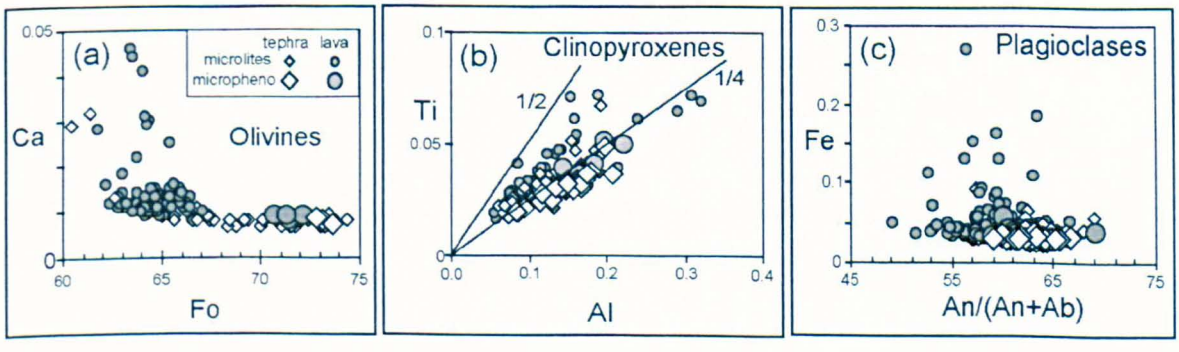

Figure 3.16: Minor elements in groundmass crystals. Caption for symbols is on (a). Ca, Ti and Al measured in number of atoms per formula unit. Note commonly high concentrations of Ca in olivines microlites (a), Fe in plagioclase microlites (b), and Ti/Al in clinopyroxene microlites (c). Distribution of peaks in minor element concentration is irregular across individual crystals.

3.5.3 Compositional variations of tephra and lava groundmass glasses

Compositional variations. Figure 3.17 plots results from whole-rock and groundmass glass compositional analyses against MgO wt.% as a differentiation index. The data is reported in Tables 3.8 and 3.9 and in Appendices D and E.

The four lava samples analysed in this study for bulk composition (XRF) fall in a small compositional range (50.41 ± 0.17 SiO_2 wt.%; 5.75 ± 0.01 MgO wt.%, see Table 3.8). Thordarson *et al.* (1996) and Thordarson (unpublished data) conducted additional bulk rock analyses of samples of lava and strombolian tephra using ICP-MS, and the average of their data plots closely to the results from this study (black square with bars on Fig. 3.17). The range of eruptive products of the Laki eruption can thus be considered as compositionally homogeneous for the purpose of this study, which agrees with previous work (e.g., Sigmarsson *et al.*, 1991). Hence, variations in the composition of groundmass glasses can be used to infer the extent of groundmass crystallization of the magma upon transport, considering a closed system.

Whole-rock data, and tephra and lava glass compositions define a typical magmatic differentiation trend of decreasing MgO with increasing TiO_2, FeO, MnO, K_2O, P_2O_5, decreasing Al_2O_3, CaO, and constant to slightly decreasing SiO_2 and Na_2O (Fig. 3.17). It is worth noting that, although most elements vary linearly with MgO wt.%, CaO is constant for tephra glasses and the least-evolved (Mg-rich) lava glasses. In addition, CaO/Al_2O_3 is significantly lower for tephra glasses than for lava glasses that show a constant ratio (CaO/Al_2O_3 = 0.75–0.80).

Groundmass glasses of tephra and lava selvages contain an average of 0.1 wt.% of dissolved H_2O, as estimated by FTIR (Table 3.10, Fig. 3.18). The high H_2O wt.% (0.3–0.4) detected by two of the repeated FTIR measurements in a highly crystalline sample (L18-1) is probably an artefact of the analysis of glasses at close distance from crystal borders and thus relatively enriched in volatile component. It is likely that the glass analysed was

located in the lava transitional zone (Fig. 3.4), where crystal boundary layers are thick and highly evolved (see below). The amount of water dissolved in tephra and lava selvages is thus considered to be roughly similar, and less than 0.1 wt.%.

Figure 3.19 plots tephra and lava glass compositions in terms of Mg# [Mg/(Mg+Fe)—Fe calculated from total FeO] as an index of liquid differentiation, against distance from the vent. Liquid differentiation increases sharply close to the vent, which is related to the tephra-lava glass compositional gap shown above. NVEF lavas are distinctly less evolved than lavas that travelled to further distances from the vent or were produced later in the eruption (also shown in Fig. 3.18); they show a slight down-flow increase in differentiation that seems to correlate with the location of the transition from shelly to spiny pāhoehoe surfaces defined in the field (Figs. 3.20a and b). Away from the vent area, the range covered by lava glass compositions is small and does not vary systematically with distance from the vent (Fig. 3.19) or along single lava lobes (see Fig. 3.20c). There is no correlation between groundmass crystallinity and sample type (Fig. 3.20c). Glasses of samples that showed evidence for partial micro-crystallization during solidification (i.e., belonging to lava transitional zone) spread over a large compositional range, following the same trend as other lava glasses, but towards distinctly more evolved compositions in all elements (see L63-9: Figs. 3.20d and e). The absence of Fe-oxide formation in that sample is notable, given TiO_2 concentrations of 4–5 wt.%.

Table 3.8: XRF whole-rock analysis of selected lava core samples

Sample no.	L13-4	L3-1	L4-4	L7-6	Average (stdev)
SiO_2	50.54	50.34	50.21	50.55	50.41 (0.17)
TiO_2	2.78	2.81	2.74	2.83	2.79 (0.04)
Al_2O_3	13.93	13.82	13.97	13.83	13.89 (0.08)
FeO	13.66	13.75	13.32	13.76	13.63 (0.21)
MnO	0.23	0.23	0.22	0.23	0.22 (0.00)
MgO	5.76	5.73	5.76	5.77	5.75 (0.01)
CaO	10.50	10.40	10.46	10.44	10.45 (0.04)
Na_2O	2.72	2.57	2.71	2.74	2.69 (0.08)
K_2O	0.43	0.41	0.41	0.43	0.42 (0.01)
P_2O_5	0.30	0.30	0.30	0.30	0.30 (0.00)
LOI	*-0.85*	*-0.35*	*-0.09*	*-0.88*	
Total	100	100	100	100	100.55

Major elements in wt.%. Stdev—1 standard deviation, *LOI*—Loss On Ignition.

Table 3.9: Average composition of glass standards and natural groundmass glasses.

Sample no.	BHVO-2	USGS*	15-08-83	16-08-83	18-08-83	22-08-83
Sample type/location	Glass standard	Glass standard	tephra/vent	tephra/vent	tephra/vent	tephra/vent
D (km)			0	0	0	0
N	295		11	5	10	10
SiO_2	50.42 (0.401)	49.90 (0.600)	50.58 (0.122)	50.72 (0.045)	50.66 (0.107)	50.49 (0.087)
TiO_2	2.75 (0.045)	2.73 (0.040)	3.01 (0.032)	2.99 (0.054)	2.97 (0.027)	3.05 (0.036)
Al_2O_3	13.54 (0.164)	13.50 (0.200)	13.17 (0.038)	13.07 (0.051)	13.10 (0.062)	13.09 (0.105)
FeO	11.02 (0.131)	11.07 (0.200)	14.11 (0.050)	14.06 (0.094)	14.49 (0.096)	14.25 (0.084)
MnO	0.17 (0.010)	0.17	0.23 (0.006)	0.23 (0.007)	0.24 (0.012)	0.23 (0.009)
MgO	7.24 (0.095)	7.23 (0.120)	5.60 (0.061)	5.59 (0.042)	5.43 (0.048)	5.49 (0.037)
CaO	11.21 (0.123)	11.40 (0.200)	9.65 (0.067)	9.71 (0.066)	9.49 (0.061)	9.83 (0.093)
Na_2O	2.20 (0.062)	2.22 (0.080)	2.84 (0.043)	2.84 (0.030)	2.82 (0.030)	2.76 (0.042)
K_2O	0.51 (0.014)	0.52 (0.010)	0.46 (0.014)	0.46 (0.006)	0.46 (0.010)	0.46 (0.011)
P_2O_5	0.28 (0.018)	0.27 (0.020)	0.35 (0.014)	0.34 (0.013)	0.34 (0.021)	0.35 (0.028)
Total	99.32 (0.518)	99.01	99.37 (0.192)	99.04 (0.164)	99.10 (0.126)	99.12 (0.224)
Mg#**	53.95 (0.43)	54	41.42 (0.26)	41.48 (0.22)	40.07 (0.26)	40.74 (0.24)

Sample no.	E3-5	L14-3-1	L14-6	L14-7	L17-1	L17-3
Sample type/location	lava/coastal plain	lava/NVEF	lava/NVEF	lava/NVEF	lava/NVEF	lava/NVEF
D (km)	45	0.05	0.2	0.05	0.25	0.1
N	5	6	5	4	7	6
SiO_2	50.14 (0.262)	50.49 (0.157)	50.63 (0.097)	50.42 (0.057)	50.40 (0.072)	50.43 (0.095)
TiO_2	4.07 (0.035)	3.50 (0.053)	3.57 (0.041)	3.54 (0.042)	3.63 (0.043)	3.61 (0.044)
Al_2O_3	11.49 (0.027)	12.26 (0.107)	11.88 (0.076)	12.41 (0.148)	11.92 (0.040)	11.99 (0.140)
FeO	17.10 (0.541)	15.32 (0.096)	15.50 (0.056)	15.16 (0.126)	15.77 (0.110)	15.65 (0.143)
MnO	0.27 (0.015)	0.25 (0.011)	0.27 (0.012)	0.24 (0.016)	0.25 (0.011)	0.25 (0.009)
MgO	4.29 (0.112)	4.99 (0.094)	4.82 (0.051)	4.90 (0.122)	4.79 (0.052)	4.86 (0.062)
CaO	9.05 (0.142)	9.79 (0.050)	9.57 (0.050)	9.79 (0.124)	9.58 (0.060)	9.53 (0.040)
Na_2O	2.52 (0.097)	2.48 (0.078)	2.85 (0.027)	2.60 (0.100)	2.72 (0.075)	2.75 (0.040)
K_2O	0.59 (0.015)	0.52 (0.015)	0.52 (0.006)	0.52 (0.011)	0.53 (0.020)	0.54 (0.014)
P_2O_5	0.47 (0.009)	0.39 (0.015)	0.39 (0.020)	0.40 (0.030)	0.40 (0.019)	0.39 (0.017)
Total	99.24 (0.164)	98.93 (0.320)	99.18 (0.203)	98.48 (0.341)	99.31 (0.175)	98.96 (0.205)
Mg#**	30.93 (1.21)	36.75 (0.47)	35.67 (0.32)	36.58 (0.39)	35.16 (0.29)	35.63 (0.28)

Sample no.	L17-5	L17-6	L18-1	L21-1	L29-13	L29-15
Sample type/location	lava/NVEF	lava/NVEF	lava/NVLF	rc tephra/highlands	lava/highlands	lava/highlands
D (km)	0.01	0.3	0.08	0.5	2	2
N	7	5	8	7	6	9
SiO_2	50.40 (0.079)	50.50 (0.080)	50.04 (0.200)	50.40 (0.106)	50.10 (0.099)	50.14 (0.067)
TiO_2	3.51 (0.062)	3.73 (0.019)	4.08 (0.041)	3.85 (0.051)	4.02 (0.048)	3.97 (0.031)
Al_2O_3	12.14 (0.104)	11.99 (0.083)	11.42 (0.131)	11.73 (0.127)	11.53 (0.087)	11.50 (0.026)
FeO	15.61 (0.118)	15.53 (0.094)	16.75 (0.100)	16.22 (0.085)	16.74 (0.136)	16.65 (0.109)
MnO	0.26 (0.007)	0.25 (0.011)	0.27 (0.010)	0.25 (0.016)	0.26 (0.013)	0.27 (0.010)
MgO	5.02 (0.056)	4.80 (0.055)	4.41 (0.070)	4.57 (0.038)	4.44 (0.077)	4.51 (0.033)
CaO	9.55 (0.041)	9.45 (0.042)	9.17 (0.039)	9.42 (0.047)	9.10 (0.092)	9.25 (0.045)
Na_2O	2.61 (0.147)	2.80 (0.038)	2.80 (0.062)	2.57 (0.025)	2.75 (0.077)	2.68 (0.099)
K_2O	0.52 (0.021)	0.53 (0.013)	0.60 (0.008)	0.57 (0.011)	0.60 (0.010)	0.58 (0.016)
P_2O_5	0.38 (0.033)	0.41 (0.021)	0.45 (0.017)	0.42 (0.021)	0.47 (0.025)	0.45 (0.020)
Total	98.68 (0.352)	98.80 (0.211)	99.50 (0.453)	99.05 (0.096)	100.22 (0.187)	99.25 (0.239)
Mg#**	36.44 (0.37)	35.54 (0.37)	31.94 (0.38)	33.43 (0.21)	32.13 (0.40)	32.59 (0.20)

Sample no.	L29-18	L33-1	L4-2	L43-2	L55-10	L63-1
Sample type/location	lava/highlands	lava/Highlands	lava/coastal plain	lava/highlands	lava/coastal plain	lava/coastal plain
D (km)	2	6	30	20	54	49
N	7	5	10	7	9	6
SiO_2	50.22 (0.042)	50.23 (0.115)	50.30 (0.249)	50.21 (0.165)	50.13 (0.218)	50.35 (0.116)
TiO_2	3.94 (0.037)	3.86 (0.054)	3.98 (0.185)	3.88 (0.038)	3.85 (0.076)	4.02 (0.056)
Al_2O_3	11.66 (0.053)	11.72 (0.036)	11.46 (0.173)	11.68 (0.042)	11.56 (0.095)	11.58 (0.018)
FeO	16.55 (0.141)	16.26 (0.115)	16.93 (0.211)	16.20 (0.178)	16.48 (0.140)	16.39 (0.130)
MnO	0.26 (0.010)	0.25 (0.012)	0.26 (0.010)	0.27 (0.011)	0.27 (0.008)	0.28 (0.015)
MgO	4.45 (0.022)	4.62 (0.053)	4.41 (0.073)	4.75 (0.108)	4.63 (0.058)	4.50 (0.049)
CaO	9.12 (0.104)	9.31 (0.062)	8.80 (0.161)	9.50 (0.062)	9.25 (0.102)	9.31 (0.021)
Na_2O	2.79 (0.101)	2.75 (0.091)	2.77 (0.068)	2.52 (0.228)	2.82 (0.085)	2.54 (0.090)
K_2O	0.58 (0.019)	0.56 (0.010)	0.62 (0.026)	0.54 (0.024)	0.56 (0.019)	0.57 (0.022)
P_2O_5	0.44 (0.023)	0.44 (0.018)	0.47 (0.020)	0.44 (0.019)	0.43 (0.027)	0.45 (0.019)
Total	99.62 (0.288)	99.13 (0.225)	98.98 (0.266)	98.74 (0.200)	99.39 (0.163)	99.47 (0.134)
Mg#**	32.41 (0.18)	33.63 (0.20)	31.72 (0.30)	34.36 (0.67)	33.40 (0.39)	32.85 (0.30)

Sample no.	L63-10	L63-5	L63-6	L63-7	L63-8	L66-3
Sample type/location	lava/coastal plain	lava/coastal plain	lava/coastal plain	lava/coastal plain	lava/coastal plain	lava/coastal plain
D (km)	49	48	48	48	48	55
N	9	5	4	5	8	7
SiO_2	50.39 (0.201)	50.27 (0.047)	50.29 (0.114)	50.11 (0.036)	50.26 (0.146)	50.17 (0.094)
TiO_2	3.95 (0.083)	3.76 (0.049)	4.02 (0.081)	3.91 (0.049)	3.88 (0.058)	3.84 (0.043)
Al_2O_3	11.54 (0.071)	11.76 (0.082)	11.50 (0.071)	11.58 (0.045)	11.73 (0.176)	11.82 (0.069)
FeO	16.62 (0.145)	16.20 (0.079)	17.01 (0.110)	16.39 (0.085)	16.47 (0.126)	16.36 (0.038)
MnO	0.27 (0.010)	0.26 (0.014)	0.28 (0.007)	0.27 (0.015)	0.25 (0.019)	0.25 (0.007)
MgO	4.47 (0.047)	4.67 (0.099)	4.49 (0.064)	4.67 (0.049)	4.62 (0.015)	4.64(0.029)
CaO	9.01 (0.080)	9.48 (0.060)	9.14 (0.040)	9.32 (0.033)	9.29 (0.054)	9.19 (0.051)
Na_2O	2.74 (0.059)	2.63 (0.075)	2.21 (0.177)	2.72 (0.067)	2.50 (0.191)	2.73 (0.025)
K_2O	0.59 (0.014)	0.55 (0.020)	0.60 (0.029)	0.59 (0.031)	0.57 (0.014)	0.56 (0.017)
P_2O_5	0.43 (0.021)	0.44 (0.019)	0.46 (0.005)	0.45 (0.021)	0.43 (0.019)	0.43 (0.026)
Total	99.15 (0.344)	99.55 (0.248)	99.27 (0.248)	99.23 (0.181)	99.06 (0.266)	98.78 (0.136)
Mg#**	32.39 (0.37)	33.94 (0.55)	32.02 (0.28)	33.72 (0.33)	33.35 (0.21)	33.59 (0.16)

Data in wt.%, normalized to 100% (except totals). Standard deviation in brackets. FeO is in total iron. Mg** = Mg/(Mg+Fe). D—distance from vent. N—number of analyses averaged for each sample. Sample type and location: NVEF— near-vent early-formed, NVLF—near-vent late-formed, rc—rootless cone. Column USGS* reports recommended value for BHVO-2 (available from: http://minerals.cr.usgs.gov /geo_chem_stand/index.html).

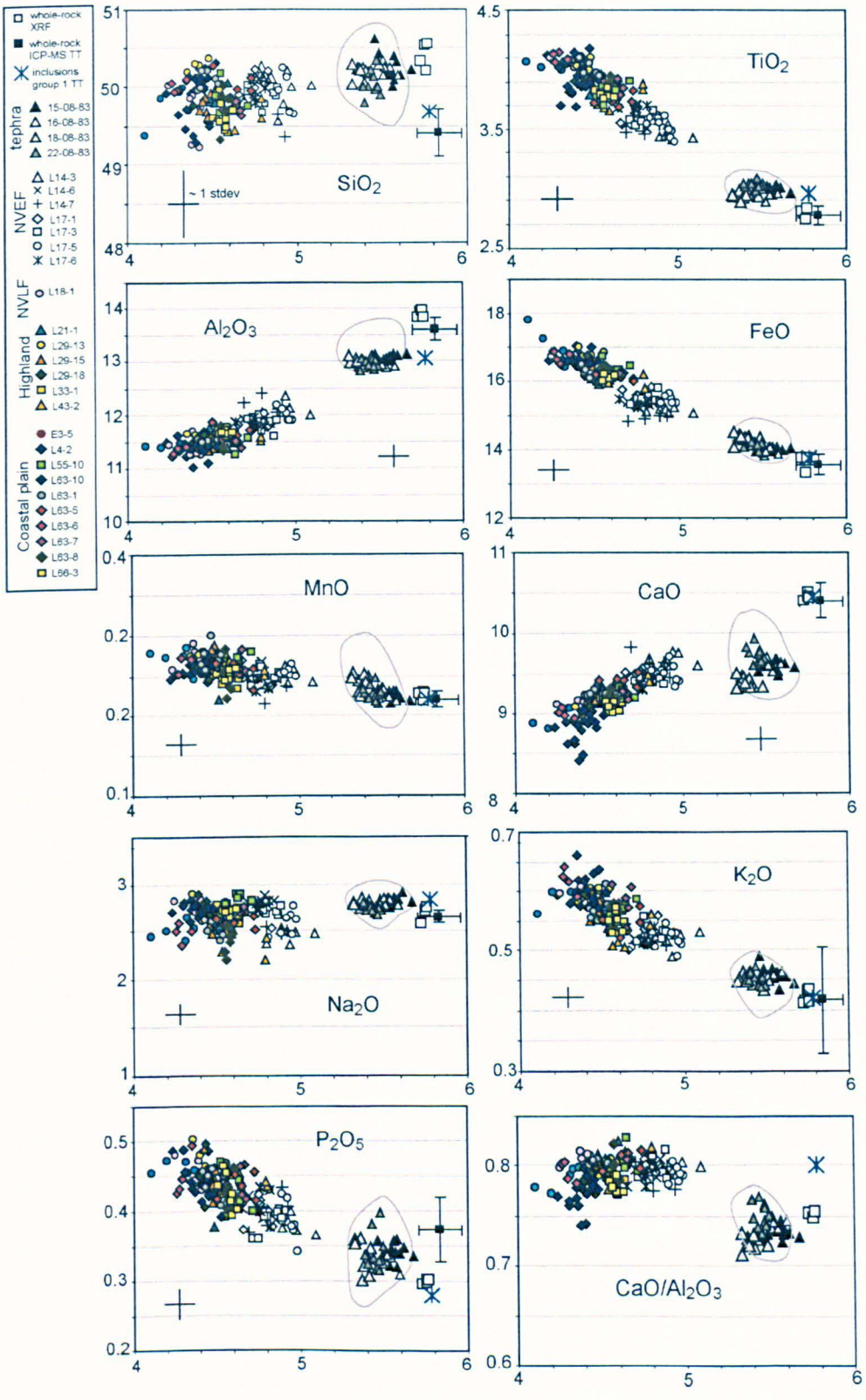

Figure 3.17: Major element composition of tephra and lava groundmass glasses, plotted with whole rock analyses. Black square with error bars show average and standard deviation of whole rock analyses of both lava and tephra samples by Thordarson et al. (1996) and T. Thordarson (unpublished). Blue asterisk shows average composition of group 1 inclusions analysed by Thordarson et al. (1996). Grey outline shows extent of Thordarson et al. (1996) and T. Thordarson (unpublished) EMP analysis of strombolian tephra glasses (note similarity with data from this study). The cross on each diagram represents 1 standard deviation of standard glass composition reported in Table 3.9.

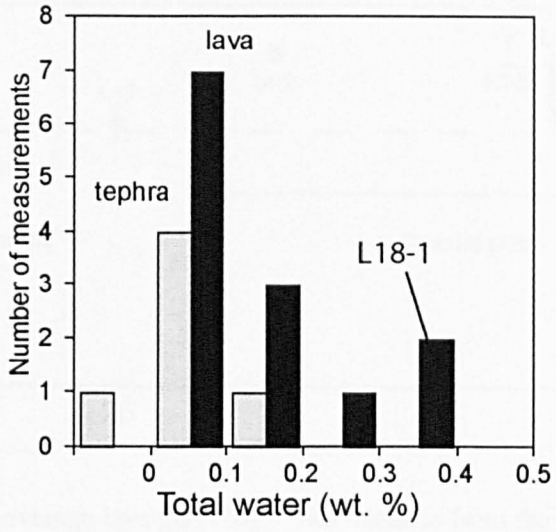

Figure 3.18: Histogram of total water content of lava (black) and tephra (grey) groundmass glasses (FTIR). High water concentrations detected in some glass patches analysed in sample L18-1 (line on figure) is attributed to volatile enrichment in boundary layers close to crystals (see text).

Table 3.10: Results from FTIR analysis of tephra and lava glasses

Sample no.	Analysis no.	Absorbance (*a*)	Thickness (μm)	H_2O+OH^- (wt.%)
Tephra glass				
16-08-83	2/1	0.066	72	0.096
18-08-83	1/1	0.062	85	0.076
18-08-83	1/2	0.05	85	0.061
18-08-83	1/3	0.084	85	0.102
18-08-83	2/1	0.073	93	0.082
Lava glass				
L14-6	2/1	0.113	130	0.090
L14-6	2/2	0.101	130	0.081
L14-6	2/3	0.142	130	0.114
L17-3	1/1	0.08	67	0.123
L17-3	1/7	0.08	67	0.123
L17-3	1/3	0.01	29	0.036
L18-1	3/1	0.051	65	0.081
L18-1	3/2	0.042	65	0.067
L18-1	3/3	0.137	65	0.219
L18-1	4/1	0.126	182	0.072
L18-1	4/2	0.101	171	0.061
L18-1	3/1b	0.101	30	0.352
L18-1	3/2b	0.088	30	0.307
L43-2	1/2	0	22	0.000

H_2O+OH^- calculated using Beer Lambert equation (see equation in text). Large variability of repeated measurements in single samples (e.g., L18-1) is ascribed to enrichment of groundmass glasses close to crystals (boundary layers) in volatiles.

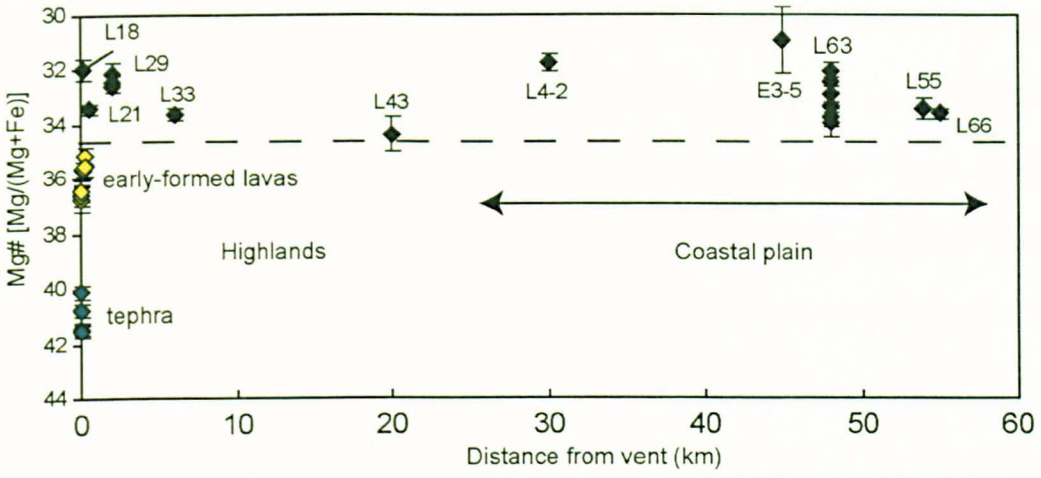

Figure 3.19: Variation of average lava glass Mg# with distance from the vent (1 standard deviation shown by error bars). Note absence of correlation between Mg# of lava glasses and travel distance of lava from vent. This signifies limited crystallization and thus cooling during down-flow lava transport.

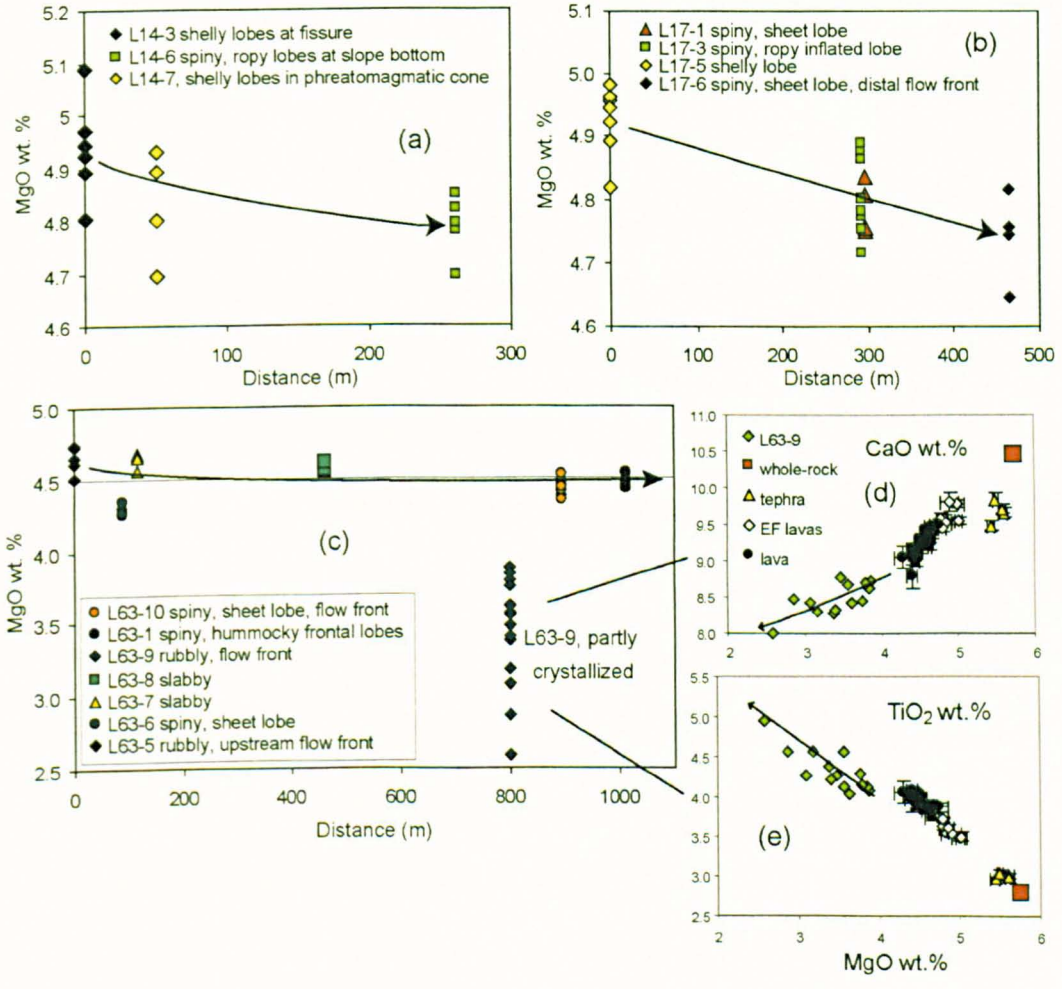

Figure 3.20: Variation of MgO wt.% in lava glasses along single flows. (a, b) Variations along NVEF flows (L14 and L17). Note trend of decreasing MgO with distance from source. (c) Variations along lava lobe on coastal plain that shows increasing surface brecciation along its length (see text). Note small range in glass compositions (except L63-9) and absence of correlation with distance from source. (d, e) Extreme differentiation of glass analysed from lava transitional zone of sample L63-9 (green diamonds). Other data is plotted as averages of multiple analyses within single lava samples with standard deviations (EF—NVEF; lava—other lava glasses).

Crystal-glass compositional gradients. In the lava transitional zone, a few millimeters away from the outermost glassy selvage (see Fig. 3.4), many crystals (mostly plagioclases) developed a compositionally distinct zone in the surrounding groundmass glass, which form crystal boundary layers (e.g., Schiffman & Lofgren, 1982). These are obvious on high-contrast BSE images where they form white haloes around plagioclases that are thickest along curved and irregular surfaces along the crystal faces, and fill the V or U-shaped zone formed between dendritic arms at the crystal tips (Fig. 3.21). Similar gradients were rarely detected at the margin of olivine and clinopyroxene crystals; those form small dark patches on high-contrast BSE images.

The boundary layers correspond to distinct compositional gradients in the glass that were sometimes detected by microprobe profiling across crystal-glass interfaces in the lava transitional zone. The most marked profiles measured are shown on Figs. 3.22 and 3.23. It is noted that although the profiles reported on Fig. 3.22 around plagioclases were common, those along clinopyroxene and olivine (Fig. 3.23) were rare. The gradients typically define a 5–10-μm-thick zone in the glass margins that is enriched in elements which are refractory with respect to the mineral phase in question (e.g, MgO, FeO, TiO_2, MnO, P_2O_5, and K_2O for plagioclases) and depleted in elements taken by the mineral (e.g., Al_2O_3 for plagioclases).

The fact that these gradients only developed in the lava transitional zone (they are very thin and not detectable using EMP in the outermost glass margin, i.e. zone 1 on Fig. 3.4) signifies that they formed at sub-solidus temperature, during the rapid quench of the outer lava margin. The concurrent growth of dendrites branched on plagioclase surfaces in this zone is consistent with extremely rapid cooling rates leading to conditions of rapid, diffusion-limited, growth of crystals, where constitutional undercooling occurs at the crystal border and surface instabilities form (e.g., Kirkpatrick, 1975, 1981; Schiffman & Lofgren, 1982). Dendrites are too thin to be compositionally analysed using EMP. They

although display a dark grey colour on BSE images (Fig. 3.21d) that is suggestive of a high concentration in Fe-Mg minerals. This is consistent with the growth of dendrites from boundary layers growing around plagioclases that are enriched in these elements. The chemical oversaturation occurring in boundary layers could in fact facilitate dendritic growth (e.g., Schiffman & Lofgren, 1982; Oze & Winter, 2005). It is worth noting that the high temperature and thus low viscosity of the fluid lava during flow, as well as its mechanical stirring, favour the diffusion of elements to and from the crystal-liquid interfaces, preventing the formation and preservation of boundary layers (e.g., Kouchi, 1986). It results that the gradients detected here and shown in Figs. 3.22 and 3.23 cannot be used to derive crystal growth rates during lava emplacement.

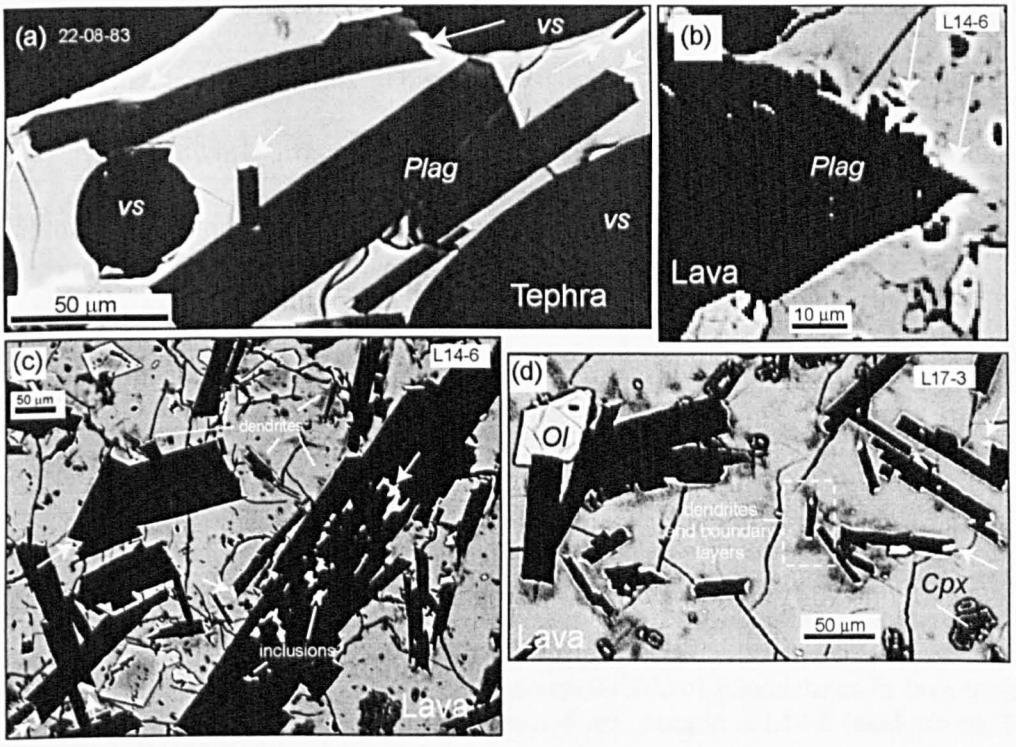

Figure 3.21: High-contrast backscatter images of tephra and lava selvages revealing compositional gradients around plagioclase borders that form white boundary layers. Images are from tephra glassy margin (a) and lava transitional zones (b, c, d; see Fig. 3.4). Plagioclases (plag) and vesicles (vs) show in black (see a), olivines (ol) in white with some with light-grey cores (see c), and clinopyroxenes (cpx) and dendrites in dark grey (see d). Sample number indicated on figure. Note extremely thin layers around crystals in outermost glassy margin of tephra (a). Layers are best developed in lava transitional zones that display dendrites (b, c, d). White arrows point to thick boundary layers that are preferentially concentrated at crystal tips and along curved faces. Plagioclase microphenocryst in (c) shows numerous small (> 10 µm) glass inclusions with compositional gradient at their edges. Spatial distribution of dendrites suggests that these are synchronous, and maybe correlated, with formation of boundary layers (see rectangular area outlined with dashed line in d).

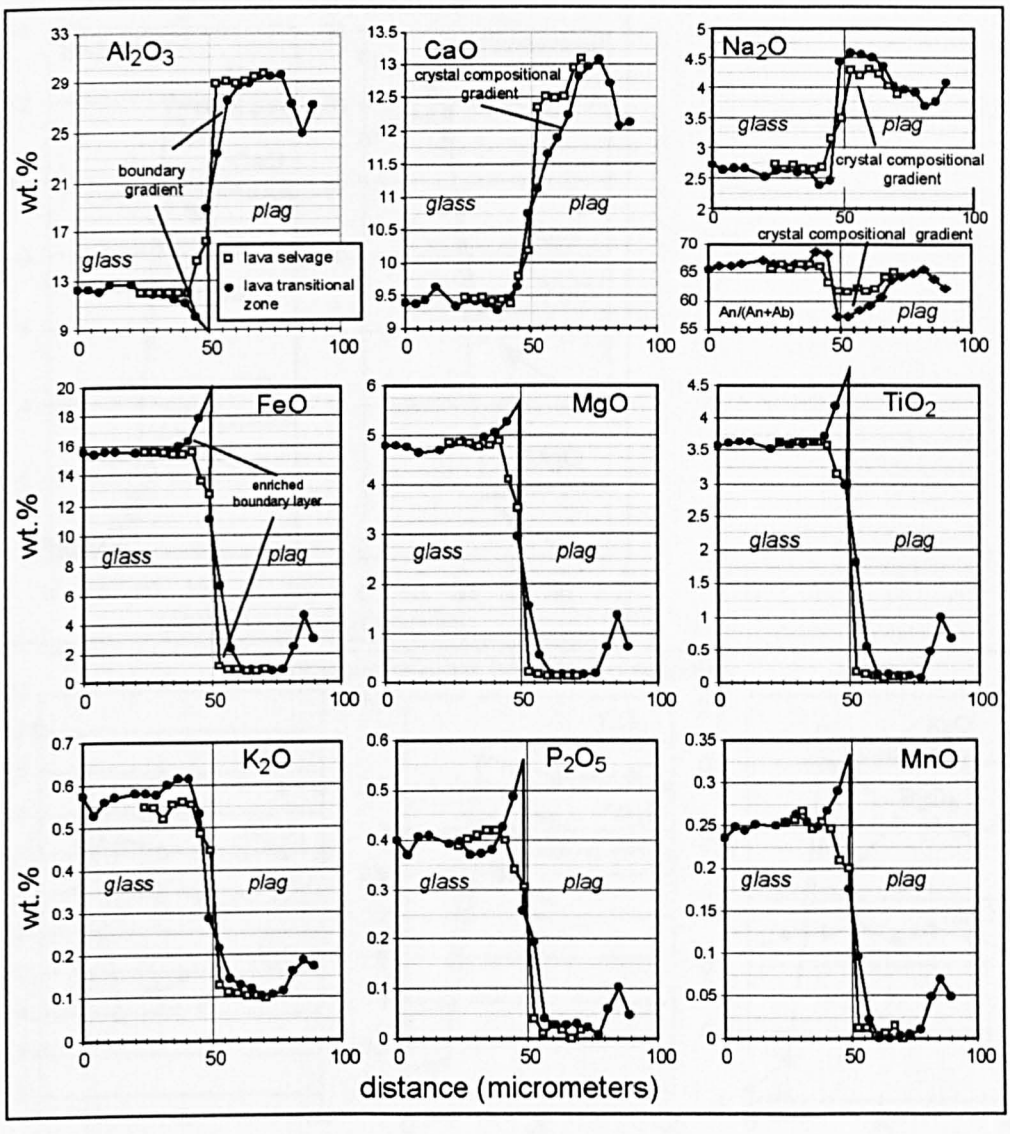

Figure 3.22: Compositional gradients at plagioclase boundaries: representative profiles. Symbols filled in white show profile across crystal-glass margin without boundary gradients, typical of crystals present in lava outermost selvage (i.e., zone 1 on Fig. 3.4). Spacing of analyses is 3.6 μm, sample is L14-6 (analysis no. 82, data reported in Appendix D3). Symbols filled in black show profile across crystal with wide boundary layer, characteristic of plagioclases in lava transitional zone (i.e. zone 2 on Fig. 3.4). Spacing of analyses is 4 μm, sample is L14-6 (analysis no. 74, data reported in Appendix D3).

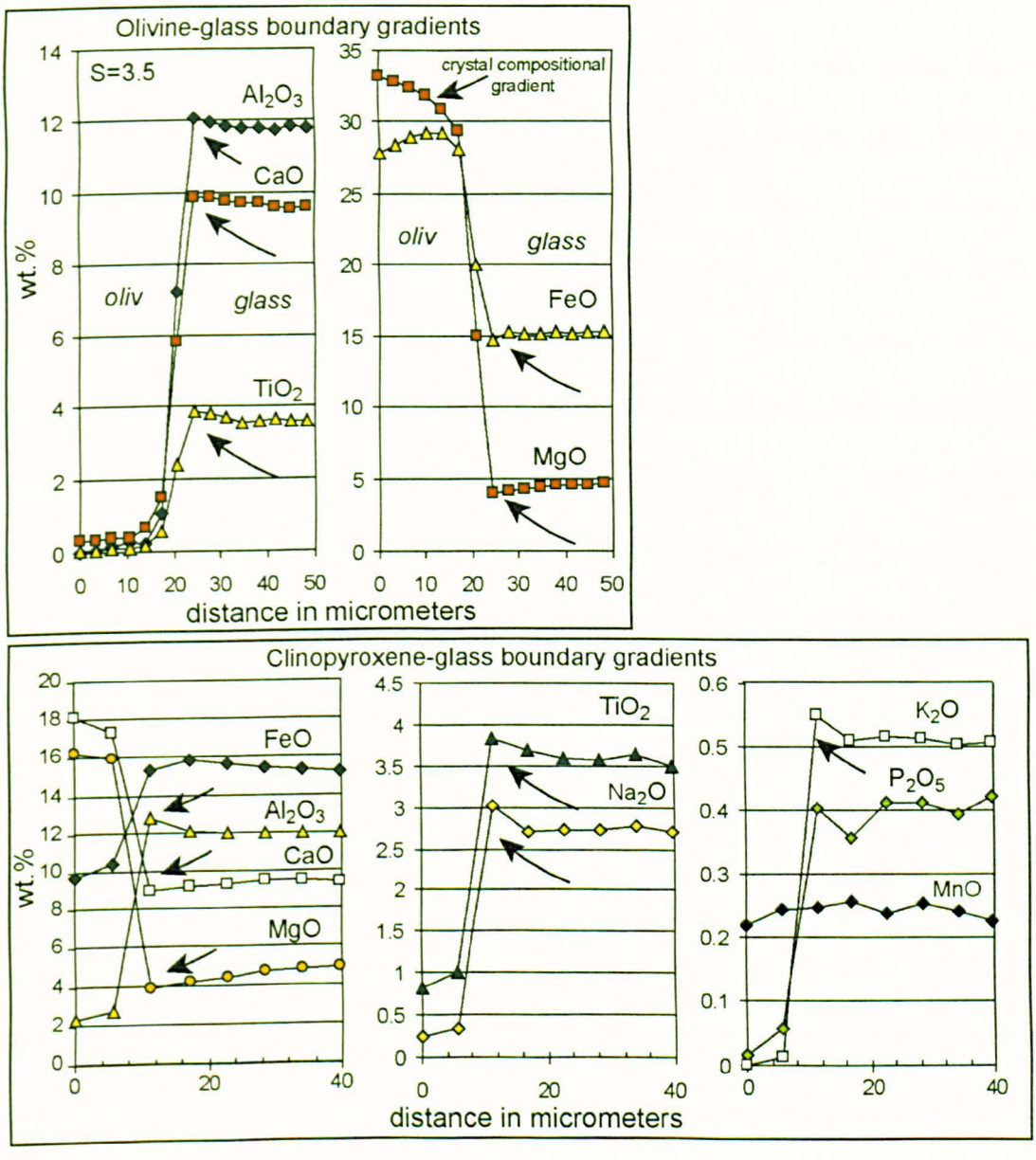

Figure 3.23: Compositional gradients at olivine and clinopyroxene boundaries: representative profiles. Arrows point to gradients. Profile across olivine-glass interface with spacing of 3.5 μm (sample L17-3 analysis no. 20, data reported in Appendix D3), and across clinopyroxene with spacing of 5.7 μm (sample L14-6 analysis 77, data reported in Appendix D3).

Interpretation of compositional variations. The pattern defined by major elements in whole-rock and lava glasses (i.e., Fig. 3.17) is consistent with the formation of tephra and lava glasses by *in-situ* fractional crystallization of a melt with initial whole-rock composition that is progressively depleted in plagioclase, olivine and clinopyroxene components, and is in accordance with the correlation between the groundmass crystal content and the MgO content of glasses (Fig. 3.7). The variation of CaO with MgO in the glasses typically mirrors the variation of clinopyroxene crystallization from the melt whereas Al_2O_3 varies according to the amount of plagioclase crystallization. The constant CaO between tephra glasses and Mg-rich lava glasses (Fig. 3.17) thus indicates that clinopyroxene crystallization was suppressed during the evolution of the melt from tephra to lava glass composition, whereas in the lava the increase in CaO with decreasing MgO and the constant CaO/Al_2O_3 of the glass compositions indicate co-crystallization of plagioclase and clinopyroxene.

Mass balance calculations were completed using the least squares program of Herrman & Berry (2002) (Tables 3.11 and 3.12) and compared to results from textural analysis presented above (Fig. 3.24). Tephra glasses are compositionally related to whole-rock after removal of 8–10 vol.% of slightly variable amounts of plagioclase, clinopyroxene and olivine (Fig. 3.24; relative proportions of 65:27:8, plagioclase/clinopyroxene = 2.5). These proportions are similar to results from textural analysis, thus showing that the contribution of phenocrysts to the compositional difference between whole-rock and tephra glasses can be neglected, which is consistent with them being present in small amounts. The relatively larger amounts of olivine (> 0.5–1 vol.%) estimated by least squares calculations in comparison with textural analysis can be explained by the similarity in colour of olivine and glass in BSE images, which makes them difficult to detect by textural analysis.

Least squares calculations relate lava glasses to whole rock after removal of 20–30 vol.% of plagioclase, clinopyroxene and olivine. In the lava glasses, plagioclase and

olivine proportions decrease with decreasing MgO wt.%, whereas clinopyroxene relatively increases in proportion. The compositional gap between the average of tephra glass compositions and Mg-rich lava glasses (L14-7) is accounted for by plagioclase, clinopyroxene, and olivine crystallization in the relative proportions 73:8:19 (plagioclase/clinopyroxene = 9.4). The range in lava glass composition (Mg-rich to Mg-poor) is reproduced by crystallization of the same phases in the relative proportions of 65:27:7. The range of glass compositions in sample L63-9 is modelled by least squares calculation by 32–42 vol.% crystallization of variable amounts of plagioclase (~20–26 vol.%), clinopyroxene (~8–12 vol.%) and olivine (~3–4.5 vol.%) from whole-rock composition. These proportions are inconsistent with the observed amount of crystals in the lava selvage (similar to sample L63-8), which is attributed to the formation of strong compositional gradients in the liquid due to the limited diffusion of elements away from the crystal-liquid interfaces during constitutional undercooling (see above and Kirkpatrick (1975)).

The relative variations in the crystallizing amounts of plagioclase over clinopyroxene in the lava glasses can also be examined using Pearce element ratios (Fig. 3.25). With this method, the transition from tephra to Mg-rich lava glass can be modelled by extraction of clinopyroxene and plagioclase in weight proportions of 1:10, compared to proportions of 1:3 to form tephra glasses from whole rock; and ~1:2 to reproduce the compositional range in lava glasses starting from the least evolved glasses. The results from the least squares calculation and the Pearce element ratios are similar, and the former compare well with the textural data, except for clinopyroxene, which is attributed to an overestimation of the clinopyroxene content by textural analysis to up to 10 vol.% (see grey-shaded area on Fig. 3.24a). This causes the large scatter in the total groundmass crystallinity estimated by textural analysis. When referring to the crystal content of the lava in the following text, the abundances and proportions given by the mass balance calculations will be used.

Table 3.11: Least squares calculations of mineral proportions (vol.%)

Sample No.	Plag	Cpx	Oliv	Total C	$\sum R^2$	Sample No.	Plag	Cpx	Oliv	Total C	$\sum R^2$
15-08-83*	5.46	2.24	0.65	8.35	0.14	L63-10*	19.57	6.79	3.33	29.70	0.02
16-08-83*	5.88	1.69	0.99	8.56	0.16	L63-1*	19.19	5.90	3.52	28.61	0.07
18-08-83*	6.63	3.26	0.74	10.64	0.08	L63-5*	17.78	5.37	3.11	26.25	0.05
22-08-83*	5.81	2.18	0.62	8.61	0.08	L63-6*	20.40	6.87	3.30	30.56	0.20
L14-3*	14.24	3.50	2.76	20.49	0.06	L63-7*	18.60	5.83	3.02	27.46	0.08
L14-6*	15.63	3.94	3.13	22.70	0.04	L63-8*	18.49	6.12	3.06	27.67	0.07
L14-7*	13.35	3.69	2.72	19.77	0.05	L66-3*	17.85	6.42	2.82	27.09	0.04
L17-1*	16.32	4.54	3.04	23.89	0.03	L63-9-1 gl05	23.10	9.44	3.52	36.07	0.31
L17-3*	15.78	4.50	2.88	23.15	0.03	L63-9-3 gl01	23.31	10.18	3.28	36.77	0.40
L17-5*	14.75	4.37	2.44	21.55	0.03	L63-9-3 gl06	20.03	8.66	3.68	32.37	0.06
L17-6*	15.85	4.58	3.07	23.50	0.07	L63-9-3 gl31	21.92	10.46	3.05	35.43	0.30
E3-5*	21.51	7.46	3.62	32.58	0.04	L63-9-4 gl20	22.30	8.97	3.34	34.60	0.15
L4-2*	20.24	7.59	3.20	31.02	0.02	L63-9-4 gl21	21.69	10.17	3.91	35.76	0.14
L18-1*	20.11	6.78	3.35	30.25	0.10	L63-9-4 gl22	19.80	9.01	4.40	33.22	0.14
L21-1*	18.24	5.50	3.39	27.14	0.05	L63-9-4 gl23	24.95	10.56	3.69	39.20	0.36
L29-13*	19.72	6.97	3.21	29.90	0.07	L63-9-4 gl25	23.52	10.21	4.45	38.18	0.17
L29-15*	19.57	6.36	3.26	29.19	0.07	L63-9-4 gl26	25.82	11.94	4.32	42.08	0.29
L29-18*	19.04	6.78	3.21	29.03	0.04	L63-9-4 gl41	21.28	8.62	3.85	33.75	0.12
L33-1*	18.11	5.89	3.08	27.09	0.05	L63-9-4 gl42	24.96	9.67	3.63	38.27	0.44
L43-2*	17.98	5.14	3.07	26.18	0.09	L63-9-4 gl43	22.78	10.95	3.30	37.02	0.29
L55-10*	18.79	6.13	3.01	27.94	0.06	L63-9-4 gl44	21.67	8.36	3.72	33.75	0.10

Sample no. indicates glass composition used for calculations. *—average composition used. Total C—total crystallinity. Results from calculations were converted from weight % to volume % using density of 2.6 for plagioclase (Plag), 3.3 for clinopyroxene (Cpx), 3.4 for olivine (Oliv) and 2.5 for glass. Compositions used as parent composition and mineral components (including the glass considered) are reported in Table 3.12. Program by Herrmann & Berry (2002) iteratively adjusts proportions of mineral components to provide good fit with input parent composition. It returns sum of residuals squared ($\sum R^2$ on table), which has to be <0.5 for the results to be acceptable.

Table 3.12: Parameters used in the least squares calculations

Analysis no.	Sample type		SiO_2	TiO_2	Al_2O_3	FeO	MnO	MgO	CaO	Na_2O	K_2O	P_2O_5	Total
Sample composition													
WR2	whole rock		50.41	2.79	13.89	13.63	0.22	5.75	10.45	2.69	0.42	0.30	100.00
Minerals													
L7-5 12/6	PH plag	An*76	49.09	0.00	31.46	0.73	0.00	0.00	15.72	2.66	0.05		99.70
L63-7 66	MP plag	An*66	52.74	0.00	29.48	0.91	0.00	0.20	13.30	3.79	0.10		100.50
L63-9 29	ML plag	An*55	55.63	0.00	26.73	1.16	0.00	0.28	10.84	4.82	0.19		99.65
L7-5 3	PH oliv	Fo71	36.64	0.00	0.01	26.36	0.37	35.50	0.28	0.00	0.00		99.15
L63-9 33	ML oliv	Fo64	37.00	0.11	0.05	30.86	0.46	31.34	0.45	0.01	0.00		100.28
L7-1 146	MP cpx	En*76	50.55	1.13	3.28	8.65	0.21	15.20	20.35	0.29	0.00		99.64
L63-7 30	ML cpx	En*74	51.37	1.20	3.28	9.42	0.24	15.07	19.57	0.32	0.01		100.47

Major elements reported in wt.%. Sample type: PH—phenocryst, MP—microphenocryst, ML—microlite, plag—plagioclase, oliv—olivine, cpx—clinopyroxene. End-member mineral compositions were chosen, avoiding primitive, xenocryst-type composition and crystals showing high amounts of minor elements. Small variations in crystal composition used had negligible impact on the results.

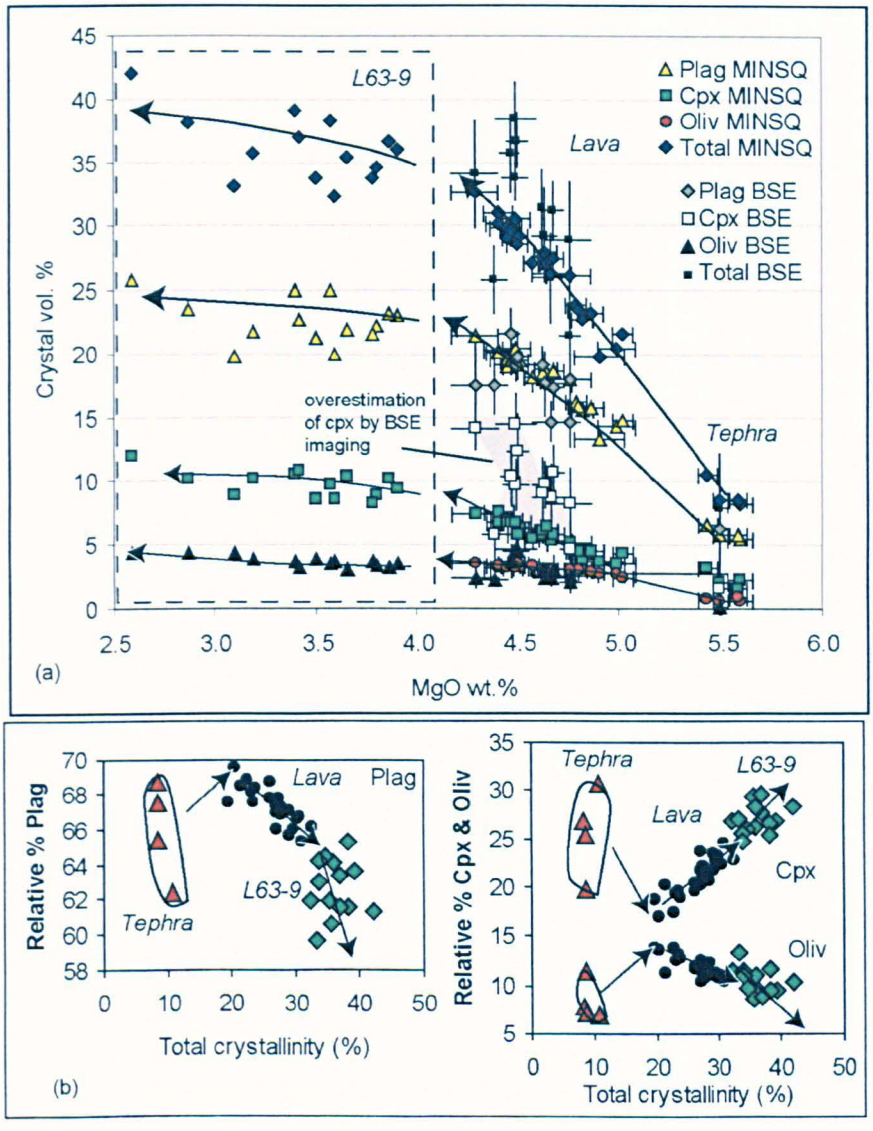

Figure 3.24: Results from least squares calculations. (a) Comparison between calculated mineral phase proportions (in vol.%) using least-squares calculations (MINSQ) and results from textural analysis (BSE). Plag—plagioclase, Oliv—olivine, Cpx—clinopyroxene, and Sum—total crystallinity. (b) Plots of crystal phase proportions versus average glass MgO wt.%. Note difference between tephra and lava and evolution of plag and cpx proportions with degree of glass differentiation.

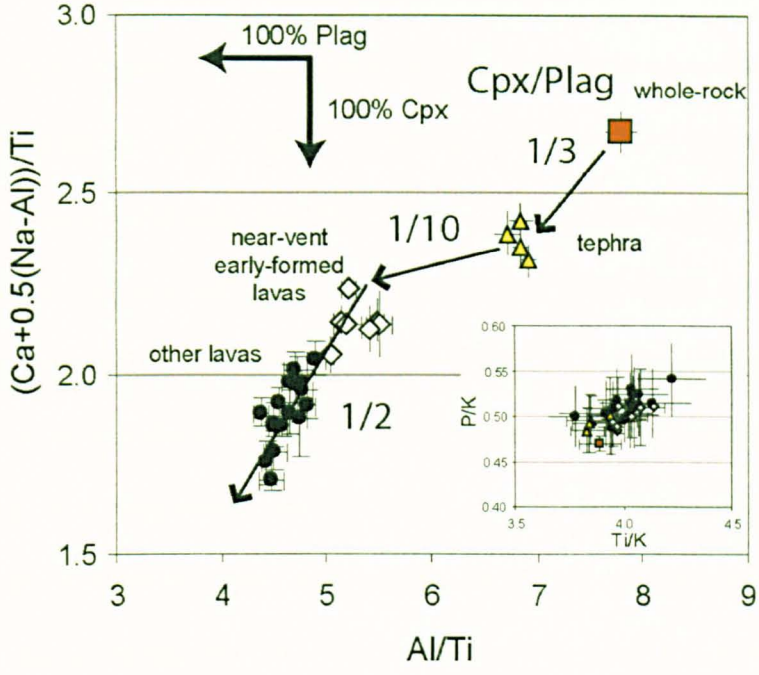

Figure 3.25: Pearce element ratio diagram used to distinguish between effects of plagioclase and clinopyroxene fractionation on the evolution of the liquid (glass). NVEF—near-vent early-formed lava (see text). In this diagram, liquids related through crystallization of clinopyroxene and plagioclase should define a line whose slope is a direct function of the relative fraction of each mineral phase (Russell et al., 1990). To calculate the ratios, the compositional data were first averaged to simplify the plot, and then converted to cation fractions (oxide % multiplied by number of cations in formula and divided by molecular weight). A plot of P/K against Ti/K (inset in figure) was used to verify the non-correlation between conserved elements used as denominators (large overlap of the data), as recommended by Russell & Nicholls (1988). To directly compare this method and the results from least-squares calculations, it is necessary to consider the slope of the lines linking any given glass composition to the whole-rock; the difference between wt.% (this method) and vol.% (corrected results from least-squares calculations) may account for small differences.

3.6 MAGMA CRYSTALLIZATION HISTORY DURING THE LAKI ERUPTION

Building on the above observations, a model describing the evolution of the magma and lava during transport and emplacement during the first five eruptive episodes of the Laki eruption is now presented. The model addresses: (1) the differences in the textural and compositional characteristics of phenocrysts, microphenocrysts and microlites, (2) the range of glass compositions, crystal content and phase proportions displayed by the tephra and lava. These two main aspects are summarized in the next section, and interpreted in the following text.

3.6.1 Petrographic evidence

1) The Laki lava contains three populations of crystals that have distinct distribution, morphology, composition, and zoning pattern (Fig. 3.9). The rare phenocrysts are sparse and record the largest compositional range (Fig. 3.10). Occasionally enclosing strongly resorbed xenocrysts, phenocryst cores are euhedral and covered by a mantle of distinct composition preferentially grown around corners (Figs. 3.9, 3.12a), with formation of an ~ 10 mol.% An gap across plagioclases (Fig. 3.11a), continuous zoning across olivine (Fig. 3.11e), and irregular zoning across clinopyroxenes (Fig. 3.11l). Smaller and more abundant than phenocrysts, microphenocrysts are mainly composed of aggregates of irregularly zoned clinopyroxenes intergrown with radiate plagioclase laths and minor olivines (Fig. 3.13c). These have compositions similar to phenocryst mantles (Fig. 3.10) and have tiny glass inclusions (Fig. 3.13f). Although rare and of primitive composition in the tephra, microlites are abundant in the lava and consist of skeletal plagioclase (Fig. 3.10), polyhedral to hopper olivines with round to irregular central inclusions (Figs. 3.11e–h), and clusters of granular clinopyroxenes (Figs. 3.9c, 3.10b).

2) The textural and compositional differences between glasses of tephra and lava are attributed to an episode of intense crystallization that occurred in the lava flows, as they travelled from the vent. At that stage, there was formation of abundant microlites of plagioclase and olivine, with a relative suppression of clinopyroxene formation that is shown by the constant CaO content of lava and tephra glasses (Fig. 3.17). The magma was largely degassed at that stage (0–0.1 wt.% H_2O). The restricted range of composition of the lava glasses quenched at various distances from the vent, and from along flows with evolving surface morphology, shows that the magma underwent limited amounts of crystallization during transport, without any direct correlation with the distance travelled or the brecciation of the surface crust (Fig. 3.19). The proportion of plagioclase and olivine

fractionated decreased with differentiation of the residual melt (lava glass) whereas the proportions of clinopyroxene relatively increased.

3.6.2 Magma crystallization conditions

In this section, the constraints that can be put on the conditions of growth of each crystal type, and the location within the magma eruption system where crystallization took place, will be presented. In a first step, the morphological characteristics of the crystals and their zoning pattern will be interpreted, building on the recognized link between crystal morphology, growth rate, and the degree of undercooling of the melt (see Chapter 1 and Dowty, 1980b; Kirkpatrick, 1981).

The euhedral shapes and homogeneous composition of phenocryst cores suggest crystallization under low degrees of undercooling with synneusis of crystals (Vance, 1969) and regular oscillatory zoning of plagioclase (Allègre et al., 1981). By contrast, microphenocrysts and compositionally similar phenocryst mantles have textures and internal zoning indicative of higher crystallization rates under diffusion-limited conditions. These are 1) the preferred growth of plagioclase mantles around corners (e.g., Kirkpatrick, 1981), 2) the irregular and sector zoning across clinopyroxene microphenocrysts indicative of differential rates of crystal growth (see Downes, 1974; Tsuchiyama, 1985), and 3) the occasional entrapment of glass inclusions along growth planes. The shapes and composition of plagioclase and olivine microlites are indicative of high rates of nucleation and growth (skeletal morphologies, entrapment of glass inclusions and minor elements) that are consistent with undercooling of the melt by 20–40°C (e.g., Longhi et al., 1976; Kirkpatrick et al., 1979; Lofgren, 1980; Kouchi et al., 1986; Faure & Schiano, 2004). The granular morphology of clinopyroxene microlites and their small size differs strongly from the large zoned microphenocrysts, suggesting high nucleation rates and low crystallization times. The higher crystallization rates of phenocryst, microphenocryst and microlite populations inferred from their texture are consistent with them describing lines with

increasing slopes and intercept in CSD plots (Fig. 3.6), following the classical CSD theory (see Cashman & Marsh (1988) and Crisp et al. (1994); developed in Chapter 4).

These textural observations can be fitted together into a sequence of events that characterise the evolution of the magma during the eruption. These will be subsequently quantified using calibrations of crystal-liquid equilibria. During the eruptive activity, the magma migrated from a deep reservoir to the surface, undergoing decompression and gas exsolution as evidenced by the vesicularity of the products and the low water content of tephra and lava glasses. The conditions of crystallization of phenocrysts and microphenocrysts can be inferred from plagioclase composition.

The ~10 mol. % higher An content of plagioclase phenocryst cores can be related to higher H_2O contents in the melt because of the well-know sharp increase of $(Ca/Na)_{Plagioclase}/(Ca/Na)_{Liquid}$ with melt H_2O content (e.g., Yoder & Tilley, 1956; Sisson & Grove 1993; Panjasawatwong et al., 1995). Conditions of relatively high dissolved water content and low undercooling (as inferred from crystal shapes) are typically met in large magma reservoirs at depth, which suggests that phenocryst cores grew in the magma chamber. The high abundance of plagioclase as phenocrysts in comparison to the olivine and clinopyroxene phases may arise from their low-density contrast with the melt, and thus represent preferential "sampling" from the top of the magma chamber by the magma that ascended to the surface.

By contrast, the texture of microphenocrysts and their low An content suggest that they formed along with phenocryst mantles after the exsolution of H_2O from the melt. Water loss from the magma increases its liquidus temperature, driving undercooling and increasing crystallization rates, which can, in turn, explain the crystal textures (see above). For low-viscosity basaltic magmas, this would typically occur in the upper level of the magma conduit (e.g., Lipman et al., 1985). The Laki eruption involved large magma ascent rates and intense lava fountaining that was driven by shallow magma degassing and

released large amounts of gas at the vent (Thordarson et al., 1996). These are conditions favourable for rapid gas loss and subsequent undercooling of the magma in the last stages of conduit ascent.

In the following, an attempt is made to quantify these processes using experimentally determined calibrations of mineral-liquid equilibria. The parameters used in the calculations are listed in Table 3.13. First, the eruptive temperature of the melt was calculated to derive its degree of undercooling relative to experimentally determined equilibrium conditions (i.e., Bell & Humphries, 1972). Using the composition of plagioclase microphenocrysts and tephra glasses as input into the plagioclase-liquid calibration of Putirka (2005) (this assumes equilibrium between the phases), temperatures of ~1150–1160 ± 23°C are obtained (1 in Table 3.13). In the anhydrous 1-atm-experiments of Bell & Humphries (1972) on Laki lava, plagioclase formed at 1170–1180°C, olivine at 1150–1160°C, and clinopyroxene at 1140–1150°C. This signifies that when erupted, the bulk magma was undercooled to up to 30°C relative to plagioclase, 10°C for olivine, and <10°C for clinopyroxene. Using the same calibration on the composition of lava glasses and plagioclase microlites, the maximum range of temperature at which the lava crystallized can be constrained to be 1110–1150 ± 23°C (2 and 3 in Table 3.13). Applying the experimentally-obtained MgO-based glass geothermometers from Mauna Loa lavas (Montierth et al., 1995) and Kilauea Iki lava lake (Helz & Thornber, 1987) gives lower temperature estimates (10–20°C lower), which can be attributed to the higher MgO content of the samples used for the experiments compared to the Laki magma (10 to 12 in Table 3.13).

An important parameter that it would be interesting to quantify is the pre-eruptive water content of the melt. To derive that information using the calibration of Putirka (2005), the pressure and temperature of phenocryst crystallization need to be independently

estimated, which was done using calibrations of olivine- and clinopyroxene-liquid equilibria.

The temperature at which phenocrysts formed was calculated using the composition of olivine phenocryst cores and whole rock as input into the olivine-liquid geothermometer by Beattie (1993) (7 in Table 3.13). A quartz-fayalite-magnetite (QFM) oxygen buffer was used (see Table 3.13 caption). The derived crystallization temperatures are similar to those estimated above for the eruptive temperature of the magma (1140–1160 ± 10°C), which is consistent with isothermal magma ascent.

Table 3.13: Parameters and results used in calculation of crystallization conditions based on mineral-melt equilibria.

Ref	Liquid	Mineral	T (°C)	H_2O (wt.%)	P (kbar)	Model used
Plagioclase-liquid equilibria						
(1)	Tephra glass (avg)	An_{63}[a]-An_{68}	1147–1160	(0-0.1)	(0.001)	Putirka (2005) model A (table 2), T ± 23°C
(2)	Lava glass (L14-3)	An_{63}[a]-An_{68}	1137–1149	(0-0.1)	(0.001)	like (1)
(3)	Lava glass (L18-1)	$An_{57.5}$	1111–1110	(0-0.1)	(0.001)	like (1)
(4)	Whole-rock	An_{76}	1152–1162	(1)	(2-4)	like (1)
(5)	Whole-rock	An_{75}	1175–1185	(0.5)	(2-4)	like (1)
(6)	Whole-rock	An_{76}	1187	(0)	(0.001)	like (1)
Olivine-liquid equilibria						
(7)	Whole-rock (avg)	Fo_{74}	1140–1160		(0.001-2.5)	Beattie (1993)[c], T ± 10 °C, QFM[d]
Clinopyroxene-liquid equilibria						
(8)	Whole-rock	En_{75-78}	(1140–1160)		3–4	Putirka et al. (1996, 2003)[b], P ± 1.7 kb
(9)	Tephra glass	En_{66-67}	(1140–1160)		4–5	Putirka et al. (1996, 2003)[b]
Liquid equilibria						
(10)	Tephra glass		1123-1126	0	0.001	Helz and Thornber (1987), T ± 10°C
(11)	Tephra glass		1137-1141	0	0.001	Montierth et al. (1995), T ± 10°C
(12)	Lava glass range		1113-1127	0	0.001	like (11)

Parameters used as inputs in calculations are in brackets. Ref—reference number mentioned in text. An and En are equivalent to An* and En* in text. Model used—precision of model as established by authors. avg—average.

[a]—composition used is average of groundmass plagioclases analysed in tephra samples.

[b]—using pressure-dependant equations (see model A in table 4 for Putirka et al. (2003) and model P1 in table 5 for Putirka et al. (1996)–both equations gave same result).

[c]—calculated using spreadsheet by Putirka (unpublished—from the internet); $K_{Fe/Mg(oliv\text{-}melt)}$ ~0.28 (calculated as molar $(Fe/Mg)_{Olivine}/(Fe/Mg)_{Liquid}$, using total FeO) which is typical of equilibrium conditions (e.g., Sisson & Grove, 1993).

[d]—oxygen fugacity along quartz-fayalite-magnetite buffer (QFM). Calculated using program of Sugawara (2000) on plagioclase-olivine equilibria, conditions of 1 bar and 1140°C.

Crystal compositions used for calculations had limited content in minor elements (i.e., such as K_2O in clinopyroxene and elements plotted in Fig. 3.16) and were therefore susceptible to have grown under equilibrium conditions.

Crystallization pressures were then constrained using calibrations based on clinopyroxene composition because these do not vary (significantly) with melt water content (see Putirka et al., 1996, 2003). Using condition 8 in Table 3.13, the calculated pressures are in the range 3–4 ± 1.7 kb. This is consistent with the inferred evolution of the Laki magma at the base of the crust prior to eruption, at a minimum depth of 10 km, i.e., > 2.5 kbars (Sigmarsson et al., 1991). Applying the same calibration to the composition of clinopyroxene microphenocrysts and tephra glass (9 in Table 3.13) yielded similar to higher-pressure estimates. This discrepancy may indicate a lack of re-equilibration of clinopyroxenes to surface conditions, in accord with the irregular zoning displayed by the crystals. Clinopyroxene thus does not appear to be a reliable geothermometer, which is consistent with the fact that its composition varies greatly with the rates of crystal growth and thus the degree of undercooling of the melt (e.g., Tsuchiyama, 1985).

From the above constraints, the amount of water dissolved in the magma at depth can then be addressed. A preliminary estimate can be made using the work by Metrich et al. (1991), who analysed the water content of glass inclusions hosted in olivine xenocrysts contained in the Laki tephra. The inclusions are at equilibrium with an olivine-tholeiite melt and have 0.47 wt.% H_2O. Assuming that the Laki magma is derived from an olivine-tholeiite melt of this composition, as suggested by Sigmarsson et al. (1991), a crystal fractionation model was applied to the composition of these inclusions, to determine the H_2O content of the residual melt when it reached the composition of the Laki magma (PELE program by Boudreau (1999) conditions of 2.5 kb, QFM buffer). Doing so, it is estimated that the Laki magma contained ~1 wt.% H_2O (equivalent of the extraction of ~50 wt.% of clinopyroxene, olivine, and plagioclase from olivine tholeiite).

The calibration of Putirka (2005) was finally applied using the composition of plagioclase phenocryst cores and whole-rock, using pressures in the range calculated above (2–4 kb), and testing the influence of a range of 0–1 wt. H_2O wt.% on the calculated

crystallization temperature, with the aim of reproducing the temperature range determined above (3 and 4 on Table 3.13). The results are consistent with formation of An-rich phenocryst cores at equilibrium with a melt containing > 1 wt.% water content. Using lower H_2O contents results in temperatures that are much higher than the previously estimated magma temperature (> 1175°C, 5 and 6 on Table 3.13) but are in agreement with the 1-atm-anhydrous plagioclase liquidus temperatures determined by Bell & Humphries (1972). It should be noted that this calibration suffers from the paucity of direct measurements of H_2O in experiments (Putirka, 2005).

In conclusion, crystal textures, compositional zoning, and mineral-melt equilibria are consistent with 1) formation of Laki An-rich phenocryst cores at 1140–1160°C in a relatively deep reservoir (2–4 kb) and from a melt containing > 1 wt.% H_2O, and 2) degassing-induced crystallization of An-poor microphenocrysts as magma rose to the surface. In the next section, the evolution of the lava as it travelled away from the vent is addressed.

3.6.3 Lava crystallization during transport

Microlites formed as the lava flowed away from the fissure, causing the residual melt composition to evolve as shown by the gap between tephra and lava glass compositions. Using major element trends and least squares calculations, this gap can be modelled by an abundant crystallization of plagioclase and olivine from the melt, with relative suppression of clinopyroxene. The skeletal shape and high number densities of microlites imply that the lava was markedly undercooled when crystallization occurred.

This rapid crystallization in the lava is inconsistent with crystallization driven by cooling. Instead, it is proposed that microlites formed as a result of the delayed response of the melt to the undercooling induced by shallow degassing. Small degrees of undercooling can have large effects on magma crystallization as nucleation and growth rates increase exponentially with undercooling (Brandeis & Jaupart, 1987a; Hammer & Rutherford,

2002; Couch et al., 2003; Larsen, 2005). Beyond a certain degree of undercooling, crystal nucleation may dominate over growth (e.g., Hammer & Rutherford, 2002); this is partly because small crystals have a larger fraction of their volume in contact with the surrounding liquid compared to large crystals. Sato (1995) experimentally showed that the undercooling of a basaltic melt by 20°C before cooling may cause a 5-order-of-magnitude increase in the number density of plagioclases formed, whereas a 2-order-of-magnitude difference in cooling rates brings less than 1-order-of-magnitude difference in plagioclase number density.

The textural differences between microlites and microphenocrysts imply an increase in the effective undercooling of the melt. This may be related to a delay in the crystallization of plagioclases following melt degassing, as plagioclase has notoriously slow crystallization kinetics and is strongly affected by water loss (controlled by large surface energies and the required structural re-adjustment, e.g., Gibb, 1974). In addition, water loss would increase melt viscosity and decrease element diffusivities, thus slowing crystal growth (e.g., Watson, 1981). The relative suppression of clinopyroxene crystallization can be explained by the low degree of undercooling of the melt relative to this phase as previously calculated, which decreases the driving force for the growth of the crystals. It is interesting to note that experiments show that decreasing pressure and H_2O content together increase plagioclase and olivine stabilities, at the expense of clinopyroxene (e.g., Gaetani et al., 1992; Sisson & Grove 1993; Danyushevsky, 2001), which supports this explanation.

Trends in lava glass compositions indicate that, after the degassing-induced burst in crystallization that occurred in the lava as it flowed to ~100 m from the vent, the lava crystallized only <5 vol.% of plagioclase, olivine, and clinopyroxene further down-flow, with little compositional evolution of the residual melt. This suggests that the lava underwent low amounts of cooling, causing equilibrium crystallization along the

plagioclase-clinopyroxene-olivine cotectic. It is noted that the emplacement of the lava at relatively high temperatures, despite its degree of differentiation due to previous degassing-induced crystallization, may have delayed Fe-oxide crystallization.

3.6.4 Model of the evolution of the magma during eruption

Combining all the evidence, a model for the evolution of the Laki magma and lava during the eruption is now presented (Fig. 3.26). The main stages in this evolution are briefly described. Phenocryst cores grew prior to eruption in a > 10-km-deep magma chamber equilibrated at 2–4 kbars, 1140–1160°C, and > 1 wt.% dissolved H_2O as inferred by the high An of plagioclases (A on Fig. 3.26). At the start of the eruption, the magma ascended to the surface, undergoing decompression, and degassing at shallow levels (< 200 m depth, Thordarson et al., 1996). Rapid gas loss from the melt caused a rise in the liquidus temperature of the melt, generating magma undercooling (Fig. 3.26b) and a subsequent rise in crystallization rates that favoured crystal nucleation (increase of nucleation/growth, Fig. 3.26c). The bubbles formed in the melt may have favoured crystallization by providing sites for crystal nucleation (Davis & Ihinger, 1998) as shown by the inclusion of vesicles in some crystals (Fig. 3.15b).

The eruption started by intense lava fountaining along newly opened fissure segments, releasing large amounts of gas (e.g., Thordarson & Self, 1993). The fragmentation of the magma in fire-fountains at the vent due to gas expansion generated pyroclasts that were efficiently quenched in the air, producing glassy vesicular tephra clasts. These clasts contain some microphenocrysts (~10 vol.%) that have textures indicative of relatively high crystallization rates. The An content of the plagioclases intergrown with the clinopyroxenes is ~10 mol.% lower than the phenocryst cores at equilibrium with high water contents and identical to phenocryst mantles. This shift in plagioclase composition can be interpreted as the signature of the degassing-induced crystallization of the microphenocrysts that occurred just before magma fragmentation (B on Fig. 3.26, Fig.

3.26d). The residual melt evolved subsequently to crystallization (tephra glass composition, Fig. 3.26e). As lava travelled away from the vent, compositionally evolved microlites formed (C on Fig. 3.26). To account for the texture of the microlites, it was inferred that the magma must have been 20–40°C below its liquidus temperature, which is attributed to a delayed response to the undercooling induced by near-surface degassing (Fig. 3.26c). This is consistent with a lack of clinopyroxene crystallization in the least crystalline lavas (NVEF) as documented by the constant CaO content of the liquid quenched in tephra glass compared to lava selvages (Fig. 3.26e), because gas loss increases plagioclase and olivine stabilities at the expense of clinopyroxene. Finally, minor crystallization of the lava during transport from 100 m from the vent to the most distal flow front, 60 km away, caused further differentiation of the residual melt with crystallization along the plagioclase-olivine-clinopyroxene cotectic at low undercooling (C to D on Fig. 3.26). The liquid was by then (i.e., from 100 m of the vent down-flow) fully re-equilibrated (Fig. 3.26c).

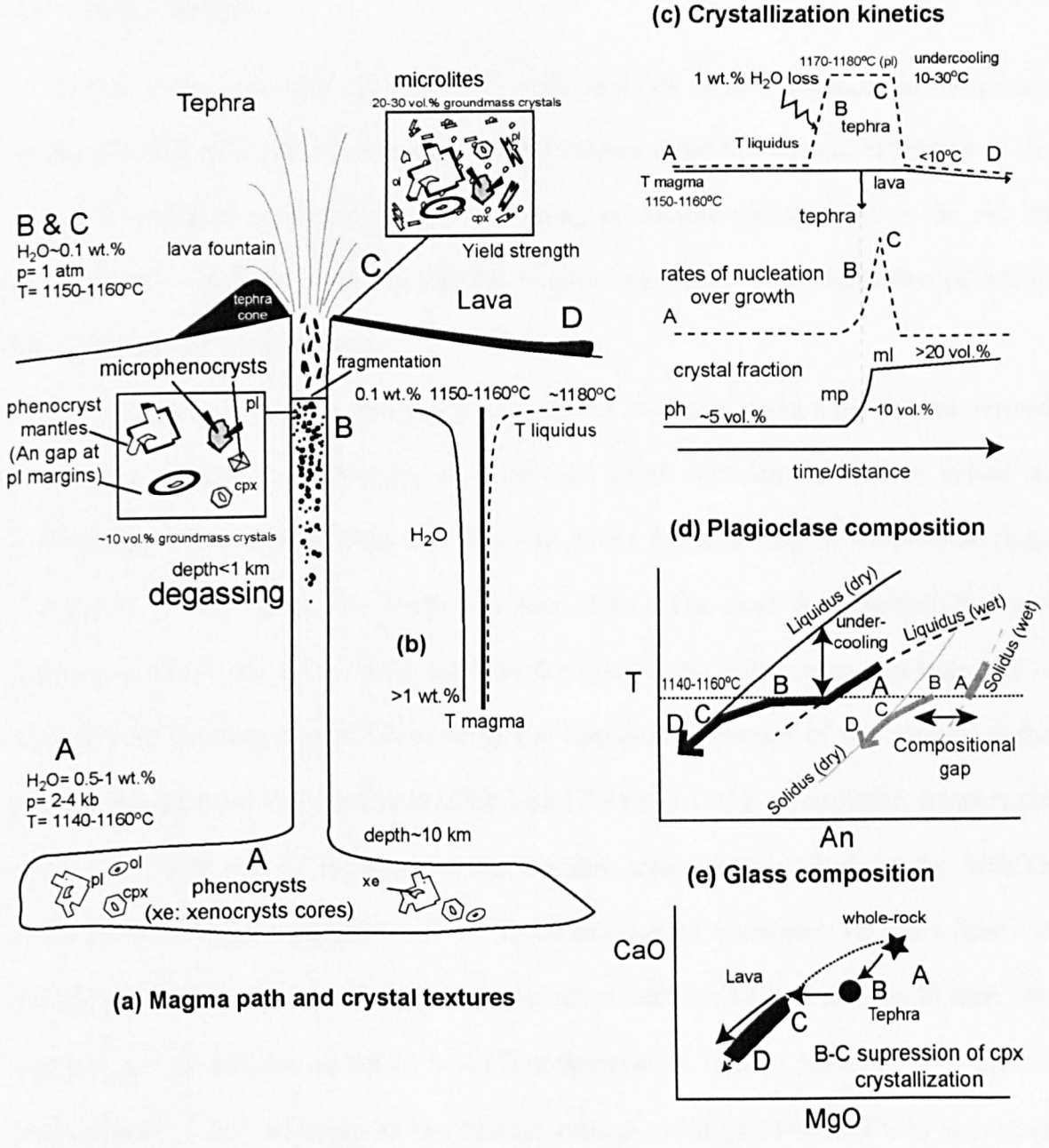

Figure 3.26: Evolution of the magma and lava during the first 5 episodes of the Laki eruption. T — temperature, p—pressure, pl—plagioclase, ol—olivine, cpx—clinopyroxene. a) Location of crystallization of each crystal type during transport and conditions of crystallization in terms of pressure, temperature, and gas content as inferred by this study. Note that, although it is known from tephra samples that microphenocrysts started to form below level of fragmentation, it is believed that some formed in lava flows. b) Coupled evolution of melt liquidus temperature with water exsolution near the surface. Magma is inferred to have undergone (near) isothermal transport. c) On sketch, impact of degassing-generated undercooling (curve at top) on crystallization rates is represented by peak in importance of nucleation over growth rates happening after time lag (second curve down). This lag is thought to result from decreasing element diffusivities for crystal growth and inefficiency of plagioclase formation responding from high degrees of supersaturation. Impact on melt crystal content is shown on bottom curve. d) Impact of H_2O loss on plagioclase composition shown as shift in equilibrium liquidus and solidus of melt relatively to plagioclase phase, resulting in compositional gap. Formation of gap requires rapid gas exsolution and/or slow crystallization rates. e) Effect of delayed microlite crystallization on composition of residual melt recorded in tephra and lava glasses (in wt.%), with constant CaO resulting from low proportions of clinopyroxene crystallization.

3.7 DISCUSSION

In this section, the implications of this work in terms of lava emplacement processes during the Laki eruption are discussed. Considerations about the thermal efficiency of the transport system of the Laki lava are first presented, before a discussion on the role of groundmass crystallinity as affected by the eruption dynamics on the formation of rubbly pāhoehoe surface morphologies.

Cooling rates of the lava during transport can be estimated using temperatures derived from glass compositions, keeping in mind that these represent maximum values as crystallization may release latent heat that can buffer the bulk magma temperature (e.g., Crisp et al., 1994; Helz et al., 1995; Thornber, 2001). The most distal sample that was analysed is L66-3 which was collected from the front of the Eldhraun coastal branch, 55–60 km from the source vent. Considering the chemical difference of this sample to the glass composition of the least crystalline lava (NVEF, L14-3), a maximum temperature change of 10°C can be estimated using liquidus temperatures calculated by MELTS software. An average cooling rate of ~0.2°C/km can thus be calculated. This lava flow was fed successively by fissure 1, 2 and 3 that opened between the 12 June and the 20 June, and reached its final distance on the 24 June (Thordarson et al., 2003; Chapter 2). This gives a maximum of 12 days of transport, and thus an average cooling rate of 0.03°C/hr at average advance rates of 0.06 m/s. These rates of cooling are comparable with the cooling of lava transported in active Kilauea lava tubes (< 0.6°C/km, Helz et al., 2003; 0.9°C/km, Thornber, 2001), and significantly lower than those reported for the transport of active lava in open-channels (6–7°C/km, Cashman et al., 1999).

These low cooling and crystallization rates support the emplacement model derived from field observations in Chapter 2 in which the surface rubble acted as an insulator for the transport of the liquid lava (e.g., Keszthelyi et al., 2004). Of interest in this context are thick viscous dacitic flows with blocky surface that can also have slow cooling rates, as

observed by Harris et al. (2004). Over a period of three years, the front of these dacitic lavas advanced at much lower rates than the Laki lavas (2–15 m/day) but with similar average core cooling rates (0.03–0.09°C/h). The piling of broken-up crust on top of lava emplaced under low shear rates can thus form a cool, nearly stagnant carapace under which the core lava can flow without cooling. The higher cooling rates of 'a'ā flows are typically attributed to 1) the incorporation of cool surface fragments in the lava core that increases the volume of lava exposed to cooling, and 2) high radiative heat loss due to large exposure of core lava to the air as the surface lava is continuously torn, dragged and fragments rolled on top and from the flow front (Cashman et al., 1999; Crisp et al., 1994). Field evidence confirms that both of these mechanisms were absent during the emplacement of Laki lavas, which explains their low cooling rates.

The factors that may have caused the formation of rubbly pāhoehoe lavas during the Laki eruption are now discussed. The two main factors thought to control lava flow surface morphologies are 1) shear rates (topography, effusion rates), and 2) lava viscosity (liquid chemistry, lava groundmass crystallinity, vesicle content) (Pinkerton & Sparks, 1976; Rowland & Walker, 1990; Peterson & Tilling, 1980; Cashman et al., 1999; Polacci et al., 1999; Soule et al., 2004; Hon et al., 2003; Soule & Cashman, 2005). The ubiquitous small-scale surface roughness of the Laki lavas (spiny surface), except for near vent shelly pāhoehoe lobes, documents the presence of a yield strength that was caused by the degassing-induced formation of > 20 vol.% of groundmass crystals (mainly plagioclase) in the lava (Philpotts & Carroll, 1996; Hoover et al., 2001). In fact, Laki lavas have groundmass crystallinity (19–32 vol.%) at which many Hawaiian lavas develop 'a'ā surface morphologies (e.g., Polacci et al., 1999; Soule et al., 2004), yet they have plagioclase vol.% and number densities (15–20 vol.% and 100–500/mm^2) similar to Hawaiian pāhoehoe lavas (see compilation of recent studies by Katz & Cashman, 2003). The closely similar Al_2O_3 content of the two magmas can explain their similar vol.% of plagioclase

(Soule et al., 2004) despite the higher plagioclase liquidus temperature for the Laki magma (1170–1180°C, Bell & Humphries, 1972) compared to Hawaiian tholeiites (~1160°C, Helz & Thornber, 1987). The small number densities of the crystals can be attributed to equilibrium crystallization during emplacement and low cooling rates (e.g., Cashman, 1993) by contrast to 'a'ā flows that show large crystal nucleation rates resulting from disequilibrium crystallization (Cashman et al., 1999). Interestingly, during the 1984 Mauna Loa eruption, lava was produced with a similar amount of groundmass crystals derived from the response to degassing as the Laki lava at the same temperature (Lipman & Banks, 1987). Yet, the Mauna Loa flows transformed from pāhoehoe to channel-fed 'a'ā flows two kilometres away from the vent.

In summary, Laki lavas seem to have a different correlation between crystal content and surface morphology than Hawaiian lavas, which their similar bulk composition and initial gas content cannot account for. It is thus probable that the specific surface morphologies developed by the lava flows rely on the special characteristics of the Laki eruption. Gross correlations between ground topography, lava effusion rates, and dominant surface morphologies were shown in Chapter 2. Building on those, it can be noted that during the most productive period of the Laki eruption, when vent lava outputs were high and could have forced transition of the flows to 'a'ā, the effective stress imposed on the lava emitted at the active flow front was low. This is because, as effusion rates peaked, the lava was emplaced as large sheet lobes on the flat terrain of the coastal plain (Eldhraun, see Chapter 2), which caused the increased influx of lava to be distributed in the internal pathways (tubes) established into the flows. Instead of forming channels, the lava surface was pushed transversally to the flow direction, producing the large ridges of rubble that are described in Chapter 2. Thus the surface was disrupted, but the rapid formation of a new crust underneath the rubble, along with the persistence of lava influx in the lobes, preserved the thermal efficiency of the transport of fluid lava from the vent to the active

front. Hence, it is deduced that it was the combination of 1) the moderate viscosity of the lava caused by intense degassing-induced groundmass crystallization, 2) the characteristics of the eruption dynamics, and 3) the local topography that contributed to the formation of rubbly pāhoehoe surface morphologies on the Laki lava flows.

3.8 CONCLUSIONS

Numerous studies have suggested that crystallization induced by degassing during magma ascent controls the eruption style and the mode of emplacement of the erupted products (e.g., Sparks & Pinkerton, 1978; Lipman & Banks, 1987; Swanson et al., 1989; Geschwind & Rutherford, 1995; Sparks et al., 2000; Hammer et al., 2000; Cashman & Blundy, 2000; Couch et al., 2003). This study demonstrates the influence of ascent degassing on magma crystallization kinetics and lava surface morphologies during a major basaltic eruption. During the Laki eruption, the exsolution of > 1 wt.% H_2O from the magma rapidly rising from ~10 km depth to the surface undercooled the melt by ~20–40°C. Crystallization was initiated close to the surface, and because of a delay in the response of the melt to the undercooling, there was abundant nucleation of microlites in the erupted lava, thus increasing the lava viscosity, and leading to the development of a yield strength in the erupted flows. This caused formation of spiny pāhoehoe lavas along the fissure, and favoured the repetitive breakage of the surface crust, forming rubbly pāhoehoe surface morphologies. Cooling-induced crystallization during emplacement was less important because the core lava was insulated by the thick layer of rubble that formed by repetitive disruption of the surface crust during emplacement. The lava was thus transported up to 60 km from the vent with <0.2 °C of cooling per kilometre.

Chapter IV

Internal texture and cooling histories of rubbly pāhoehoe lavas

Exposure through thick rubbly flow top with large intrusions of lava from the core (white outline) Columbia River Basalts, Snake River

4.1 ABSTRACT

Young Icelandic basaltic lava flow-fields produced by the AD 1783-84 eruption of Laki and < 10,000-years-old fissure eruptions in the Reykjanes Peninsula, and sheet lobes of the Grande Ronde Basalt from the Columbia River Province, are covered by a thick layer of rubble formed by disruption of earlier-formed pāhoehoe lobes. Petrographic and textural analysis of sections through the flows and tephra and lava surface samples for the Icelandic flows are reported. The results reveal correlations between the average size, number density, and aspect ratio of groundmass plagioclases in the lava. In turn, these correlate with the eruptive style and emplacement mechanisms of the flows inferred from field study of lava surface morphologies and internal structures, and analysis of the flow-field organization using aerial photographs for the Icelandic flows. Patterns of increasing average size and decreasing number density of groundmass plagioclase with increasing depth in these flows indicate sharply decreasing inwards solidification rates. Calculated from crystal size distribution (CSD) analysis, plagioclase growth and nucleation rates changed from about 10^{-7} to 10^{-10} cm/s and 10^{1} to 10^{-1} no./cm^4 s, respectively, as the solidification front propagated through the lava interior, indicating decreasing degrees of melt undercooling that promoted interface-controlled crystal growth. Clear textural differences between sections are attributed, in part, to the role of the degree of undercooling of the erupted lava and the mode of transport of the flows in controlling the extent and mode of groundmass plagioclase crystallization in fluid lava. Lava solidification rates were mainly controlled by duration of lava inflation, incorporation of rubble in the lava's core, and water infiltration in fractures through the lava's upper crust. Building on other textural studies, a model correlating lava surface morphologies with textural parameters derived from CSD analysis of groundmass plagioclase in samples from flow interiors is presented. Pāhoehoe and 'a'ā have low and high plagioclase number densities respectively (< 10^{9} no./cm^4 compared to > 10^{11} no./cm^4), which are inversely correlated

with plagioclase average size and aspect ratio through the total crystal content; rubbly pāhoehoe lavas have intermediate characteristics. This method may prove a useful tool for interpreting the mode of eruption and emplacement of ancient lava flow-fields.

4.2 INTRODUCTION

Two main lava types are generally recognized within basaltic lava flow-fields: pāhoehoe and 'a'ā. These are primarily defined by the strikingly different character of their surface crust. Pāhoehoe have, typically, smooth, regular to ropy, blue to silvery surfaces whereas 'a'ā lavas are covered by an unstable pile of dark jagged fragments (e.g., Wentworth & MacDonald, 1953). Studies have related this dichotomy to the balance between the shear stresses imposed to the lava and its capacity to viscously deform or break that is related to the bulk viscosity of the fluid lava and its yield strength (e.g., Peterson & Tilling, 1980; Kilburn, 1989; Cashman et al., 1999; Soule et al., 2004). An important factor controlling that balance is the abundance of crystals in the lava that 1) acts on the lava surface morphology by changing the mode of response of the lava to shear stresses (e.g., Kilburn, 1989; Soule & Cashman, 2005), and 2) reflects the evolution of the thermodynamic properties (temperature, gas content, undercooling) of the magma before extrusion and of the lava during surface transport (e.g., Sparks & Pinkerton, 1978; Kilburn, 1989; Crisp et al., 1994; Cashman et al., 1999). It follows that the lava surface morphology at m- to km-scale is, to some extent, related to the texture of the lava at μm- to mm-scale, restricted to the characteristics of the microlite population. This has been documented by changes in the texture of the lava in samples collected along single flows which show evolving surface morphologies, whether active (Crisp et al., 1994; Cashman et al., 1999) or solidified (Polacci et al., 1999; Soule et al., 2004), and by distinct differences between the mode of cooling of the lava at depth depending on its surface crust characteristics, which was inferred from the study of samples from cross-sections (e.g., Friedman, 1998; Bücker et al., 1999; Katz & Cashman, 2003). Recognizing the former could help monitoring of the

evolution of active lava flows, whereas defining the latter would be particularly useful for interpreting the conditions of emplacement of ancient lava flow-fields. The information such studies provides helps to understand the role of the many parameters that act on the mode of flow of the lava, and eventually govern its final length, which is especially crucial for hazard assessment.

The mode of transport of the lava and its thermal efficiency control the kinetics of lava crystallization, which may feedback on the lava surface morphology by affecting lava rheology. Textural studies on lavas have shown that pāhoehoe lavas are characterized, in general, by low total crystal contents, limited heat loss and crystallization during transport (Helz et al., 2003), and a large increase in groundmass crystal sizes through cross-sections because of low internal cooling rates (Friedman, 1998; Bucker et al., 1999; Katz & Cashman 2003). In contrast, 'a'ā lavas show measurable down-flow changes in surface temperature (Harris et al., 2005) and crystal content (Crisp et al., 1994; Cashman et al., 1999), and limited internal textural variations which can be attributed to rapid internal cooling (Friedman, 1998; Bucker et al., 1999; Katz & Cashman 2003).

This chapter aims to characterize the mode of transport and internal cooling of rubbly pāhoehoe lavas. Observed in Iceland (Kesthelyi et al., 2004, 2006; Guilbaud et al., 2005) and recognized from Columbia River basalts (Self et al., 1997; Kesthelyi et al., 2006), and in drill cores from the Kerguelen plateau (Keszthelyi, 2000, 2002), rubbly pāhoehoe lavas show a wide range of surface and internal features that are transitional between pāhoehoe and 'a'ā. More specifically, they display spiny to rough lava surfaces, have a brecciated flow top and a smooth pāhoehoe base, and in cross-sections present a structure that is similar to that of pāhoehoe lavas.

In Chapters 2 and 3, the surface morphologies and petrological characteristics of rubbly pāhoehoe lavas produced by the 1783-84 Laki eruption—hereafter simply called Laki—in South Iceland were presented. The purpose of this chapter is two-fold: 1) describe the

surface characteristics of rubbly pāhoehoe lavas from ~1000-years-old fissure eruptions on Reykjanes Peninsula (RP; southwest Iceland) and from sections through sheet flows of the Columbia River Basalts (CRB; Washington State, USA), compare them to features observed in the Laki lava flow-field, and interpret them in terms of emplacement processes; 2) examine the textures of these flows in cross-section and compare them to understand the relationships between the chemical composition of the lavas studied, their structural and morphological characteristics, and the rates of cooling and crystallization of the flow interiors in specific emplacement conditions.

To retrieve quantitative information about crystallization kinetics during solidification, the method of crystal size distribution (CSD) analysis was used. Plagioclases are abundant in the rocks studied and their mode of crystallization is inherently sensitive to undercooling conditions; they thus best record the cooling history of the rocks (e.g., Cashman, 1993). Petrographical observations were thus combined with CSD analysis of plagioclase microlites in a selection of samples collected from sections through the flows. The variations observed were then analyzed in relation to the chemical composition of the different lavas studied, their pre-existing cooling history as recorded in surface samples of tephra (spatter) and lava, and their structural and morphological features. This data set was then compared to the available data on variations across other lavas, lava lakes, and sills to understand what the data means in terms of the cooling regime of the flows. As a result of this investigation, a diagram is presented in which the impact of eruption, transport, and solidification processes on basaltic lava textures (plagioclase size and number density) can be analysed.

The approach adopted here contributes to a better understanding of the links between lava textures and emplacement mechanism, in particular by providing new data on the internal textures of lavas that is currently sparse in the literature. It also strengthens the

case for studying lava flows which show characteristics between the two recognized end-members pāhoehoe and 'a'ā.

4.3 LAVA FLOW-FIELDS: SURFACE MORPHOLOGIES, FIELD OBSERVATIONS AND SAMPLING

The location and respective extent of all the lava flow-fields studied are shown on Fig. 4.1, along with the location of the complete cross-sections examined in detail. This section aims to describe the flow-fields studied and introduce the structure of the lavas in the cross-sections. In the first part of this section, the terms used to characterize the lavas in cross-sections are introduced. The structure and morphology of the lava flow-fields are then described using field observations and aerial photo analysis for Reykjanes Peninsula lavas. For each flow-field, simplified sketches of the structure of the sections studied (graphic logs) are presented with representative electron backscatter (BSE) images of the lava groundmass texture acquired on the microprobe. Photographs of each section and of some general features of the flow-fields are also shown.

Figure 4.1 (next page): Maps of lava flow-fields studied and location of cross-sections studied in detail (labels such as R15, AD etc). These will be located more precisely on aerial photographs shown later on, and their GPS location will be reported. Numbers in ellipses indicate major roads at proximity of exposures. Dashed lines with arrows indicate main flow direction. Lines with arrow point to location of cross-sections. (a) Map of Iceland with location and outline of Laki lava flow-field. Rectangle shows location of Reykjanes Peninsula in (c). NVZ, EVZ, WVZ—approximate extent of North, East, and West Volcanic Zones. (b) Simple map of Laki lava flow-field with location of sections studied on coastal plain. (c) Map of Reykjanes Peninsula with major cities and roads. Rectangles show location of separate maps of lava flow-fields studied. (d, e, f) Outline map of lava flow-fields (different grey tones) presented in figures d, e, and f, showing the vent locations and sections studied. **, note that this is not the whole extent of Hussfellsbruni but only of the three lava flow-fields studied. The broken arrows indicate the main direction of flow. (g) Approximate outline of Columbia River Basalts (CRB) with location of sections studied in detail in inset. Dashed lines indicate location of dike swarms attributed to the Grande Ronde Formation (Hooper, 1997). In inset, thick grey lines show roads along which rubbly flows outcrop. Dark-grey patches on main map locate other areas where rubbly flows were seen exposed.

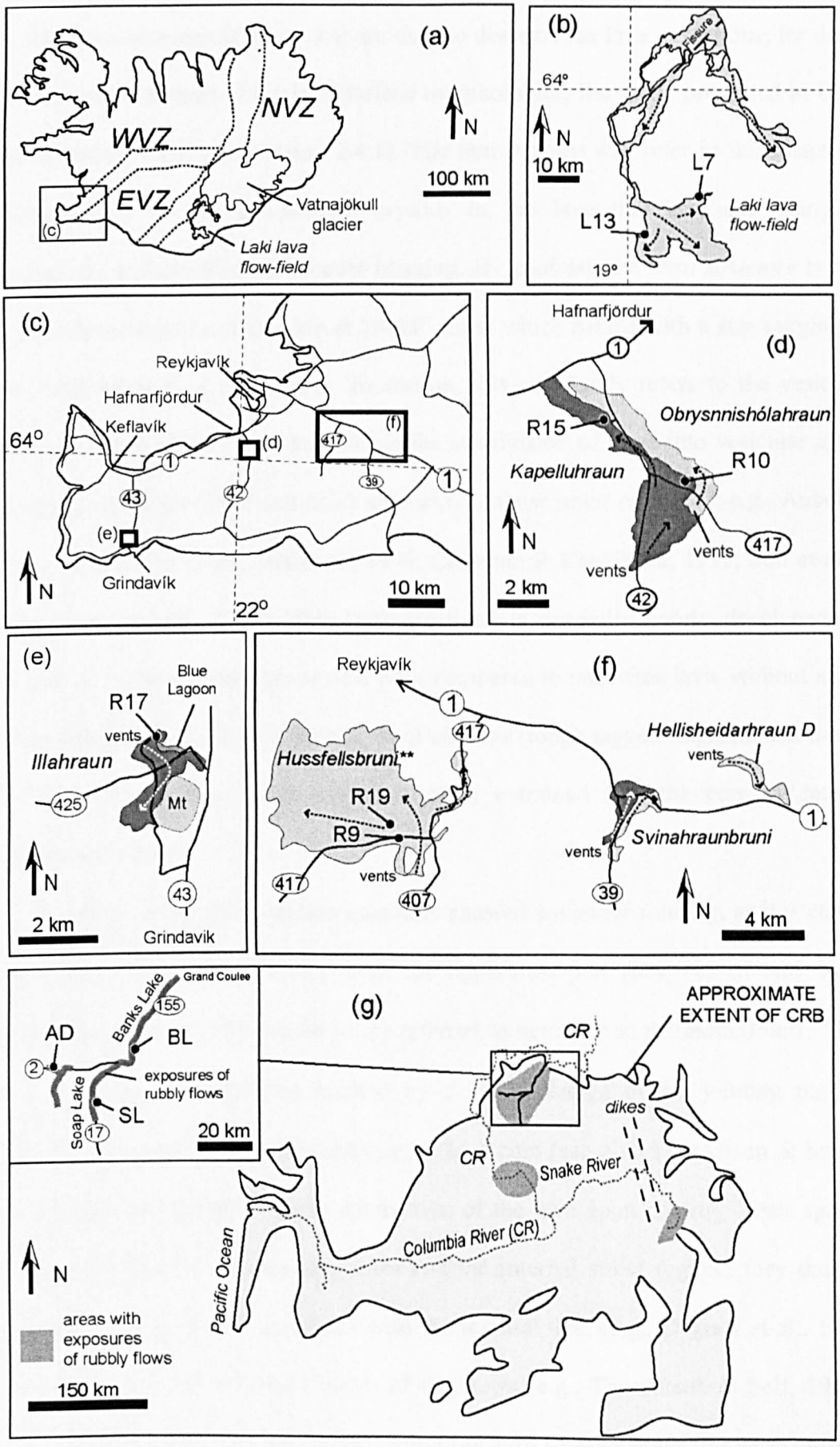
(a)
NVZ
WVZ
EVZ
(c)
Vatnajökull glacier
Laki lava flow-field
N
100 km
(b)
Fissure
64°
N
10 km
L7
L13
Laki lava flow-field
19°
(c)
Reykjavík
Hafnarfjördur
Keflavík
64°
(d)
(f)
(e)
43
42
39
1
417
N
Grindavík
10 km
22°
Hafnarfjördur
(d)
R15
Obrysnnishólahraun
Kapelluhraun
R10
N
vents
417
vents
2 km
42
(e)
Blue Lagoon
R17
vents
Illahraun
425
Mt
N
43
2 km
Grindavik
Reykjavík
(f)
1
417
Hussfellsbruni**
Hellisheidarhraun D
vents
R19
R9
vents
Svinahraunbruni
417
vents
407
39
N
4 km
Grand Coulee
Banks Lake
155
AD
BL
2
exposures of rubbly flows
Soap Lake
SL
17
20 km
(g)
APPROXIMATE EXTENT OF CRB
CR
dikes
CR
Snake River
Columbia River (CR)
Pacific Ocean
N
areas with exposures of rubbly flows
150 km

4.3.1 Terminology

This section presents terms that are used to describe the lava in sections; for describing the large-scale feature of the lava surface morphologies, the terms presented in Chapter 2 will be mainly used (see section 2.4.1). The term *texture* will refer in this chapter to the characteristics of the groundmass crystals in the lava that are seen using optical microscopy and electron backscatter imaging. By contrast, the term *structure* is reserved for the characteristics of the lava at "field" scale, which means with a size ranging from a few centimetres to a few meters. In section, this commonly refers to the vesicular and jointing pattern of the flows that dictate the subdivision of lavas into vesicular *upper* and *basal crustal zones* (*UCZ* and *LCZ*) enclosing a dense inner *core* (*CO*; e.g., Aubele et al., 1988; Thordarson, 1995; Self et al., 1996; Cashman & Kauhikaua, 1997; Self et al., 1997; Thordarson & Self, 1998). This "stratification" is generally poorly developed or non-existent in 'a'ā lavas; they are vesicle-poor compared to pāhoehoe lava, without a coherent crust, and characterized by a thick layer of *clinkers* (rough jagged fragments) at the top and the base of the flow, with fragments often entrained into the core (Wentworth & MacDonald, 1953).

The flows observed in section generally showed *columnar jointing*, as it is common in basalt flows (e.g., Spry, 1961), with the uppermost part (few 10s of cm) sometimes displaying small, closely-spaced joints referred to hereafter as *prismatic joints*. The crust-core boundary is sometimes marked by a sharp change in the jointing pattern with distinctly more widely spaced joints in the lava core (see also Thordarson & Self, 1998). These joints are products of the contraction of the lava upon cooling. Their spacing and shape vary with the lava cooling rates and the internal stress regime; they thus provide information that may be correlated with the textural data (e.g., Degraff et al., 1989), and related to the mode of emplacement of the flows (e.g., Thordarson & Self, 1998). Also used in the literature to refer to the jointing pattern of lava flows, the term *colonnade* is

generally used to define a basal zone with regularly spaced well-defined columnar joints whereas the term *entablature* is regularly used to describe irregularly jointed lava (e.g., Spry, 1961). Some confusion exists in the literature over the definition of these two terms and their implications in terms of lava emplacement mechanism; their use will therefore be avoided here. Characteristics that are specific to the sections studied will be presented in the relevant parts of the text further along.

Terms referring to the vesicular pattern of the flows will now be presented, following mainly the terminology defined by Thordarson & Self (1998) (Table 1). Vesicular features are abundant across pāhoehoe sections. In the crust there are numerous round-shaped vesicles that generally decrease in number and size from the uppermost and lowermost margins inwards (e.g., Aubele et al., 1988; Cashman & Kauhikaua, 1997). In the upper crust there may be laterally persistent horizontal vesicular zones (*HVZ* on graphic logs) that form during lava emplacement. These may correspond to variations in the gas content of the lava being injected in the inflating lobe and subsequently quenched along the inwards-propagating solidification front, or, alternatively, correspond to episodes of lava breakouts from the active flow front or from the top of the flow that created sudden depressurisation and resulting vesiculation events in the molten interior of the feeding lobe (see Cashman & Kauhikaua, 1997; Thordarson & Self, 1998). *Gas blisters* are large cavities (10–50 cm) that are sometimes present in the lava upper crust and are thought to form by gas accumulation in large pockets at the base of the solidifying crust (Walker, 1989). In the systematically thinner lower crust, there may also be *pipe-vesicles* (*PV* on graphic logs) that consist of vertical hollow tubes that form by segregation of gas at the bottom of the solidifying lobes during emplacement, and are preserved when the lava is emplaced on low slopes (< 4°, Walker, 1987) (see also Philpotts & Lewis, 1987, and Thordarson & Self, 1998). Poorly vesicular, the lava core sometimes shows *megavesicles* (*MV* on graphic logs), which are elongated cavities a few cm in size often concentrated at

the core-upper crust boundary. These can reach tens of centimetres in the thick sheet lava lobes of the Columbia River basalts (Thordarson & Self, 1998). Identified in many lobes with clear pahoehoe surface morphologies and well-defined upper and basal crusts, segregated vesicular features (e.g., Goff, 1996) consist of vertical cylinders (VC on graphic logs) sometimes merging into *horizontal vesicular sheets* (HVS on graphic logs) of vesicle-rich differentiated material. Their process of formation is distinctly different from the formation of horizontal vesicular zones in the upper crust as presented above and involves the density-driven migration of evolved, gas-rich interstitial liquids during the slow cooling of the lava core, after the input of fluid lava in the lava core has ceased.

More specific of 'a'ā flows, *lava intrusions* are sheet-like bodies of often vesicle-poor lava originating from the lava core and piercing through the upper rubble (also called lava spines, tongues or fingers; see Wentworth & MacDonald, 1953). *Accretionary lava balls* are large masses of heterogeneous material often draped by vesicular layers of lava, which are formed by rolling of crustal material on top of mobile lava in open-channels (Wentworth & MacDonald, 1953). Other terms will be introduced along with the descriptions.

4.3.2 Laki lava flow-field

The Laki lava flow-field is composed of shelly pāhoehoe lavas near the vent and lavas ranging from spiny, to slabby, and to rubbly pāhoehoe elsewhere (see Chapter 2). Complete cross-sections through individual lobes were observed in river cuts along the flow-field margins, which were accessible only on the coastal plain. The sections studied (L13 and L7: photographs in Fig. 4.2, graphic logs in Fig. 4.3) are located respectively about 30 and 50 km down-flow from the vents. Section L7 cuts at an angle through a 20-m-long, 4.3-m-thick lava lobe covered by a generally flat, ~20–30-cm-thick layer of vesicular rubble. The location of the lobe in the flow-field as determined using the aerial photos and field observations, and a critical assessment of historical accounts (see Chapter

2 and more specifically the inferred timing of lava flow emplacement shown in Fig. 2.8D), suggest that this lobe broke out from the leading edge of the flow between the 12 and the 14th of July 1783, as the lava invaded a depression that was occupied by a branch of the Skaftá river before the eruption. Section L7 is characterised, from top to bottom, of an ~20-cm-thick top rubble made of broken-up pāhoehoe slabs underlying a vesicular upper crust with a zone of larger, stretched vesicles at ~50 cm depth. The upper part of the upper crust displays closely spaced prismatic joints, which merge downwards into more widely spaced columnar joints. Megavesicles mark the inferred upper crust-core boundary at ~1.8–1.9 m depth. The core is sparsely vesicular, with some vesicle cylinders. At about 3 m depth, there is a zone with irregular, crosscutting hackly joints (see Fig. 4.2) that can also be observed in the core of adjacent lobes exposed along the same river cut. The lower crust is finely vesicular (inwards coarsening) and displays a radial jointing pattern. A thin layer of rubble is present at the base of the lobe.

Section L13 cuts through the margin of a large 3.8-m-thick sheet lobe that has a basal overlying contact with sediments and lavas predating the Laki eruption (lavas from Eldgjá eruption, see Thordarson et al., 2001). The sheet lobe was emplaced at the most marginal part of the Eldhraun branch of the Laki flow-field to the west (probably in the period 1–12 July 1983, see Fig., 2.8D). The internal vesicular pattern of the lobe is remarkably similar to that displayed by section L7 (see Fig. 4.2), and there is also a zone of irregularly jointed lava (hackly joints) in the lava core. A sharp change in jointing pattern defines the limit between crust and core. The lobe overrides small pāhoehoe-type lobes. These may correspond to small lava breakouts formed along the active flow front before the main lava lobe was emplaced.

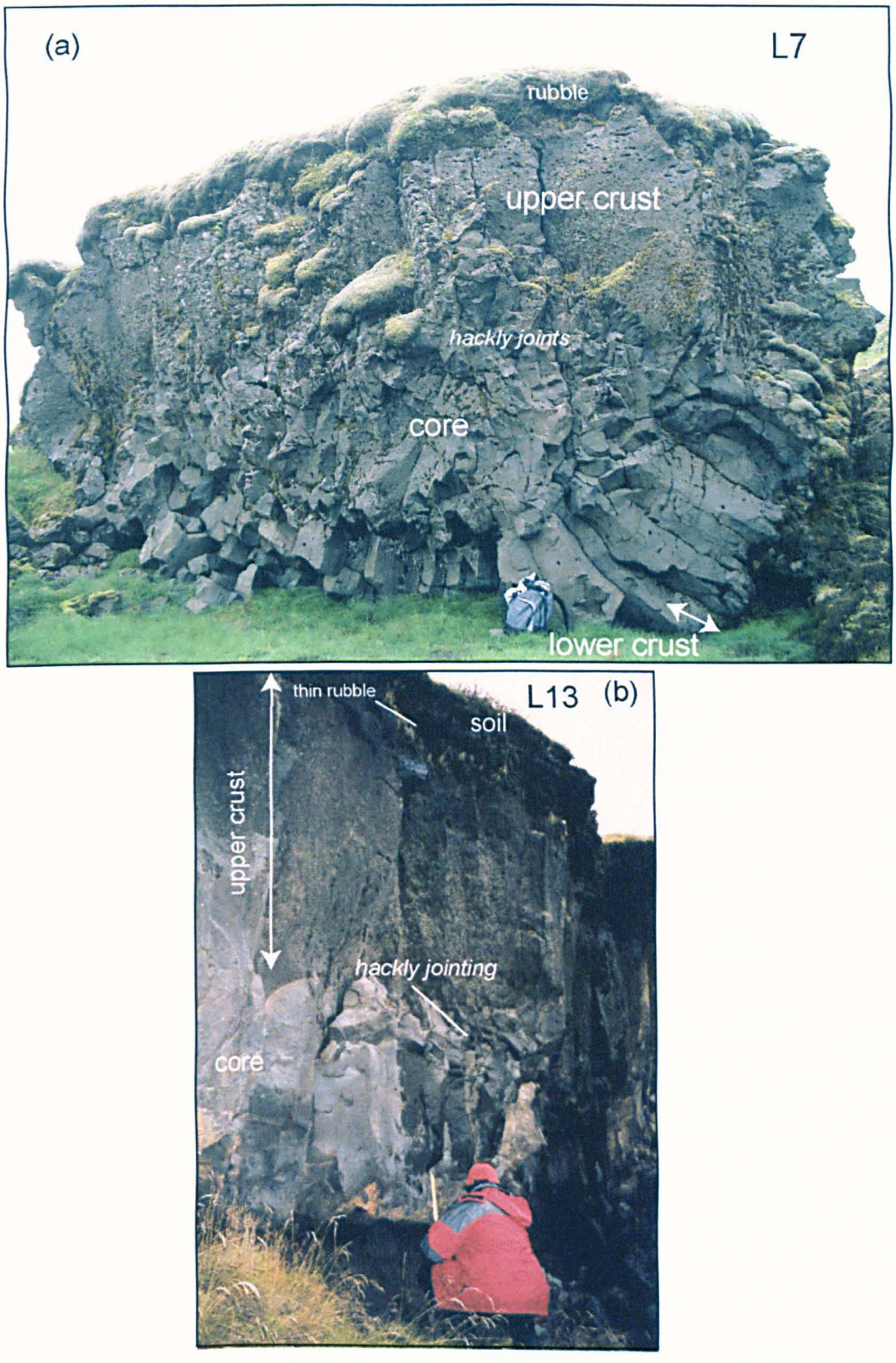

Figure 4.2: Photographs of Laki lava sections L7 and L13 studied in detail. L13 GPS: N63° 40.331', W018° 24.668'. Note zones with irregular jointing in lava cores (hackly jointing) that may be related to lava-water interaction. Note also the distinct jointing pattern between upper crust and core. More details are reported on graphic logs shown in Fig. 4.3.

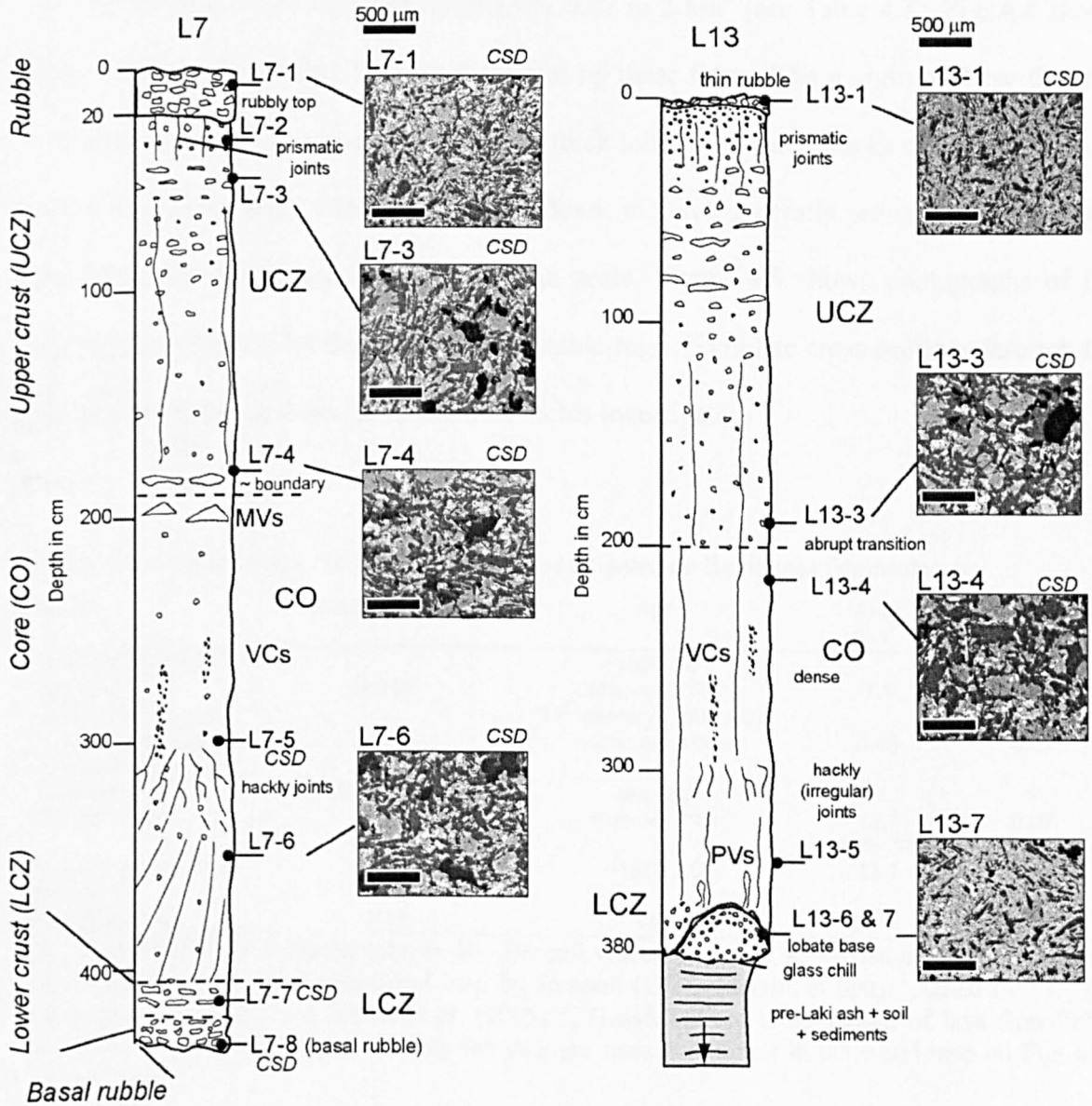

Figure 4.3: Graphic logs of sections L7 and L13. Representative backscatter (BSE) images of samples collected at different levels of sections are reported (plagioclase shows in dark grey, clinopyroxene in light grey, olivine in light-grey with white rim, oxides in bright white (needle shape), and vesicles in black; note that plagioclase is the dominant mineral phase). *CSD*—BSE images studied by CSD analysis, UCZ—upper crustal zone, CO—core, LCZ—lower crustal zone, MVs—megavesicles at inferred UCZ-CO boundary, VCs—vesicular cylinders (segregation feature). Vertical scale is shown in centimetres. Vesicles are not drawn to scale; their shape and distribution simply illustrate the general vesicular pattern of the flows. BSE images are 1.3 × 1.1 mm in all graphic logs reported in this chapter.

4.3.3 Reykjanes Peninsula lava flow-fields

These flow-fields were produced by fissure eruptions that mainly occurred in the 11th to 13th century. Flow volumes range from 0.07 to 2 km^3 (see Table 4.1). Fig. 4.4 shows some of the main surface features displayed by these flows. The margin of these flows is often lobate, formed by short sequences of thick lobes with steep flanks directly connected to the flow front (Fig. 4.4b). Along these flows, the lava generally presents a rough, often disrupted, surface at cm to tens of cm in scale. Figure 4.5 shows photographs of the sections and Figure 4.6 the constructed graphic logs. Complete cross-sections through the flows were found in three of the six flow-fields investigated.

Table 4.1: Characteristics of lava flow-fields investigated on Reykjanes Peninsula

Name	Geological map	Age	Area (km^2)	Volume (km^3)
Hellisheidarhraun D		~1800 AD[1]		
1. Svinahraun (Nyrdrieldborg vent)	H158	Christianity fires, 11th century (1000 AD)[1]	7.3	0.17
2. Lambafellshraun (Sydrieldborg vent)	H159	same as above	4.65	0.07
Hussfellsbruni[2]	H149, H150, H154	see text	?	?
Kapelluhraun	H97	Krisuvik fires	13.7	0.07
Obrysnnishólahraun	H99	~1850 AD	1151-1188 13.1	0.26
Illahraun (Blue Lagoon)	H19	13th century.	2.43	0.05

B—Brennisteinsfjöll volcanic system. H—Hengill volcanic system. K—Krisuvik volcanic system. Information mainly from geological map by Jonsson (1978) (details in text). [1], dated by ^{14}C, see Saemundsson (1995) and Sinton et al. (2005). [2], Hussfellsbruni is composed of lava flow-fields produced by different eruptions. Only the younger ones (see labels in table and map on Fig. 4.9) were studied.

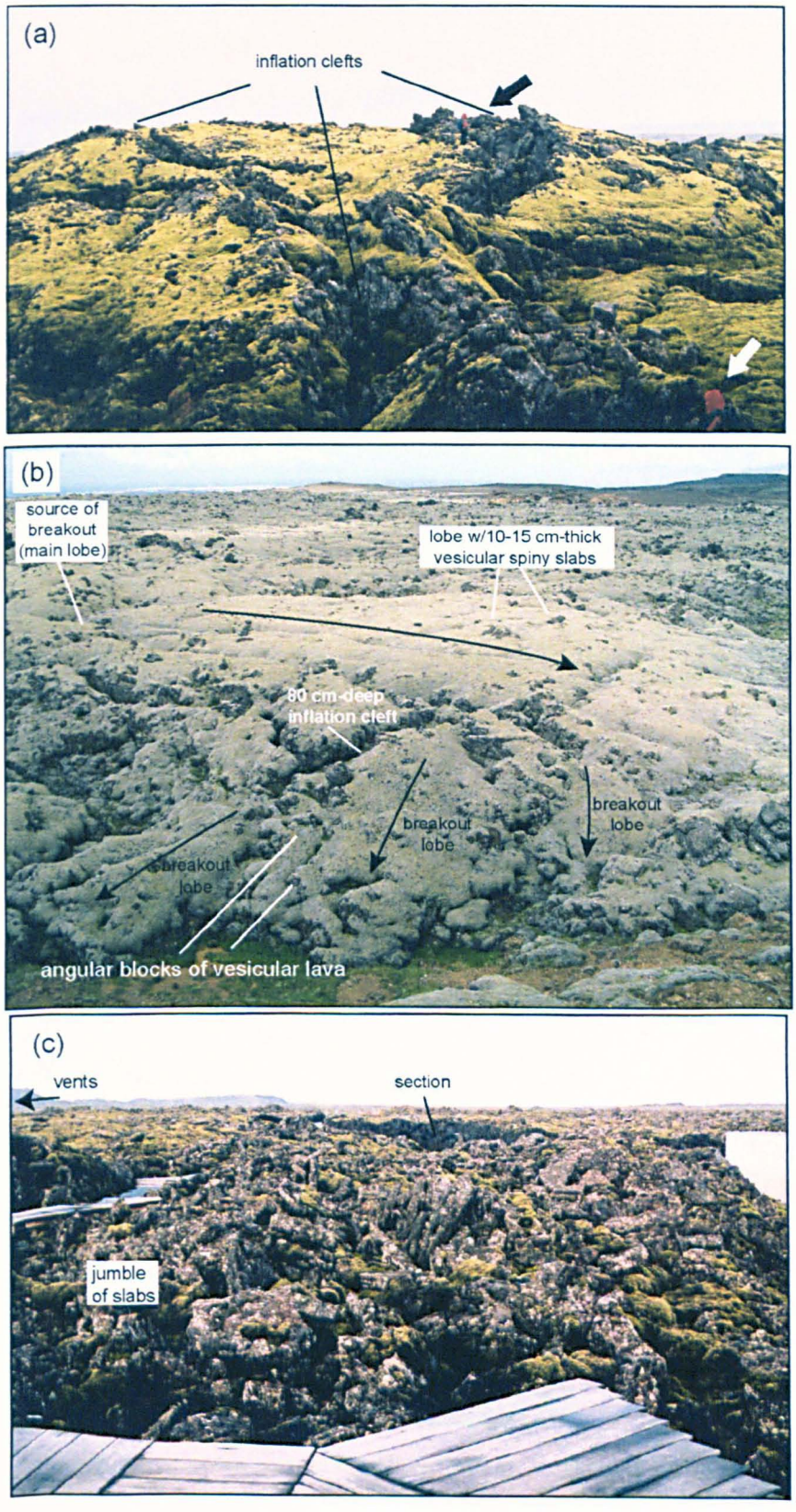

Figure 4.4: Photograph of some surface features of Reykjanes Peninsula lavas described in text. (a) Large lava rise feature in Hussfellsbruni flow-field next to section R19 (possibly three interconnected tumuli structures). Note the few-m-deep inflation clefts (cracks) and tilted flanks. Persons for scale (see arrows). (b) Large (~200 m wide) lava lobe branching from margins of rubbly flows in Hussfellsbruni flow-field (location on aerial photographs on Fig. 4.9). Note frontal 3- to 5-m-thick lava breakouts (black arrows show flow direction of individual lobes). (c) Surface of margins of Illahraun flow-field as seen from Blue Lagoon pool tourist path, looking north. Note disrupted character of flow surface (see text for details).

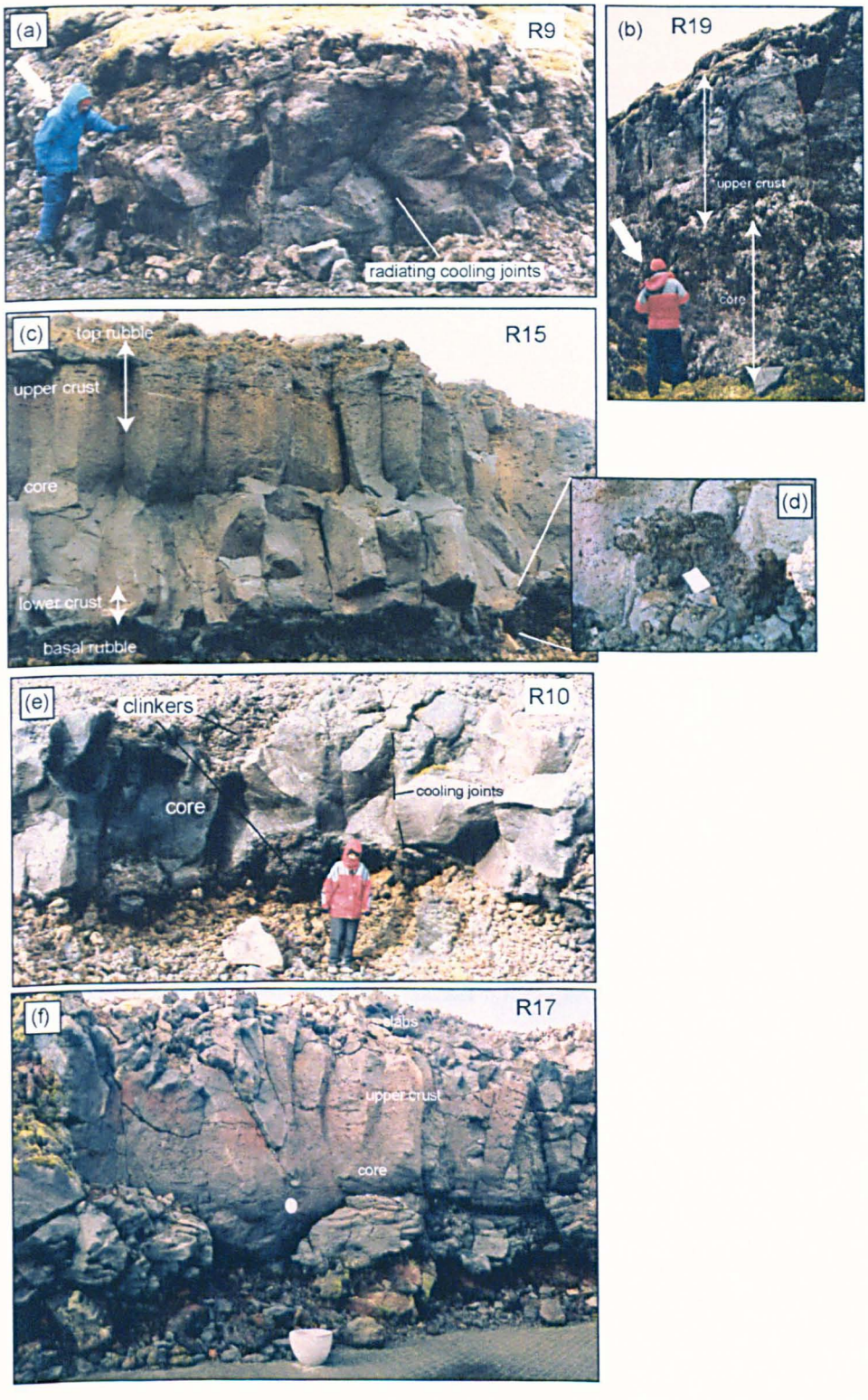

Figure 4.5: Photographs of cross-sections studied through Reykjanes Peninsula lavas (located on Fig. 4.1). (a, b) Hussfellsbruni field; (c, d, e) Kappellhraun flow-field; (f) Illahraun flow-field. (a, b) Person for scale (arrows). (a) Section R9: note radial cooling joints. (b) Section R19: note that core is coated by lava that was viscously torn apart during crack opening. (c) Section R15: note well-marked cooling joints that cut across upper crust and core of flow, meeting at middle of section (flow thickness is ~5 m). (d) Section R15: close view of lower crust contact with basal clinkers; note that contact of rubble with coherent lava is marked by 2- to 3-cm-thick vesicle-poor zone (chilled margin). (e) Section R10: central part of flow consists of single, dense zone with simple jointing pattern. (f) Section R17: note fragmented character of flow top. Part of flow below the core is not exposed. Height of exposure is ~7 m.

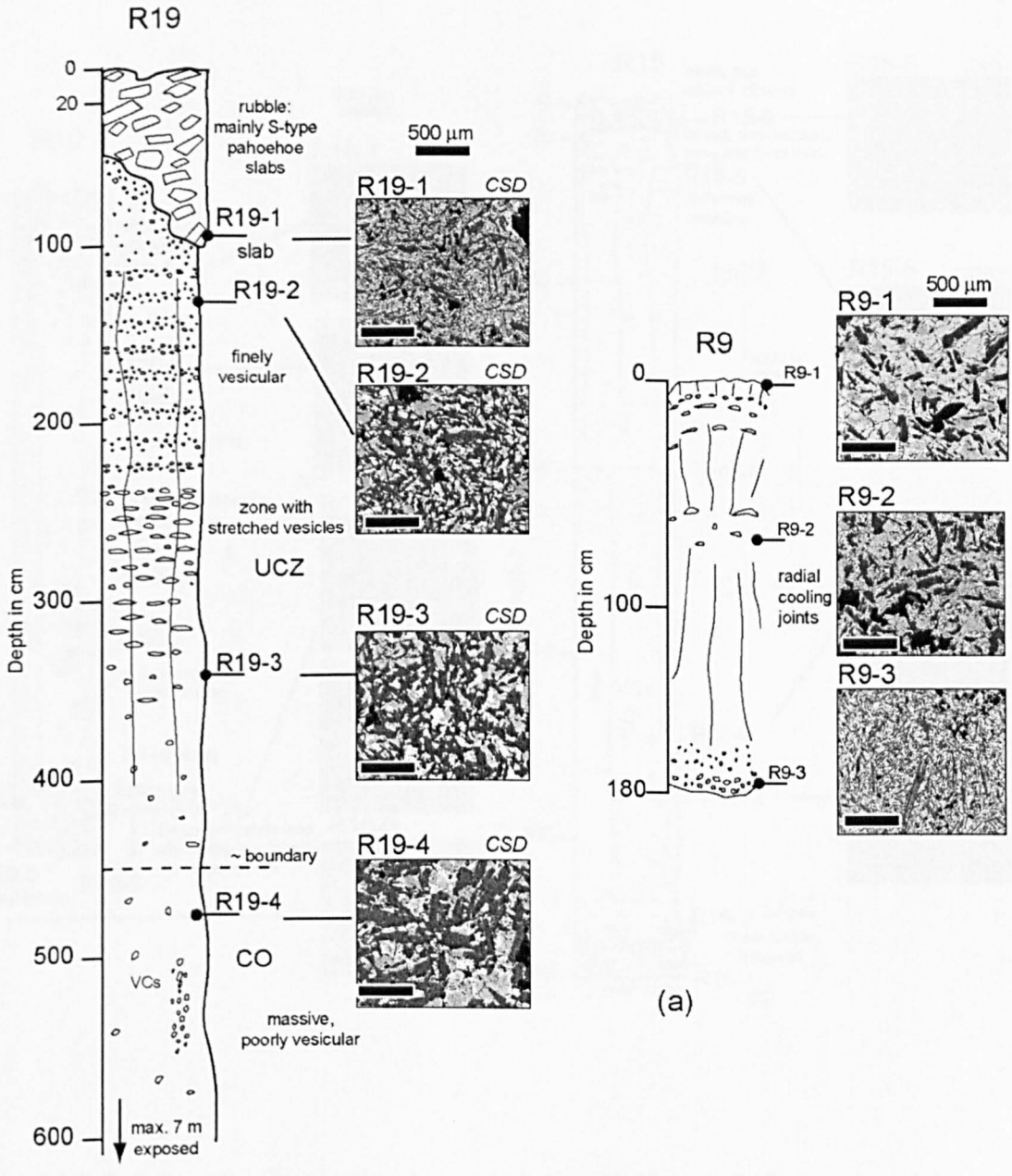

Figure 4.6: Graphic logs of Reykjanes lava cross-sections studied in detail. Representative backscatter images for some samples are shown. Scale bar on images is ~500 µm. UCZ—upper crustal zone; LCZ—lower crustal zone; CO—core; MVs—mega-vesicles; PVs—pipe-vesicles; HVS—horizontal vesicular sheets; VCs—vesicle cylinders (see terminology section and Thordarson & Self, 1998 for definitions).

(a) Graphic logs of sections R9 and R19 (sheet lobes, Hussfellsbruni lava fields). Note difference in thickness of each lobe (base of section R19 not exposed). For section R19, vesicular zones in upper crust not drawn to scale. Note large inwards increase in groundmass crystal sizes across both sections.

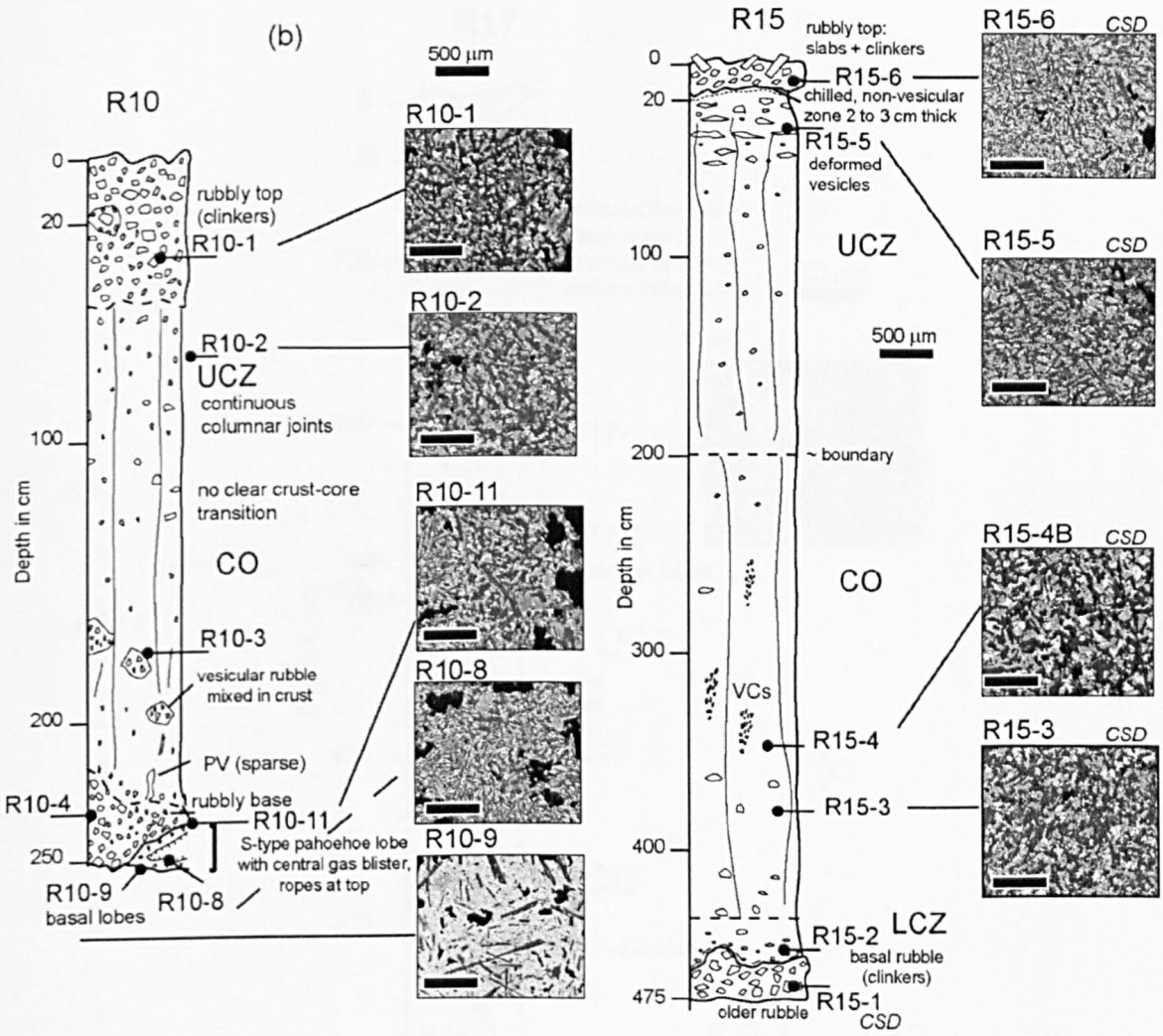

Figure 4.6 (continued): (b) Graphic logs of sections R10 and R15 (marginal lobes from channelized 'a'ā flow; Kapelluhraun flow-field). phh—pāhoehoe, aa—'a'ā. Note difference in vesicular and jointing patterns between sections. Section R10 (top) is typical of 'a'ā lobes with single set of widely-spaced cooling joints and stretched vesicles in core. There is no clear crust-core transition and vesicular segregation features are absent. Section R15 shows characteristics that are intermediate between typical pāhoehoe and 'a'ā sections with layers of top and basal clinkers and vesicular segregation features in core (e.g., compare with sections R19 and R10).

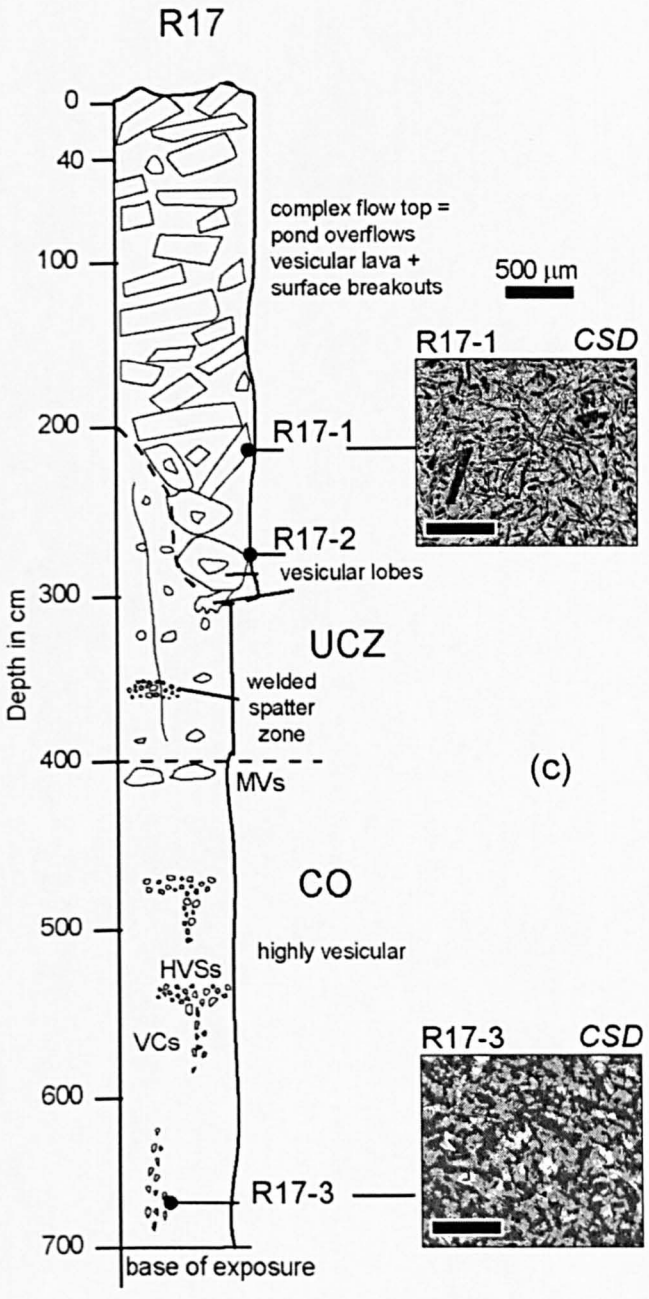

Figure 4.6 (continued): (c) Graphic log of section R17 (frontal lobes; Illahraun flow-field). Note fragmental character of upper part of flow made of a stack of thin layers of vesicular lava probably representing drifted and disrupted channel overflow levees. Some vesicular features in upper crust are interpreted as blocks of spatter that were transported on flow surface and later incorporated in the flow interior, probably during inflation (i.e. zone of welded spatter on figure).

Hellisheidarhraun D (Nesjahraun flow-field: labeled Orrustuholshraun on recent 1:100 000 topographic map). This lava field (outlined in Fig. 4.7) is the youngest of a succession of flows that were produced from a short fissure segment trending NE

(Nesjahraun flow-field, figure 4 in Sinton et al. 2005). It consists of single lava flow that is 3 km long and was emplaced on slopes of about 1° (see Fig. 4.7). According to Kristjansson et al. (2003), this lava flow covers 32.7 km^2 and its volume is about 0.26 km^3. The Nesjahraun flow-field has a ^{14}C age of 1865 BP (e.g., geological map by Saemundsson, 1995; figure 4 in Sinton et al. 2005) and lavas have a homogeneous bulk rock composition with ~7.75 wt.% MgO (Sinton et al., 2005, from Saemundsson, 1992, 1995). An examination of the aerial photos permits to divide the flow into 4 main branches that have specific morphological characteristics (labelled A to D, see extent on Fig. 4.7). The flow shows a central, 50- to 150-m-wide and up to 700-m-long open-channel. In branch A, the open-channel is well developed, whereas along branch B, going down-flow, the limits of the channel become unclear and the lava gradually develops a coherent surface. The lava at the sides of the channel in branch A displays a smooth, bright surface on the aerial photos, which suggests that it is covered by flat vesicular overflows from the channel. The margins of the flow in branch B are formed by sequences of steep-flanked lobes partially coalesced into large sheets (labelled lobate margins on Fig. 4.7). Branches C and D consists of two fan-shaped lobes which are directed respectively to the south and to the east, topographically constrained by older flows and hyaloclastite ridges. The lobes have a central part with transversal ridges made of compressed rubble that are cross-cut by discrete shear zones parallel to the flow direction, and lobate margins composed of 5–6-m-high inflated lobes with vesicular upper crusts and steep flanks. The margins are separated from the central part by long, well-defined shear zones. Exposed at a quarry located near the flow front (see Fig. 4.7), the surface of the flow consists of a 2 to 3-m-thick layer of rubble formed of fragments of vesicular pāhoehoe-like crusts mixed with turned over slabs, and grading into spinose 'a'ā clinkers at the bottom of the pile. Protrusions of coherent lava through the top rubble are common.

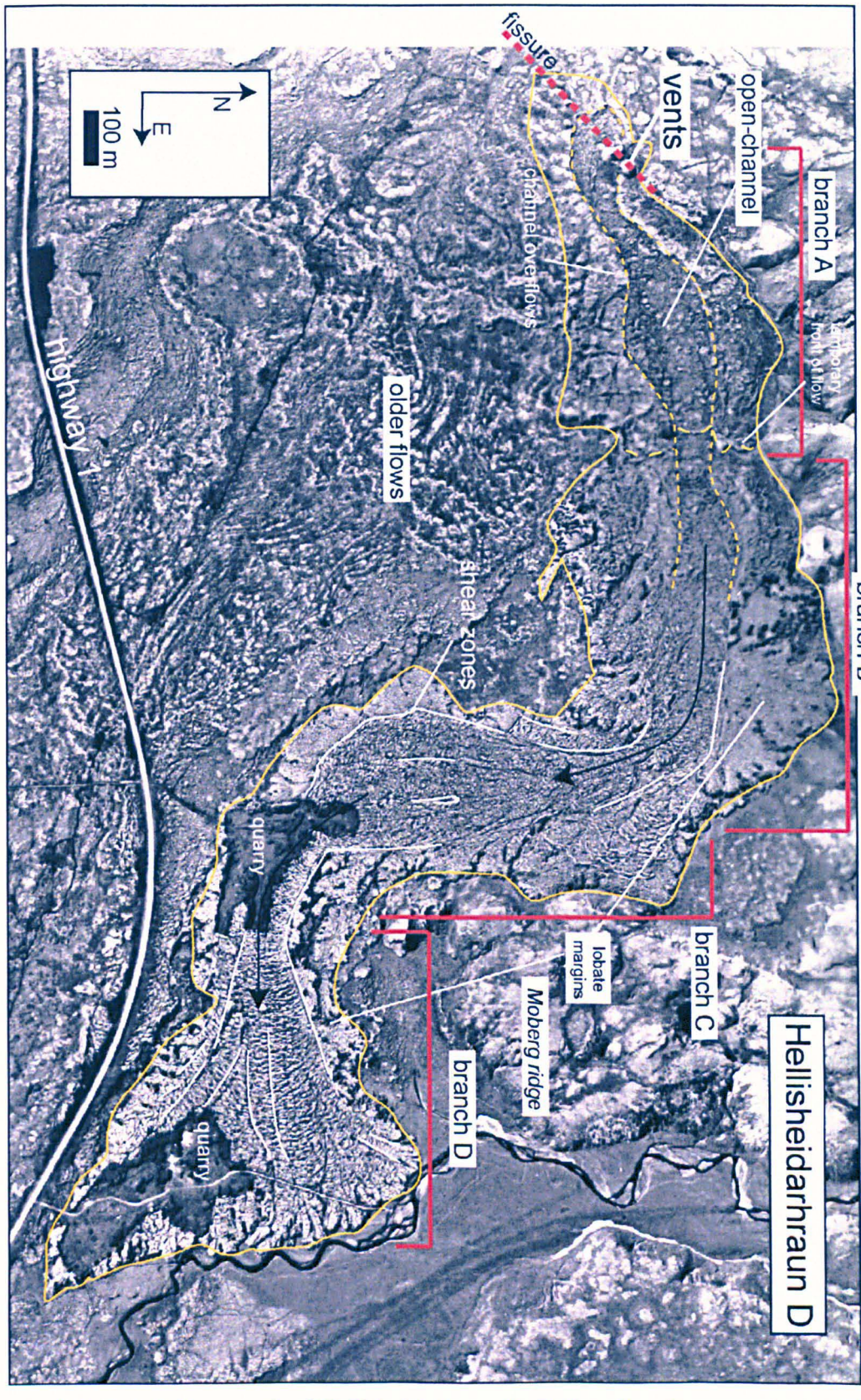

Figure 4.7: Aerial photograph of Hellisheidarhraun D. Yellow line draws contours of lava field described in text. Dark continuous lines indicate flow direction. Margins of open channels in dashed lines. Distinct zones (or domains, labeled A to D) are identified and surface morphologies are described in text. Flow interior was observed in quarries near distal-most part of flow (dark areas on aerial photos).

The type of the transition between the different lava branches provides information about the flow emplacement style. More specifically, the channel becomes narrow at the transition between branch A and B (see lobe shape termination of branch A on Fig. 4.7), and the flow gets restricted at the limit between branch B and C, and branch C and D. This feature is consistent with a lobe-by-lobe emplacement according to which each branch represents a distinct episode of large lava output followed by a major frontal breakout. It is most likely that the channelized area in the centre of each lobe was established after the episode of lava outbreak from the leading flow front, as this would have led to an increase in the lava flux in the central part of the flow. A stable open-channel would have developed in the proximal part of the flow, delivering lava to the most distal parts.

Svinahraunsbruni flow-field: Svinahraun and Lambafellshraun. The study area is composed of two fissure-fed lava flows, Svinahraun and Lambafellshraun. These were produced respectively from Nyrdri-Eldborg and Sydri-Eldborg vents (see Fig. 4.8). According to Jonsson (1978, 1979), these two vents were formed during the same eruption, and the two lava flows thus form a single lava flow-field. The eruption is dated at ~1000 AD from historical accounts (e.g., figure 4 in Sinton et al., 2005). The flows display a proximal part formed by sheet lobes, leading down-flow to narrow lobes with prominent central open-channels in the proximal and medial zones. The distal zone of the two flows consists of branching, fan-shape lobes (see Fig. 4.8). These show transversal rubbly ridges, shear zones parallel to the flow direction, and lobate margins formed sequences of ~3-m-thick inflated lobes with steep flanks and vesicular lava squeeze-outs along inflation cracks. The surface of these consists of a thick upper layer of jagged spinose rubble mixed with fragments of pāhoehoe crust. There are some accretionary lava balls. Protrusions of coherent lava are common, showing scrape marks on their outer faces, which attest of a formation by late extrusion of lava from the interior of the flows into the rubble. The presence of large masses made of piles of thin layers of vesicular lava can be linked to the

disruption and subsequent rafting of parts of channel overflow levees during flow emplacement.

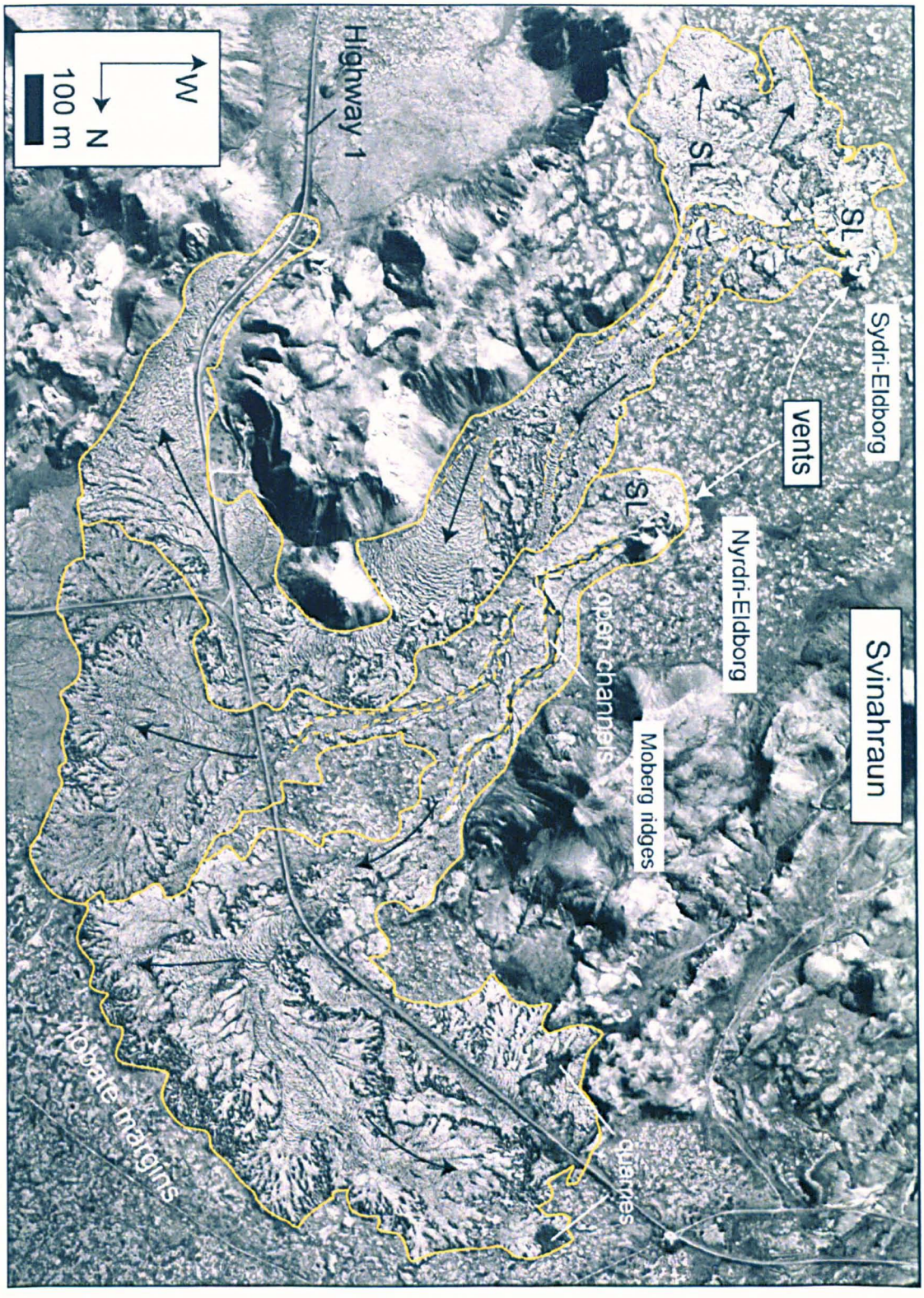

Figure 4.8: Aerial photograph of Svinahraunbruni. Yellow line draws contours of the two separate lava flows described in text. SL—proximal flows with sheet-like surface morphologies (some with slabby or platy surfaces). They are partly covered by channel overflows near channel margins (see text for more details). Note the open-channels that define the proximal part of each flow, and the lobate shape of the distal flow front.

Hussfellsbruni (or Husafellsbruni) lava flow-fields. Hussfellsbruni consist of at least 9 separate lava flow-fields (Jonsson, 1978). The extent and surface morphologies of three of the youngest flow-fields labelled and referred to as H149, H150 and H154 on Fig. 4.9 after Jonsson (1978) were studied using aerial photos and field observations (see also map by Vikingsson et al., 1995). Kongsfellshraun flow-field (H149, hu2 on map by Vikingsson et al., 1995, red in map drawn on Fig. 4.9) is the youngest of the flows studied. Its exact age is not known but it is historic and could have been produced in the 10^{th} century or earlier as it covers the Rjupnadyngjuhraun flow-field (H154, blue on Fig. 4.9) which rests on the settlement layer dated at 870 AD (Jonsson, 1978). The eruption that produced H149 occurred on a high plateau formed by pre-glacial hyaloclastite ridges and the lava was emitted from a short fissure segment on which three spatter cones formed. Lava flowed on either side of the Stora-Kongsfell (SK) Moberg ridge before spreading at the base of the plateau and forming two main long branches oriented to the north and to the west, constrained by the hyaloclastite ridges and pre-existing flows (i.e., H154 and H150, see Fig. 4.9). In the near-vent area, the flows form large sheet lobes whose surface is sometimes disrupted in large plates and meter-sized slabs (see area north of the SK Moberg ridge). The two flow branches, on the east and west side of the SK Moberg ridge, display a central open-channel formed on ground slopes > 1.5°. The flows spreading at the base of the plateau form long and narrow, branching lobes that reach a maximum distance of 7 km from the vents. They are typically 5–10 m thick and 100–500 m wide and were formed on slopes > 2°. They show a central channelized area, with segmented, few-meters-high channel walls and lobate margins made of short sequences of inflated lobes. A mixture of heterogeneous rubble and rafts of stacked thin vesicular layers cover the floor of channels. The most distal front of the flows consists of inflated flat-topped lobes branching from a thick rubbly flow front. The flows display morphological evidence of lobe-by-lobe emplacement and it seems likely that the central open-channels formed after major

breakouts from the leading flow front. In terms of lava surface type, they thus can be considered as transitional to 'a'ā, and defined as rubbly pāhoehoe although they are significantly different from the lavas observed on Laki (Chapter 2).

The Eldborgarhraun flow-field (H150, green on Fig. 4.9, ~18 km^2 and ~0.36 km^3 after Jonsson, 1978) was produced by an eruption predating the formation of H149. The flows mainly show surface morphologies transitional to 'a'ā, with central open-channels and lobate margins made of spiny to rubbly lava which are best developed in places where the lava was emplaced onto flat terrain (see for example lavas emplaced on the western margin of Sandfell hyaloclastite ridge). The flow surface is dominantly formed of a mixture of various types of rubble ranging from cm-sized rounded blocks to m-scale slabs with basal scrape marks. Accretionary lava balls and drifted parts of channel overflow levees (stack of shelly-type lava) are present on the flow surface. The flows forming the easternmost part of this flow-field were emplaced onto slopes > 10° and define clear 'a'ā morphologies with open-channels bordered by 2–5-m-high channel walls. They have margins formed of inflated slabby- to rubbly-surfaced lobes with steep flanks.

The Rjupnadyngjuhraun flow-field (H154, blue on Fig. 4.9) was clearly formed before H149, but its time relation with H150 is not known. According to Jonsson (1978), it covers ~20–25 km^2 and its volume is ~0.5 km^3. The upstream-most part of the exposed part of the flow-field is formed of a lava field with large inflation features (lava rises as illustrated on Fig. 4.4a, tumuli, and sheet lobes bordered by steep monoclinal uplift margins). The surface of this field is very flat, and forms a distinct feature on aerial photos characterised by a high refractive index (see area near location of section R19 on Fig. 4.9). Section R19 was exposed by deep inflation cracks that propagated into the solidified part of a large inflated sheet lobe in this area. The vesicular and jointing pattern of the flow across the section is drawn in Fig. 4.6. The surface of the flow is formed by a mixture of cm-sized rubble and disrupted thin vesicular crusts. The upper crust is very vesicular with distinct

horizontal vesicular zones. The lower part of the upper crust shows larger, stretched vesicles. Cooling joints extend through the upper crust to the limit with the core. The core of the flow is coated in its lower part by a more viscous layer that was torn apart when the fracture opened. It is difficult to estimate the entire thickness of the flow in that area, but it could be over 15 m as it was probably emplaced in a depression. Observed nearby, section R9 is exposed along the main road and cuts through a smaller sheet lobe emplaced over the sheet lobes just described, and subsequently covered by channel-fed flows. A study of the location of this lobe in the flow-field using the aerial photos suggests that it belongs to the H149 flow-field. The internal structure of this lobe is simple with vesicular upper and basalt crust, and a core with large vesicles with uneven shapes. Joints meet at about the middle of the flow.

Kapelluhraun and Obrysnnishólahraun. These two flow-fields were produced from nearby fissure segments covered by spatter cones (Fig. 4.10). Kappelluhraun was produced during the Krisuvik fires, ~1150 AD (Johannesson & Einarsson, 1989, see also map by Vikingsson et al., 1995), about 3000 years later than Obrysnnishólahraun (Jonsson, 1974, 1983). According to Jonsson (1978), it covers ~13.7 km^2 and its volume is ~0.07 km^3. The flows reached the seacoast at a distance of ~10 km from the vent. The area most proximal to the source is composed of a complex field of superimposed flows that is labelled branch A on Fig. 4.10. The westernmost side of the flows is cut by a 100- to 200-m-wide open-channel bordered by shear zones (inset on Fig. 4.10) which lead down-stream to a narrow lava branch with a central channelized zone and lobate margins (branch B on Fig. 4.10; see also Oskarsson, 2005). This flow is considered as representative of a typical 'a'ā flow (Oskarsson, 2005). A quarry exposes the interior of the flow along its northern margin, ~7 km from the vent, where section R15 was studied (see Fig 4.5c; same quarry as studied by Oskarsson, 2005). At that location, the flows form up to 5-m-thick inflated lobes ranging from oval-shaped tumuli to wide and flat sheet lobes (up to 30 m wide, see Oskarsson,

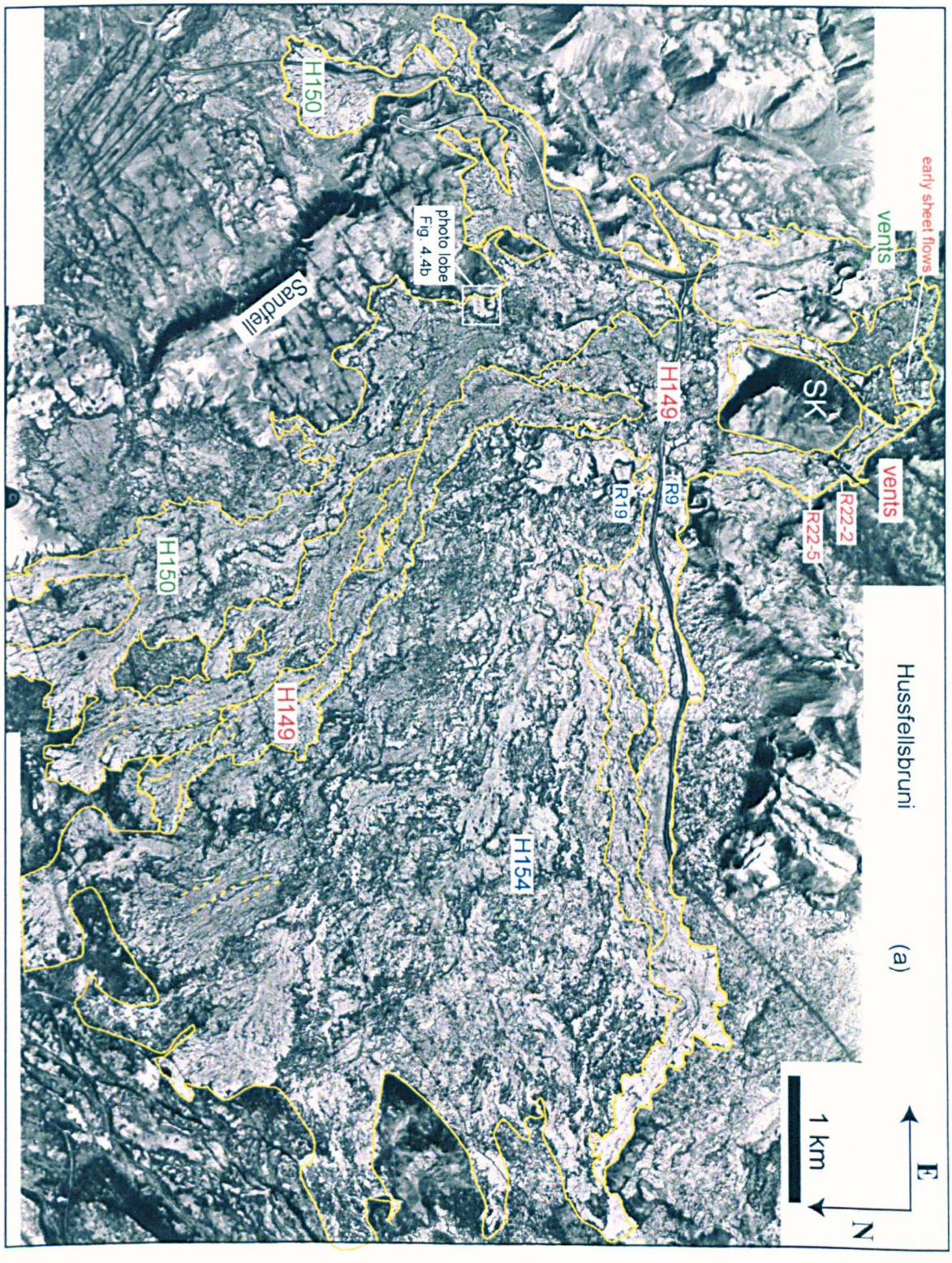

Figure 4.9: Hussfellsbruni lava field. (a) Aerial photograph of lava flow-fields studied with drawn contours of individual flows (dashed lines: clear open-channel walls. SK is Stora-Kongsfell mount just next to source cones. Sandfell is another old hyaloclastite ridge that was partly covered by the flows. Location of sections R19 and R9 (GPS N64° 00'45.3'', W021° 40'28.3''), and glassy surface samples R22-2 and R22-5 is indicated.

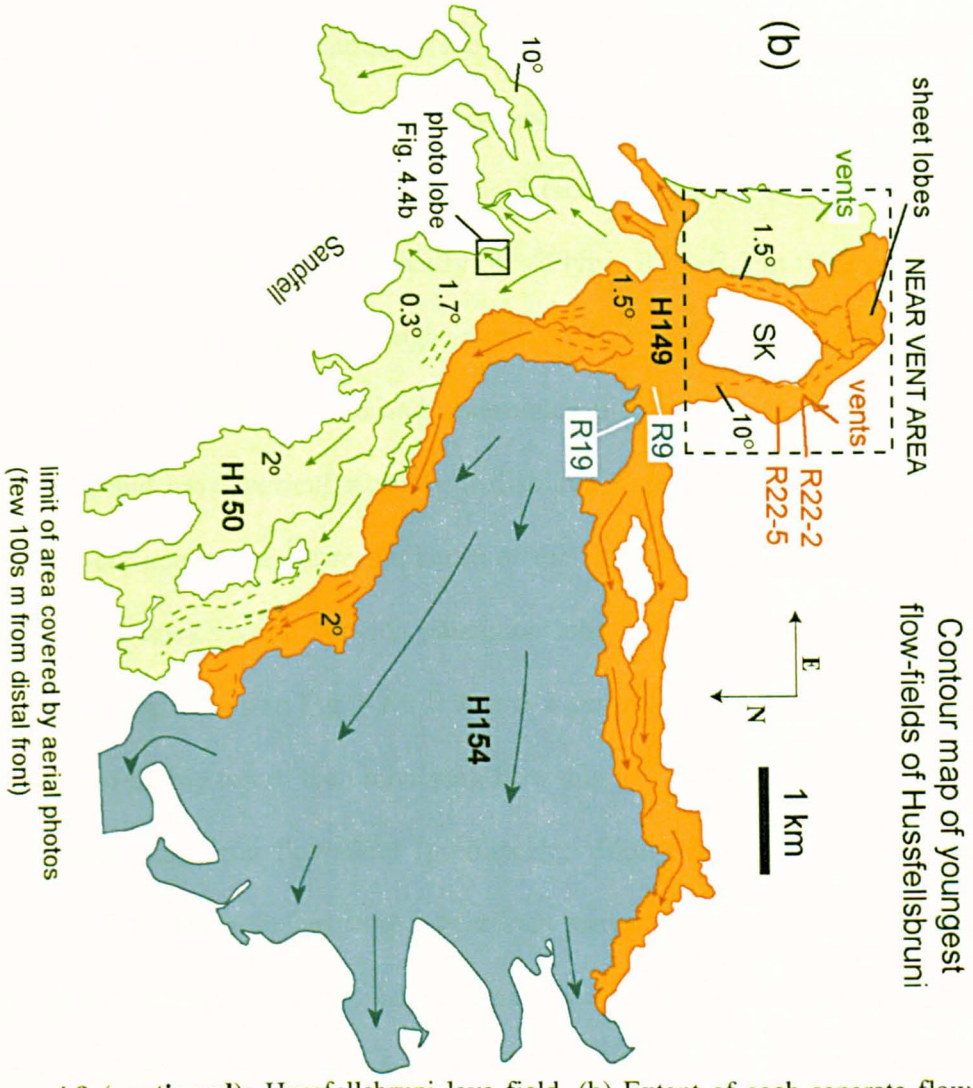

Figure 4.9 (continued): Hussfellsbruni lava field. (b) Extent of each separate flow-field (H149, H150 and H154) and associated vents (for H149 and H150 only) described in the text. Contours drawn from aerial photo.

2005). The lobes change from spiny to slabby and to rubbly along their length. The flow top is formed of a mixture of broken-up vesicular slabs, jagged lava fragments (clinkers), with some blocks of spatter and, in some places closer to the central part of the flow, m-scale accretionary lava balls. The lobe studied for textural analysis (section R15: graphic log on Fig. 4.6), presents a top and basal layer dominated by clinkers partly entrained in the core at the base (Fig 4.5d), and vesicular upper and basal crustal zones. Some vesicular

segregation features (vesicle cylinders) are present in the lava core. Basal clinkers show evidence for formation by "in-situ" tearing of viscous lava at the base of the flow. The jointing pattern is that of regular columnar joints cutting across the upper and basal part of the flow, and meeting at the middle of the section (see details in Oskarsson, 2005).

Section R10 (Fig. 4.5e) was studied at another quarry located along the northern border of branch A of the Kapelluhraun flow-field (see location on Fig. 4.10). The main flow exposed in section (Fig. 4.6) is typically of 'a'ā type. It is ~2.5 m thick at most, and shows thick basal and upper layers of rough jagged fragments (clinkers) enclosing a dense core with scattered stretched vesicles and assimilated pieces of vesicular rubble. There are no clear upper and basal vesicular crusts. It displays a single set of widely spaced columnar joints that cut across the entire thickness of the flow. Along the same quarry face, a thin (50 to 70 cm thick), vesicular-rich pāhoehoe lobe is exposed in section (base of section R10 graphic log shown in Fig. 4.6). It shows a central gas blister and basal pāhoehoe toes intruding the rubbly top of the underlying flow unit.

Obrysnnishólahraun flow-field (prehistoric, Vikingsson et al., 1995) is formed by a major lava flow that branches from a near-vent area made of early-formed sheet flows later disrupted into large plates (Fig. 4.10). The central part of the flow is formed by a mixture of large vesicular slabs and smaller fragments that are piled in compressional ridges in the channelized area next to the cones. In some places, there are large blocks, 1–5 m in size, made of piles of highly vesicular lava and agglutinated spatter. Margins are formed by sequences of spiny to slabby-surfaced pāhoehoe lobes separated from the central part by shear zones.

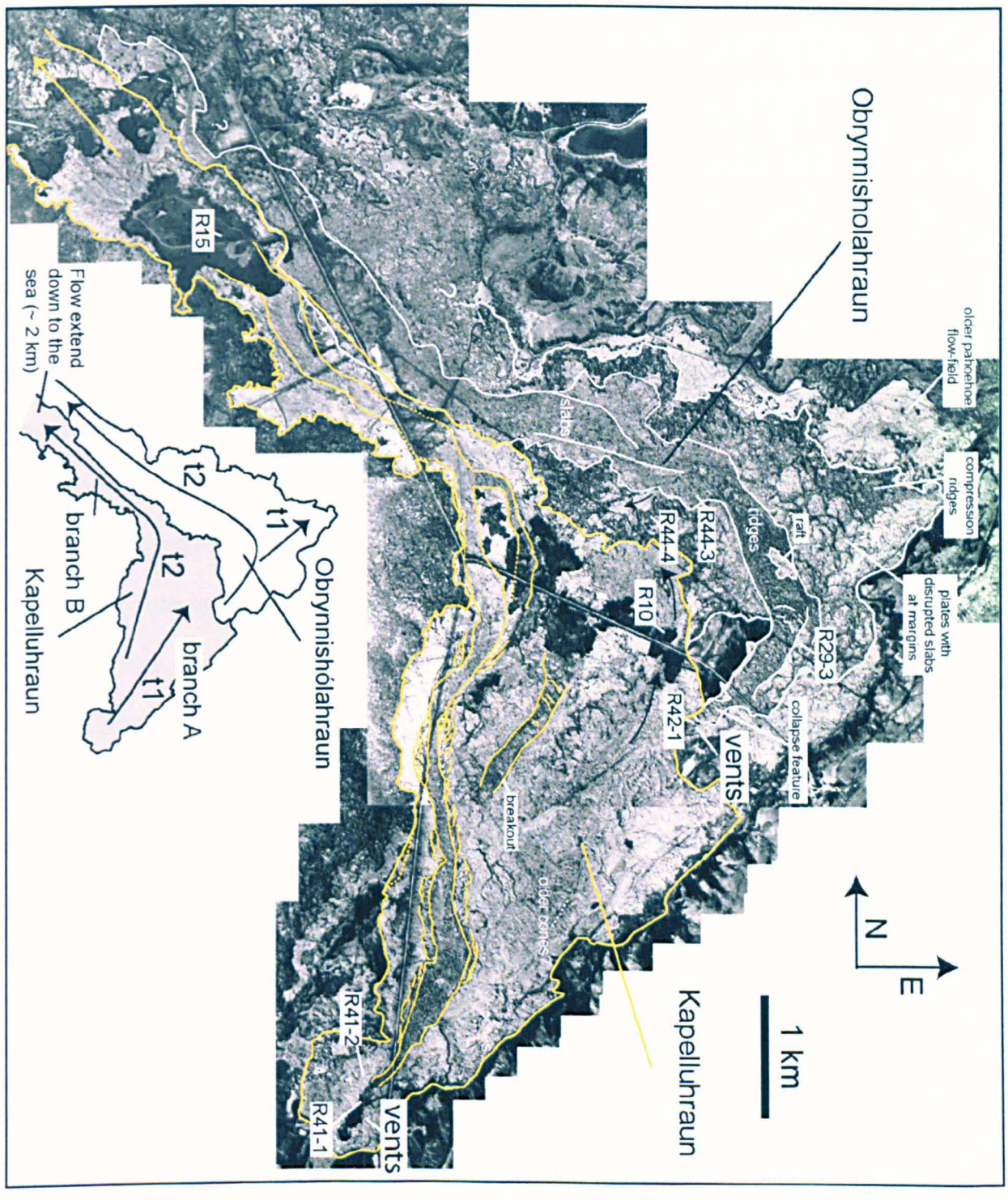

Figure 4.10: Aerial photograph of Kapelluhraun and Obrysnnishólahraun flow-fields. Lines draw flow-field outlines and main shear zones. Sketch at bottom locates branches discussed in text. Arrows labelled t1 and t2 show inferred emplacement sequence of each lava field. Location of sections R15 (GPS N64° 01'19.3'', W021° 58'60.5'') and R10 (GPS N64° 00'26.0'', W021° 55'07.8''), and glassy surface samples R29-3, R41-1 (GPS N63° 58.676', W021° 57.343'), R41-2 (GPS N63° 58.751', W021° 57.615'), R42-1 (GPS N64° 01.091', W021° 56.232'), R44-3 (GPS N63° 00.933', W021° 54.878') and R44-4 (GPS N64° 00.940', W021° 55.329') is shown. Kapelluhraun distal front is not seen on photographs (inhabited area). Flows extend to the sea at left of area mapped (i.e. general map shown on Figure 2.1 in Thordarson & Hoskuldsson, 2002).

Illahraun (Blue Lagoon). Illahraun (see Johannesson & Einarsson, 1988) is formed of a main 500- to 600-m-long lava flow that was emitted from a 100–150-m-long fissure. Two main lava branches, A and B, can be distinguished on the basis of surface morphological characteristics (Fig. 4.11). Along branch A, the surface of the lava is formed by a mosaic of 10–50-m-wide plates (coherent domains with nearly-flat upper surfaces). The organisation of the plates suggests that the flow was mainly directed to the north. At field scale, the plates are composed of a jumble of metre-size slabs with ropy surfaces that creates the small-scale bumpiness of the plates that can be seen on the aerial photos (see Fig. 4.4c). Along branch B, the lava surface is clearly more disrupted and only a few plates can be seen from the aerial photos. The main flow direction of this lava branch is to the southwest, constrained along the eastern side by an elongated hyaloclastite ridge (see Fig. 4.4). Near the vent, the lava forms a clear collapse structure made of a disrupted central part bordered by longitudinal cracks that cut across the proximal area of branch A lava (see Fig. 4.11). A sequence of emplacement can be proposed to explain the morphological characteristics of the flows. Branch A most likely formed at an early stage, whereas branch B was formed after a major lava breakout from the southern edge of the flow. This implies that the formation of branch B was associated to an increase in the lava pressure within the flows, which may have been caused by an increase in lava production rates from the fissure or result from the blockage of the advance of the flows further to the east by the hyaloclastite mount. The near-vent collapse structure may be the consequence of the late drainage of the interior of the proximal part of the early-formed crusted flows.

The section studied (section R17) is located along the northern part of the flow, near to the distal flow front, and is exposed along the path that leads to the Blue Lagoon pool (Fig. 4.11). The 5-m-thick section is composed of a thick vesicular upper crust and a dense core with some vesicular segregation features (Fig. 4.6). The flow top is made of a 2–3-m-thick layer composed of meter-sized stacks of vesicular lava (probably rafted parts of channel

overflow levees later disrupted by inflation of the underlying flow) mixed with cm-sized fragments of shelly pāhoehoe lava and spatter material. Surface breakouts of pāhoehoe lobes intrude the base of this fragmental upper layer. The upper crust of the lobe incorporates a vesicular zone of welded spatter possibly assimilated in the flow interior by sinking of surface material into the flow prior to or during inflation.

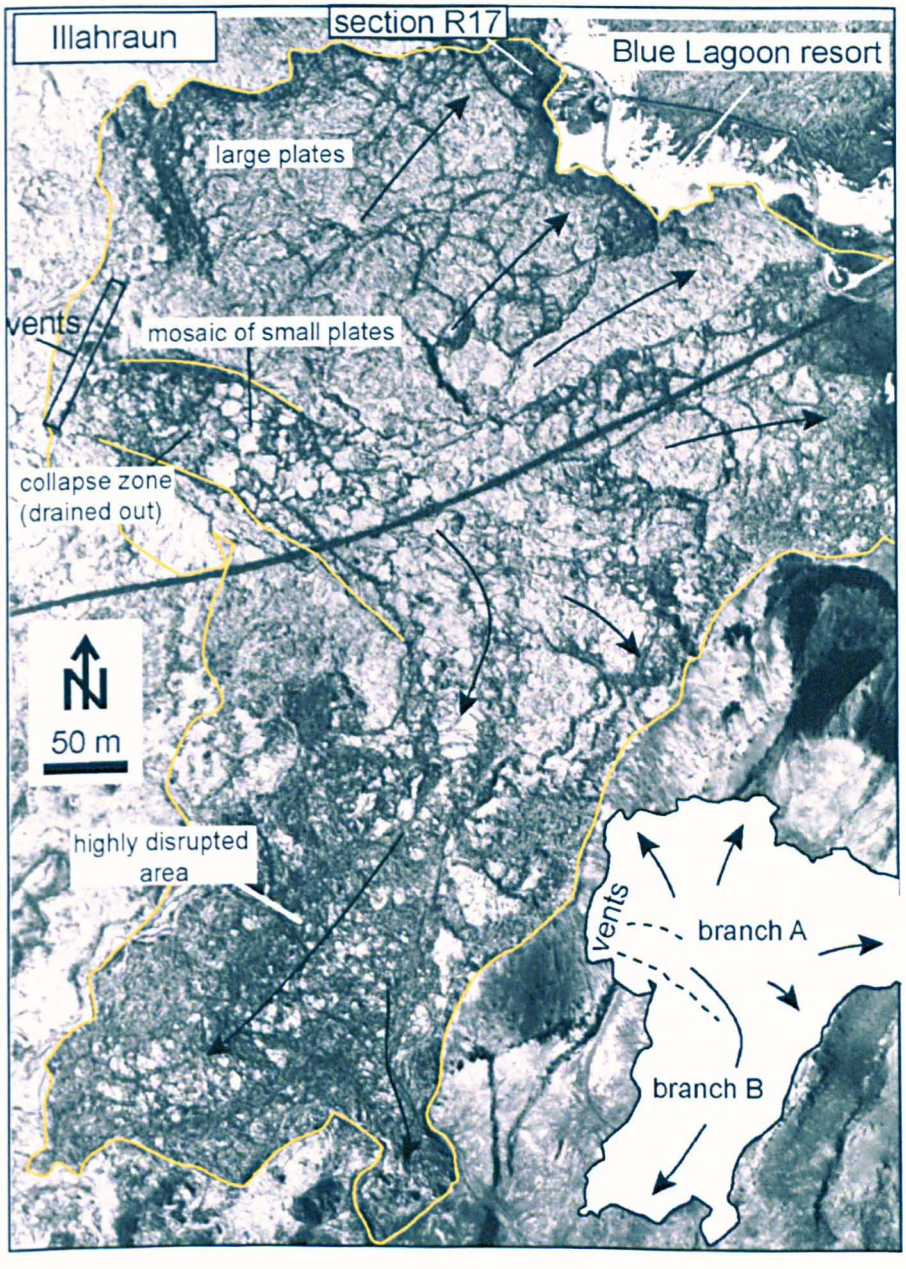

Figure 4.11: Aerial photograph of Illahraun flow-field. Map on lower right locates two different lava branches described in text. Dashes on schematic map (lower right) locate collapsed area proximal to vents described in text. Note platy surface morphology of flows, especially in proximal area (branch A). Black arrows show main flow direction inferred from alignment of plates in branch A and curvature of surface ridges in branch B.

4.3.4 Columbia River Basalts (CRB)

The CRB range in age from 6–17 Ma but the bulk were erupted in 15–14 Ma, the remnants now covering ~164,000 km^2. The main plateau area of the Columbia River Basalt Group is composed of numerous 1,000–3,000 km^3 lava units (Tolan et al., 1989) that mainly consist of large sheet lobes (Thordarson & Self, 1996, 1998; Self et al., 1997). The interiors of the flows are exposed at different places in deep fluvially carved canyons. They are exceptionally well preserved, which is important for completing an investigation of the physical and chemical characteristics of the flows.

Field investigation of these sections reveals that at a number of places in the stratigraphy the lava surface is formed by a thick layer of rubble made of fragments of pāhoehoe crust. Rubbly pāhoehoe lavas are mainly observed in the Grande Ronde Formation (GR) that forms ~87 % of the total volume of the province (Tolan et al., 1989, Riedel et al., 1989). The Grande Ronde lavas formed during the most productive period of volcanic activity of the province, which makes the understanding of the mode of emplacement of rubbly pahoehoe lavas important for interpreting volcanological processes during this major flood basalt eruption.

Where rubbly tops occur, they are laterally persistent and can be, in some places, followed for several kilometres along the roads. They are present at the surface of thin lobes that are a few m thick on thick sheet lobes up to 50 m thick, without any apparent systematic variation with the thickness of the flows. However, very thick rubbly tops (> 5 m) are only present on top of the thickest lava lobes (> 30 m). Most of the lobes with rubbly tops display a smooth pāhoehoe-like, rubble-free base. Pictured in Fig. 4.12, the rubble consists on partly weathered, contorted to angular vesicular fragments ranging from ~10 to 30 vol. % in vesicularity. The rubble often contains fragments of typical vesicular pāhoehoe toes with a stretched skin (Fig. 4.12) while jagged 'a'ā-type clinkers are rare.

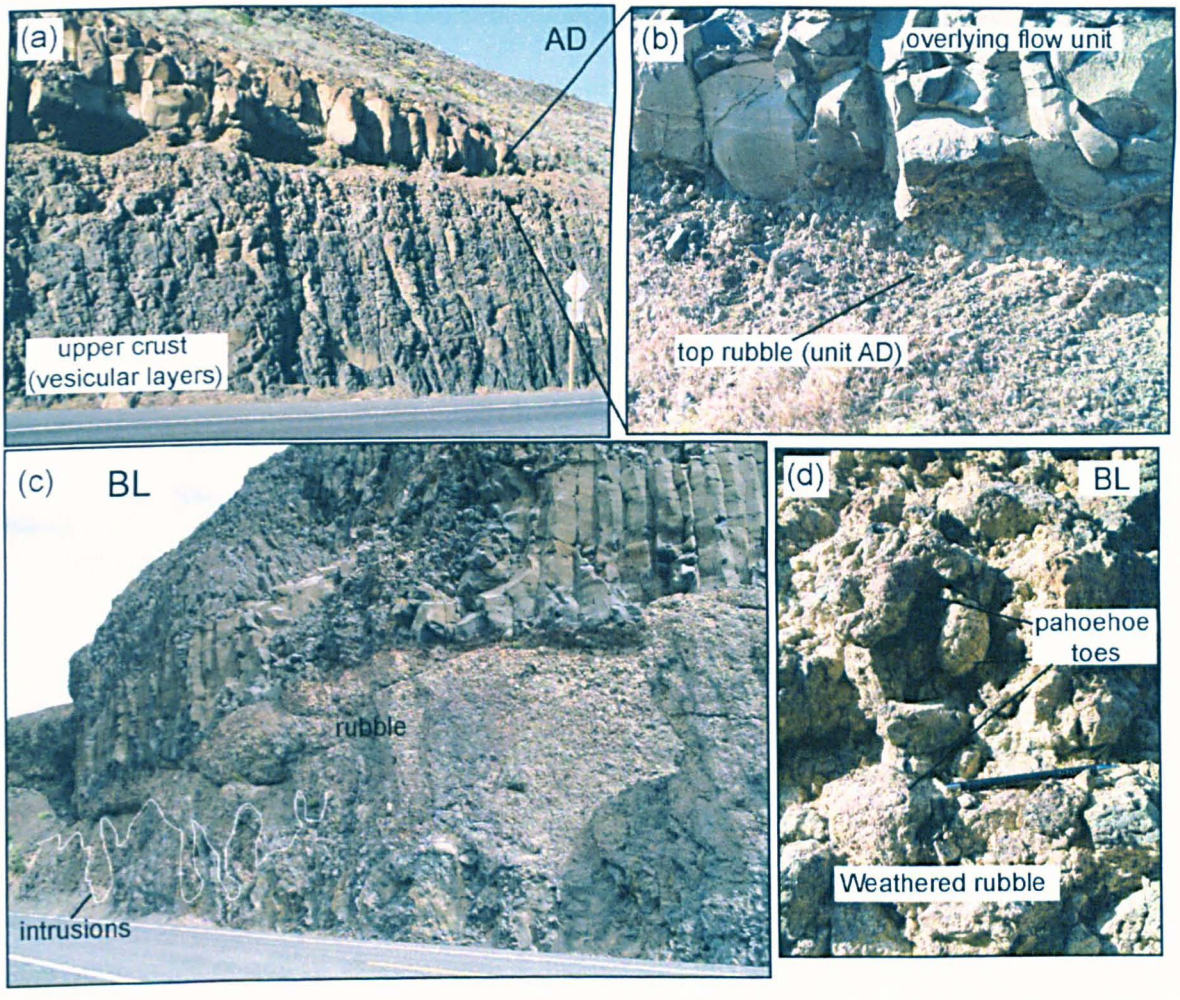

Figure 4.12: Photographs of features seen in sections through rubbly flows from the Grande Ronde Formation. (a) Section AD: upper crustal part of flow exposed along road. (b) Close view on surface rubble on same flow unit shown in (a); (c) Section BL: view of thick upper rubbly part of flow with few-m-high finger-like protrusions of coherent lava into rubble (outlined on lower left of photograph). Note irregular outline of protrusions; most of them displayed assimilated vesicular rubble with wavy contours.

A detailed study of three sections through rubbly pāhoehoe flows from the GRN2 unit was completed and samples were collected at different levels of their upper parts (AD-Armour Draw, SL-Soap Lake, BL-Banks Lake, Fig. 4.12; graphic logs are shown on Fig. 4.13). The GRN2 unit represents an important magnetostratigraphic sub-unit of the GRB (Swanson et al., 1979). The flow exposed in section AD is formed of a thin 1–2-m-thick top layer of rubble, a very thick vesicular upper crust, and a dense core that is only partly exposed. The rubble is dominated by angular fragments of vesicular lava (sample AD5). The upper crust can be divided into several units with different vesicular patterns as depicted in Fig. 4.13. Sample AD4 was sampled from the base of a thick zone

characterised by abundant gas blisters. Sample AD3 was collected from the base of a thick vesicular zone about 1 m above the upper crust-core boundary. Hackly (irregular) joints possibly related to lava-water interaction (see further along) were observed at one stratigraphic level across the section (see Fig. 4.13). Columnar joints were observed in the upper crust, typically less marked across vesicular zones. These vesicular zones are laterally persistent (one could be followed for over 50 m laterally) and correspond to HVZ (horizontal vesicular zones) as defined in the terminology above (4.3.1). They may represent variations in the hydrostatic pressure maintained in the fluid portion of the slowly-cooling lobes (Thordarson & Self, 1998) or be linked to variations in the rates and amount of gas exsolution triggered by crystallization in the crystal mush trapped along the solidification front (McMillan et al., 1989). The exposed upper part of the core displays a regular jointing pattern forming 2- to 4-m-thick sequences of vertically jointed lava alternating with thinner "platy zones". Thordarson & Self (1998) accurately describe these features as "horizons of closely spaced horizontal platy joints, splitting the lava into 2 to 20-cm-thick and 20 to 200-cm-long plates that show well-developed internal flow banding paralleling the joints". They attribute the formation of this feature to the build-up of mechanical stresses along the upper and lower crustal boundaries as hot fluid lava continues to circulate in the core after the advance of the flow front has stopped. A similar process was invoked by Spry (1961) and other authors referenced in this paper to explain the formation of what they define as the entablature zone.

The two other sections studied have thicker rubbly flow tops (~5 m thick for section BL and ~15 m thick for section SL), and a more simple internal structure with poorly vesicular and not well defined upper crusts overlying dense cores. Large, irregularly shaped sub-vertical fingers of coherent lava form meter-scale protrusions (or intrusions) in the rubbly top. The rubble trapped between large protrusions show wavy blended contours that indicate that it was "cooked" and partially "digested" (or assimilated) by the intruding

hot, still fluid lava. Samples of top rubble (SL8 and BL6), assimilated rubble (SL7 and BL8), and upper crusts (SL6 and BL7) were studied petrographically.

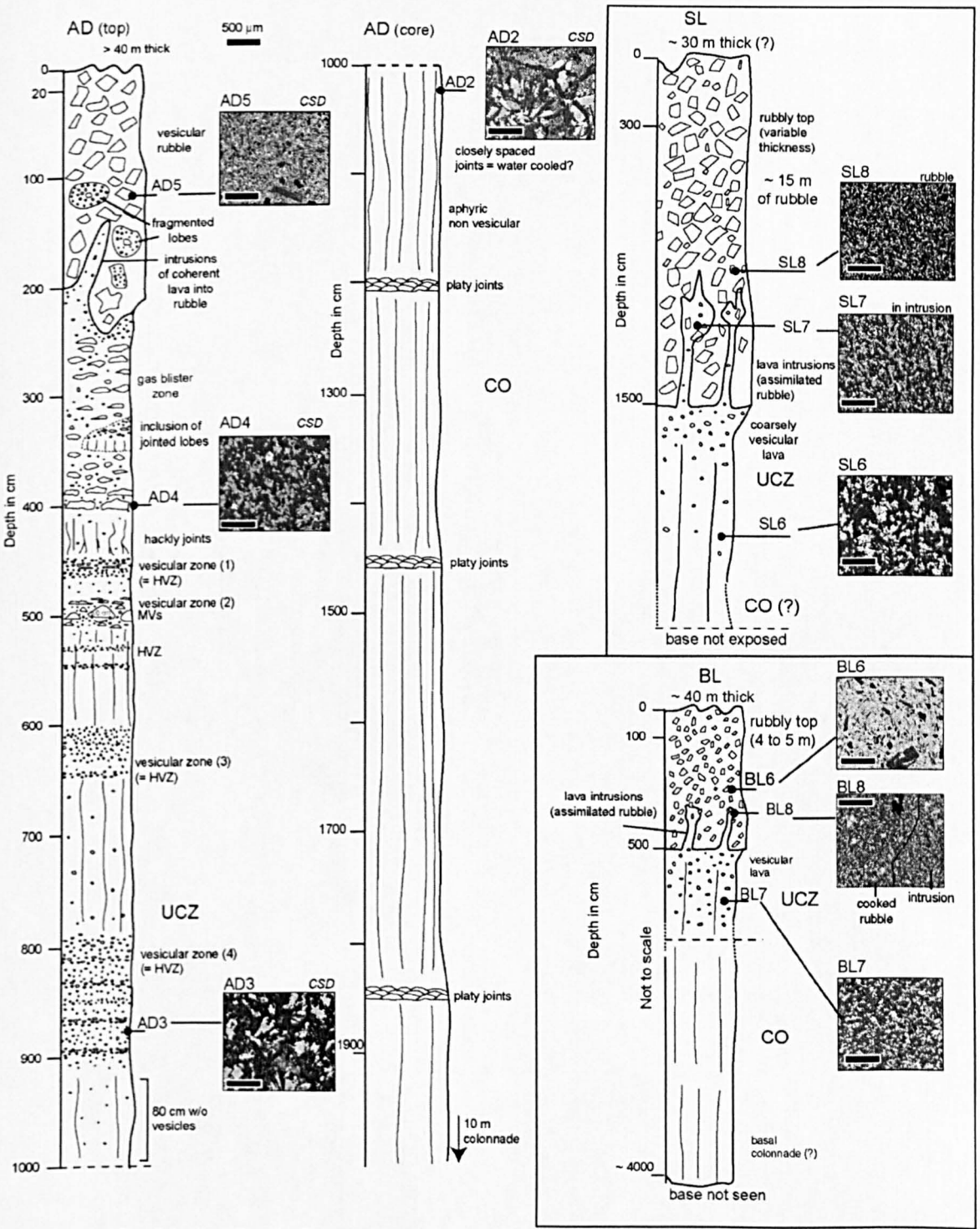

Figure 4.13: Graphic logs of sections AD (GPS N47° 35.059', W119° 41.793'), BL (GPS N47° 43.456', W119° 15.178') and SL studied through major rubbly pāhoehoe flows of the Grande Ronde Formation of the Columbia River Basalts. Note the thick upper crust and small thickness of top rubble of section AD compared to the two other sections. By contrast, sections BL and SL show thick top rubble and poorly-vesicular upper crusts without any clear crust-core transition. Base of sections BL and SL was not exposed. UCZ—upper crustal zone; CO—core; MVs—mega-vesicles; HVZ—horizontal vesicular zones.

4.3.5 Other lavas

Some sections across "strict" pāhoehoe and 'a'ā lava lobes were studied for comparison. Pictures of the sections are shown on Fig. 4.14 and the derived graphic logs on Fig. 4.15. The pāhoehoe section was observed from a sea cliff exposure through the distal part of the 1990 Kalapana lava flow-field on Kilauea (see Mattox et al., 1993). Note the high vesicle content of the upper crust and the large inwards increase in crystal sizes. The 'a'ā cross-sections were observed from the products of the 1907 eruption of Mauna Loa (samples amiably collected by L. Keszthelyi) and the 2001 eruption of Mt Etna. These sections are characterised by low vesicular contents and limited internal textural variations. The top and basal rubble consists of jagged lava fragments that were torn apart from viscous lava at the flow top during emplacement and partly incorporated into the lava interior (core).

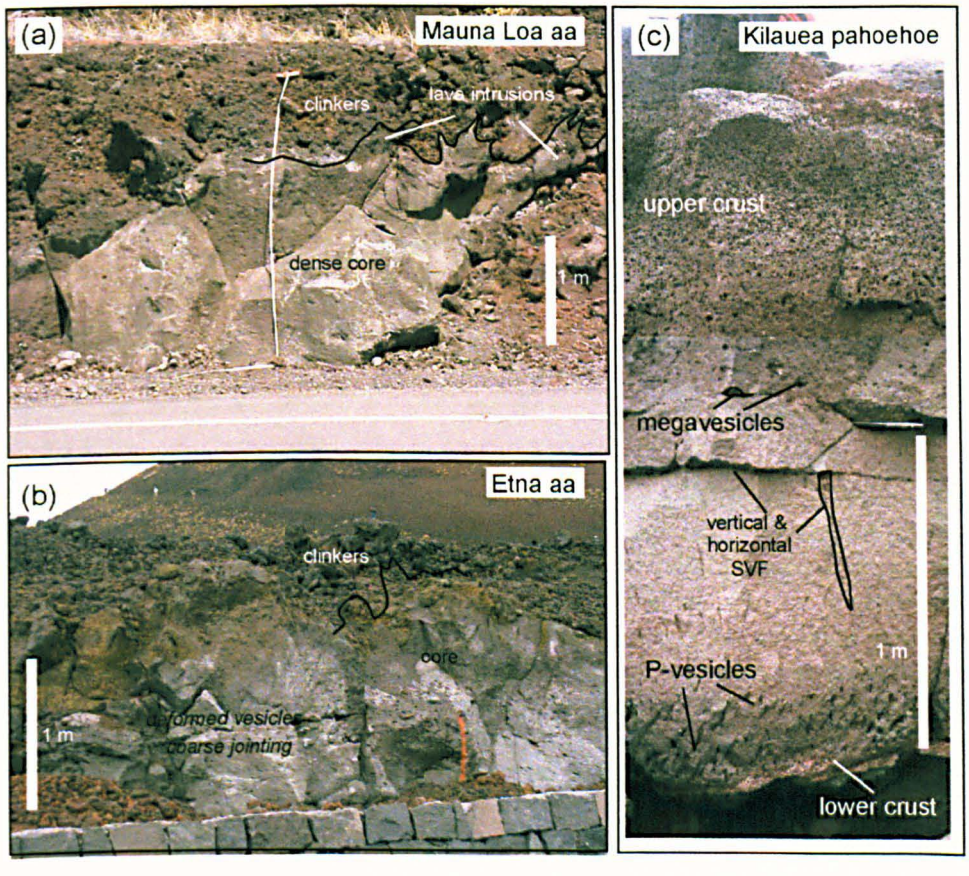

Figure 4.14: Field photographs of sections investigated for comparison with rubbly lavas. (a) Section through 'a'ā flow from 1907 eruption of Mauna Loa (referred to as ML in text and graphic log, GPS N19° 04'22.2'', W155° 44'28.3''). (b) Section through ~1.8 m-thick 'a'ā flow from 2001 eruption of Etna, collected along road at Sapienza, about 1 km from vent (referred to as ETNA, GPS 33S 0500275, UTM 417 2460). (c) Typical pāhoehoe lobe sampled from Kalapana lava flow-field (samples K02). Note different vesicular and jointing patterns across both lava types.

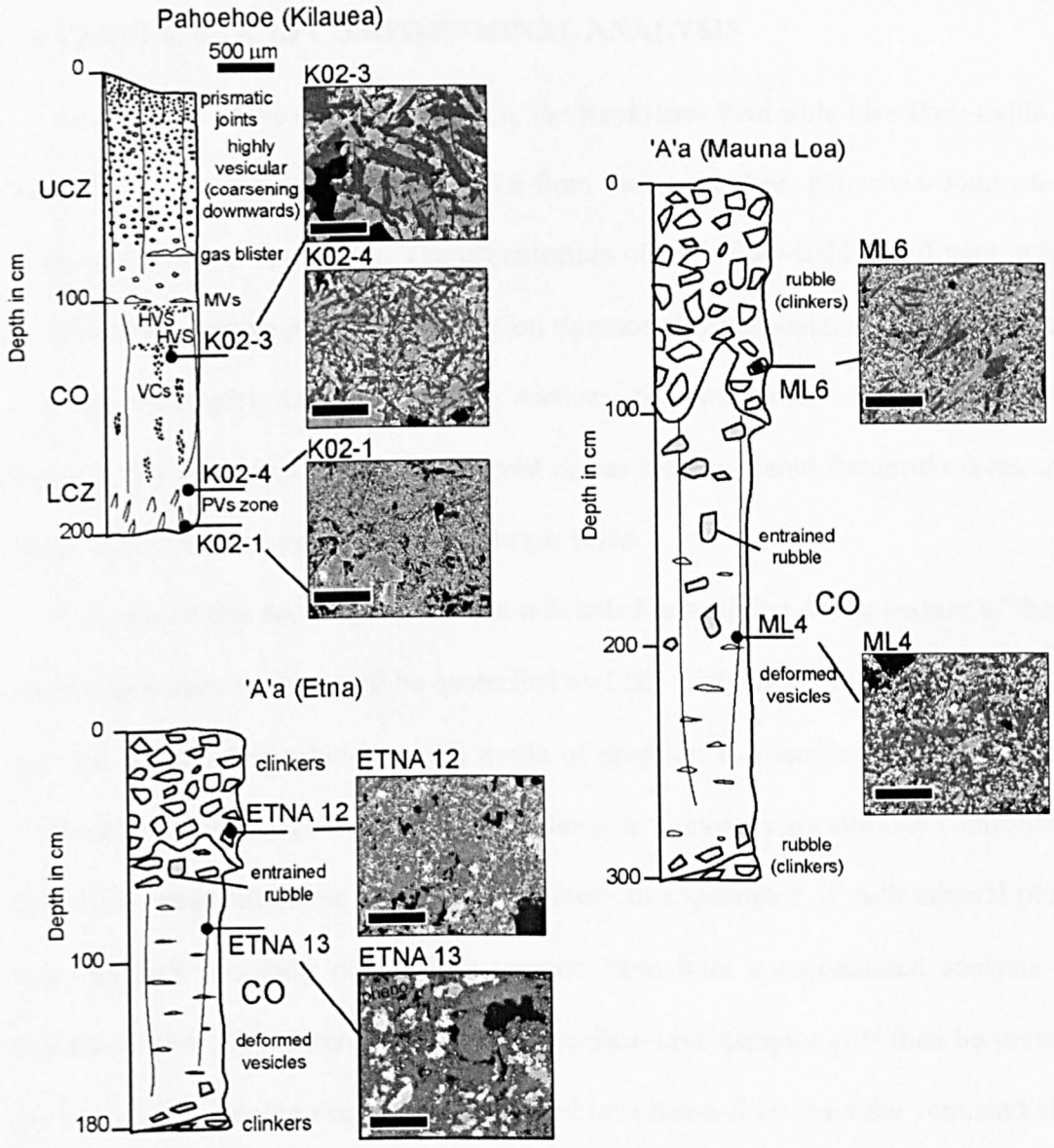

Figure 4.15: Graphic logs of sections pictured in Fig. 4.14, with representative BSE images. Sections through 'a'ā lava do not display the crust-core separation typical of sections through pāhoehoe lava. Thickness of rubble at base of 'a'ā sections is variable and not drawn to scale. Note sparse elongated plagioclases at quenched base of K02 and large inwards increase in crystal size despite small thickness of lobe (short emplacement time). Samples collected across section ML show limited increase in crystal size. As is common in Etnean lavas, lava in section sampled shows large amounts of plagioclase phenocrysts, and some limited increase in crystal size in core compared to surface. UCZ—upper crustal zone; LCZ—lower crustal zone; CO—core; MVs—mega-vesicles; PVs—pipe-vesicles; HVS—horizontal vesicular sheets; VCs—vesicle cylinders.

4.4 TEXTURAL AND COMPOSITIONAL ANALYSIS

In summary of the above description, the Reykjanes Peninsula lava flow-fields studied show surface morphologies which range from near-vent sheet pāhoehoe-dominated lavas to channelized 'a'ā down-flow. The organization of each flow-field is different, which can be related to eruptive parameters (eruption duration, lava production rates) and to the pre-existing topography. Observed only in sections, the Grande Ronde rubbly flows display features that are similar to those observed across the Reykjanes Peninsula lavas and Laki lavas, although these occur on a much larger scale.

The aim of this section is to present a detailed description of the texture of the lava in the sections above, which will be quantified by CSD analysis in the following section. This will be examined in relation to the mode of eruption and emplacement of the flows as inferred from their surface morphologies. Since lava textures are strongly controlled by the lava bulk composition that determines the order of appearance of each mineral phase, and also the bulk viscosity of the lava, results from bulk compositional analysis will be described first. The texture of tephra and surface lava samples will then be presented as those are related to the evolution of the fluid lava down-flow from the vent, and allow the mode of formation of microlites in the lava to be inferred. Finally, the internal textural variations across the lavas in section will be described. The last part of this chapter will focus on the theory, method and results of the CSD analysis.

4.4.1 Bulk composition

The bulk chemistry of the lavas can account for some textural differences as it controls the viscosity, phase relations, and liquidus temperature of the melt. Core samples from some of the Laki and Reykjanes Peninsula lava sections studied for CSD were analysed for bulk major and trace element composition using X-ray fluorescence spectroscopy (XRF) (see Chapter 3 for operating conditions). Results are presented in Table 4.1 and plots of some major elements on Fig. 4.16. The data shown for Grande Ronde lava samples was

collected at Washington State University GeoAnalytical Laboratory (see Hooper et al., 1993). The data were recalculated in terms of plagioclase, clinopyroxene, and olivine components following Grove et al. (1992) and plotted in a pseudo-ternary diagram (Fig. 4.17). Bulk viscosity, liquidus temperatures and phase relations were estimated for anhydrous and surface conditions using the PELE model (Boudreau, 1999; see details in Fig. 4.18). Schiffman & Lofgren (1982) present phase equilibria determined experimentally using a sample of Grande Ronde lava with nearly identical composition to those reported here (see Fig. 4.18). Their results are very similar to those given by the PELE model and presented below.

The Grande Ronde lavas studied are silica-rich (SiO_2 ~54 wt.%) basaltic andesites with relatively low MgO, FeO, CaO and Al_2O_3 content (Fig. 4.16). Laki lavas have ~50 wt.% SiO_2 and Reykjanes Peninsula lavas (R15 and R19) are the least SiO_2 rich (~48–49 wt.%) and the most MgO, CaO and Al_2O_3 rich. Note that Reykjanes Peninsula lavas have MgO contents similar to Hawaiian tholeiites, accounting for the common presence of olivine phenocrysts in these lavas.

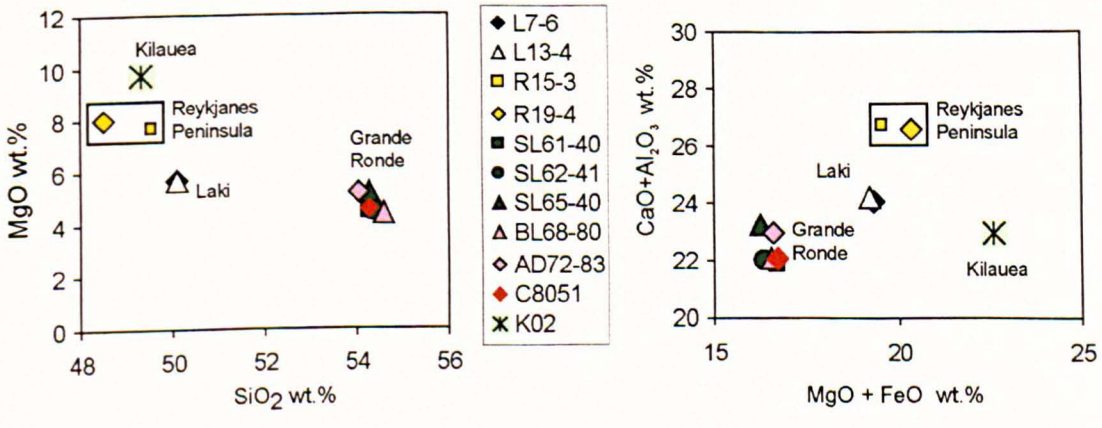

Figure 4.16: Major element plots of bulk composition of Laki lava (L13, L7), Grande Ronde lava (AD, SL, AD) and Reykjanes Peninsula lava (RP: R15, R19). C8051: starting composition of cooling experiments conducted by Schiffman & Lofgren (1982) on Grande Ronde lava. Kilauea: bulk composition of lava sampled across Kalapana lobe shown in Fig. 4.14 and 4.15.

The higher SiO_2 content of Grande Ronde lavas accounts for their higher bulk viscosity (see Table 4.1). Differences in other elements affect the crystallization sequence of the lavas. Grande Ronde lavas are comparatively richer in the plagioclase component as calculated using the scheme defined by Grove et al. (1992) than the other lavas (Fig. 4.17). For all lavas plagioclase is the first phase on liquidus, when calculated using the PELE model, followed closely by clinopyroxene and olivine (Fig. 4.18). Reykjanes Peninsula lavas have significantly higher liquidus temperatures than Laki and Grande Ronde lavas. Grande Ronde lavas crystallize at ~1130°C, and therefore reach solidification temperature (~1050°C, Schiffman & Lofgren, 1982) after only 40% crystallization instead of 60% for the other lavas. In accord with their relatively lower MgO content, they crystallize higher mass proportions of plagioclase over clinopyroxene (2.5–3 instead of 2–2.5 for the other lavas).

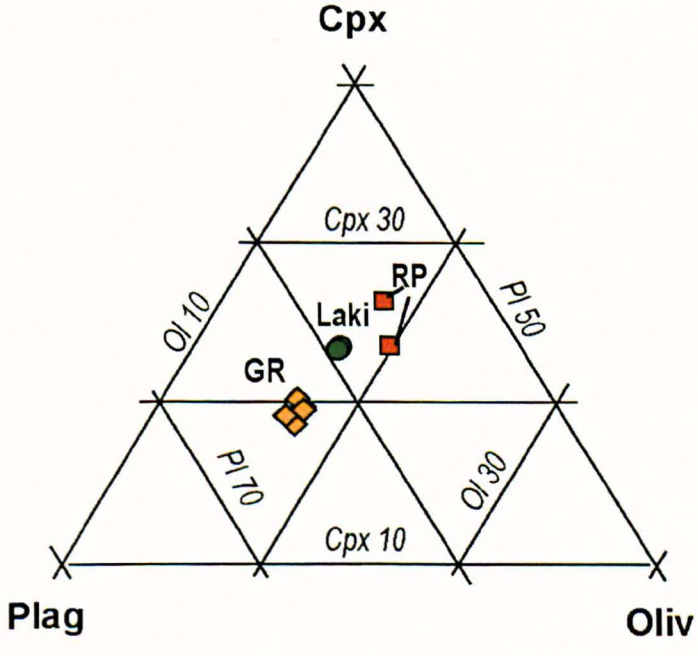

Figure 4.17: Projection of whole-rock compositional data in scheme developed by Grove et al. (1992) as a function of plagioclase (Plag), olivine (Oliv), and clinopyroxene (Cpx) components. RP—Reykjanes Peninsula (in red); GR—Grande Ronde (in orange); Laki in green.

Table 4.2: Whole-rock compositions analysed using XRF.

Location	Laki	Laki	RP	RP	GR	GR	GR	GR	GR
wt. %	L7-6	L13-4A	R15-3	R19-4	AD72-83	SL61-40	SL62-41	SL65-40	BL68-80
Normalized Results (Weight %):									
SiO_2	50.11	50.11	49.54	48.49	54.03	54.27	54.37	54.29	54.59
TiO_2	2.80	2.76	1.51	1.86	1.78	2.10	2.10	1.76	1.99
Al_2O_3	13.71	13.82	14.45	14.75	14.11	13.59	13.68	14.16	13.70
FeO	13.64	13.55	11.90	12.36	11.38	12.28	11.89	11.08	12.11
MnO	0.23	0.23	0.21	0.21	0.204	0.21	0.22	0.20	0.21
MgO	5.72	5.71	7.66	7.99	5.21	4.44	4.46	5.20	4.42
CaO	10.35	10.41	12.28	11.83	8.85	8.25	8.31	9.08	8.37
Na_2O	2.72	2.70	2.12	2.12	2.98	3.16	3.24	2.89	2.88
K_2O	0.43	0.43	0.18	0.22	1.16	1.24	1.27	1.09	1.41
P_2O_5	0.30	0.30	0.14	0.18	0.31	0.46	0.46	0.26	0.32
Trace elements in ppm (detection limits in brackets)									
Rb (2)	7	8	4	4					
Sr (2)	235	237	158	197					
Y (2.0)	40.6	39.4	24.9	26.2					
Zr (2)	187	184	76	92					
Nb (1.5)	18.9	17.0	8.6	10.4					
Ba (12)	106	106	62	79					
Pb (5)	4	2	0	0					
Th (4)	2	1	0	1					
U (3)	0	2	0	0					
Sc (5)	38	40	43	38					
V (5)	385	381	341	345					
Cr (4)	59	61	131	255					
Co (2)	36	40	42	47					
Ni (3)	40	37	79	109					
Cu (4)	105	104	167	164					
Zn (3)	128	121	90	91					
Ga (3)	20	24	18	17					
Mo (2)	0	0	0	0					
As (5)	1	5	2	0					
S (50)	98	86	56	41					
η (Pa.s)	44		20	17	230				
T Plag liquidus	1166	1161	1195	1190	1133	1130	1133	1135	1150
T Cpx liquidus	1145	1146	1185	1175	1132	1125	1129	1130	1145
T Oliv liquidus	1145	1146	1185	1185	1129	1130	1124	1126	1145
Projection Scheme - Grove et al. (1992)									
Cpx	23.4	23.3	26.4	23.6	19.6	18.8	19.2	20.3	19.5
Plag	59.2	59.4	55.5	56.5	62.9	63.8	64.1	62.9	62.9
Oliv	17.5	17.4	18.1	19.9	17.4	17.5	16.7	16.8	17.5

Bulk viscosities (η) were estimated at liquidus temperatures using the PELE model (based on Shaw, 1972). Liquidus temperatures for each major mineral phase are results from fractional crystallization calculations performed using PELE model (see text, results plotted in Fig. 4.18). Plagioclase-clinopyroxene-olivine components were calculated following Grove et al. (1992) and normalized to 100%. T—temperature (°C), Plag—plagioclase, Cpx—clinopyroxene, Oliv—olivine. RP—Reykjanes Peninsula; GR—Grande Ronde.

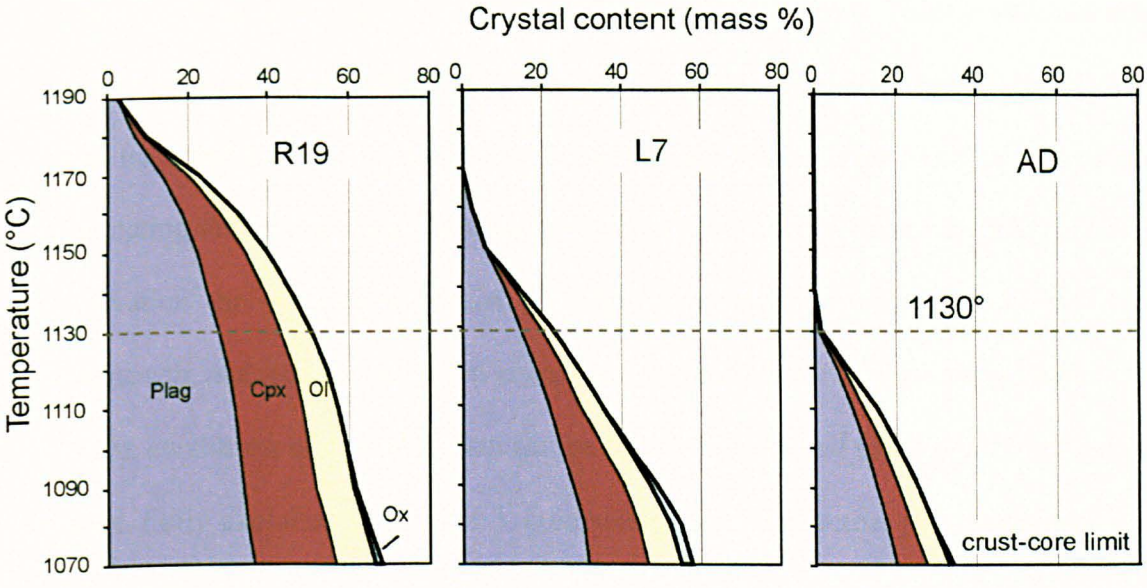

Figure 4.18: Crystallization sequence of different lava types calculated using PELE model. Results are similar for R19 and R15, and L13 and L7. Oxygen buffer is QFM (Quartz-Fayalite-Magnetite), as estimated in Chapter 3 for Laki magma and generally considered for Reykjanes Peninsula lavas (i.e., Jakobsson, 1978) and Grande Ronde lavas (Schiffman & Lofgren, 1982). Crust-core limit corresponds to 1070°C isotherm (see text). Plag—plagioclase, Cpx —clinopyroxene, Ol—olivine, Ox—Fe-oxides.

4.4.2 Crystallization during transport

The texture of lava preserved at any location down-flow is dependent on its history before solidification. In particular, the location and timing of formation of microlites (defined as anhedral crystals < 20 μm in size) will determine their abundance in the lava, which will affect the resulting texture and determine the rheology during flow. Thin-sections of spatter, near-vent lava, and distal lava surface samples from the Reykjanes Peninsula lava flow-fields were examined to constrain the evolution of the groundmass crystallinity of the lava during transport. Fig. 4.19 presents microphotographs of the textures for samples from Hussfellsbruni (H149 lava field) and Kappelluhraun (the same general pattern was found for Obrysnnishólahraun and Illahraun). The textural variations between the samples appear similar to those for Laki lavas, as presented in detail in Chapter 3. Microlites are absent in the spatter and thus formed in the lava flows, near the vent, as shown by their abundance in proximal lavas (Fig. 4.19). They seem to increase in

number with distance from the vent in the Kappelluhraun flows. Their maximum eruptive temperature can be constrained at 1170°C for Reykjanes Peninsula lavas, 1140°C for Laki lavas (see also Chapter 3), and 1130°C for Grande Ronde lavas. This is constrained by considering the temperature-phase relationships defined above using the PELE model, the observation that microlites consist of plagioclase, clinopyroxene and olivine often in intergrowth, and thus that the lavas crystallized at the cotectic of these three phases.

The conditions of crystallization can be further constrained using crystal compositional ranges. Fully exploited in Chapter 3, compositional zoning across plagioclase phenocrysts (defined as euhedral crystals > 100 μm) can record rapid changes in melt-dissolved water content during crystallization that can be related to degassing during magma ascent. Compositional data were collected for Kappelluhraun and Obrysnnishólahraun lava samples that contain plagioclase phenocrysts (Fig. 4.20, data reported in Appendix C). These show a primitive core and an evolved rim compositionally similar to microphenocrysts (subhedral, 20–100 μm) and microlites, thus suggesting, in comparison with Laki lavas (Chapter 3), that the primitive core of plagioclase phenocrysts was formed at depth in a water-undersaturated magma, whereas the phenocryst rims, microphenocrysts and microlites formed after water exsolution, near the surface.

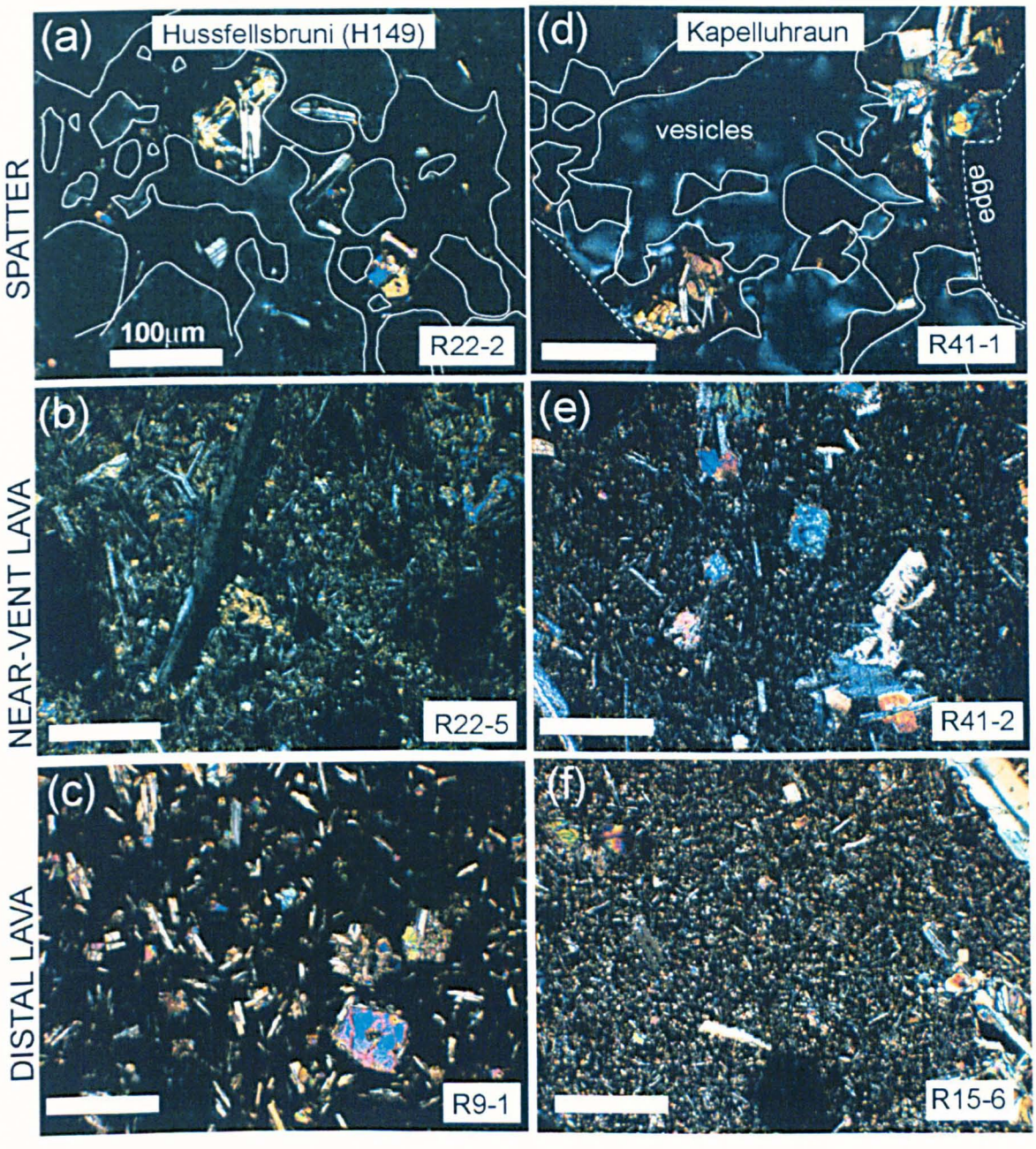

Figure 4.19: Cross-polarized photomicrographs of spatter and surface lava textures from Hussfellsbruni (H149) and Kapelluhraun lava fields. All pictures are at scale 2.8 × 2.1 mm (scale bar on pictures is 100 µm wide). Samples are located on aerial photographs on Figs. 4.9 and 4.10. Crystal phases seen on photographs are plagioclase (white-grey), olivine (yellow-blue), and clinopyroxene (small blue-red granular crystals in groundmass). Vesicles are outlined in white on pictures of spatter samples (a and d). Note large abundance of groundmass crystals in surface lava samples compared to spatter samples and marked increase in number density of groundmass crystals along Kapelluhraun flow (difference between samples R41-2 and R15-6).

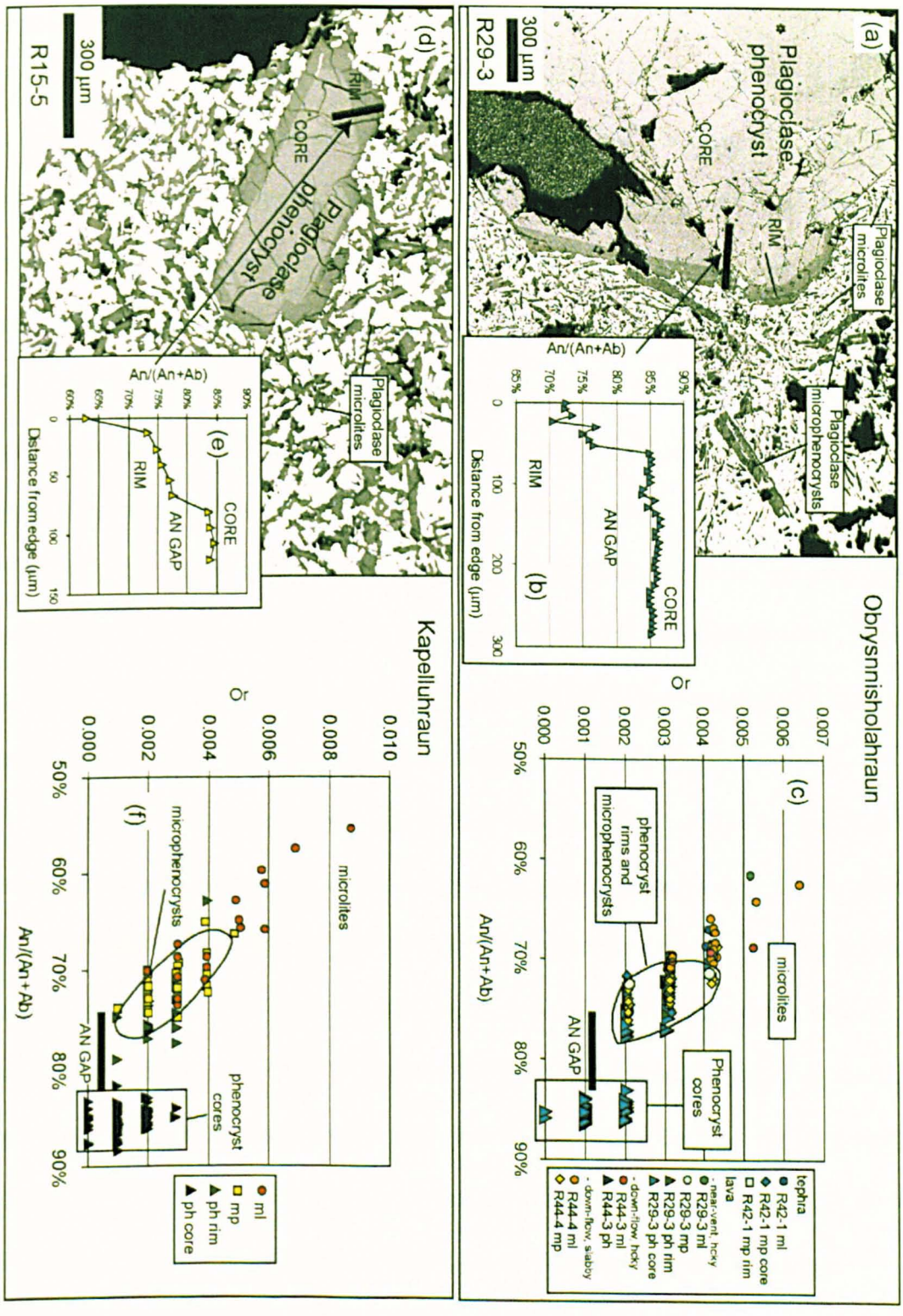

Figure 4.20: Plagioclase compositions in lava samples from Obrysnnishólahraun (a to c) and Kappelluhraun (d to f). Sample analysed for Kapelluhraun are R15-3, R15-4, R15-5 and R15-6 (see Fig. 4.6). Samples analysed for Obrysnnishólahraun are located on Fig. 4.10. Figure present high-contrast backscatter images of plagioclase phenocrysts and groundmass. Variations in colour on the images (a and d) correspond to changes in An content of the plagioclases as shown by microprobe compositional profiles (b and e). Compositional ranges of each crystal type is shown on plot of Or (K/(Ca+Na+K)) against An/(An+Ab) (=Ca/(Ca+Na)) (c and f). ph—phenocryst, mp—microphenocrysts, ml—microlites. Note similar colour and thus An content of phenocryst rims and groundmass crystals.

4.4.3 Lava textural variations in cross-section

Lava groundmass textures show systematic variations through the cross-sections of flow lobes studied and presented here. Textural differences between pāhoehoe, 'a'ā and rubbly pāhoehoe will be stressed. The modal data presented are reported on Table 4.3 (see Appendix A for method and all the raw data on Appendix B). Samples for which textural parameters were quantified are: 1) samples from each structural unit for sections L7 and R15; 2) samples from the top surface, upper crust and core for sections AD and R19; 3) samples from surface and core for sections R17 and L13; 4) glassy sample from basal pāhoehoe toes at section R10 (R10-9) for comparison purposes.

Lava textures follow a similar pattern across the sections. From the margins (top and base of sections) to the core there is an increase in 1) mineral phase proportions, 2) crystal sizes, 3) degree of differentiation of crystal rims, and 4) degree of connectivity and mutual intergrowth between crystals. Each of these characteristics is detailed below.

1) The proportion of microlites, microphenocrysts, and phenocrysts has been quantified for samples through section L7 (Laki) and plotted against depth on Fig. 4.21 with modal proportions estimated by BSE image analysis. Both define a general pattern of sharply increasing proportions near the lobe margins and a rather uniform profile through lava crust and core. There is no sign of crystal settling. The distinctly higher proportion of phenocrysts in the crust and core suggests the injection of a more phenocryst-rich lava batch in the lobe interior after the margins had solidified. Microlites amount to > 60 vol.% of the total crystallinity and are the only crystal type considered in the following.

The modal data for all sections studied is plotted in Fig. 4.22. Plagioclase forms > 50 vol.% of the groundmass phases (Fig. 4.22a), with ~30 vol.% clinopyroxene and < 5 vol.% olivine (Table 4.3). Core and crust samples cluster at 60–80 vol.% total groundmass crystallinity while surface samples have 10–35 vol. % crystals. Plagioclase modal % is plotted against sample depth for all sections in Fig. 4.22c. There is a sharp increase in

plagioclase content at the margins (over ~1 m), with a uniform profile through the crust and core of the lobes (~40 vol.%). The plagioclase/clinopyroxene ratio is significantly higher for samples from AD section compared to the others (Fig. 4.22d), which is consistent with their bulk composition and phase relations as described above. Through the other sections this ratio increases with depth in the upper 1 m (upper crust) and then decreases inwards.

2) The increase in crystal size, for plagioclases in particular, is obvious from the observation of the BSE images. Plagioclase crystal width/length is ~1/3 and both crystal width and length increase from surface to core (Fig. 4.22b). There are noticeable differences between sections. For instance, the largest crystal size increase seems to be across the 1.4-m-thick Kalapana pāhoehoe lobe (Fig. 4.15). The Reykjanes Peninsula 'a'ā sections show, in comparison, little internal variation in plagioclase crystal size (e.g., R10-1, R10-2, Fig. 4.6). The number of crystals visibly increases across the section through the Mauna Loa 'a'ā section while the size of individual crystals remains ~constant (Fig. 4.15). The Etnean 'a'ā lobe shows limited internal coarsening (Fig. 4.15). Sections through rubbly flows show, unsurprisingly, variations that are intermediate between these two end-members, which will be quantified by CSD analysis below.

3) As observed in BSE images of internal samples, crystal rim zoning shows as pale borders around clinopyroxenes and olivines, and dark irregular borders around plagioclases. Microprobe analysis of microlites was done for L7 samples using the same operating conditions as presented in Chapter 3. This revealed a general inwards increase in the degree of differentiation of microlites (i.e., decrease in Fo in olivines, An/(An+Ab) in plagioclases, and Wo/(En+Fs) for clinopyroxenes), with a sharp gradient at the margins (Fig. 4.23). This trend was also found in samples from other sections (e.g. plagioclases are An_{65-70} in surface sample R19-1 compared to An_{50-75} in core sample R19-4). No significant

variations in the concentration of minor elements in the crystals such as Fe in plagioclase, Ca in olivine and Ti in clinopyroxene were found.

4) In lava selvages, crystals are usually detached and have clear, flat faces, and relatively large number densities and elongated shape. In contrast, in the crust and the core, crystals are significantly larger and form a dense touching and interconnected network of generally more equant crystals. They have rims with irregular outlines (wavy, rounded) that tend to fill the interstices between neighbouring crystals. As for differences between sections, plagioclases have distinctly high aspect ratios in selvages of well-defined pāhoehoe lobes (K02-1, R10-9, and to a lesser extent in R9-3). They form radiating clusters intergrown with clinopyroxene in the internal samples from these same sections (K02-3, K02-4, R10-11, R10-8, see also AD3, AD2). Crystals in rubbly pāhoehoe and 'a'ā lavas display more blocky shapes.

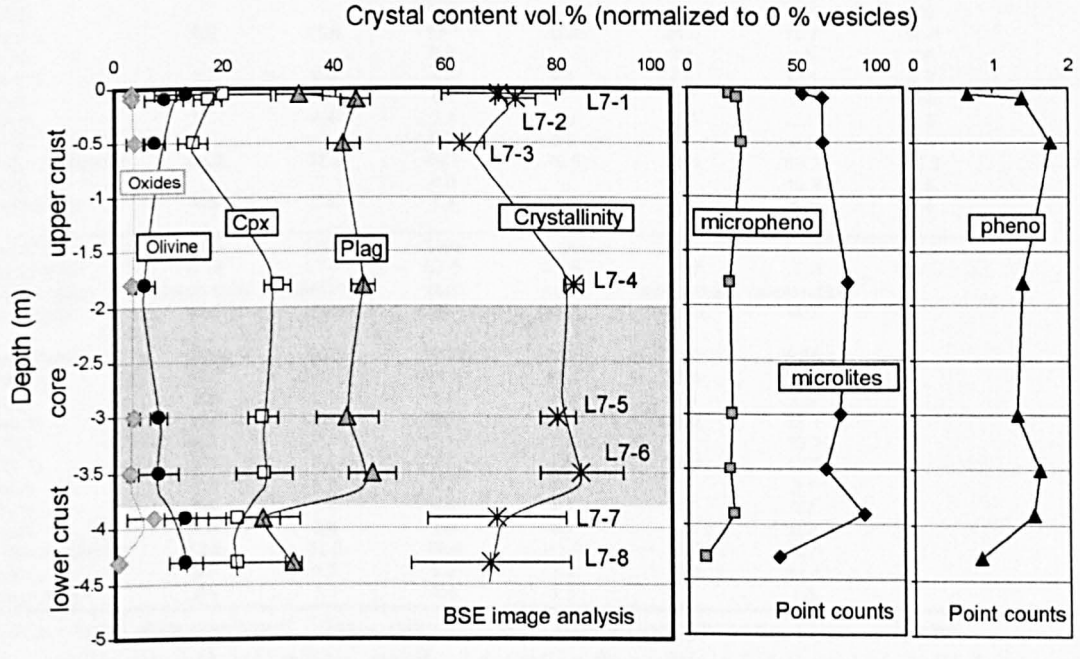

Figure 4.21: Variations in crystal type proportions (point counts) and groundmass mineral phases (backscatter image analysis) through cross-section L7 of Laki lava (see location of samples on Fig. 4.3). Note that phenocrysts are not considered for backscatter image analysis, and that the large standard variations in data collected results from the irregular distribution of microphenocrysts (especially clinopyroxene) in the groundmass. The surface sample studied (L7-1) was not glassy (i.e., crypto-crystalline) and lava crystallinity at quenching stage is likely to have been 30–35 vol.% instead of ~60 vol.% as reported here. The anomalously low total groundmass crystal content reported for sample L7-3 results from low measured clinopyroxene contents, which is considered to be an artefact of BSE image analysis. The distinctly higher phenocryst content of the lobe interior may reflect change in phenocryst content of lava supplied (see text).

Table 4.3: Textural data collected

Location	RP	RP	RP	RP	RP	RP	RP
Sample no.	R10-9	R15-6	R15-5	R15-4	R15-3	R15-1	R19-1
Sample type	surface	rubble	upper crust	core	lower crust	base rubble	top slab
Depth (m)	0	0	-1	-3.5	-4.4	-4.8	0
Area (mm^2)	1.33	0.77	0.65	1.39	0.67	0.30	0.77
Plag %	10.4	13.8	21.2	39.8	22.4	8.7	28.5
Cpx %	12.8	9.5	6.3	26.6	8.2	2.8	13.8
Oliv %	0.0	2.2	1.9	4.1	3.8	1.0	3.7
Ox %	0.5	0.5	2.1	2.7	2.9	1.2	1.5
Total crystallinity	23.2	26.0	31.5	72.9	37.4	13.7	47.6
Plagio/Cpx	0.8	1.5	3.4	1.5	2.7	3.1	2.1

Location	RP	RP	RP	RP	RP	GR	GR
Sample no.	R19-2	R19-3	R19-4	R17-1	R17-3	AD5	AD4
Sample type	crust	crust	core	top rubble	core	rubble	upper crust
Depth (m)	-1	-3	-5	0	-4.5	0	-2
Area (mm^2)	1.37	1.40	1.42	0.78	1.42	1.40	1.28
Plag %	38.7	44.8	43.8	27.8	43.4	17.9	46.6
Cpx %	13.4	20.1	27.8	18.7	36.5	3.5	12.2
Oliv %	4.0	3.0	4.2	0.0	0.0	2.7	1.2
Ox %	3.0	3.0	2.6	4.8	5.5	0.0	0.0
Total crystallinity	59.1	75.8	78.4	51.3	85.4	17.7	60.0
Plagio/Cpx	2.9	2.2	1.6	1.5	1.2	5.2	3.8

Location	GR	GR	Laki	Laki	Laki	Laki	Laki
Sample no.	AD3	AD2	L13-1	L13-3	L13-4	L7-1	L7-2
Sample type	upper crust	core	top rubble	upper crust	core	rubble	upper crust
Depth (m)	-5	-12	0	-1.8	-2.1	0	-0.3
Area (mm^2)	1.37	2.39	8.26	1.07	5.2	15.87	9.69
Plag %	42.7	40.6	23.6	47.4	43.0	33.3	43.4
stdev			2.2		5.3	4.2	2.6
Cpx %	8.9	16.8	17.1	22.8	24.9	19.7	16.8
stdev			3.0		3.5	8.5	2.6
Oliv %	2.7	0.0	7.2	5.1	7.5	13.1	8.9
stdev			1.1		3.7	5.9	3.4
Ox %	5.0	4.4	2.1	4.2	2.7	3.1	3.2
stdev			0.3	0.3	0.3	0.9	0.4
Total crystallinity	54.9	61.8	49.9	79.5	78.1	69.2	72.3
stdev			4.8			10.3	3.6
Plagio/Cpx	4.8	2.4	1.4	2.1	1.7	1.7	2.6

Location	Laki	Laki	Laki	Laki	Laki	Laki
Sample no.	L7-3	L7-4	L7-5	L7-6	L7-7	L7-8
Sample type	upper crust	upper crust	core	core	lower crust	basal rubble
Depth (m)	-0.5	-1.8	-3	-3.5	-3.75	-4.3
Area (mm^2)	13.13	5.13	11.37	7.67	7.00	6.56
Plag %	41.2	44.7	41.8	44.0	28.4	32.0
stdev	2.8	2.1	5.6	5.2	5.3	1.6
Cpx %	14.1	29.3	26.6	26.7	22.2	22.1
stdev	2.6	2.3	5.1	2.7	8.2	10.2
Oliv %	7.2	5.5	7.8	7.9	13.8	12.7
stdev	1.8	1.6	1.5	3.6	2.7	3.1
Ox %	3.6	3.0	3.4	2.7	7.7	0.7
stdev	1.4	0.6	1.0	0.7	4.9	0.2
Total crystallinity	62.5	82.5	79.6	81.7	31.5	32.5
stdev	3.9	1.7	3.2	7.4	12.4	14.4
Plagio/Cpx	2.9	1.5	1.6	1.6	1.3	1.5

Area—total area analysed, Plag—plagioclase, Cpx—clinopyroxene, Oliv—olivine, Ox—oxides (in vol. %), stdev—standard deviation for multiple (~10) analyses of L7 and L13.

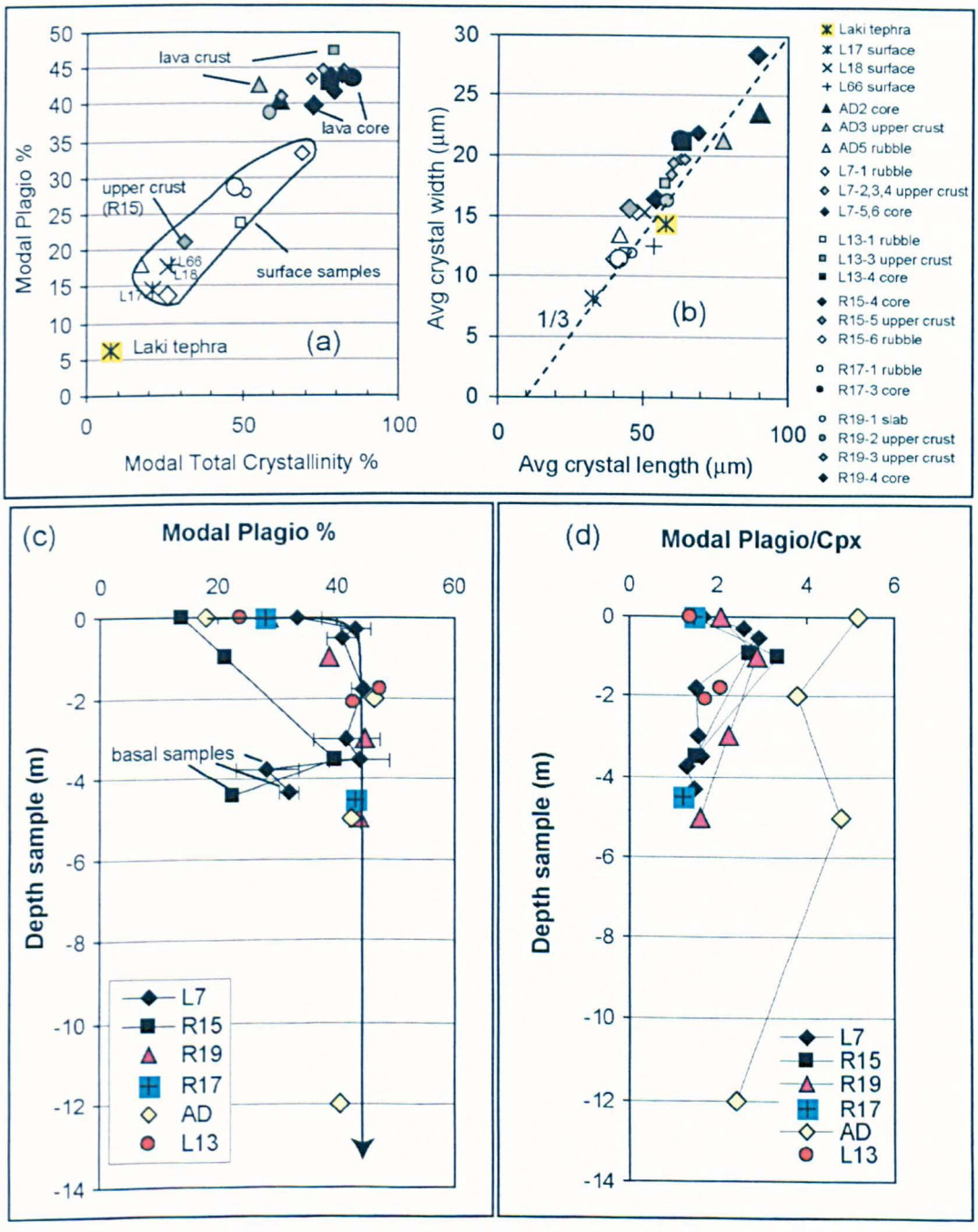

Figure 4.22: General characteristics of plagioclase mode and shape in Laki (L7, L13), Reykanes Peninsula (R15, R17, R19), and Grande Ronde (AD) sections studied (BSE imaging). plagio—plagioclase. In (a) and (b) are reported results for Laki tephra and other surface samples (simple crosses, labelled) presented in Chapter 3. Surface samples are shown in empty symbols, lava upper crust in filled grey and lava core in filled black. Small crystal content of R15 crust sample can be noted. avg—average. (d) Variation of plagioclase mode with depth through sections studied. (c) Variation in plagioclase/clinopyroxene modal proportion with depth.

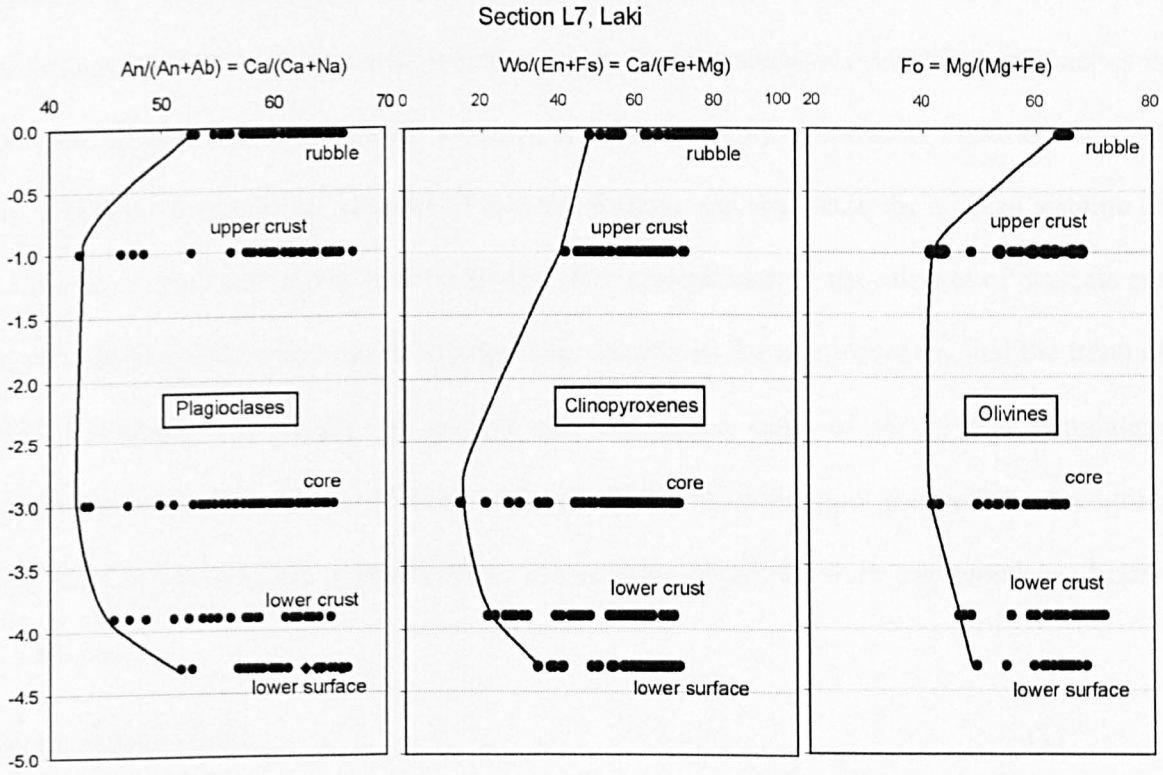

Figure 4.23: Variations in composition of microlites and microphenocrysts rims through section L7. Note increase in differentiation degree in flow interior attributed to overgrowth of evolved rims around crystals. Vertical scale is depth in meters from flow top. Data reported for upper crust combine microprobe data for samples L7-2, L7-3 and L7-4 (location shown in Fig. 4.21).

4.5 CRYSTAL SIZE DISTRIBUTION (CSD) ANALYSIS

4.5.1 Theory

Developed and used for some time in chemical engineering (Randolph & Larson, 1971), CSD analysis aims to give a better understanding of crystallization kinetics using quantitative size and number density data on crystals. Marsh and co-workers (Marsh, 1988; Cashman & Marsh, 1988) were the first to apply it to the study of crystallization kinetics in natural igneous and metamorphic systems. In its simplest form, the theory uses the concept of a balance between the number of crystals formed and their size for a given volume of material crystallized. In the case of steady-state crystallization, the number of crystals per unit volume within a size range will decrease linearly as the size increases, and the trend of this evolution will reflect the growth and nucleation rates of the crystal population averaged over the period of time during which crystallization proceeded. Assuming crystal-size-independent crystallization rates, these relations were expressed by Marsh (1988) as:

$$n = n^\circ \exp(-L/G\tau) \quad (1)$$

or:

$$\ln(n) = \ln(n^\circ) - L/G\tau \quad (2)$$

where L is the crystal size; n is the crystal number density (number of crystals per unit volume per size range); n° is the "theoretical" number density of crystal nuclei (corresponds to n when L approaches zero); and G and τ the respective growth rate and residence time (or growth time) of a dominant crystal size Ld ($Ld = G\tau$) across the crystallization interval (see Cashman & Marsh, 1988; Marsh, 1988).

In practical terms, the function ln(n) versus L is derived from crystal size measurements by 1) calculating a frequency distribution choosing an appropriate size bin (i.e. large enough not to have "gaps" in the distribution); 2) dividing by the total area

studied and applying some correction to obtain a volumetric number density (i.e. number of crystals per a given size range per volume); 3) calculating the cumulative distribution and 4) deriving the numerical derivative of the distribution. The specific method adopted in this study is specified in the following section of the text (4.5.2).

Arising from (2), a plot of ln(n) against L (typically called CSD plot) gives a straight line with a slope of $-1/G\tau$, and an intercept of $n°$. The dominant crystal size Ld can be extracted from the measured CSD plot using:

$$Ld = -1/\text{CSD slope} = G\tau \quad (3)$$

If τ or G is known, the other can be calculated, and the nucleation rate J can then be derived from:

$$J = n°G \quad (4)$$

Thus:

$$n° = J/G \quad (5)$$

Hence, with everything else being constant, the slope of the line in the CSD plot will decrease as a result of 1) extended crystallization time, 2) higher growth rate, or 3) lower nucleation rate. On the other hand, the intercept of the line ($n°$) will increase with increasing nucleation/growth rates (see equation 4), which corresponds to an increase in undercooling (e.g., Shaw, 1965; Cashman & Blundy, 2000).

It is generally considered that any process that alters the balance of the system, such as loss of crystals due to processes such as crystal settling or resorption, or sharp changes in growth or nucleation rates will introduce some curvature and/or kinking in the measured CSD plot (Marsh, 1988, 1998). A log-linear CSD plot should thus reflect a simple crystallization history although Marsh (1988) accepts that many processes can produce this linearity.

The soundness of the method has been debated, for example by Pan (2001) who questions the validity of the ln(n) versus L plots and Eberl et al. (2002) who challenge the independence of crystal growth rates on crystal size. Nevertheless, CSD analysis remains a useful tool that is *complementary* to petrographic observations for studying rock textures. Its interpretation should be relatively straightforward for the purpose of this study as lava flows represent, like dikes, simple systems because of the constant bulk composition of the magma and the predominance of conductive cooling (e.g., Brandeis & Jaupart, 1987b; Cashman, 1990). Finally, it is noted that, compared to other studies based on measurements of maximum or mean crystal size (e.g., Kirkpatrick, 1977), this technique has the advantages of allowing investigation of the co-variation of crystal number densities and size, and being less affected by textural heterogeneities as it considers a wide range of crystal sizes.

4.5.2 Method used

The strict procedure followed to collect the raw crystal size data and, at the same time, quantify crystal modes using part-automatic image analysis, is detailed in Appendix A. In brief, plagioclase size data (apparent short and long axis, referred to as width and length hereafter) was collected from scaled BSE images. Plagioclases were chosen because they are abundant in the lavas studied, and in basalts in general, and are good indicators of cooling conditions because of the sensitivity of their mode of crystallization to the degree of undercooling of the melt (e.g., Cashman, 1993). The program by Higgins (2000) was used to correct the crystal width data for 3D effects (see Appendix A for procedure) and derive the CSD plots. The program by Morgan & Jerram (2006) was used to calculate the crystal aspect ratio necessary to apply the correction method by Higgins (2000). Crystal widths were used mainly because these are least affected by cut-sectioning effects, and thus require minimum correction (Cashman, 1990; Higgins, 2000). They may also be in longer contact with the liquid in comparison to the other directions that get preferentially

impinged (Kirkpatrick, 1977). An alternative view is that plagioclase length is more sensitive to growth kinetics, and its measurement would give the maximum crystallization rates (Cashman, 1990). The effect of using either crystal width or length and the use of different correction methods was thus tested for selected samples.

The method of Cashman & Marsh (1988) was used to derive crystal growth and nucleation rates, normalizing crystal sizes and number densities to the most surficial, crystal-poor samples, and nucleation rates to the amount of liquid available.

The equations they use are:

$$m' = 1/(G\tau_1 - G\tau_0) = 1/(Ld_1 - Ld_0) \quad (6)$$

$$n^\circ \text{ norm} = (n^\circ_1/Ld_1 - n^\circ_0/Ld_0) \times m' \quad (7)$$

$$J' = J/(1-f) \quad (8)$$

where the subscripts 1 and 0 refer to the sample "normalized" and the reference sample respectively, m' to the normalized CSD slope of sample 1, n° norm to the normalized intercept of sample 1, and J' to the recalculated crystal nucleation rate. For this part, basal samples (below core) were not considered; these should experience cooling rates 70% higher (Hon et al., 1994).

Either growth rates or residence time had to be estimated to calculate nucleation rates following equation 4, which was limited by the data currently available. Hon et al. (1994) empirically derived an equation describing the evolution of crustal thickness with time at the surface of active sheet flows from Kilauea, which was taken as identical to residence time for the purpose of this study. Consistent with a conductive cooling model and with data on Kilauea lava lakes (see Fig. 9 in Hon et al. (1994)), it is expressed as:

$$\tau = 164.8 \times C^2 \quad (9)$$

where τ is the time in seconds and C is the thickness of the crust or the limit of the 1070°C isotherm in meters. For this study, the distance from the surface was taken as C, considering that the bulk of the crystallization was completed at 1070°C. It is, however,

difficult to appreciate how this relation varies with crystallinity and emplacement style, which currently limits the interpretation of the data.

Comparison of the results to other studies are not straightforward since almost every study uses a different method which depends on the samples available and the specific textures studied, and also on the debated choice of the method for 2D-3D conversion. Table 4.4 summarizes the methods used by the studies that were compared to this work.

Table 4.4: Comparison of methods used by CSD studies referred to in the text.

Reference	Samples	Measurement	Conversion 2D-3D	Time constraint
Cashman & Marsh (1988)	Crust and core lava from drill cores through upper part of 1965 Makaopuhi lava lake	Crystal length on images from optical microscope	$Nv=Na^{3/2}$	Direct measure of solidification rate (Wright & Okamura, 1977)
Crisp et al. (1994)	Quench lava from active channelized 'a'ā flows during 1984 Mauna Loa eruption	Crystal area (Ac) on images from microscope	$L=4(Ac/\pi)^{1/2}$	Direct record flow duration from flow velocities and distance from vent
Burkhard (2002)	Margin of pāhoehoe lobes, current eruption at Kilauea	Crystal width on BSE images	$Nv=Na^{3/2}$	Cooling rates calculated using Keszthelyi & Denlinger (1996) and estimation of temperature interval for crystallization
Oze & Winter (2005)	Margin of dense pāhoehoe lobes, current eruption at Kilauea	Crystal area from automatic BSE image analysis	Nv=Na/d (d bin size)	Similar as Burkhard (2002) (calculated for 0% porosity)
Zieg & Marsh (2002)	Intrusions (norites, diabases) from Sudbury igneous complex and Ferrar dolerites	Crystal length on digital image of thin-section	CSD Corrections 1.1 (Higgins, 2000)	Simplified cooling model
This study	Surface, crust, and core lava from solidified rubbly pāhoehoe flows	Crystal width and length on BSE images	CSD Corrections 1.36 (Higgins, 2000)	Empirical conductive cooling model (Hon et al., 1994)

Na—number of crystals per unit area, Nv—number of crystals per unit volume, L—volumetric crystal diameter defined by Crisp et al. (1994). Note different conversion method adopted by each study.

4.5.3 Results

The CSD plots obtained (ln(nV) versus L, see Fig. 4.24) can be fitted by a straight line at 70 μm < L < 500 μm for surface samples and 100 μm < L < 800 μm for internal samples. CSDs parameters (slope, intercept) were derived from the line fitted to the data using the linear regression operation of Microsoft Excel (see raw data in Appendix B). They are reported with results from crystallization rate calculations in Table 4.5. The scatter of the data at L > 500–800 μm (see Fig. 4.24) is attributed to 1) the occasional presence of

microphenocrysts or phenocrysts on the BSE images that reflect the pre-emplacement history of the magma and 2) the effects of crystal aggregation that can lead to an artificial increase in the proportion of larger crystals (see Appendix A). The downward curving of the data that was often observed for crystal sizes <70 μm is attributed to limits of the method in the detection of small crystals.

Table 4.5: Parameters of plagioclase crystal size distribution with calculations of growth and nucleation rates.

Sample	Depth (m)	t (hr)	t (months)	CSD slope (μm^{-1})	CSD intercept (μm^{-4})	R^2	Ld (μm)	n^0 (cm^{-4})	m' (cm^{-1})	n^0 norm (cm^{-4})	G (cm/s)	J ($no.cm^{-3}/s$)	J' ($no.cm^{-3}/s$)
R10-9	0	0	0	-0.027	-16.62	0.996	37.3	6.07E+08					
R15-6	0	0	0	-0.037	-13.64	0.997	26.9	1.20E+10					
R15-5	-1	165	0.22	-0.029	-13.87	0.999	34.4	9.49E+09	-1336	2.26E+15	1.26E-09	1.20E+01	1.75E+01
R15-4	-3.5	2019	2.71	-0.020	-16.14	0.999	50.0	9.75E+08	-433	1.84E+15	3.18E-10	3.10E-01	1.15E+00
R15-3	-4.4	133	0.18	-0.022	-15.73	0.994	45.9	1.47E+09	-527	2.18E+15	3.95E-09	5.80E+00	9.26E+00
R15-1	-4.8			-0.039	-13.47	0.974	25.5	1.41E+10					
R19-1	0			-0.023	-15.89	0.994	44.2	1.25E+09					
R19-2	-1	165	0.22	-0.020	-16.17	0.990	51.0	9.48E+08	-1477	1.44E+14	1.14E-09	1.08E+00	2.65E+00
R19-3	-3	1483	1.99	-0.015	-17.34	0.986	68.0	2.96E+08	-421	1.01E+14	4.45E-10	1.32E-01	5.44E-01
R19-4	-5	4120	5.54	-0.009	-19.35	0.986	112.4	3.95E+07	-147	4.11E+13	4.59E-10	1.81E-02	8.41E-02
R17-1	0	0	0	-0.025	-15.69	0.989	39.8	1.53E+09	0				
R17-3	-4.5	3337	4.49	-0.017	-16.59	0.990	58.1	6.23E+08	-546	1.51E+14	1.52E-10	9.48E-02	6.50E-01
AD5	0			-0.029	-15.38	0.997	34.8	2.09E+09	0				
AD4	-2	659	0.89	-0.016	-16.76	0.991	61.0	5.27E+08	-383	1.97E+14	1.10E-09	5.80E-01	1.45E+00
AD3	-5	4120	5.54	-0.015	-17.25	0.994	65.8	3.21E+08	-323	1.78E+14	2.09E-10	6.70E-02	1.48E-01
AD2	-12	23731	31.90	-0.011	-18.79	0.997	93.5	6.90E+07	-171	1.01E+14	6.86E-11	4.73E-03	1.24E-02
L13-1	0			-0.026	-15.86	0.984	38.8	1.29E+09	0				
L13-3	-1.8	534	0.72	-0.014	-17.71	0.993	71.9	2.05E+08	-301	9.20E+13	1.73E-09	3.53E-01	1.72E+00
L13-4	-2.1	727	0.98	-0.013	-17.99	0.995	77.5	1.54E+08	-258	8.10E+13	1.48E-09	2.28E-01	1.04E+00
L7-1	0			-0.020	-16.25	0.999	49.5	8.74E+08	0				
L7-2	-0.3	15	0.02	-0.015	-17.50	0.998	69.0	2.51E+08	-514	7.20E+13	3.64E-08	9.16E+00	3.31E+01
L7-3	-0.5	41	0.06	-0.015	-17.24	0.999	68.0	3.25E+08	-540	6.95E+13	1.25E-08	4.06E+00	1.08E+01
L7-4	-1.8	534	0.72	-0.017	-17.07	1.000	60.6	3.87E+08	-901	1.01E+14	5.78E-10	2.24E-01	1.28E+00
L7-5	-3	1483	1.99	-0.014	-17.31	0.999	71.4	3.04E+08	-456	6.11E+13	4.11E-10	1.25E-01	6.10E-01
L7-6	-3.5	2019	2.71	-0.013	-18.00	0.998	80.0	1.52E+08	-328	5.17E+13	4.20E-10	6.36E-02	3.47E-01
L7-7	-3.75			-0.021	-15.95	0.995	47.4	1.18E+09	4736				
L7-8	-4.3			-0.033	-14.90	0.987	30.7	3.38E+09	531				
Laki tephra	0			-0.020	-18.62	0.998	51.3	8.23E+07					
L17	0			-0.031	-15.26	0.991	32.4	2.35E+09					
L18	0			-0.019	-16.88	0.998	52.6	4.69E+08					
L66	0			-0.018	-17.43	0.992	56.2	2.70E+08					

t—time (calculated using equation 9); R^2—least square regression fit; m'—normalized slope (equation 6); n° norm—normalized intercept (equation 7); G, J—growth and nucleation rates (equations 3 and 4); J'—recalculated nucleation rates (equation 8). Note that n corresponds to the number of crystals per given size range and per volume, accounting for a unit in cm^{-4} (number per cm^4)

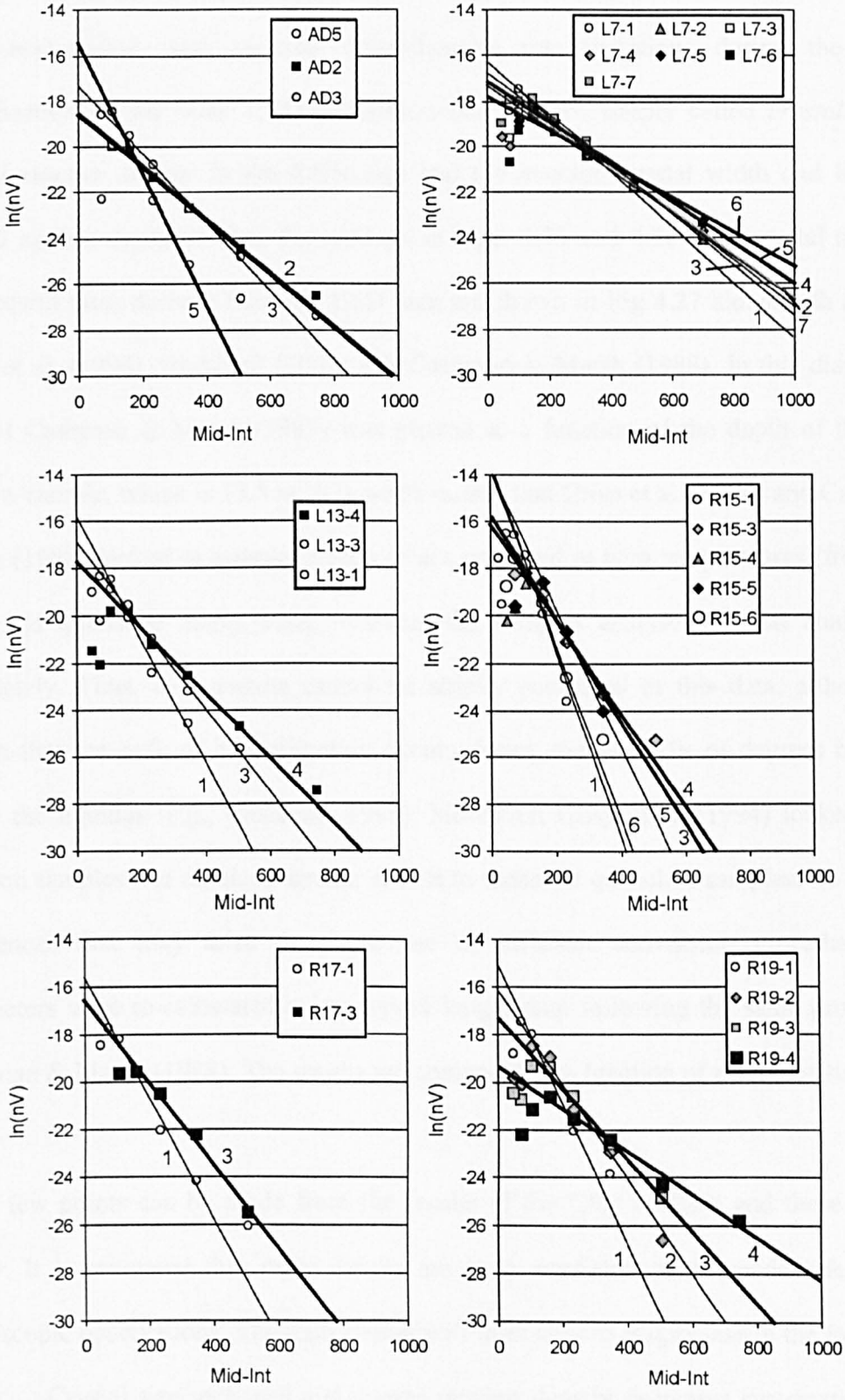

Figure 4.24: CSD plots acquired using program by Higgings (2000). ln(nV) is in no./μm^4, Mid-Int is in μm (corresponds to middle of size interval defined by program). Each number on fitted line represents sample number of each series. Lines fitted to textural data for core samples are thicker to show the flattering of slopes with increasing distance from margins. Parameters used were: Log 10 scale, 6 bins per decade (results choosing 5 bins per decade were essentially similar, but gave linear fits with lower squared residuals), box width, blocky crystal shape (tabular), and massive rock fabric.

CSD analysis was used here to quantify the textural variations observed within each lava cross-section, and estimate crystallization rate variations during the inwards solidification of the lavas. CSD parameters (Ld and n°, simply called *crystal size* and *crystal number density* in the following) and the average crystal width and length are plotted against depth through the sections in Figs. 4.25 and 4.26. The crystal nucleation and growth rates derived from the CSD data are shown in Fig 4.27 along with data from Crisp et al. (1994), Burkhard (2002) and Cashman & Marsh (1988). In this diagram, the data of Cashman & Marsh (1988) was plotted as a function of the depth of their most shallow sample, which is 13.5 m. It is worth noting that Crisp et al. (1994) and Cashman & Marsh (1988) looked at samples which where collected at high temperatures (from active lava) and quenched using water, whereas the samples analysed in that study cooled completely. Thus, their results cannot be strictly compared to this data, although it is known that the bulk of crystallization occurs during the first 10s of degrees of cooling below the liquidus (e.g., Cashman, 1993). Moreover, Crisp et al. (1994) looked at post-eruption samples and obtained similar results to those for quenched samples. To check for differences that may arise from the use of different conversion procedures, CSD parameters were re-calculated using crystal length data following the same procedure as Cashman & Marsh (1988). The results are compared as a function of residence time in Fig. 4.28.

A few points can be made from the results of the CSD analysis and these are listed below. It is reiterated that these results are fully consistent with trends inferred from microscopic observations. The term *crystal* will refer only to plagioclase in the following.

1) Crystal size increases and crystal number density decreases systematically with distance from lava margins to core. The amplitude of the variations is largest near the margins.

2) Samples from the crust and core of section R15 have crystal sizes markedly lower than the other sections (< 50 μm) and number densities of an order of magnitude higher (> 10^{10} no./cm^4 at margins to 10^9 no./cm^4 in core). Similar trends were obtained using Cashman & Marsh (1988) method (Fig. 4.28)

3) Samples through section R19 show the largest range in crystal size (44–120 μm) and number density ($1.25 \times 10^9 - 3.95 \times 10^7$ no./cm^4). It is noted that samples from the Kalapana lobe showed, visually, larger variations (see above) but those were not quantified.

4) The profile of crystal size and number density is flat across the crust and core of section L7 (as for variations in modal %), except from a marked decrease in crystal size (and increase in crystal number) in a sample collected from the base of the upper crust (Fig. 4.25).

5) Samples through the sections show in general increasing width/length ratio with margins to cores, except for samples from section AD that show a continuous increase in aspect ratio (Fig. 4.26).

6) There is a continuous decrease in crystal nucleation and growth rates with depth (Fig. 4.27). Variations of crystal sizes in time through the cross-sections studied are similar to those observed in the upper part of the Makaopuhi lava lake by Cashman & Marsh (1988), except for section R15; yet plagioclase number densities are markedly lower for the lava lake samples (Fig. 4.28).

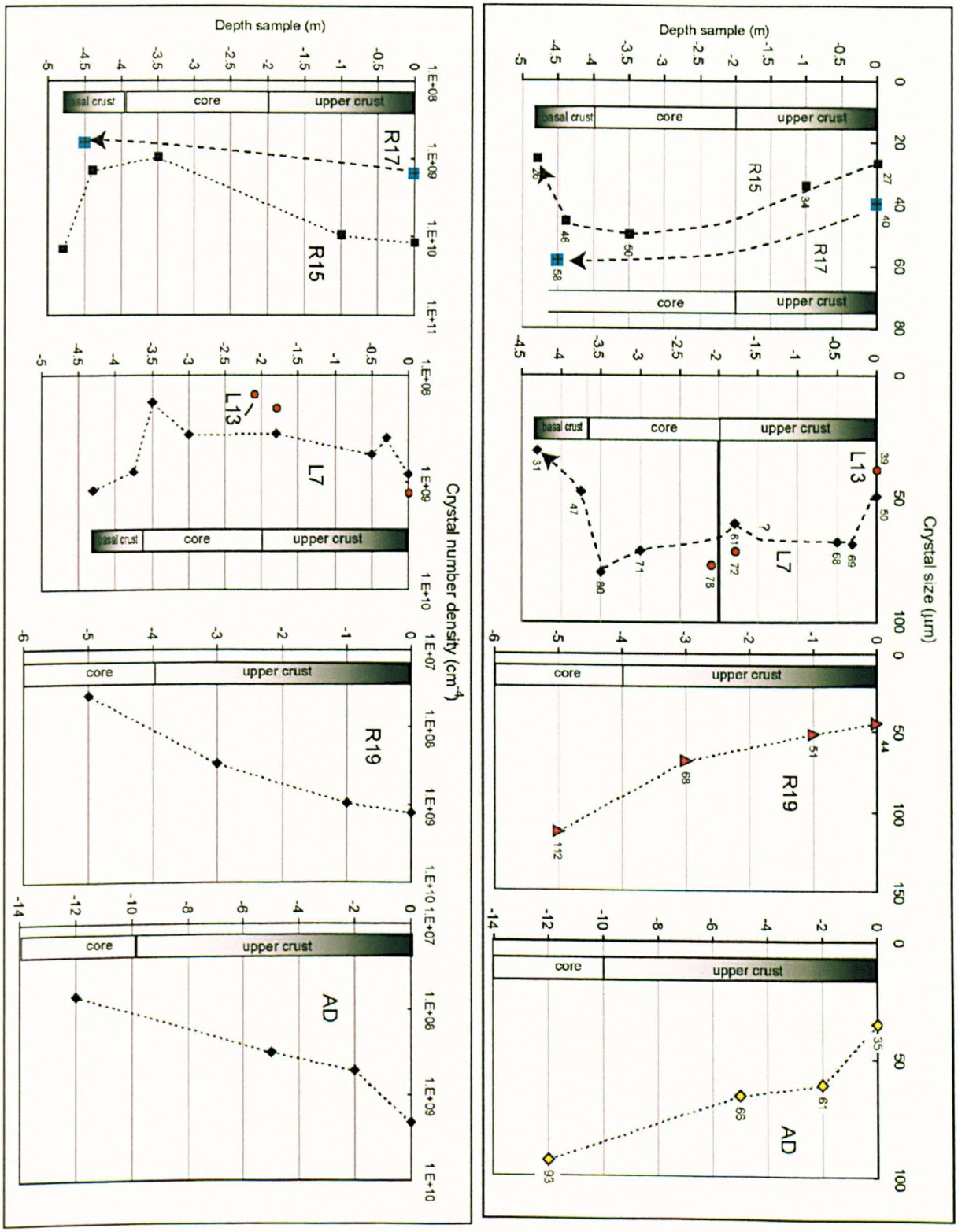

Figure 4.25: Plot of plagioclase dominant size (-1/CSD slope) and crystal number density (intercept CSD slope) against depth (m) through lava cross-sections. Boxes indicate extent of crust and core in sections studied. Note that basal samples were analysed only for sections R15 and L7.

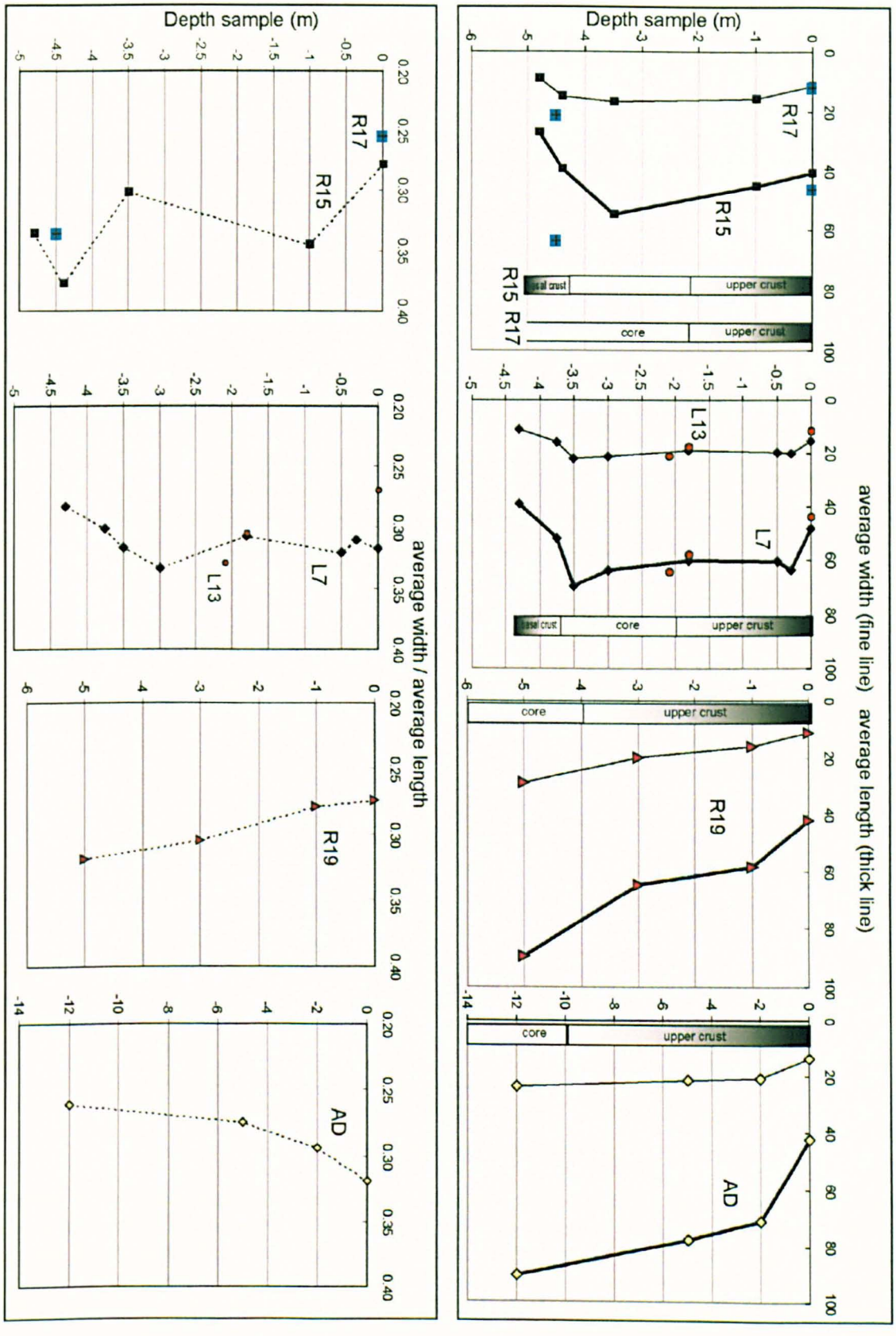

Figure 4.26: Variation of plagioclase average width and depth (in μm), and ratio of width/depth (aspect ratio), with depth through the sections.

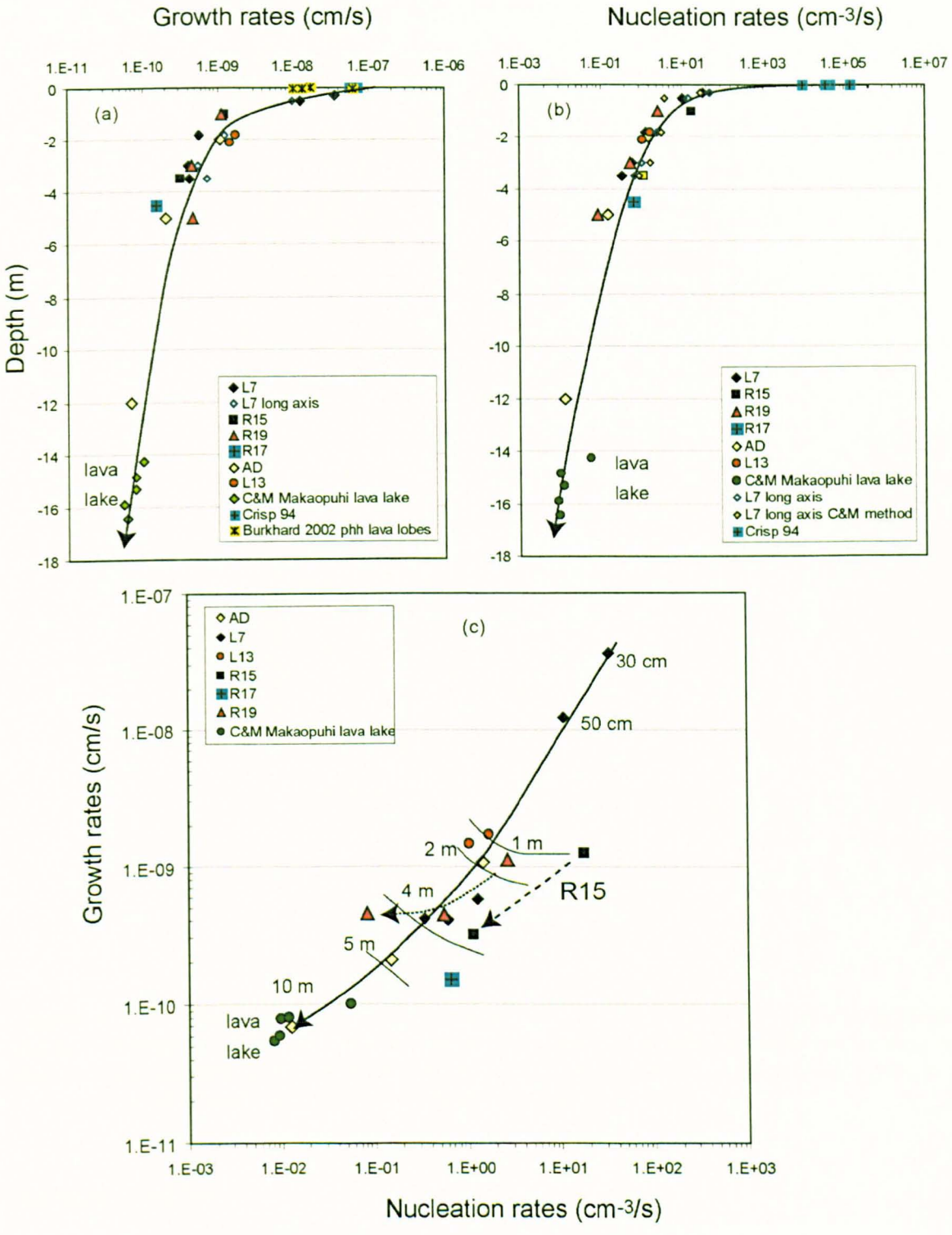

Figure 4.27: Nucleation and growth rates calculated from the CSD data collected in this study (nucleation rates are number of crystals per cm^3 per second). Residence time was taken from sample depth using Hon et al. (2003) calibration. Only samples from upper crust and core were considered and these were normalized to surface samples to obtain lava crystallization rates during inwards solidification. Data collected using other methods is reported on a) and b) (L7 long axis was calculated using crystal length data as input in Higgins (2000) program, and box length option). On c) approximate depth of samples is reported. Note rapid decrease in crystallization rates. Growth rates level off in lava interior while nucleation rates keeps decreasing, which is attributed to low undercooling conditions.

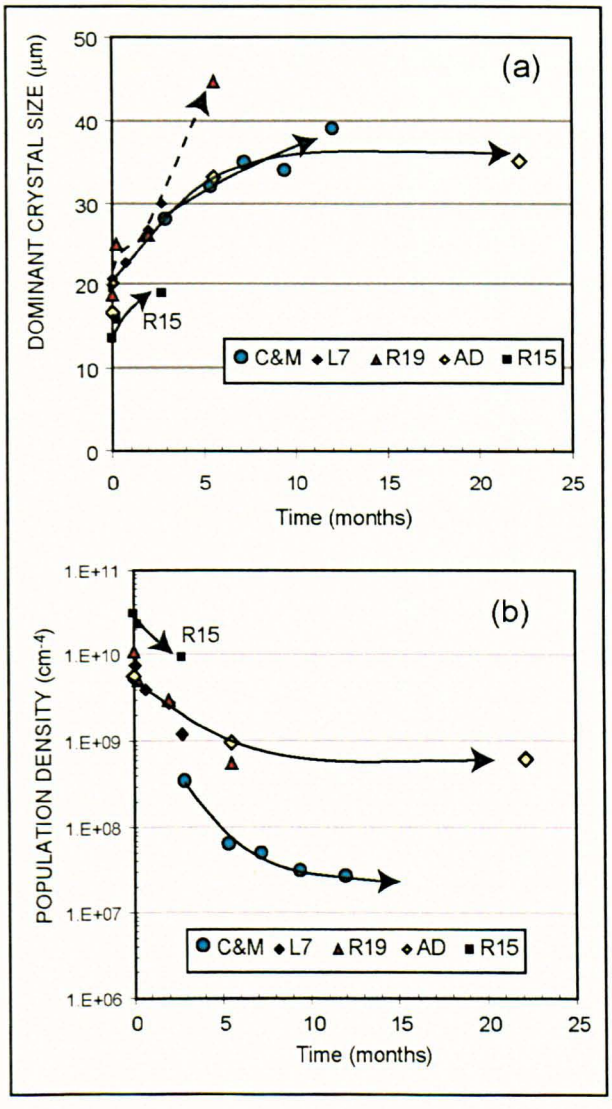

Figure 4.28: Comparison of variation of dominant crystal size (CSD slope) and crystal number density (intercept of CSD slope) against emplacement time (in months) for different sections and thus lava emplacement style. Emplacement (or crystallization) time is estimated using Hon et al. (1994) empirical relation fitted to sheet flows and lava lakes in Hawaii.

4.6 DISCUSSION

The textural and compositional data collected on the lava flow-fields studied will now be compared with their mode of eruption, transport, and emplacement as inferred from the organization of the flow-fields and the lava surface morphologies. At first, the field and aerial photo observations presented in section 4.2 will be used to interpret the mode of emplacement of the flows and their eruptive conditions. The role of bulk lava composition

and erupted temperature will also be discussed, referring to data presented in section 4.3.1. Next, the results from cross-section textural analysis presented in sections 4.3 and 4.4 will be interpreted in terms of crystallization kinetics during lava solidification. Finally, building on this work and other studies, a diagram linking the characteristics of plagioclase microlite population to the lava type and the impact of eruption and emplacement mechanisms on textural variations will be proposed.

4.6.1 Mode of emplacement of rubbly pāhoehoe lava flow-fields

The mode of emplacement of Laki lavas was described in detail in Chapter 2. This section focuses on the mode of emplacement of Reykjanes Peninsula and Grande Ronde lavas and discusses how they compare to Laki lavas and active flows observed in Hawaii.

Reykjanes Peninsula lavas. In general, Reykjanes Peninsula lavas show evidence for more "viscous" or 'a'ā-like behavior than Laki lavas. They have many surface characteristics that have been observed on active 'a'ā flows from Hawaii (e.g., Wentworth & MacDonald, 1953; Lipman & Banks, 1987). These are open-channels, steep flanks, large masses of agglutinated material carried on top of the flows, which all signal that lava had a significant yield strength. The abundance of lava intrusions into the top rubble suggests significant lava viscosity, slow flow advance, and the inability of lava to thicken markedly by inflation.

The lava features formed during the well-documented 3-week-long 1984 Mauna Loa eruption represent a good analogue for the Reykjanes Peninsula lavas studied. Described by Lipman & Banks (1987), the first days of the 1984 Mauna Loa eruption produced near-vent sheet pāhoehoe lavas that transformed down-slope into channelized 'a'ā-crusted flows which are similar in surface structure to the lava fields of Hellisheidarhraun D and Svinahraunsbruni. Lipman & Banks (1987) distinguish the following zones from vent to flow front: 1) an upper stabilized channel, 2) a transitional channel zone with wide lateral margins deformed by "shear lenses" and dynamic motion accompanying up-flow lava

surges, and 3) a zone of dispersed flow (flow toe), where "the movement of the upper surface of the flow tended to occur along discrete shears, between which ridges of blocky 'a'ā moved fairly coherently". The match between these features and those of the Reykjanes Peninsula flow-fields is striking. The flow-fields of Kapelluhraun and Obrysnnishólahraun show the same general structure as those of Mauna Loa, although the flows have a less viscous appearance that can be linked to larger proportions of pāhoehoe surfaces, in particular along the flow margins. For conditions of similar temperature and lava viscosity, this could be related to the lower emplacement slopes of the lava or to lower effusion rates.

Most of the flows studied in the Hussfellsbruni lava field display central open-channels and evidence for lobe-by-lobe emplacement, which makes them somewhat transitional between pāhoehoe and 'a'ā in terms of emplacement style. The highly elongated shape (high length/width ratio) of many of the flows can be related to the relatively steep ground slopes on which these were emplaced, which would also have promoted the formation of channels in the central parts of the flows.

The lava field with large inflation features that includes section R19 probably formed during a period of slow and steady effusion rate near the start of the eruption forming the Rjupnadyngjuhraun flow-field, when lava formed dominantly pāhoehoe surfaces and developed a system of tubes. This period could have lasted a few months to account for the thickness of the flows upper crust (see time calculated following equation 6, plotted in Fig. 4.28). The extensive inflation of the flows at that location could have resulted from their emplacement in a pre-existing depression.

Finally, the organization of Illahraun lava field suggests that the flows were initially emplaced as large sheet lobes spreading on near-horizontal ground. The surface crust of the sheet lobes was subsequently disrupted and rafted in large intact plates. This disruption event could have been caused by a marked increase in lava production rates from the

fissure, or be related to the high viscosity of the flows which would have led to an increase in fluid lava pressure within the flows, leading to disruption of the near-stationary crust. Furthermore, as suggested before, the hyaloclastite mount located along the eastern margin of the flows may have acted as a barrier to the advance of the flows, which could have caused a temporary halt in the flow advance followed by pressure building inside the flows and partial collapse of the lava crust in the proximal part of the flows when the lava finally broke out along the southern margin to form branch B.

The characteristics of most Reykjanes Peninsula lava flows differ from Laki lavas, where open-channels formed only in some of the small-volume late-erupted lava flows that cover the Varmárdalur area on the highlands (see Chapter 2). Several parameters can account for these differences: 1) higher shear stresses imposed by the generally higher emplacement slopes (1 to up to 10°) for the Reykjanes Peninsula lavas compared to the < 0.1° slopes on which the largest volume of the Laki lava field was emplaced (see Chapter 2), and 2) the shorter duration of the Reykjanes Peninsula eruptions and low volumes erupted. These latter are factors promoting the formation of compound flow-fields in contrast to the long duration and high volumes of the Laki eruption which favours tube formation (e.g., Rowland & Munro, 1993; Calvari et al., 2002). The viscosities of the Reykjanes Peninsula and Laki lavas at liquidus temperature are similar (Table 4.2), thus their viscosity upon eruption cannot account for their differences in morphology.

Columbia River basalts (CRB). There is evidence for the emplacement of CRB lavas on very shallow slopes (< 0.1°, Tolan et al., 1989) and frequent interaction of lava with water, as documented by the presence of irregular jointing patterns (Long & Wood, 1986) and basal pillow lavas (e.g., Schiffman & Lofgren, 1982). The large volumes of lava erupted and the presumed long duration of individual lava outputs favoured the formation of very thick, thermally efficient flows that grew by inflation (Self et al., 1997, Keszthelyi et al., 2006).

The Grande Ronde lavas are more silica-rich than Reykjanes Peninsula and Laki lavas, and other lavas from the CRB (Hooper, 1997 and references within). Moreover, they were probably erupted at relatively low temperature (< 1130°C) given their liquidus temperatures (see Table 4.2). These parameters would have increased lava viscosity, thus promoting crust disruption and formation of rubble at the flow tops. Nevertheless, higher lava viscosities could favour lava inflation because of the higher strength of the lava. The presence of large intrusions into thick rubbly tops can be attributed to the load of the rubble that resisted the uplift of the upper part of the flow, thus causing the still fluid lava to intrude the flow top. This feature was observed on a smaller scale in the middle of the Eldhraun branch of the Laki lava flow-field (see section 2.5.2).

4.6.2 Mode of crystallization of lavas during internal solidification

Building on previous work on magma solidification and crystallization kinetics (e.g., Cashman, 1990, 1993), this section aims to describe the pattern of internal cooling, crystallization and solidification of the lavas as inferred from the textural variations observed in cross-section. In general, the temperature gradients will be the largest at the margins of the cooling body, which will drive higher degrees of melt undercooling and thus enhance crystallization rates.

The analysis shows that plagioclase crystallization rates rapidly decreased from the lava margins to their cores (Fig. 4.27a, b), following an increase in the modal % and size of the crystals, and a related decrease in the crystal number densities (Fig. 4.22, Fig. 4.25). It is noted, however, that the shape of the trend in crystallization rates shown in Fig. 4.27 is strongly controlled by the assumption of conductive cooling and calculation of residence time as a function of the square of the distance from the margins (equation 9), which introduces some bias to the results that cannot be resolved at present. Besides, the rates calculated here should be taken as minima as they represent averages across the crystallization interval (Cashman, 1990).

These variations are consistent with the decrease in cooling rate and increase in crystallization time that occur concurrently during the inwards progression of the solidification front, as the zone where crystallization takes place (mush) thickens due to decreasing temperature gradients, reducing the amount by which the melt is undercooled at any location and time. An alternative possibility is that of progressive changes in the properties of the lava that is injected into the lobes over time and is subsequently solidified at different levels. This is considered unlikely in the cases examined by this study given the consistency of the trend in crystal sizes and number density observed, although it cannot be completely ruled out for the thickest flows that were emplaced over significant amounts of time. The bell-shape variation of the plagioclase/clinopyroxene modal ratio that is observed it the upper part of the sections (Fig. 4.22d) can be linked to the large increase in plagioclase modal % and crystallization rates in that same portion which rapidly stagnates as the total crystallinity reaches > 80 vol.% (Fig. 4.22a).

Growth rates tend to level off in the lava core whereas nucleation rates keep decreasing (Fig. 4.27c). This may reflect low degrees of melt undercooling, when crystallization proceeds by growing the existing crystals rather than forming new ones, as consistent with the blocky morphology of the crystals and their tendency to form aggregates so as to reduce surface energies. The presence of thick evolved rims around crystals in the lava cores is interpreted as resulting from slow crystal growth and liquid differentiation near the crystal-liquid interface, while the irregular outline of the rims is attributed to the limited space between crystals at the end of the crystallization. The decrease in crystal number in lava cores reflects the increase in the size of individual crystals and the effect of crystal aggregation.

The calculated plagioclase crystallization rates for the cross-sections studied are bracketed by results from other studies (Fig. 4.27). Growth rates of $\sim 10^{-10}$ cm/s at depth are consistent with existing data on equilibrium crystallization kinetics in shallow magmatic

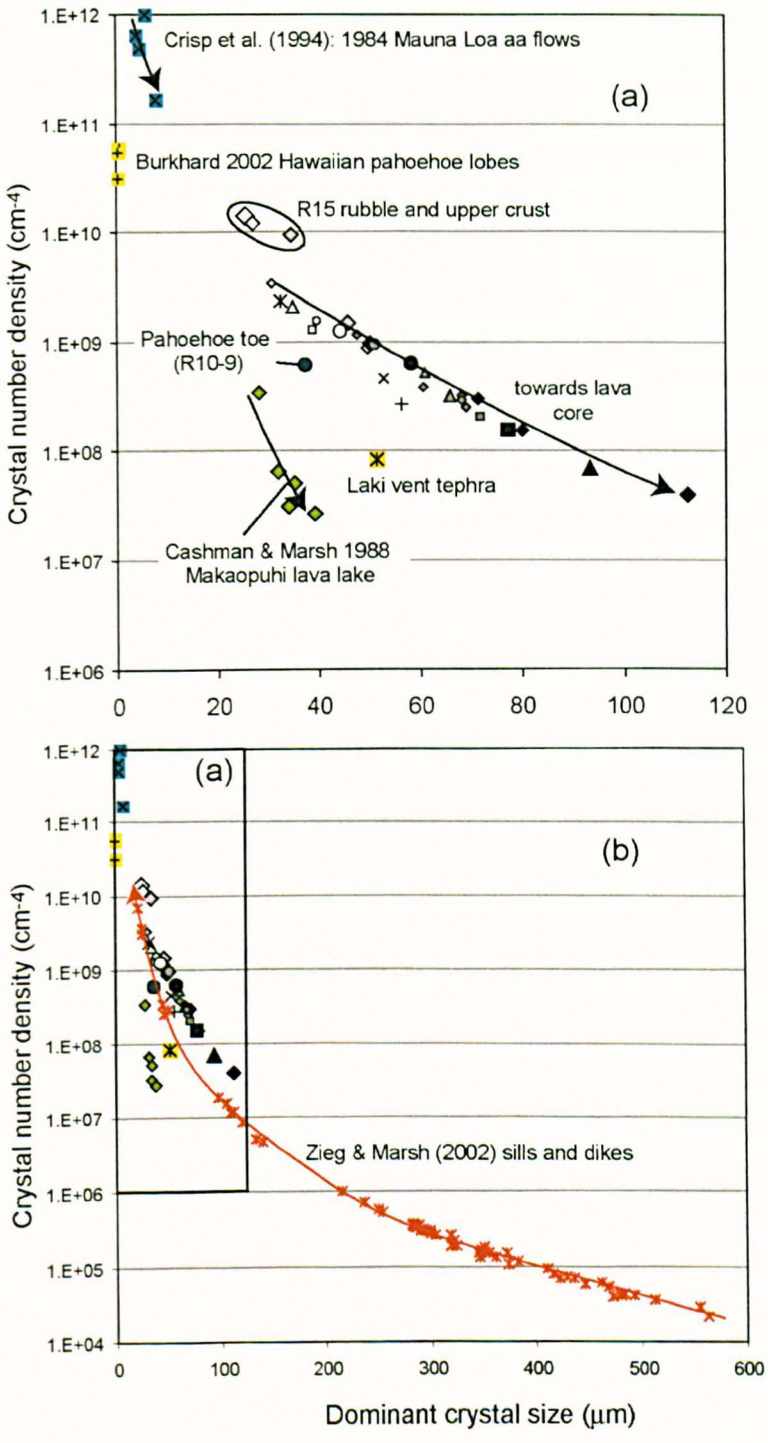

Figure 4.29: Coupled variations in crystal number density (intercept CSD slope) and crystal size (-1/CSD slope) for this study and others. Symbols are the same as in Fig. 4.27. Note trend defined by data collected from sections across rubbly pāhoehoe lavas (sections L7, L13, R17, R19, AD) without distinction between different lava bulk compositions. Data collected on surface and crust samples from section R15 (sheet lobe from channelized flow), sample R10-9 (basal pāhoehoe breakouts), and Laki tephra plot apart from this trend, showing about one order of magnitude difference in crystal number densities. Note the low crystal number densities reported for samples across Makaopuhi lava lake (Cashman & Marsh, 1988). These textural differences can be ascribed to emplacement processes and linked cooling and degassing histories of lava (see text).

4.6.3 The origin of textural differences/similarities between cross-sections studied

Although the general pattern of inwards solidification described above applies for all sections, there are noticeable textural differences between the cross-sections studied which were listed in section 4.4.3. The main parameters that may have caused these variations are now discussed.

Lava bulk composition. Its impact on the lava textures is considered to be negligible here, as all the lavas studied crystallized along the plagioclase-clinopyroxene-olivine cotectic and formed plagioclase in similar volumetric proportions (Fig. 4.22). Nevertheless, the lower amounts of clinopyroxene crystallized by Grande Ronde lavas can explain the distinct intergranular to subophitic texture of the AD section crust and core samples (see AD4, AD3 and AD2, Fig. 4.13). The abundance of plagioclase crystals can account for their high degree of intergrowth, in comparison to conditions where clinopyroxenes provide alternative sites for nucleation (Lofgren, 1983). In addition, the relatively low liquidus temperature of the Grande Ronde lavas implies low emplacement temperatures and a short crystallization interval, which would result in smaller amounts of crystallization before solidification, and thus lower internal variations in crystal sizes.

Eruptive mechanism. The lava flows studied have relatively high amounts of microlites that formed in large numbers as lava was emitted at the vent (see 4.3.2). In Chapter 3, this burst of crystallization was attributed to the response of the Laki lava to the undercooling generated by degassing during magma ascent. This process caused the formation of a compositional gap at the margins of plagioclase phenocrysts that corresponds to the shallow formation of groundmass crystals. Interestingly, this feature was detected in lava samples from Kapelluhraun and Obrysnnishólahraun that contain plagioclase phenocrysts (see Fig. 4.20). The number density of microlites in the lava erupted at the vent may thus be commonly regulated by the intensity of decompression-driven magma degassing during eruption and the capacity of the magma to re-equilibrate

quickly to the undercooling induced. The relative liquidus temperatures of the phases in the melt, as controlled by the bulk magma composition, may play a role, as it will determine the effective degree of undercooling of the melt. The amount of water dissolved in the magma at depth may, however, have a stronger impact. It is a parameter that is difficult to estimate in the absence of glass inclusions. The plagioclase compositional gap of ~An_{10} measured in the Laki lavas was attributed to the presence of > 1 wt.% water in the melt (Chapter 3); this could also apply for the Reykjanes Peninsula lavas studied. Phenocrysts being absent in the Grande Ronde lavas studied, this process cannot be unravelled for those.

Lava transport processes. The distinctly finer-grained texture of the surface sample from section R15 may be related to the high cooling rates of the (fluid) lava during transport. This could have been promoted by the circulation of the lava in an open-channel (see Fig. 4.10) as this favours radiative heat losses and promotes lava cooling by entraining surface fragments in the flow interior (Kilburn, 1989; Crisp & Baloga, 1994; Cashman et al., 1999; Harris et al., 2005). Higher cooling rates of the melt can increase its effective degree of undercooling and thus increase the relative importance of nucleation rates over growth rates (e.g., Cashman & Blundy, 2000). Alternatively, this intense nucleation of crystals during transport could result from delayed re-equilibration of the melt to the degassing-induced undercooling as discussed above, which affected the lavas produced during the 1984 Mauna Loa eruption (Lipman et al., 1985).

Lava emplacement processes. As a given conductive model had to be chosen to estimate the duration of crystallization in the interior of the flows, the significance of the calculated crystallization rates is limited (see above). There appear to be, however, distinctive patterns that can be related to the conditions of emplacement of the lava.

Distinctly high nucleation/growth rates were calculated from samples through the Kapelluhraun lava flow in section R15, as resulting from the large increase in plagioclase content (Fig. 4.22) and number densities (Fig. 4.26) through the section. This suggests high

crystallization rates driven by substantial degree of undercooling of the melt. Enhanced cooling of the magma during transport as suggested above could have caused an increase in the melt undercooling by lowering the melt temperature. This however may have been balanced by the latent heat released by the crystallization observed (Crisp et al., 1994). It is also possible that the high cooling rates of the interior of the flow were caused by its mode of advance, as the presence of basal clinkers evidences the continuous surface disruption of the flow, with rolling of the fragments down along the flow front (Fig. 4.5). This could have enhanced flow cooling at the margins, thus creating higher temperature gradients in the lava interior and increasing cooling rates.

Samples through section R19 that cuts across the margins of a large sheet lobe at Hussfellsbruni, display the largest range in crystal number densities and size that was measured here, illustrating a large degree of inwards textural coarsening. This suggest low internal cooling rates, which can be related to the long duration of emplacement of the sheet flow, as inferred from its size and thick upper crust. The continuous influx of lava in sheet flows can significantly lower their cooling rates and thus crystallization rates by slowing the propagation of the solidification front, as empirically observed by Hon et al. (1994).

Sections L7 and L13 display limited internal variations in terms of crystal sizes, which suggests that cooling rates did not vary significantly with depth in the flows, and stayed relatively low. The presence of a zone of irregular jointing in the lava core across these sections may provide evidence for enhanced core cooling due to interaction with surface water infiltrated along open fractures through the upper crust, as it was observed, for example, during the solidification of the Kilauean lava lakes (e.g., Hardee, 1980). Such process has been proposed to explain the systematically finer-grained textures of irregular-jointed lava (entablature zone) compared to regularly jointed lava (colonnade) across lava sections in the Columbia River Basalts (Degraff et al., 1989). Historical accounts of the

Laki eruption provide valuable information on the conditions of emplacement of the flows that permit the hypothesis of interaction of the lava with large amounts of surface water to be tested. In fact, the accounts tell that, while spreading on the coastal plain, the Laki lava invaded many distributaries of the major Skaftá River that drives the water outflow from the Vatnajökull glacier to the ocean (see Chapter 2 Fig. 2.8c and related text, and extracts of historical accounts in Thordarson et al., 2003). This must have greatly disturbed the local river system, damming some parts of the river streams and causing dramatic overflows on lava lobes. It is thus likely that the surface of flows emplaced along the margins of the Laki flow-field was periodically flooded. Textural information, field observations, and historical evidence thus consistently show that the rates of internal solidification of some lava lobes at the margins of the flow-field were locally enhanced due to the interaction of the flows with the local river system. However, this must have had limited impact on the overall thermal efficiency of the lava transport system as it only affected marginal lobes.

The limited increase in crystal sizes measured across the thick upper crust of section AD may also be partly related to enhanced cooling due to water infiltration (in addition to the effect of low emplacement temperatures and small crystallization intervals, see above). This is suggested by the presence of some irregular jointing across the section (Fig. 4.13) and numerous evidence for the emplacement of Grande Ronde lavas in areas characterised by shallow lakes and extensive river systems (see Long & Wood, 1986 and references within). The extent of this process is difficult to assess without further comparative work on other sections with different field and textural characteristics. For example, the processes that create the complex vesicular pattern of the upper crust of section AD are still not well understood, but are likely to result from variations in the conditions of growth of the sheet lobe whose impact on the rates of cooling and crystallization of the lava is unknown.

4.6.4 An integrated model for the origin of basaltic lava flow textures

The textural data collected in this study, along with their interpretation in the context of field-based observations, have been used to construct a general diagram that links lava microtextures, through the characteristic crystal nuclei number density and dominant crystal size measured by CSD analysis, to lava surface morphologies and eruptive processes (Fig. 4.30a). Although the data on which this diagram is based is limited (more data is needed on the pāhoehoe and 'a'ā endmembers), this representation provides a tool that may be useful for inferring flow emplacement processes from CSD textural analysis of lava samples. It is noted that, although this diagram only considers groundmass crystals owing to their major impact on lava rheology and large abundance in basaltic melts, phenocrysts can have a similar impact on lava viscosity and emplacement style, if volumetrically important.

The agreement of this representation with other textural data and general considerations on lava flow processes can be tested. Primarily, the position of the pāhoehoe and 'a'ā field respectively at the low and high crystal number pole is in accord with available textural data (Sato, 1995; Cashman et al., 1999; Polacci et al., 1999; Katz & Cashman, 2003; Soule et al., 2004). Also, the total crystal content globally increases from the left side to the right and to the top of the diagram, i.e., as the characteristic number density and dominant size of the crystals increase, which implies that 'a'ā lavas will tend to have higher crystal content. This has been observed in textural works (Kilburn, 1989; Soule et al., 2004; Soule & Cashman, 2005) and results from the fact that large crystal contents increase lava viscosity and yield strength, factors promoting crust disruption and formation of 'a'ā lavas, and that, in turn, the disrupted crust of 'a'ā flows allows high radiative heat losses and subsequent down-flow cooling and crystallization (Cashman et

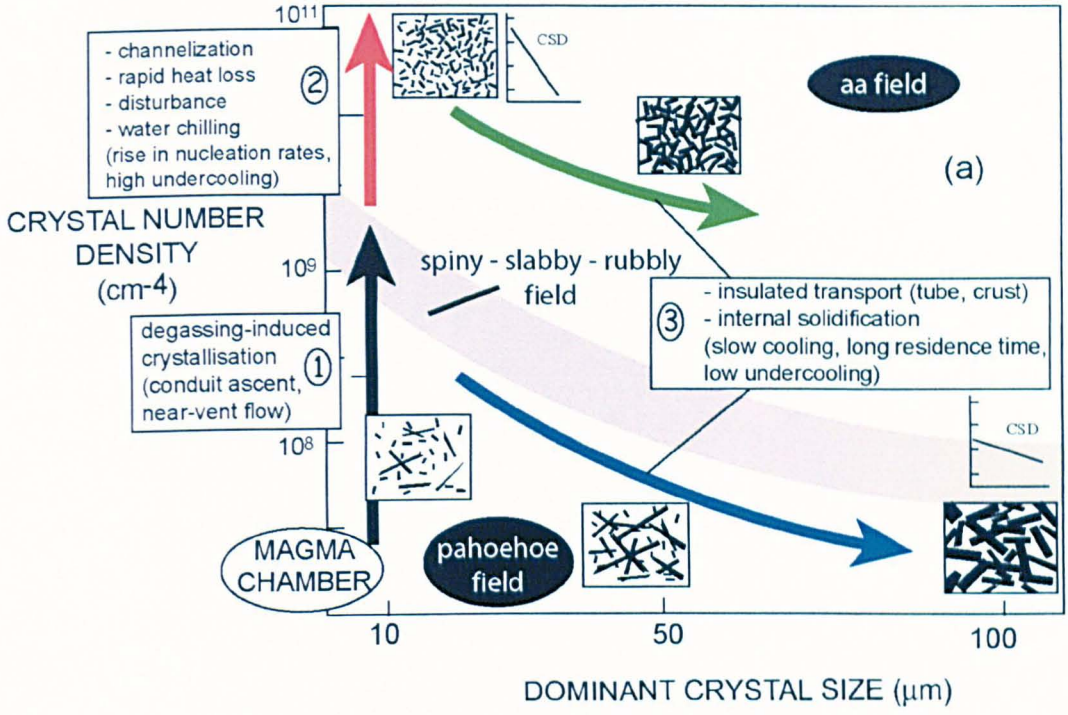

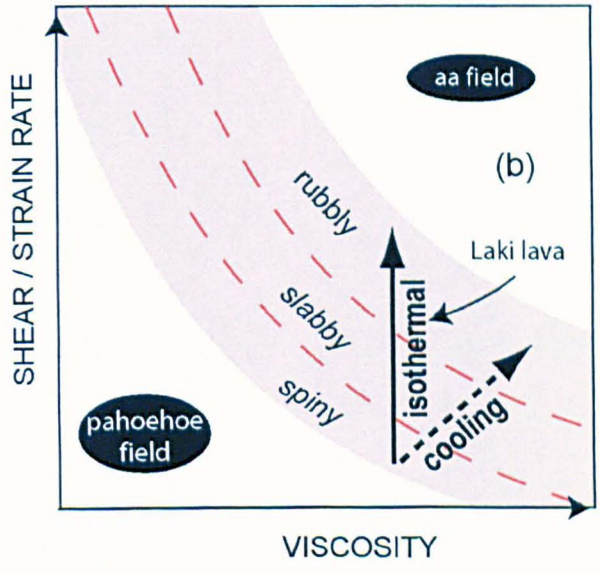

Figure 4.30: Lava groundmass textures and main controlling factors. (a) Diagram representing lava types in terms of their variations in the size and number density of plagioclase microlites derived respectively from slope and intercept of CSD plots. Main factors controlling evolution of textural parameters are listed in rectangles and discussed in text. Ranges of values along both axes are taken from data presented in this work. Plot of any other data collected from specific lava field in this diagram may allow inferring flow emplacement mechanism of lava and importance of cooling/degassing-crystallization upon eruption. (b) Representation of transition between pahoehoe, spiny pāhoehoe, slabby pāhoehoe, rubbly pāhoehoe, and 'a'ā fields in a schematic diagram of shear / strain rate versus lava viscosity, following Peterson & Tilling (1980). Continuous arrow shows that, as demonstrated in Chapter 3 for the Laki lava, a change in surface morphology caused by an increase in imposed shear rate may not be associated with increase in fluid lava cooling, and thus a subsequent change in lava viscosity and groundmass textures (see text).

al., 1999; Harris et al., 2005). This relation, however, is not systematic and some 'a'ā flows have low crystal contents (see for example, the low crystallinity of lava sampled across section R15). It is noted that, in apparent contradiction, the crust and core of pāhoehoe lavas are much more crystalline than the interior of 'a'ā lavas, due to low cooling rates and long crystallization times.

In comparison to the pāhoehoe and 'a'ā endmembers, rubbly pahoehoe lavas tend to have "intermediate" number densities and crystal content. Consistently, they develop spiny surfaces (see also Chapter 3), which reflect a subsequent viscosity or yield strength (Hulme, 1974), but the lava is rarely torn apart in a partly solidified viscous state along the flow top, which is a clear 'a'ā characteristic. There is also ample field evidence, especially along the Laki lava (Chapter 2), that the flow emplacement mechanism was dominated by inflation. This is characteristic of pāhoehoe lavas and leads to low cooling rates, high thermal efficiency, and low down-flow crystallization.

An important remark is that because this representation is based on the impact of groundmass crystals on flow rheology and *vice versa*, surface morphological transitions will be represented by a single point if these do not involve changes in the properties of the fluid lava (i.e., increase in cooling or degassing leading to crystallization). This case applies for the transition from spiny to slabby and to rubbly pāhoehoe surfaces along Laki lavas as the petrological and textural analysis of lava selvages along the flows indicated isothermal lava transport (see Chapter 3). In this case, changes in lava types are better represented in a diagram of shear rate versus lava viscosity, as illustrated in Fig. 4.30b (isothermal path).

The discussion will now focus on the physical processes that induce crystallization during magma transport and thus affect the resulting lava texture. An important concept to recognize is that the vertical axis in the diagram, the number density of crystal nuclei n°, varies with the degree of undercooling of the melt (Cashman & Marsh, 1988), and thus

vary accordingly to cooling, degassing and crystallization rates. The major textural-controlling factors revealed by this work are reported in three main groups on Fig. 4.30a, depending on their main impact on the lava texture (i.e., crystal-forming or crystal-growing process). In the following these processes will be put in context of the evolution of the magma at different stages of its transport. In the magma chamber, the magma typically contains negligible amounts of groundmass crystals. Groundmass crystals (dominantly plagioclases) will form mainly on the way to the surface, or in the flows erupted at the vent as a result of degassing-induced magma undercooling (1 on Fig. 40a). The degree of undercooling will control the size distribution of the crystals formed with, in general, positive correlations between the initial amount of volatiles (mainly H_2O) dissolved in the melt, the degree of magma undercooling, and the number density of plagioclase formed in the erupted lava (see Chapter 3). Other factors that intervene are the magma bulk composition that determines phase equilibria, and the magma temperature.

While being transported at the surface, the lava texture may evolve either because of late re-equilibration to the degassing-induced undercooling, or to crystallization induced by cooling during transport. The relative importance of nucleation/growth rates will be determined by the degree of exposure of the lava to the air that controls the amount of radiative cooling. Channelized transport may cause a large increase in the number of crystals in the melt (2 on Fig. 4.30), whereas the lava is more likely to undergo low cooling rates when transported in tubes, which will increase the crystal size and relatively reduce their number density (3 on Fig. 4.30).

Finally, when breaking out at the surface and emplaced as a single lava lobe, the lava surface morphology as influenced by its viscosity and crystal content, and also by the local supply rates and topography, will determine the rates of internal cooling of the lava and thus the textural variations that are observed in solidified cross-sections. The duration of emplacement will also play a role and will favour an increase in crystal size, while the

involvement of water in locally increasing crystallization rates or stopping the crystallization (quenching effect) will raise the crystal number density, and thus relatively reduce the crystal size.

In a more general view, what the diagram shown in Fig. 4.30a recognizes and attempts to quantify is the link between 1) microprocesses (crystal scale) that fundamentally reflect the kinetics of crystallization and control lava rheology at small scale, and 2) macroprocesses that are physical mechanisms linked to the eruption dynamics and the environmental conditions which bring the system out of equilibrium, forcing crystallization. This correlation is fundamental because, with further refinement, it may be used as:

1) An interpretative tool: textural analysis of lava samples could be used to infer the physical conditions of magma transport;
2) A monitoring tool: lava microtextures or direct measurements of the heat and gas budget of active flows could be used to follow down-flow changes in lava properties that affect the mode of advance of the flows or, alternatively, syn-eruptive changes in the lava emitted at the vent, which may provide insights into sub-surface processes;
3) A predictive tool: based on an assessment of the chemical and physical conditions of magma transport, one may be able to predict lava emplacement style and major controls on flow-length.

4.7 SUMMARY AND CONCLUSIONS

Rubbly pāhoehoe lavas show a wide range of surface morphologies that may be attributed either to the pāhoehoe or 'a'ā lava types as they were classically defined (e.g., Wentworth & MacDonald, 1953). Among the Reykjanes Peninsula flow-fields these variations can be attributed to differences in the eruption characteristics (eruption rates, duration and volume erupted) and the local topography. The internal textures of the lava examined in cross-sections show variations that are interpreted to reflect a sharp decrease

in the lava cooling rates with increasing depth (and time). Differences between the cross-sections studied can be attributed to the roles of lava bulk composition, pre-existing crystallization history of the lava during transport to the point of surface quenching, and the duration of emplacement of the lava. The main factor controlling the texture of the lava is the initial number density of the crystals in the lava (i.e., dominantly plagioclase microlites) because it controls the initial distribution of crystals in the melt, and thus their maximum size and intergrowth pattern. The number density is also important through its impact on the bulk viscosity of the magma and thus on lava rheology during transport. The initial number density of crystals is governed by 1) eruption processes such as decompression-induced degassing, or 2) the conditions of transport of the fluid lava away from the vent such as the formation of open-channels or tubes. The size of groundmass crystals appears to be mostly controlled by their residence time in the cooling lava, which is mostly dependent on the duration of emplacement of the lava flows and on the distance of the lava from the flow margins. Finally, the identification of a link between measurable textural characteristics of the lava and the chemical and physical processes that affect the magma and lava transport upon eruption provides means to interpret, predict and monitor lava flow dynamics, which will be useful for hazard assessment and risk prevention.

Chapter V

Conclusions

This study shows that the surface morphologies, internal structure, and texture of basaltic lava flows are intimately linked through the processes of cooling, degassing and groundmass crystallization that occur at different stages of the eruption, emplacement and solidification of the magma and lava. In the following, the main outcomes of each chapter are summarized (5.1). Those are then combined in a general scheme which links the main processes that control the texture of solidified lava (5.2). The significance of this study is finally highlighted (5.3), along with its implication for the understanding of basaltic volcanic systems and the improvement of hazard assessment and risk prevention.

5.1 SUMMARY OF RESULTS

Lavas produced by the AD 1783-84 Laki eruption display a wide range of surface morphologies. The lava surface changed from spiny, to slabby, and then to rubbly pāhoehoe during the emplacement of single flows, through crust disruption at the active flow front and compression from the back. Shelly pāhoehoe is a minor lava surface type that formed during the outflow of gas-rich lava from the fissure at an early stage of the eruptive episodes. During the emplacement of the flows, the rubble was piled up in ridges when lava advance was obstructed or constricted, which led, in some cases, to large breakouts of fluid lava from the flow interior. Episodes of intense lava production rates along the fissure, which corresponded to the opening of new fissure segments, caused extensive surface compression of rubbly sheet pāhoehoe lobes emplaced on the flat terrain of the coastal plain, and induced major lava outbreaks. After each episode of surface disruption, a thick crust formed underneath the rubble during lava inflation, which allowed an extensive transport system to develop within the flow interiors. Surface crustal slabs range from 5 cm to 1.5 m in thickness, which suggest inflation durations of 20 minutes to 2 weeks before crust breakage occurred.

The Laki lavas contain 20–40 vol.% of microlites that mainly formed in the early stages of flow, less than 100 m from the vent (Chapter 3). This sudden crystallization

responds to the undercooling of the melt by 20–40°C driven by the shallow, <200 m deep, exsolution of ~1 wt.% H_2O during magma ascent, which is recorded by the formation of a ~10% anorthite gap across plagioclase phenocryst margins, and the delay of clinopyroxene crystallization in the erupted flows. Microlites are dominantly composed of skeletal plagioclases which impacted on the mechanical behaviour of fluid lava to cause the formation of spiny lava surfaces and the repetitive fracture of lava crust. It is thus inferred that degassing-induced groundmass crystallization was the dominant controlling factor for the formation of rubbly pāhoehoe surfaces along the Laki lava flows.

The shelly surface of early-formed gas-rich lava produced along the Laki fissure changed down-flow to spiny as the lava lost gas and crystallized, acquiring a greater yield strength. The small crystal content change of the fluid lava during further transport to up to 60 km from the vent implies that the lava was thermally insulated under the thick rubbly layer that formed over the lava surface during flow emplacement. It is estimated from down-flow changes in glass compositions and thermodynamic modelling that the lava transport cooling rates averaged 0.2°C/km. This suggests that, to a certain extent, the temperature of the magma and liquid lava remained constant throughout the eruption, which permitted the flows to travel to distances far from the vent. The ultimate length and aerial extent of the lava flow-field were thus only limited by the volume of lava emitted at the vent.

It is thus inferred that the main changes in the intrinsic properties of the lava occurred close to the vent. Down-flow transitions in surface morphologies were correlated with changes in the amount of stress imparted on the fluid lava which had acquired substantial yield strength through microlite formation. The shearing forces imposed on the lava crust during inflation resulted in detachment of small crustal slabs at the flow top. Increasing lava pressure in the lobes, as induced by the resistance of the viscous layer at the base of the crust to inflation, drove large crust disruption followed by major lava outbreak when

the lava yield strength was overcome. Field evidence shows that this process occurred at different scales that ranged from the surface brecciation of lobes forming at the active flow front to the large-scale detachment of plates on top of large sheet lobes (Chapter 2). The piling of rubble into ridges resulted from the large compressional forces induced by obstacles to the flow advance or was linked to increases in lava input, as discussed above.

Rubbly pāhoehoe lavas were observed among basaltic flow-fields other than Laki. These were produced by eruptions with varied characteristics, causing the lava to develop a wider range of surface morphologies and emplacement mechanisms (Chapter 4). Young lava flow-fields in Reykanes Peninsula in southwest Iceland show surface and internal structures that are intermediate between rubbly pāhoehoe and 'a'ā. The lava fields are mainly composed of multiple overlapping flows with central open-channels and spatially restricted hummocky margins that contrast with the large sheet lobes formed during the Laki eruption. They were emplaced on higher slopes than the bulk of the Laki lava (1–10° in opposition to <0.5°), which accounts, in part, for the formation of shear gradients across the flows that led to channel formation. Their size and structure as compared, for example, to products from the Mauna Loa 1984 eruption, suggest eruption durations of less than a few months. Many pāhoehoe sheet lobes exposed in the Grande Ronde Basalt from the Columbia River Province in northwest United States feature a thick upper layer of pāhoehoe crust fragments. Flows with thick rubbly tops lack well-defined vesicular upper crusts and have large intrusions of core lava into the rubble, which is typical of high yield strength lavas. These lava fields formed over near-flat terrain during months of sustained activity.

Vertical sections through Laki, Reykanes Peninsula, and Grande Ronde lavas were studied using petrographical observations and crystal size distribution analysis of groundmass plagioclases. Results reveal a common trend of increasing plagioclase average size and decreasing number density with distance from the margins of the flows, which are

balanced by the total crystal content. As calculated from the CSDs, plagioclase nucleation and growth rates decreased from about 10^{1} to 10^{-1} no./cm^3/s and 10^{-7} to 10^{-10} cm/s respectively as the solidification front propagated inwards, which indicates that the degrees of melt undercooling decreased during lava solidification, reaching near-equilibrium conditions in the centre of the lobes. The bulk lava composition governed the proportions of plagioclase crystallizing in the cooling lava, which was seen by the relatively higher plagioclase/clinopyroxene content of MgO-poor Grande Ronde lavas compared to Laki and Reykjanes Peninsula lavas.

Lava internal textures were also, to some extent, dependent on eruption processes since those determined the initial amount and size of microlites in the flows, which controlled the ultimate size each crystal could reach after total crystallization. The bulk of the microlites present in Reykanes Peninsula lavas formed in the early stages of flow, as for Laki lavas. In addition, when present in the lavas, plagioclase phenocrysts displayed an ~ 10% anorthite gap similar to that observed in Laki lavas. This suggests microlite crystallization driven by substantial lava undercooling at the vent, which may have been induced by gas loss at a late stage of magma ascent (see above).

Textural differences between sections can be linked to flow emplacement processes as inferred from flow-field organization, lava surface morphologies and internal structures. Prolonged transport of lava in open-channels was linked to the formation of high number densities of plagioclase microlites (> 10^{10} no./cm^{-4}) with, consequently, low average sizes (< 30 μm), as shown by lavas forming the Kapelluhraun flow-field. The rapid internal solidification rates of an open-channel outbreak (i.e., section R15) was attributed to high lava heat loss during transport and the incorporation of cool rubble in the lava core during the 'a'ā-style emplacement of the lobe. Alternatively, this pattern could have resulted from large degrees of lava undercooling at the vent leading to melt re-equilibration through intense crystal nucleation during lava transport and solidification. The emplacement of

flows under low effusion rates and over a significant amount of time (i.e., section R19) increased the duration of lobe growth by inflation, decreasing the internal solidification rates of the lava and yielding important inwards textural coarsening. The infiltration of water in fractures through the upper crust of lava flows emplaced in areas with extensive river systems increased the lava internal solidification rates, coinciding with formation of hackly jointing. This was observed in sections L7 and L13 through Laki lava and section AD across Grande Ronde lava.

The textural study of rubbly pāhoehoe lava lobes emplaced under different conditions thus reveals the strong link between eruptive dynamics, lava flow emplacement mechanisms, and the surface and internal structure and texture of solidified lava. Plagioclase average size and number density are proven to be key parameters for depicting textural variations across and between sections and relating them to emplacement processes.

Pāhoehoe, 'a'ā, and rubbly pāhoehoe morphological types can thus be readily identified from the texture of groundmass plagioclases in the lava, which provides a tool for inferring eruption and emplacement processes from textural measurements of lava samples from the surface and interior of ancient flows. Plagioclases in pāhoehoe and 'a'ā lava typically have low and high number densities (or crystal nuclei) respectively ($< 10^9$ no./cm^4 compared to $> 10^{11}$ no./cm^4). Crystals tend to be more elongate (higher length/width ratios) in surface samples from pāhoehoe lavas compared to those from rubbly and 'a'ā lavas due to lower crystal number densities. The number density and the total crystal content determine the average size of the crystals. Accordingly, pāhoehoe lava shows, typically, higher average crystal sizes than 'a'ā lava that may reach 100 μm in slowly-cooled lava core, by contrast to <50 μm in cores of 'a'ā lava lobes with similar thickness. Rubbly pāhoehoe lava shows intermediate characteristics that vary with eruption characteristics and flow emplacement mechanisms as presented above.

5.2 MAIN PROCESSES THAT AFFECT LAVA FLOW TEXTURES

This study reveals the processes that have a major influence on the mode of degassing and cooling of magma and lava during eruption, and therefore control the rates of groundmass crystallization, and thus the final lava texture. Figure 5.1 presents in a schematic way these key factors and their link, highlighting the main controlling parameters:

- The amount of gas dissolved in the magma at depth (1), which depends on the geodynamical volcanic setting and the evolution of magma at depth. For instance, magma differentiation can lead to higher proportions of dissolved gas in the melt by concentrating the gas into the liquid phase, whereas gas can be passively lost by the magma during stagnation at shallow depth or slow migration to the surface.

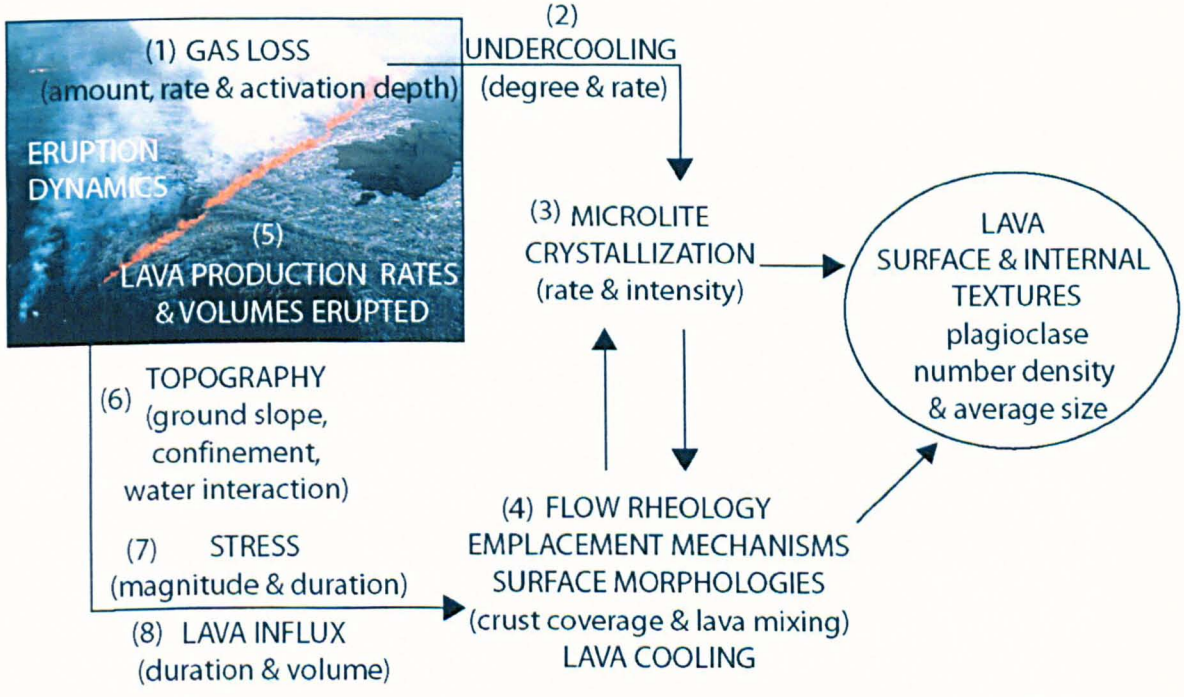

Figure 5.1: General sketch of the main processes that intervene in the making of basaltic lava textures. Numbers are referred to in text. Note major impact of ascent degassing (1) on melt undercooling (2), crystallization kinetics (3) and thus lava rheology (4). Other acting factors are related to the impact of lava effusion rates (5) and topography (6) on lava deformation regime (7) and characteristics of lava supply (8). This study shows how lava textures, through the study of the characteristics of groundmass crystals (composition, shape, CSD parameters) and the composition of groundmass glasses, can be used to determine the relative importance of each factor on the resulting lava rheology and emplacement style.

- The rate of gas exsolution (1) that will vary with magma ascent rates and the viscosity of the liquid phase. This will determine the rate of magma undercooling (2) and thus control the amount of crystallization required for melt re-equilibration, and then the extent of microlite formation in the flows (3). Rapid gas loss will result in large degrees of over-saturation of the melt, which favours high nucleation/growth rates when the lava finally crystallises.
- The bulk composition of the magma and its temperature that will determine the bulk viscosity of the lava and its degree of undercooling relative to plagioclase.
- The rate and intensity of microlite crystallization (3) that will control lava rheology (4) and increase the resistance of lava to flow (i.e., yield strength). Large microlite contents will promote surface crust disruption, and thus increase radiative heat losses and high lava cooling rates during transport. On the other hand, crystallization releases latent heat, which can slow the rates of lava cooling and lower the melt viscosity. It seems obvious that the rate of these processes will determine their effect on the lava; these relations would deserve further investigation.
- The lava production rates from the vent (5) that govern, along with ground slope (6), the lava flow rates and the stress imposed on lava during transport (7). This may induce lava surface disruption (4), which may increase lava cooling rates. It is to be noted that lavas produced by the Laki eruption, despite their high degree of surface disruption, were transported with little cooling. This was induced by the low shear stresses imposed on the lava that caused the pile of surface rubble to behave as an additional crust, thus insulating the fluid lava transported underneath. It is therefore deduced that the use of lava surface disruption as an indicator of high lava cooling rates, which could imply conditions of cooling-limited flow length, should be made with care.

- The duration of magma output (5) controls the structure of the lava flow-field and the lava emplacement mechanisms. Lavas produced by long-lasting eruptions develop, in general, thermally efficient transport systems that correspond to a large network of crusted tubes. The volume of lava erupted and thus emplaced at any location (8) may represent the controlling parameter in this process. In large-volume inflated flows, the fluid lava in the interior is positioned at large distances from the cooling margins, which leads to low internal cooling rates and promotes the development of large internal pathways for transporting fluid lava. Emplacement on low slopes (6) will also favour long durations of lava supply at any location and the development of large sheet lobes.

5.3 MAIN ACHIEVEMENTS AND IMPLICATIONS

This study has showed how lava flow characteristics at different scales (flow-field architecture, surface morphologies, internal structure and vesicular and jointing pattern, crystal and glass compositional variations, crystal shape and crystal size distribution—CSD) can be used to characterize the mode of emplacement of lava flows. This section stresses the main achievements of this study and their implications for the understanding of basaltic volcanism and the assessment and monitoring of hazards around volcanoes.

5.3.1 Development of petrological tools to study lava flow emplacement and controlling factors

First, this study has improved the way petrological data can be used to identify, quantify, and model the processes that control lava flow rheology and emplacement style:

- Compositional profiles across early-formed (phenocrysts) plagioclase crystals inform about changes in the conditions of growth of the crystals. In particular, in the absence of evidence for magma mixing or intense magma cooling, sharp

gradients in the anorthite content may be related to the rapid depletion of water from the melt (a gap of An=10% may represent lost of ~1 wt.% H_20), which suggest the occurrence of shallow, degassing-induced crystallization. The additional presence of large amounts of small plagioclase crystals in the groundmass which have the composition of phenocryst rims, suggest rapid, nucleation-dominated groundmass crystallization in conditions of marked undercooling (> 20°C), an expression of very shallow, decompression-driven melt degassing.

- The composition of groundmass glasses preserved in rapidly quenched tephra clasts and lava selvages can be used to track the progression of groundmass crystallization in the fluid lava during transport from the vent to the distal front (in case of homogeneous bulk composition). This crystallization responds primarily to the cooling of the liquid lava upon transport, and compositional variations can thus be used to estimate the thermal efficiency of the transport system established within the flows.
- Textural and petrological analysis of lava samples collected at different levels in vertical sections across flows can be used to study the mode of inward cooling and solidification of the lava. A useful tool that permits to quantify these variations is the CSD analysis of groundmass plagioclases observed on backscatter images of thin-sections of these lava samples. Based on a comparative study of sections across flows whose emplacement style can be inferred from their surface morphologies, this can be used to interpret the mode of emplacement of lavas whose surface is not exposed. It thus provides a way to study the emplacement mechanisms of flows from ancient eruptions, although other interfering parameters are involved such as the initial lava temperature (liquid temperature), the bulk magma composition, and processes occurring

during solidification such as the circulation of water within fractures in the lava's upper crust. Additional work on a larger range of sections than those studied here (see Chapter 4) could help identify more precisely the separate effect of each of these parameters on the final lava texture.

5.3.2 Identification of new lava type: rubbly pāhoehoe

Second, using these tools complemented by detailed field observations and aerial photo analysis, this study has identified a "new" lava type, named rubbly pāhoehoe. Rubbly pāhoehoe lavas are identified by a fragmented upper surface, an internal structure characterised by upper and basal vesicular crusts and a dense lava core with or without vesicular segregation features, and a smooth, pāhoehoe-like base. Forming an important fraction of lavas produced by the Laki eruption, the largest basaltic eruption ever witnessed, these flows demonstrate low cooling and crystallization rates during transport, similar to those measured along Hawaiian pāhoehoe lavas. Also observed on small flows on Reykjanes Peninsula in Iceland, and, perhaps more importantly, along the "giant" flows of the Columbia River Basalts, they thus represent a mode of lava transport that has to be considered for small basaltic eruptions as well as for dramatic, flood-like eruptions on the Earth and other planets (e.g., Keszthelyi et al., 2000, 2001, 2004, 2006).

Rubbly pāhoehoe lavas represent an interesting lava type for that despite a fragmented surface layer, they develop an emplacement mode dominated by endogeneous growth and rapid formation of internal pathways, key features of pāhoehoe lavas (e.g., Self et al., 1997). This implies that repetitive crust disruption at the surface of lava flows does not necessary affect the temperature and thus viscosity of the fluid lava core that are critical for the final distance reached by the flows. The increase in lava cooling requires that surface fragments become spatially detached on the flow surface (and not piled up such as at the surface of rubbly pāhoehoe lavas), so as to allow the lava core to be exposed directly to the

air. This is of course promoted by high shear rates and low resistance of the lava crust to the pull exerted by underlying moving lava. The mixing of cool fragments in the moving lava and the stirring and shearing of the fluid lava during transport are additional factors that enhance cooling and crystallization rates along 'a'ā flows.

The starting question may be asked again: what is(are) the origin(s) of rubbly pāhoehoe lavas? The major factor that this study highlights is the presence of a finite yield strength in the lava that promotes crust brecciation and formation of velocity gradients and shear zones. This in turn may be induced by intense groundmass crystallization triggered by degassing during shallow magma ascent. Whether or not the lava will develop channels during flow and adopt a more 'a'ā-like behaviour with high heat losses and cooling-limited flow advance is mainly determined by the pre-existing topography and the longevity and continuity of the eruption.

Rubbly pāhoehoe lavas are probably not restricted to Iceland. The observation of some in the Columbia River Basalts (this study) and patches of spiny, slabby or "toothpaste" pāhoehoe lavas on Hawaii (e.g., Peterson & Tilling, 1980; Rowland & Walker, 1987) suggests that this "intermediate" lava type may be present elsewhere. They seem to be, as far as it is currently known, best developed along the Laki lava flows, although this probably results from the good conditions of surface exposure of the flows and their unusual size. Additional work on other lava flows in the world will thus probably reveal other places where rubbly pāhoehoe lavas formed, and help define the complete set of conditions that lead to their formation. It is stressed that the identification of these flows is important for the assessment of the emplacement style and heat budget of lavas that may be about to be produced from a given volcanic centre. For example, until now, lavas with fragmented surfaces were generally assumed to be of 'a'ā type, and, more importantly, associated with high down-flow cooling and crystallization, and cooling-limited advance. This may not be the case. This study thus stresses the need of improved characterisation of

lava surfaces and crust characteristics to better assess syn-emplacement cooling that may lead to major rheological changes, and, by consequence, control flow paths and the final length of lava flows.

5.3.3 Study of the dynamics of basaltic eruptions and hazard assessment

A third main achievement of this study is the identification of a clear link between the textures, field characteristics, and thus emplacement mechanisms of lava flows, and the eruption dynamics. This comes from the influence of shallow, degassing-driven processes on the degree of undercooling of the melt and thus on the resulting amount of groundmass crystals in the lava and its rheology. This study proposes some tools belonging to petrology and textural analysis to understand these processes. With further quantification of the rates at which these processes operate and how these vary with magma composition among other parameters, it may be possible to use these relations to develop a multitude of interpretation, prediction and monitoring tools (see also end of Chapter 4). For example, it may be possible to predict the style of emplacement of lava flows from an assessment of the dynamics of ascent of the magma. Inversely, studying the structure and microtextures of the lava produced by an eruption may be used to infer the geometry of the shallow-seated magma system that control magma ascent rates, and thus degassing and crystallization kinetics. The study of these parameters during an eruption may permit to predict changes in the eruptive activity and thus help in risk management and evacuation procedures for areas susceptible to be inundated by lava.

Results from this study further emphasize that the down-flow evolution of lavas is mostly dependant on cooling processes that are controlled by the initial properties of the lava (temperature, degree of undercooling, composition and groundmass crystal content) and the degree of disruption of the lava crust influenced by effusion rates and the topography (ground slope, flow confinement). It thus supports the recent development of

thermal imagery techniques to quantify the heat losses experienced by flowing lava (e.g., Harris et al., 2005; Coppola et al., 2005). Moreover, it stresses the need to combine these studies with compositional and textural analysis of lava samples. It is indeed essential to link thermal and rheological measurements to processes that occur in the lava at microscopic scale, in order to improve our understanding of crystallization kinetics and its sensitivity of response to measurable surface temperature changes. Also, a more accurate quantification of the kinetics of groundmass crystallization during lava flow emplacement would greatly improve the accuracy of physical models that often rely on other thermodynamical models based on the assumption of chemical equilibrium, which is clearly not maintained in rapidly emplaced flows, especially in near-vent areas. More quantitative data needs to be acquired to constrain the timing of groundmass crystallization and its rheological effects.

Finally, it is expected that the application of the methods developed in this thesis to other lava flow-fields will help define more precisely what controls the conditions of emplacement of lava flows, and provide adequate data to improve and constraints models of eruption and lava flow dynamics. This would undeniably lead to more efficient management of eruptive crisis. As the population living close to volcanoes is continuously rising, there will be an increasing demand for accurate and real-time prediction and monitoring procedures. In the future, it can be envisaged, for example, the development of detailed hazard maps showing variations of flow paths and advance rates as a function of eruption intensity or lava properties measured at the vent, and the development of monitoring techniques allowing real-time measurement of lava core temperature and rheological properties, and prediction of flow behaviour. These techniques will contribute to reduce damages linked to lava flow hazards, and allow better planning of eventual evacuation procedures and relocation for the endangered population.

References

Allègre, C. J., Provost, A., and Jaupart, C., 1981, Oscillatory zoning - a pathological case of crystal-growth: Nature, v. 294, no. 5838, p. 223–228.

Aubele, J. C., Crumpler, L. S., and Elston, W. E., 1988, Vesicle zonation and vertical structure of basalt flows: Journal of Volcanology and Geothermal Research, v. 35, p. 349–374.

Bailey, J., Harris, A. J. L., Dehn, J., Calvari, S., and Rowland, S. K., 2005, The changing morphology of an open lava channel on Mt. Etna: Bulletin of Volcanology (in press).

Beattie, P., 1993, Olivine-melt and orthopyroxene-melt equilibria: Contributions to Mineralogy and Petrology, v. 115, p. 103–111.

Bell, J. D., and Humphries, D. J., 1972, Lakagigar fissure eruption: Progress in experimental petrology, National Environmental Council UK Publication, Series D, v. 2, p. 110–112.

Boudreau, A. E., 1999, PELE; a version of the MELTS software program for the PC platform: Computers & Geosciences, v. 25, no. 2, p. 201–203.

Brandeis, G., Jaupart, C., and Allègre, C. J., 1984, Nucleation, crystal-growth and the thermal regime of cooling magmas: Journal of Geophysical Research, v. 89, no. B12, p. 161–177.

Brandeis, G., and Jaupart, C., 1987a, The kinetics of nucleation and crystal-growth and scaling laws for magmatic crystallization: Contributions to Mineralogy and Petrology, v. 96, no. 1, p. 24–34.

Brandeis, G., and Jaupart, C., 1987b, Crystal sizes in intrusions of different dimensions; constraints on the cooling regime and the crystallization kinetics, Geochemical Society Special Publications no.1, p. 307–318.

Bücker, C. J., Cashman, K. V., and Planke, S., 1999, Physical and magnetic characterization of aa and pahoehoe flows; Hole 990A, *in* Proceedings of the Ocean Drilling Program, Scientific Results, v. 163, p. 41–49.

Burkhard, D. J. M., 2002, Kinetics of crystallization; example of micro-crystallization in basalt lava: Contributions to Mineralogy and Petrology, v. 142, no. 6, p. 724–737.

Calvari, S., Neri, M., and Pinkerton, H., 2002, Effusion rate estimations during the 1999 summit eruption on Mount Etna, and growth of two distinct lava flow fields: Journal of Volcanology and Geothermal Research, v. 119, no. 1–4, p. 107–123.

Cashman, K. V., 1990, Textural constraints on the kinetics of crystallization of igneous rocks: Reviews in Mineralogy, v. 24, p. 259–314.

Cashman, K. V., 1993, Relationship between plagioclase crystallization and cooling rate in basaltic melts: Contributions to Mineralogy and Petrology, v. 113, no. 1, p. 126–142.

Cashman, K. V., and Kauahikaua, J. P., 1997, Re-evaluation of vesicle distributions in basaltic lava flows: Geology, v. 25, no. 5, p. 419–422.

Cashman, K. V., and Marsh, B. D., 1988, Crystal Size Distribution (CSD) in rocks and the kinetics and dynamics of crystallization .2. Makaopuhi Lava Lake: Contributions to Mineralogy and Petrology, v. 99, no. 3, p. 292–305.

Cashman, K., and Blundy, J., 2000, Degassing and crystallization of ascending andesite and dacite: Philosophical Transactions of the Royal Society of London Series a-Mathematical Physical and Engineering Sciences, v. 358, no. 1770, p. 1487–1513.

Cashman, K. V., Thornber, C., and Kauahikaua, J. P., 1999, Cooling and crystallization of lava in open channels, and the transition of pahoehoe lava to a'a: Bulletin of Volcanology, v. 61, no. 5, p. 306–323.

Costa, A., Blake, S., and Self, S., 2006, Segregation processes in vesiculating crystallizing magmas: Journal of Volcanology and Geothermal Research (in press).

Couch, S., Sparks, R. S. J., and Carroll, M. R., 2003, The kinetics of degassing-induced crystallization at Soufriere Hills volcano, Montserrat: Journal of Petrology, v. 44, no. 8, p. 1477–1502.

Crisp, J., and Baloga, S., 1990, A model for lava flows with two thermal components: Journal of Geophysical Research, v. 95, no. B2, p. 1255–1270.

Crisp, J., and Baloga, S., 1994, Influence of crystallization and entrainment of cooler material on the emplacement of basaltic aa lava flows: Journal of Geophysical Research, v. 99, no. B6, p. 11,819–11,831.

Crisp, J., Cashman, K. V., Bonini, J. A., Hougen, S. B., and Pieri, D. C., 1994, Crystallization history of the 1984 Mauna Loa lava flow: Journal of Geophysical Research, v. 99, no. B4, p. 7177–7198.

Danyushevsky, L. V., 2001, The effect of small amounts of H_2O on crystallisation of mid-ocean ridge and backarc basin magmas: Journal of Volcanology and Geothermal Research, v. 110, p. 265–280.

Davis, M. J., and Ihinger, P. D., 1998, Heterogeneous crystal nucleation on bubbles in silicate melt: American Mineralogist, v. 83, no. 9-10, p. 1008–1015.

DeGraff, J. M., Long, P. E., and Aydin, A., 1989, Use of joint-growth directions and rock textures to infer thermal regimes during solidificaton of basaltic lava flows: Journal of Volcanology and Geothermal Research, v. 38, no. 3-4, p. 309–324.

Dixon, J. E., Stolper, E. M., and Delaney, J. R., 1988, Infrared spectroscopic measurements of CO_2 and H_2O in Juan de Fuca Ridge basaltic glasses: Earth and Planetary Science Letters, v. 90, p. 87–104.

Dixon, J. E., Stolper, E. M., and Holloway, J. R., 1995, An experimental study of water and carbon dioxide solubilities in mid-ocean ridge basaltic liquids; Part I, Calibration and solubility models: Journal of Petrology, v. 36, no. 6, p. 1607–1631.

Donaldson, C. H., 1979, An experimental investigation of the delay in nucleation of olivine in mafic magmas: Contributions to Mineralogy and Petrology, v. 69, no. 1, p. 21–32.

Downes, M. J., 1974, Sector and oscillatory zoning in calcic augites from M. Etna, Sicily: Contributions to Mineralogy and Petrology, v. 47, no. 3, p. 187–196.

Dowty, E., 1980a, Crystal-chemical factors affecting the mobility of ions in minerals: American Mineralogist, v. 65, no. 1–2, p. 174–182.

Dowty, E., 1980b, Crystal growth and nucleation theory and the numerical simulation of igneous crystallization, Physics of Magmatic Processes: Princeton University Press, Princeton, p. 419–486.

Eberl, D. D., Kile, D. E., and Drits, V. A., 2002, On geological interpretations of crystal size distributions constant vs. proportionate growth: American Mineralogist, v. 87, p. 1235–1241.

Einarsson, T., 1949, The eruption of Hekla 1947–1948: IV, 3.The flowing lava. Studies of its main physical & chemical properties: Reykjavik, Soc. Scientarium Islandica, p. 1–70.

Johannesson, H., Einarsson, S., 1988. The age of Illahraun at Svartsengi. Fjolrit Natturufraedistofnunar, v. 7, p. 1–11.

Einarsson S, and Johannesson H, 1989, The age of Arnarsetur lava on the Reykjanes Peninsula. Fjolrit Natturufraedistofnunar, no 8.

Faure, F., and Schiano, P., 2004, Crystal morphologies in pillow basalts; implications for mid-ocean ridge processes: Earth and Planetary Science Letters, v. 220, p. 331–344.

Friedman, R. C., 1998, Petrologic clues to lava flow emplacement and post-emplacement processes [Ph.D. thesis]: University of Hawaii, Honolulu, Hawaii.

Gaetani, G. A., Grove, T. L., and Bryan, W. B., 1992, The influence of water on the petrogenesis of subduction-related igneous rocks: Nature, v. 365, no. 6444, p. 332–334.

Geschwind, C. H., and Rutherford, M. J., 1995, Crystallization of microlites during magma ascent - the fluid mechanics of 1980-1986 eruptions at Mount-St-Helens: Bulletin of Volcanology, v. 57, no. 5, p. 356–370.

Gibb, F. G. F., 1974, Supercooling and the crystallization of plagioclase from a basaltic magma: Mineralogical Magazine and Journal of the Mineralogical Society, v. 39, no. 306, p. 641–653.

Goff, F., 1996, Vesicle cylinders in vapor-differentiated basalt flows: Journal of Volcanology and Geothermal Research, v. 71, p. 167–185.

Gottsmann, J., Harris, A. J. L., and Dingwell, D. B., 2004, Thermal history of Hawaiian pahoehoe lava crusts at the glass transition; implications for flow rheology and emplacement: Earth and Planetary Science Letters, v. 228, no. 3-4, p. 343–353.

Griffiths, R. W., 2000, The dynamics of lava flows: Annual Review of Fluid Mechanics, v. 32, p. 477–518.

Grönvold, K., 1984, The petrochemistry of the Laki lava flow, *in* Einarsson, T., Gudbergsson, G.M., Gunnlaugsson, G.A., Rafnsson, S. and Thorarinsson, S., eds., Skaftáreldar 1783-1784: Ritgerdir og Heimildir. Mál og Menning, Reykjavík, pp 49–58.

Grove, T. L., and Bence, A. E., 1979, Experimental study of pyroxene-liquid interaction in quartz-normative basalt 15597, *in* Proceedings Lunar Science Conference 8th, p. 1549–1579.

Grove, T. L., Kinzler, R. J., and Bryan, W. B., 1992, Fractionation of mid-ocean ridge basalt (MORB): Geophysical Monograph no. 71, American Geophysical Union, p. 281–310.

Gudmundsson, A., 1987, Formation and mechanics of magma reservoirs in Iceland: Geophysical Journal of the Royal Astronomical Society, v. 91, p. 27–41.

Gudmundsson, A., 2000, Emplacement of dikes, sills and crustal magma chambers at divergent plate boundaries: Tectonophysics, v. 176, p. 257–275.

Guest, J. E., Kilburn, C. R. J., Pinkerton, H., and Duncan, A. M., 1987, The evolution of lava flow-fields; observations of the 1981 and 1983 eruptions of Mount Etna, Sicily: Bulletin of Volcanology, v. 49, no. 3, p. 527–540.

Guilbaud, M. N., Self, S., Thordarson, T., and Blake, S., 2005, Morphology, surface structures, and emplacement of lavas produced by Laki, AD. 1783-1874: Geological Society of America Special Paper no. 396, p. 81–102.

Hammer, J. E., Cashman, K. V., and Voight, B., 2000, Magmatic processes revealed by textural and compositional trends in Merapi dome lavas: Journal of Volcanology and Geothermal Research, v. 100, no. 1-4, p. 165–192.

Hammer, J. E., and Rutherford, M. J., 2002, An experimental study of the kinetics of decompression-induced crystallization in silicic melt: Journal of Geophysical Research, v. 107, no. B1, p. ECV 8–1.

Hammer, J. E., Rutherford, M. J., and Hildreth, W., 2002, Magma storage prior to the 1912 eruption at Novarupta, Alaska: Contributions to Mineralogy and Petrology, v. 144, no. 2, p. 144–162.

Harris, A. J. L., Flynn, L. P., Matias, O., Rose, W. I., and Cornejo, J., 2004, The evolution of an active silicic lava flow-field: an ETM+ perspective: Journal of Volcanology and Geothermal Research, v. 135, p. 157–168.

Harris, A. J. L., Bailey, J., Calvari, S., and Dehn, J., 2005, Heat loss measured at a lava channel and its implications for down-channel cooling and rheology: Geological Society of America Special Paper no. 396, p. 125–146.

Heliker, C., and Mattox, T. N., 2003, The first two decades of the Pu'u 'O'o-Kupaianaha eruption; chronology and selected bibliography: United States Geological Survey Professional Paper no. 1676, p. 1–27.

Helz, R. T., and Thornber, C. R., 1987, Geothermometry of Kilauea Iki lava lake, Hawaii: Bulletin of Volcanology, v. 49, no. 5, p. 651–668.

Helz, R. T., Banks, N. G., Heliker, C., Neal, C. A., and Wolfe, E. W., 1995, Comparative geothermometry of recent Hawaiian eruptions: Journal of Geophysical Research, v. 100, no. B9, p. 17,367–17,657.

Helz, R. T., Heliker, C., Hon, K., Mangan, M. T., Swanson, D. A., and Takahashi, T. J., 2003, Thermal efficiency of lava tubes in the Pu'u 'O'o-Kupaianaha eruption: United States Geological Survey Professional Paper no. 1676, p. 105–120.

Higgins, M. D., 2000, Measurement of crystal size distributions: American Mineralogist, v. 85, no. 9, p. 1105–1116.

Herrmann, W., and Berry, R. F., 2002, MINSQ – a least squares spreadsheet method for calculating mineral proportions from whole rock major element analyses, Geochemistry: Exploration, Environment, Analysis, v. 2, p. 361–368.

Hon, K., Kauahikaua, J., Denlinger, R., and Mackay, K., 1994, Emplacement and inflation of pāhoehoe sheet flows; observations and measurements of active lava flows on Kilauea Volcano, Hawaii: Geological Society of America Bulletin, v. 106, no. 3, p. 351–370.

Hon, K., Gansecki, C. A., and Kauahikaua, J., 2003, The transition from 'a'a to pahoehoe crust on flows emplaced during the Pu'u 'O'o-Kupaianaha eruption: United States Geological Survey Professional Paper no. 1676, p. 89–103.

Hooper, P. R., Johnson, D. M., and Conrey, R. M., 1993, Major and trace element analyses of rocks and minerals by automated X-ray spectrometry: Washington State University, Geology Department, Open File Report, 36 p.

Hooper, P. R., Mahoney, J. J., and Coffin, M. F., 1997, The Columbia River flood basalt provinces; current status: Geophysical monograph no. 100, American Geophysical Union, p. 1–27.

Hoover, S. R., Cashman, K. V., and Manga, M., 2001, The yield strength of subliquidus basalts - experimental results: Journal of Volcanology and Geothermal Research, v. 107, p. 1–18.

Hulme, G., 1974, The interpretation of lava flow morphology: The Geophysical Journal of the Royal Astronomical Society, v. 39, no. 2, p. 361–383.

Jakobsson, S.P., Jonsson, J. and Shido, F., 1978, Petrology of the western Reykjanes Peninsula, Iceland. Journal of Petrology, v. 19, no. 4, p. 669–705.

Jonsson, J, 1974, Obrinnisholar. Natturufraedingurinn, v. 44, p. 109–119.

Jonsson, J., 1978, Jardfraedikortaf Reykjanesskaga, OS JHD 7831, 303p.

Jonsson, J., 1979, Kristnitökuhraunid (On the age of the Svinahraun lava flow), Natturufraedingurinn, v. 49, p. 46–50.

Jonsson J, 1983, Volcanic eruptions in historical time on the Reykjanes Peninsula, southwest Iceland. Natturufraedingurinn, v. 52, p. 127–139.

Katz, M. G., and Cashman, K. V., 2003, Hawaiian lava flows in the third dimension: Identification and interpretation of pahoehoe and 'a'a distribution in the KP-1 and SOH-4 cores: Geochemistry Geophysics Geosystems, v. 4, no. 2, 8705.

Kauahikaua, J. P., Sherrod, D. R., Cashman, K., Heliker, C., Hon, K., Mattox, T., and Johnson, J. A., 2003, Hawaiian lava-flow dynamics during the Pu'u 'O'o-Kupaianaha eruption; a tale of two decades: United States Geological Survey Bulletin no. 1676, p. 63–87.

Keszthelyi, L., 1995, Measurements of the cooling at the base of pahoehoe flows: Geophysical Research Letters, v. 22, no. 16, p. 2195–2198.

Keszthelyi, L., 2000, The brecciated lava flows of the Kerguelen Plateau: what are they?: AGU meeting, Eos, Transactions, American Geophysical Union, 8:S431.

Keszthelyi, L., 2002, Classification of the mafic lava flows from ODP Leg 183, *in* Proceedings Ocean Drilling Program, Scientific Results, v. 183, p. 1–28.

Keszthelyi, L., and Denlinger, R., 1996, The initial cooling of pāhoehoe flow lobes: Bulletin of Volcanology, v. 58, no. 1, p. 5–18.

Keszthelyi, L., and Thordarson, T., 2000, Rubbly pāhoehoe: A previously undescribed but widespread lava type transitional between 'a'ā and pāhoehoe: Geological Society of America Abstracts with Programs, v. 32, no. 7, Abstract no. 52593.

Keszthelyi, L., and Self, S., 1998, Some physical requirements for the emplacement of long basaltic lava flows: Journal of Geophysical Research, v. 103, no. B11, p. 27,447–27,464.

Keszthelyi, L., McEwen, A.S., and Thordarson, T., 2000, Terrestrial analogs and thermal models for Martian flood lavas: Journal of Geophysical Research, v. 105, p. 15,027–15,049.

Keszthelyi, L., Thordarson, T., and Self, S., 2001, Rubbly Pāhoehoe: implications for flood basalt eruptions and their atmospheric effects: AGU fall meeting, Eos, Transactions, American Geophysical Union, 82:F1407.

Keszthelyi, L., Thordarson, T., McEwen, A., Haack, H., Guilbaud, M., Self, S., Rossi, M., 2004, Icelandic analogs to Martian flood lavas: Geochemistry, Geophysics, Geosystems, v. 5, no. 11.

Keszthelyi, L., Self, S., and Thordarson, T., 2006, Flood lavas on Earth, Io and Mars: Journal of the Geological Society, London, v. 163, p. 253–264.

Kilburn, C. R. J., 1989, Surfaces of aa flow-fields on Mount Etna, Sicily; morphology, rheology, crystallization and scaling phenomena, *in* International Union of Geodesy and Geophysics XIX general assembly 1987, Springer Verlag, Berlin, p. 129–156.

Kirkpatrick, R. J., 1975, Crystal growth from the melt; a review: American Mineralogist, v. 60, no. 9–10, p. 798–814.

Kirkpatrick, R. J., 1977, Nucleation and growth of plagioclase, Makaopuhi and Alae lava lakes, Kilauea Volcano, Hawaii: Geological Society of America Bulletin, v. 88, no. 1, p. 78–84.

Kirkpatrick, R. J., Klein, L., Uhlmann, D. R., and Hays, J. F., 1979, Rates and processes of crystal growth in the system anorthite-albite: Journal of Geophysical Research, v. 84, no. B7, p. 3671–3676.

Kirkpatrick, R. J., 1981, Kinetics of crystallization of igneous rocks: Reviews In Mineralogy, Mineralogical Society of America, Washington, DC, p. 321–395.

Kohut, E., and Nielsen, R. L., 2004, Melt inclusion formation mechanisms and compositional effects in high-An feldspar and high-Fo olivine in anhydrous mafic silicate liquids: Contributions to Mineralogy and Petrology, v. 147, no. 6, p. 684–704.

Kouchi, A., Tsuchiyama, A., and Sunagawa, I., 1986, Effect of stirring on crystallization kinetics of basalt; texture and element partitioning: Contributions to Mineralogy and Petrology, v. 93, no. 4, p. 429–438.

Kristjánsson, K., 2003, Vestfjarðavegur nr. 60, Bjarkalundur - Eyri í Reykhólahreppi í Austur-Barðastrandarsýslu. Tillaga að Matsáætlun. Vegagerðin.

Larsen, J. F., 2005, Experimental study of plagioclase rim growth around anorthite seed crystals in rhyodacitic melt: American Mineralogist, v. 90, p. 417–427.

Lénat, J.-F., Bachelery, P., and Desmulier, F., 2001, Genèse du champ de lave de l' Enclos Fouqué; une éruption d'envergure exceptionnelle du Piton de la Fournaise (Réunion) au 18^{e} siècle: Bulletin de la Société Géologique de France, v. 172, no. 2, p. 177–188.

Lesher, C. E., Cashman, K. V., and Mayfield, J. D., 1999, Kinetic controls on crystallization of Tertiary North Atlantic basalt and implications for the emplacement and cooling history of lava at Site 989, Southeast Greenland rifted margin, *in* Proceedings of the Ocean Drilling Program, Scientific Results, v. 163, p. 135–148.

Lipman, P. W., Banks, N. G., and Rhodes, J. M., 1985, Degassing-induced crystallization of basaltic magma and effects on lava rheology: Nature, v. 317, no. 6038, p. 604–607.

Lipman, P. W., and Banks, N. G., 1987, Aa flow dynamics, Mauna Loa 1984: United States Geological Survey Professional Paper no. 1350, p. 1527–1567.

Lofgren, G., 1980, Experimental studies on the dynamic crystallization of silicate melts, Physics of Magmatic Processes: Princeton University Press, Princeton, NJ, p. 487–565.

Lofgren, G. E., 1983, Effect of Heterogeneous Nucleation on Basaltic Textures - a Dynamic Crystallization Study: Journal of Petrology, v. 24, no. 3, p. 229–255.

Long, P. E., and Wood, B. J., 1986, Structures, textures, and cooling histories of Columbia River Basalt flows: Geological Society of America Bulletin, v. 97, no. 9, p. 1144–1155.

Longhi, J., Walker, D., and Hays, J. F., 1976, Fe and Mg in plagioclase, *in* Proceedings Lunar Science Conference 7th, p. 1281–1300.

Lowry, R. K., Henderson, P., and Nolan, J., 1982, Tracer diffusions of some alkali, alkaline-earth and transition element ions in a basaltic and an andesitic melt, and the implications concerning melt structure: Contributions to Mineralogy and Petrology, v. 80, no. 3, p. 254–261.

Marsh, B. D., 1988, Crystal size distribution (CSD) in rocks and the kinetics and dynamics of crystallization; 1, Theory: Contributions to Mineralogy and Petrology, v. 99, no. 3, p. 277–291.

Marsh, B. D., 1998, On the interpretation of crystal size distributions in magmatic systems: Journal of Petrology, v. 39, no. 4, p. 553–599.

Mattox, T. N., Heliker, C., Kauahikaua, J., and Hon, K., 1993, Development of the 1990 Kalapana Flow-Field, Kilauea Volcano, Hawaii: Bulletin of Volcanology, v. 55, no. 6, p. 407–413.

McMillan, K., Long, P. E., Cross, R. W., Reidel, S. P., and Hooper, P. R., 1989, Vesiculation in Columbia River Basalts, Geological Society of America Special Paper no. 279, p. 157–167.

Metrich, N., Sigurdsson, H., Meyer, P. S., and Devine, J. D., 1991, The 1783 Lakagigar eruption in Iceland; geochemistry, CO_2 and sulfur degassing: Contributions to Mineralogy and Petrology, v. 107, no. 4, p. 435–447.

Metrich, N., and Rutherford, M. J., 1998, Low pressure crystallization paths of H_2O-saturated basaltic-hawaiitic melts from Mt. Etna; implications for open-system degassing of basaltic volcanoes: Geochimica et Cosmochimica Acta, v. 62, no. 7, p. 1195–1205.

Mock, A., and Jerram, D. A., 2005, Crystal size distributions (CSD) in three dimensions: insights from the 3D reconstruction of a highly porphyritic rhyolite: Jounal of Petrology, v. 46, no. 8, p. 1525–1541.

Montierth, C., Johnston, A. D., and Cashman, K. V., 1995, An empirical glass-composition-based geothermometer for Mauna Loa lavas, Geophysical Monograph no. 92, p. 207–217.

Morgan, D. J., and Jerram, D. A., 2006, On estimating crystal shape for crystal size distribution analysis: Journal of Volcanology and Geothermal Research (in press).

Natland, J. H., 1980, Crystal morphologies in basalts dredged and drilled from the East Pacific Rise near 9 degrees N and the Siqueiros fracture zone: Initial Reports of the Deep Sea Drilling Project, v. LIV, p. 605–634.

Oze, C., and Winter, J. D., 2005, The occurrence, vesiculation, and solidification of dense blue glassy pahoehoe: Journal of Volcanology and Geothermal Research, v. 142, p. 285–301.

Oskarsson, N., Sigvaldason, G. E., and Steinthorsson, S., 1982, A dynamic model of rift zone petrogenesis and the regional petrology of Iceland: Journal of Petrology, v. 23, no. 1, p. 28–74.

Oskarsson, B. V., 2005, Lava-rise structures in pahoehoe and a'a: Examples from the Hrutagja lava shield and Kapelluhraun a'a flow-field on the Reykjanes peninsula, B.Sc-Thesis, University of Iceland, Reykjavik, Iceland.

Pan, Y., 2001, Inherited correlation in crystal size distribution: Geology, v. 29, no. 3, p. 227–230.

Panjasawatwong, Y., Danyushevsky, L. V., Crawford, A. J., and Harris, K. L., 1995, An experimental study of the effects of melt composition on plagioclase; melt equilibria at 5 and 10 kbar; implications for the origin of magmatic high-An plagioclase: Contributions to Mineralogy and Petrology, v. 118, no. 4, p. 420–432.

Passmore, E., Maclennan, J., and Fitton, G., 2006, Quantifying geochemical variation in basalt from Laki, southeast Iceland: Volcanic and Magmatic Studies Group Annual Meeting, Leeds, UK (abstract).

Peterson, D. W., and Tilling, R. I., 1980, Transition of basaltic lava from pahoehoe to aa, Kilauea Volcano, Hawaii; field observations and key factors: Journal of Volcanology and Geothermal Research, v. 7, p. 271–293.

Philpotts, A. R., and Carroll, M., 1996, Physical properties of partly melted tholeiitic basalt: Geology, v. 24, no. 11, p. 1029–1032.

Philpotts, A. R., and Lewis, C. L., 1987, Pipe vesicles—an alternate model for their origin: Geology, v. 15, no. 10, p. 971–974.

Pinkerton, H., and Norton, G., 1995, Rheological properties of basaltic lavas at sub-liquidus temperatures; laboratory and field measurements on lavas from Mount Etna: Journal of Volcanology and Geothermal Research, v. 68, no. 4, p. 307–323.

Pinkerton, H. and Stevenson, R. J., 1992, Methods of determining the rheological properties of magmas at sub-liquidus temperatures: Journal of Volcanology and Geothermal Research, v. 53, p. 47–66.

Pinkerton, H., and Sparks, R. S. J., 1976, The 1975 sub-terminal lavas, Mount Etna; a case history of the formation of a compound lava field: Journal of Volcanology and Geothermal Research, v. 1, no. 2, p. 167–182.

Pinkerton, H., James, M., and Jones, A., 2002, Surface temperature measurements of active lava flows on Kilauea Volcano, Hawai'i: Journal of Volcanology and Geothermal Research, v. 113, no. 1-2, p. 159–176.

Polacci, M., Cashman, K. V., and Kauahikaua, J. P., 1999, Textural characterization of the pahoehoe-'a'a transition in Hawaiian basalt: Bulletin of Volcanology, v. 60, no. 8, p. 595–609.

Putirka, K., Johnson, M., Kinzler, R., Longhi, R., and Walker, D., 1996, Thermobarometry of mafic igneous rocks based on clinopyroxene-liquid equilibria, 0–30 kbar: Contributions to Mineralogy and Petrology, v. 123, no. 1, p. 92–108.

Putirka, K. D., Mikaelian, H., Ryerson, F., and Shaw, H., 2003, New clinopyroxene-liquid thermobarometers for mafic, evolved, and volatile-bearing lava composition, with applications to lavas from Tibet and the Snake River plain, Idaho: American Mineralogist, v. 88, no. 10, p. 1542–1554.

Putirka, K. D., 2005, Igneous thermometers and barometers based on plagioclase+liquid equilibria; tests of some existing models and new calibrations: American Mineralogist, v. 90, no. 2-3, p. 336–346.

Ramsey, M. H., Potts, P. J., Webb, P. C., Watkins, P., Watson, J. S., and Coles, B. J., 1995, An objective assessment of analytical method precision: comparison of ICP-AES and XRF for the analysis of silicate rocks: Chemical Geology, v. 124, no. 1–2, p. 1-19.

Randolph, A. D., and Larson, M. A., 1971, Theory of particulate processes: Academic Press, New York & London, 251 p.

Reidel, S. P., Tolan, T. L., Hooper, P. R., Beeson, M. H., Fecht, K. R., Bentley, R. D., and Anderson, J. L., 1989, The Grande Ronde Basalt, Columbia River Basalt Group; stratigraphic descriptions and correlations in Washington, Oregon, and Idaho: Geological Society of America Special Paper no. 279, p. 21–53.

Rowland, S. K., and Munro, D. C., 1993, The 1919-1920 Eruption of Mauna-Iki, Kilauea - chronology, geologic mapping, and magma transport mechanisms: Bulletin of Volcanology, v. 55, no. 3, p. 190–203.

Rowland, S. K., and Walker, G. P. L., 1987, Toothpaste lava; characteristics and origin of a lava structural type transitional between pahoehoe and aa: Bulletin of Volcanology, v. 49, no. 4, p. 631–641.

Rowland, S. K., and Walker, G. P. L., 1990, Pahoehoe and aa in Hawaii; volumetric flow rate controls the lava structure: Bulletin of Volcanology, v. 52, no. 8, p. 615–628.

Russell, J. K., Nicholls, J., Stanley, C. R., and Pearce, T. H., 1990, Pearce element ratios; a paradigm for testing hypotheses, *in* Eos, Transactions, American Geophysical Union, v. 71, no. 5, p. 234-236, 246–247.

Russell, J. K., and Nicholls, J., 1988, Analysis of petrologic hypotheses with Pearce element ratios: Contributions to Mineralogy and Petrology, v. 99, no. 1, p. 25–35.

Saar, M. O., Manga, M., Cashman, K. V., and Fremouw, S., 2001, Numerical models of the onset of yield strength in crystal-melt suspensions: Earth and Planetary Science Letters, v. 187, no. 3-4, p. 367–379.

Saemundsson, K., 1992, Geology of the Thingvallavatn area: OIKOS v. 64, p 40–68.

Saemundsson, K., 1995, Hengill, jarðfræðikort (berggrunnur), 1:50.000, Orkustofnun, Hitaveita Reykjavíkur og Landmælingar Íslands.

Samoylovich, Y. A., 1979, Oscillatory crystallization of a magma: Geochemistry International, v. 16, no. 3, p. 79–84.

Sato, H., Ida, Y., and Voight, B., 1995, Textural difference between pahoehoe and aa lavas of Izu-Oshima volcano, Japan; an experimental study on population density of plagioclase: Journal of Volcanology and Geothermal Research, v. 66, p. 101–113.

Schiffman, P., and Lofgren, G. E., 1982, Dynamic crystallisation studies on the grande ronde pillow basalts, Central Washington: Jounal of Petrology, v. 90, p. 49–78.

Scholze, H., 1959, Der Einbau des Wassers in Glasern: Glastechnische Berichte, v. 32, p. 81-88, 142-145, 278-281.

Self, S., Thordarson, T., Keszthelyi, L., Walker, G. P. L., Hon, K., Murphy, M. T., Long, P., and Finnemore, S., 1996, A new model for the emplacement of Columbia River Basalts as large, inflated pahoehoe lava flow fields: Geophysical Research Letters, v. 23, no. 19, p. 2689–2692.

Self, S., Thordarson, T., and Keszthelyi, L., 1997, Emplacement of continental flood basalt lava flows: Geophysical monograph no. 100, American Geophysical Union, p. 381–410.

Self, S., Keszthelyi, L., and Thordarson, T., 1998, The importance of pahoehoe: Annual Review of Earth and Planetary Sciences, v. 26, p. 81–110.

Shaw, H. R., 1965, Comments on viscosity, crystal settling, and convection in granitic magmas: American Journal of Science, v. 263, no. 2, p. 120–152.

Shaw, H. R., 1972, Viscosities of magmatic silicate liquids; an empirical method of prediction: American Journal of Science, v. 272, no. 9, p. 870–893.

Sigmarsson, O., Condomines, M., Gronvold, K., and Thordarson, T., 1991, Extreme magma homogeneity in the 1783-84 Lakagigar eruption; origin of a large volume of evolved basalt in Iceland: Geophysical Research Letters, v. 18, no. 12, p. 2229–2232.

Sinton, J., Grönvold, K., and Sæmundsson, K., 2005, Postglacial eruptive history of the Western volcanic zone, Iceland: Geochemistry, Geophysics and Geosystems, v. 6, Q12009, doi:10.1029/2005GC001021.

Sisson, T. W., and Grove, T. L., 1993, Experimental investigations of the role of H_2O in calc-alkaline differentiation and subduction zone magmatism: Contributions to Mineralogy and Petrology, v. 113, no. 2, p. 143–166.

Soule, S. A., Cashman, K. V., and Kauahikaua, J. P., 2004, Examining flow emplacement through the surface morphology of three rapidly emplaced, solidified lava flows, Kilauea Volcano, Hawai'i: Bulletin of Volcanology, v. 66, no. 1, p. 1–14.

Soule, S. A., and Cashman, K. V., 2005, Shear rate dependence of the pahoehoe-to-'a'a transition; Analog experiments: Geology, v. 33, no. 5, p. 361–364.

Sparks, R. S. J., Murphy, M. D., Lejeune, A. M., Watts, R. B., Barclay, J., and Young, S. R., 2000, Control on the emplacement of the andesite lava dome of the Soufriere Hills Volcano, Montserrat by degassing-induced crystallization: Terra Nova, v. 12, no. 1, p. 14–20.

Sparks, R. S. J., and Pinkerton, H., 1978, Effect of Degassing on Rheology of Basaltic Lava: Nature, v. 276, no. 5686, p. 385–386.

Steingrímsson, J., 1788, Fires of the earth; the Laki eruption 1783-1784: Reykjavik, Iceland, Nordic Volcanological institute and the University of Iceland Press, 93 p. (English translation of the original 1788 text).

Stolper, E., 1982, Water in silicate glasses; an infrared spectroscopic study: Contributions to Mineralogy and Petrology, v. 81, no. 1, p. 1-17.

Sugawara, T., 2000, Thermodynamic analysis of Fe and Mg partitioning between plagioclase and silicate liquid: Contributions to Mineralogy and Petrology, v. 138, no. 2, p. 101–113.

Swanson, D. A., 1973, Pāhoehoe flows from the 1969-1971 Mauna Ulu Eruption, Kilauea Volcano, Hawaii: Geological Society of America Bulletin, v. 84, p. 615–626.

Swanson, D. A., and Fabbi, B. P., 1973, Loss of volatiles during fountaining and flowage of basaltic lava at Kilauea volcano, Hawaii: Journal of Research of the United States Geological Survey, v. 1, no. 6, p. 649–658.

Swanson, D. A., Wright, T. L., Hooper, P. R., and Bentley, R. D., 1979, Revisions in stratigraphic nomenclature of the Columbia River basalt Group: United States Geological Survey Bulletin no. 1457-G, 59 p.

Swanson, S. E., Naney, M. T., Westrich, H. R., and Eichelberger, J. C., 1989, Crystallization history of Obsidian Dome, Inyo Domes, California: Bulletin of Volcanology, v. 51, no. 3, p. 161–176.

Thordarson, T., 1995, Volatile release and atmospheric effects of basaltic fissure eruptions [Ph.D. thesis]: University of Hawaii, Honolulu, 570 p.

Thordarson, T., and Hoskuldsson, A., 2002, Iceland, Classic Geology in Europe 3: Terra Publishing, 200 p.

Thordarson, T., and Self, S., 1996, Sulfur, chlorine and fluorine degassing and atmospheric loading by the Roza eruption, Columbia River Basalt Group, Washington, USA: USA. Journal of Volcanology and Geothermal Research, v. 74, p. 49–73.

Thordarson, T., and Self, S., 1993, The Laki (Skaftár Fires) and Grímsvötn eruptions in 1783–1785: Bulletin of Volcanology, v. 55, no. 4, p. 233–263.

Thordarson, T., and Self, S., 1998, The Roza Member, Columbia River Basalt Group; a gigantic pahoehoe lava flow field formed by endogenous processes?: Journal of Geophysical Research, v. 103, no. B11, p. 27,411–27,445.

Thordarson, T., Self, S., Óskarsson, N, and Hulsebosch, T., 1996, Sulfur, chlorine and fluorine degassing and atmospheric loading by the 1783—1784 AD Laki (Skaftar Fires) eruption in Iceland: Bulletin of Volcanology, v. 58, p. 205–225.

Thordarson, T., Miller, D. J., Larsen, G., Self, S., and Sigurdsson, H., 2001, New estimates of sulfur degassing and atmospheric mass-loading by the 934 AD Eldgja eruption, Iceland: Journal of Volcanology and Geothermal Research, v. 108, p. 33–54.

Thordarson, T., Miller, J., Larsen, G., 1998, New data on the age of the Leidolfsfell Cone Group in south Iceland: Jökull, v. 46, p. 3–15.

Thordarson, T. L., Larsen, G., Steinthorsson, S., Self, S., 2003, The 1783–1785 A.D. Laki-Grímsvötn eruptions II: Appraisal based on contemporary accounts: Jökull, v. 53, p. 11–48.

Thornber, C. R., 2001, Olivine-liquid relations of lava erupted by Kilauea Volcano from 1994 to 1998; implications for shallow magmatic processes associated with the ongoing east-rift-zone eruption: Mineralogical Association of Canada, v. 39, p. 239–266.

Tolan, T. L., Reidel, S. P., Beeson, M. H., Anderson, J. L., Fecht, K. R., Swanson, D. A., and Hooper, P. R., 1989, Revisions to the estimates of the areal extent and volume of the Columbia River Basalt Group: Geological Society of America Special Paper no. 279, p. 1–20.

Tsuchiyama, A., 1985, Crystallization kinetics in the system $CaMgSi_2O_6$–$CaAl_2Si_2O_8$; development of zoning and kinetics effects on element partitioning: American Mineralogist, v. 70, no. 5–6, p. 474–486.

Vance, J. A., 1969, On synneusis: Contributions to Mineralogy and Petrology, v. 24, no. 1, p. 7–29.

Vikingsson, S., Eiriksson, J., Hjarrtarson, A., Norddahl, H., Johannesson, H., Saemundsson, K., and Torfason, H., 1995, Map of superficial deposits, Ellidavatn 1613/III SV-J, 1:25000: Iceland Geodetic Survey, National Energy Authority, and the towns of Gardabaer, Hafnarfjordur, Kopavogur, Seltjarnarnes and the City of Reykjavik.

Walker, G. P. L., 1987, Pipe vesicles in Hawaiian basaltic lavas: Their origin and potential as paleoslope indicators: Geology, v. 15, p. 84–87.

Walker, G. P. L., 1989, Spongy Pahoehoe in Hawaii - a Study of Vesicle-Distribution Patterns in Basalt and Their Significance: Bulletin of Volcanology, v. 51, p. 199–209.

Walker, G. P. L., 1991, Structure, and origin by injection of lava under surface crust, of tumuli, lava rises, lava-rise pits, and lava-inflation clefts in Hawaii: Bulletin of Volcanology, v. 53, no. 7, p. 546–558.

Walker, D., Kirkpatrick, R. J., Longhi, J., and Hays, J. F., 1976, Crystallization history of lunar picritic basalt sample 12002: Phase equilibria and cooling-rate studies: Geological Society of America Bulletin, v. 87, p. 646–656.

Walker, D., Powell, M. A., Lofgren, G. E., and Hays, J. F., 1978, Dynamic crystallization of a eucrite basalt, *in* Proceedings Lunar Planetary Science Conference 9th, p. 1369–1391.

Watson, E. B., 1981, Diffusion in magmas at depth in the Earth; the effects of pressure and dissolved H_2O: Earth and Planetary Science Letters, v. 52, no. 2, p. 291–301.

Wentworth, C. K., and Macdonald, G. A., 1953, Structures and forms of basaltic rocks in Hawaii: United States Geological Survey Bulletin, v. 994, p. 1–98.

Wilson, S.A., 1997, Data compilation for United States Geological Survey reference material BHVO-2, Hawaiian Basalt: United States Geological Survey Open-File Report.

Wood, C., and Watts, R., 2002, Laki Underground 2000: School of conservation Sciences, Bournemouth University, UK, 32 p.

Wright, T. L., and Okamura, R. T., 1977, Cooling and crystallization of tholeiitic basalt, 1965 Makaopuhi lava lake, Hawaii: United States Geological Survey Professional Paper no. 1004.

Yoder, H. S., Jr., and Tilley, C. E., 1956, Natural tholeiite basalt-water system: Geological Society of America Bulletin, v. 67, no. 12, p. 1746–1747.

Zieg, M. J., and Marsh, B. D., 2002, Crystal size distributions and scaling laws in the quantification of igneous textures: Journal of Petrology, v. 43, no. 1, p. 85–101.

Appendix A: Methods of textural analysis

A1. Modal analysis

This technique is used in Chapters 2 and 3 to quantify differences in the texture of tephra and lava samples. The proportion of each crystal type (i.e., phenocrysts, microphenocrysts, and microlites) was estimated using manual point counting under an optical microscope. Modal analysis was conducted using automated image analysis of electron microprobe backscatter images (BSE), using the software Scion Image. Differences between the results both methods in total crystal content (see Tables 3.3 and 3.4) can be attributed to the distinct scales of the areas studied and related detection limits.

Point-counting. Point counts were done on selected thin-sections using count totals of 500 to 1000, and following a standard procedure. Soon after I started to use the equipment it broke down, so that I had to develop the method of image analysis of backscatter images instead (see below). Yet, the few measurements conducted provide reliable information that is presented and discussed in Chapter 3.

Software-assisted analysis of backscatter electron (BSE) images. This method exploits the difference in grey tone of plagioclase (dark), clinopyroxene (grey to light grey), and olivine (light grey to white) on BSE images. BSE images were acquired on the microprobe, using a beam of 1 μm and a resolution of 1024 × 768 pixels per image. About ten images per thin-section were commonly analyzed to account for natural textural variability. The software Scion Image (NIH version for PC) was used for automated analysis of the images. Each separate mineral phase was treated separately. The procedure adopted is as follows. The images were scaled at 0.4 pix/μm using the function *Set scale* in the menu *Analyse*. The range of grey values corresponding to the mineral phase analyzed was selected using the *Density Slice* option in the menu *Option*. The pixels selected were then converted into black and the background to white using the function *Make Binary* in the menu

Process/binary. The function *Analyze particles* in the menu *Analyse* was then used to carry out the automatic count of these objects and determine the area of each continuous object in μm^2. A minimum size value was specified to avoid overestimating the objects by including small defects in the count. It was set at 3 μm^2 for plagioclases and 5 μm^2 for clinopyroxenes and olivines. The remaining area (not counted as crystals or vesicles) was reported as groundmass (crystal size < 5 μm^2, or glass). Plagioclases were particularly appropriate for that treatment, given that they have a distinctly-low atomic number compared to the glass and the other crystals. By contrast, clinopyroxene and olivine spread over a large and overlapping range of colour on BSE images, largely because of their compositional zoning. This then results in higher uncertainties in their respective proportion, which shows in the high standard deviations of the results (see Fig. 3.7, Table 3.4).

A similar procedure was used to estimate the vesicularity of some samples, using high-resolution photographs of thin-sections. Limitations of this technique reside in the great disparity of vesicularity between thin-sections from the same sample and in different textural zones in the lava.

A2. Collection of crystal size data for Crystal Distribution Analysis

Used for CSD analysis of Laki surface samples in Chapter 3, and internal lava samples in Chapter 4, the apparent short axis (width) and long axis (length) of all plagioclase crystals present in a finite area were measured on selected BSE images, using the hand-measurement tool provided by Scion Image. The use of automatic image analysis was not found appropriate for the precise quantification of crystal numbers and sizes because of its high sensitivity to small defects on the images and also, more importantly, joined crystals could not be resolved (i.e., they would be counted as a single crystal of larger size).

The size of the BSE image was chosen so as to over 300 crystals would be counted and measured for each sample, in accord with the minimum sampling size of 200 recommended by Mock & Jerram (2005) from a comparative study of CSDs constructed from 2D thin-sections to 3D analysis. Increasing the number of crystals measured (and thus the area studied) generally resulted in some variations in the number density of crystals because of natural textural heterogeneities, but this did not seem to have a significant impact on the slope of the CSD curves obtained.

The main concern was about distinguishing individual crystals that are touching, and may thus appear as a large individual crystal on the BSE images. This required some subjective judgment. This dilemma could however be resolved in most cases from the geometry of the aggregate, since individual crystals often have different length and slightly different orientation, and also some small gaps between them. Parallel branching crystals were generally considered are separate entities, although this is discussable. It indeed depends on the time at which crystals were completely jointed, and thus grew as a single entity, which cannot be known. Working on high-contrast BSE images appeared to be helpful in reducing these possible sources of errors since the more evolved crystal rims would often appear in a darker tone than their cores (see Fig. A1). The erroneous interpretation of some crystal aggregates as single crystals probably shows in the scatter of the CSD data at larger crystal sizes (also recognized by Cashman & Marsh, 1988). Crystals that were truncated by the edge of the image were not considered in the analysis, which may have caused some artificial decrease in the number of crystals measured in coarse samples.

To limit the artificial variations introduced by these problems, a strict procedure was followed that includes five major steps:

1) Cropping of the central part of the selected BSE image to limit the effects of photographic deformation along the edges. Saving of the image as greyscale and in a tif format. Printing of the image at large scale (A4 landscape).
2) Importation of the image in Scion Image software. Definition of the scale (fixed scale of 0.4 μm/pixel).
3) Measure of the total size of the image analyzed (in area) and modal analysis of each mineral phase using *threshold* for vesicles, *invert* + *threshold* for oxides, and *density slice* for plagioclase, clinopyroxene, olivine (see details above). Copy of the results into an Excel spreadsheet.
4) Measure of each crystal short and long axis using hand tool, drawing white lines across crystals. Writing of the set of measure by hand on a paper sheet. Saving of the final image to allow later check (see Fig. A1).
5) Typing of the numbers (dimensions of crystals) onto excel spreadsheet (see data in Appendix B). Plot of the CSD curves using parameters given by applying the program by Higgings (2000) on crystal width data as explained in text (see Fig. 4.24 caption for details). Selection of range of size adequate (see text) and use of the function *Add trend-line* in Microsoft Excel to get the slope and the intercept of the line best fitting the data. Calculation of the textural parameters and rates of crystallization using equations presented in text.

Figure A1: Plagioclase dimensions measured on a high-contrast backscatter image (sample AD4). Note zoning at border of crystals that was used to distinguish individual crystals in intergrowth.